2010-10-01

Extracting Physical and Environmental Information of Irish Roads Using Airborne and Mobile Sensors

Salman Mumtaz
Technological University Dublin

Recommended Citation

Mumtaz, S.A. (2010) *Extracting Physical and Environmental Information of Irish Roads Using Airborne and Mobile Sensors.* Doctoral Thesis. Dublin, Technological University Dublin. doi:10.21427/D7F01M

Extracting Physical and Environmental Information of Irish Roads Using Airborne and Mobile Sensors

Presented in Partial Fulfillment of the Requirements for

the Degree Doctor of Philosophy in the

Department of Spatial Information Sciences

The Dublin Institute of Technology

By

Engr. Salman Ali Mumtaz (M.Sc.)

12th October 2010

Supervisors:
Mr. Kevin Mooney (Senior Lecturer)[1]
Dr. Eugene Mc Govern [1]
Prof. Dr. -Ing. Eberhard Gülch[2]

[1] Department of Spatial Information Sciences
The Dublin Institute of Technology
Dublin, Ireland.
[2] Department of Geomatics, Computer Science and Mathematics
Stuttgart University of Applied Sciences
Stuttgart, Germany.

Declaration

I certify that this thesis, which I now submit for examination for the award of PhD degree, is entirely my own work and has not been taken from the work of others, save and to the extent that, such work has been cited and acknowledged within the text of my work.

This thesis was prepared according to the regulations for postgraduate study by research of the Dublin Institute of Technology and has not been submitted in whole or in part for another award in any Institute.

The work reported on in this thesis conforms to the principles and requirements of the Institute's guidelines for ethics in research.

The Institute has permission to keep, lend or copy this thesis in whole or in part, on condition that any such use of the material of the thesis be duly acknowledged.

Signature ___________________________________ Date ________________

Candidate

Abstract

Airborne sensors including LiDAR and digital cameras are now used extensively for capturing topographical information as these are often more economical and efficient as compared to the traditional photogrammetric and land surveying techniques. Data captured using airborne sensors can be used to extract 3D information important for, inter alia, city modelling, land use classification and urban planning. According to the EU noise directive (2002/49/EC), the National Road Authority (NRA) in Ireland is responsible for generating noise models for all roads which are used by more than 8,000 vehicles per day. Accordingly, the NRA has to cover approximately 4,000 km of road, 500m on each side. These noise models have to be updated every 5 years. Important inputs to noise model are digital terrain model (DTM), 3D building data, road width, road centre line, ground surface type and noise barriers.

The objective of this research was to extract these objects and topographical information using nationally available datasets acquired from the Ordnance Survey of Ireland (OSI). The OSI uses ALS50-II LiDAR and ADS40 digital sensors for capturing ground information. Both sensors rely on direct georeferencing, minimizing the need for ground control points.

Before exploiting the complementary nature of both datasets for information extraction, their planimetric and vertical accuracies were evaluated using independent ground control points. A new method was also developed for registration in case of any mismatch. DSMs from LiDAR and aerial images were used to find common points to determine the parameters of 2D conformal transformation. The developed method was also evaluated by the EuroSDR in a project which involved a number of partners. These measures were taken to ensure that the inputs to the noise model were of acceptable accuracy as recommended in the report (Assessment of Exposure to Noise, 2006) by the European Working Group.

A combination of image classification techniques was used to extract information by the fusion of LiDAR and aerial images. The developed method has two phases, viz. object classification and object reconstruction. Buildings and vegetation were classified based on Normalized Difference Vegetation Index (NDVI) and a normalized digital surface model (nDSM). Holes in building segments were filled by object-oriented multi-resolution segmentation. Vegetation that remained amongst buildings was classified using cues obtained from LiDAR. The short comings there in were overcome by developing an additional classification cue using multiple returns. The building extents were extracted and assigned a single height value generated from LiDAR nDSM. The extracted height was verified against the ground truth data acquired using terrestrial survey techniques.

Vegetation was further classified into three categories, viz. trees, hedges and tree clusters based on shape parameter (for hedges) and distance from neighbouring trees (for clusters). The ground was classified into three surface types i.e. roads and parking area, exposed surface and grass. This was done using LiDAR intensity, NDVI and nDSM.

Mobile Laser Scanning (MLS) data was used to extract walls and purpose built noise barriers, since these objects were not extractable from the available airborne sensor data. Principal Component Analysis (PCA) was used to filter points belonging to such objects. A line was then fitted to these points using robust least square fitting.

The developed object extraction method was tested objectively in two independent areas namely the Test Area-1 and the Test Area-2. The results were thoroughly investigated by three different accuracy assessment methods using the OSI vector data. The acceptance of any developed method for commercial applications requires completeness and correctness values of 85% and 70% respectively. Accuracy measures obtained using the developed method of object extraction recommend its applicability for noise modelling.

Keywords: LiDAR, Fusion, Object Extraction, Noise Modelling

DEDICATION

This is to

My Parents

(Late Mumtaz Ali, for being a loving father who I know would be very proud of me today)

(Rukhsana Khan, my mother who is my strength and for whom I am still a child)

And

Sarah Samdani

(For being my motivation, a loving wife and a great friend)

Acknowledgements

I would like to express my deepest and sincerest gratitude to

The Almighty for watching over me and blessing me at each and every step I take in life, for giving me the wisdom to undertake this challenge and the strength and the inspiration to complete it.

Mr. Kevin Mooney, my supervisor, for frequently going above and beyond his duties to provide me with excellent supervision, for sharing his thoughts on the topic with me, for providing useful feedback and advice at every stage particularly during the development of the methodology, for helping me improve the quality of my research and for being the nicest supervisor a research student can possibly wish for.

Prof. Dr. -Ing. Eberhard Gülch, my supervisor at the Stuttgart University of Applied Sciences, for providing his deep insight and expertise on the topic, for taking a continued interest in the completion of this study by providing timely guidance and scheduling regular meeting sessions to monitor the progress and for giving me the liberty to use Ecognition software through the server of the Stuttgart University.

Dr. Eugene Mc Govern, also my supervisor for demonstrating the equipment usage of the Network RTK system and the reflectorless total station for measuring building heights to me and for reading my draft chapters and giving useful feedback.

The staff at the National Roads Authority, Ireland (NRA) for detailing the requirements of noise modelling in Ireland and providing information about the datasets accessible to them.

Ordinance Survey Ireland for being extremely accommodating and providing the data sets used in this research.

Dr. Tim McCarthy at the National University of Ireland at Maynooth for providing mobile laser scanning data for the Test Area-2.

The administrative staff at the DIT for their continued assistance throughout the course of this study.

Sarah, my wife for her perpetual love, support and patience, for being the most consistent source of encouragement throughout this journey, for preparing countless meals and cakes which are always an exquisite culinary experience, for proof reading my thesis at the expense of her own work and for always reminding me that I can do this.

Those back home for their prayers and unconditional love especially my mother for always placing her trust and pride in me, for always wishing the best for me and for always fretting over the slightest details concerning me. I owe everything that I am today to you.

All my friends here in Ireland for the fun filled weekends and an immensely memorable time. A special thanks to Shahzaib for assisting me with my field work at Maynooth.

The fellow researchers at Zhivago building who helped in brightening the daily routine namely Tadgh O' Mahony, who has shared the research room with me for the longest, Martin Somers for being extremely kind assisting me with my field work, Dorothy Stewart for her cheerfulness and liveliness and Frank Bondzio who inspires me with his energy and love for the outdoors. Finally, I would like to thank to all those who have helped and inspired me in any way during my doctoral study.

Abbreviations

2D	2 Dimensional
3D	3 Dimensional
AD	Anisotropic Diffusion
ADS	Airborne Digital Sensor
ALS	Airborne Laser Scanning
BSP-Tree	Binary Space Partitioning Tree
CCD	Charge Coupled Device
DSM	Digital Surface Model
DTM	Digital Terrain Models
EU	European Union
EuroSDR	Euro Spatial Data Research
GCPs	Ground Control Points
GIS	Geographical Information System
GNSS	Global Navigation Satellite System
GPS	Global Positioning System
IMU	Inertial Measurement Unit
LAR	Least Absolute Residuals
LiDAR	Light Detection and Ranging

LPS	Leica Photogrammetric Suite
LRV	Local Range Variation
MLS	Mobile Laser Scanning
ND	Normalized Difference
nDSM	Normalized Digital Surface Model
NDVI	Normalized Difference Vegetation Index
NDWI	Normalized Difference Water Index
NIR	Near Infrared
NRA	National Roads Authority
OSI	Ordnance Survey Ireland
RGB	Red, Green, Blue
ROI	Republic of Ireland
RTK	Real Time Kinematic
SR	Surface Roughness
TLS	Terrestrial Laser Scanning
VSNs	Variance of Surface Normals

Table of Content

List of Figures

List of Tables

1 Introduction

1.1 Research Context

Roads have always been one of the basic pillars of economy and society. In the European Union, 44% of all goods are moved by trucks over roads and 81% of all people are transported by cars, buses or coaches on roads (Europa, 2010). As a society develops, road transport increases, and consequently the issues of noise pollution and road safety become more important. The European Commission Directive 2002/49/EC of 25th June, 2002 (European Parliament, Council, 2002) has resulted in a pressing need on part of the National Roads' Authorities in Europe to assess cost-effective and reliable methods for the modelling of physical objects within the environment of national roads. The directive requires that inter alia noise maps and action plans (noise policy) be developed for major roads with more than 6 million vehicle passages per year (approximately 8,000 per day), agglomerations with more than 250,000 inhabitants, major railways which have more than 60,000 train passengers per year and major airports. Limits L_{den} (noise level: day evening and night) and L_{night} (noise level: night) for major roads, railways and airports should be less than, or equal to, 55 dB and 50 dB respectively (WG-AEN, 2006). The European Environment Agency in Copenhagen, Denmark, collates the noise maps in a central European database. The first maps for major areas were required by mid 2007. Action plans for areas having noise levels greater than the prescribed limit were to be implemented within one year (mid 2008). These activities are to be repeated at five year intervals. All defined areas are to be completed by 30th June 2012 (European Parliament, Council Deadlines, 2002).

A European Commission Working Group provides a general description of all the objects and relevant input parameters required for noise modeling, in order to ensure high quality and consistency (WG-AEN, 2006). All participating countries are required to follow these guidelines in preparing strategic noise maps. A strategic noise map refers to a map designed for the global assessment of noise exposure in a given area due to different noise sources or overall predictions for such an area (WG-AEN, 2006). The working group suggests that every effort should be made to obtain actual local data, representative of the area being modelled. A brief overview of the important noise propagation model inputs is given by the working group which serves as a guide line for the NRA (National Roads Authority).

1.2 NRA Requirement of Noise Model

Any model that meets the requirements of the noise directive should be as detailed as possible and as a minimum, should contain the following topographic features (NRA, 2004).

1. Surface contours
2. Details of ground cover
3. All buildings in the vicinity of roads
4. Road alignments
5. Road surface details
6. Other significant features that may have a bearing on sound propagation, e.g. walls, crash barriers, bunds and side slopes.

WG-AEN (2006) sets the guidelines for how these inputs related to noise propagation can be acquired using different techniques, achievable accuracies and their effect on the overall accuracy of generated noise model. The report also compares different data acquisition techniques in terms of their financial suitability.

These topographic features can be subdivided into two categories. The first represents the physical properties of roads and the second constitutes the road environment.

1.2.1 Road Properties

The physical properties of roads have a direct relationship with the emission of sound from the vehicles. Important parameters related to the noise produced by vehicles are road gradient, road surface type, number of lanes and the location of roundabouts and intersections. WG-AEN (2006) recommends that the modelled road (or lane centre lines if these are used) should not normally fall outside the edge or perimeter of the road corridor.

1.2.2 Road Environment

1.2.2.1 Ground Surface Elevation (Contours)

Strategic noise maps are often prepared using contours with a vertical resolution of 5 m to 10 m. This resolution is inappropriate to generate noise propagation models near sources which might be located either in embankments or cuttings such as roads and railway lines. In order to obtain better height information accurate to 1 m, a DTM (Digital Terrain Model) from LiDAR is preferred over other data acquisition techniques.

1.2.2.2 Ground Surface Type

Ground surface type in the environment of the road needs to be mapped as it effects sound dissipation. Hard surface reflects more sound as compared to grassy surfaces. Noise modelling using a hard ground type for the whole area is the worst possible scenario. However; different ground types can exist in one area. The working group recommends that areas where ground surface change is less than 250 m^2 with respect to its neighbours should be ignored. It was also considered appropriate to ignore long, narrow areas of land where the length is less than 3 meters or narrow roads in the open country.

1.2.2.3 Noise Barriers

Noise barriers are built specifically closer to the source to reduce the noise propagation and should be modelled with high planimetric and vertical accuracy. Maximum allowable error in determining their position and height is 1 m and 0.5 m respectively.

1.2.2.4 Buildings

Accurate building height data is needed wherever possible. Different methods have been proposed for building height estimation such as counting the number of floors in each building or using a default height of 8 m for rural areas. However; it was recommended that these heights should be measured from aerial photographs, particularly for the urban areas. Depending upon the sources used for building height estimation, error expected in the determined noise levels has been provided by the working group which is less than 0.5 dB if the heights are measured using aerial photographs or LiDAR.

Simplifying shapes of buildings and other objects that may influence sound propagation is necessary to avoid complex calculations and computational time in noise propagation modelling. The working group warns that over simplification will reduce the model accuracy.

A building roof can consist of multiple parts. In order to keep the model simple and computationally less intensive, a single height value is typically assigned to each building block. The working group recommends that a single building with varying heights can be assigned the height of the majority of the building where the difference in these heights is no more than a specific figure, for example 2 m. Also, for all adjacent (connected) buildings, with similar heights, for example within 2 m, all can be assigned the lower of these heights.

1.2.2.5 Sound Absorption of Building Façades and Barriers

Sound is propagated by building façades and barriers directly and by reflections from other buildings or objects. Absorption coefficients are known for the commonly used construction materials or could be measured and incorporated into the noise model. If default values of absorption coefficients are used or measured in the field then the noise model will be accurate to 1 dB or 0.5 dB respectively.

These physical and environmental parameters of roads are the fundamental inputs and should be determined. Ground surface type and elevation, 2D (2 Dimensional) building boundaries with single height attribute, noise barriers, road surface and gradient, trees and forest patches were extracted in the course of this research, using high resolution multispectral aerial images, LiDAR and Mobile Laser Scanning (MLS) data.

1.3 Problem Statement

The National Roads Authority of Ireland, the organization responsible for producing noise maps, needs to survey approximately 4,000 km of national roads to an extent of 500 m on either side for the purpose of noise modelling. Acquisition of the required input data can be very expensive, time consuming and labour intensive if acquired manually. It is also not possible to do so without causing hindrance to road users. The need for economic, efficient and robust generation of this data to an acceptable accuracy is a key requirement which provides the main impetus for this research.

There is a need to investigate the currently available geo-data capturing sensors and the characteristics of their acquired data in the ROI for the successful extraction of all objects or features of interest. This is because of the dependency of the object extraction techniques on the used sensor and their acquired data characteristics. These technologies include both airborne (aerial images & LiDAR) and terrestrial (MLS) sensors. The extracted objects should be of acceptable accuracy as recommended by the working group and explained in the previous section.

1.4 Rationale Behind this Research

Geospatial information is mostly extracted from remotely sensed data acquired using airborne and space-borne platforms (Baltsavias and Gruen, 2003). These platforms offer varying spatial, radiometric and temporal resolutions. Traditional film-based aerial cameras provide panchromatic and visible true colour (Red, Green, Blue (RGB)) images. These images are mostly used for thematic land use or land cover mapping but not for land cover classification as the Near Infrared (NIR) band is missing. Multispectral bands in satellite imagery are however widely used for land cover classification where man made features can be efficiently separated from natural objects such as trees, grass and other vegetation using Red and NIR bands.

Object extraction in the urban areas requires individual buildings and trees to be modelled (Taubenböck et al., 2006) which is still not possible from commercially available satellite images, although spatial resolution has been increased to sub metre. Ireland has few full sunny days which make it impracticable to rely only on satellite data. For this reason, the national mapping agency Ordnance Survey Ireland (OSI) uses airborne sensors for mapping which provide flexible operational mobility and high spatial resolution up to 5 cm (Geosystems, 2010).

The Leica Airborne Digital Sensor (ADS) is a large format digital line scanner used by OSI which can capture multispectral images i.e. Red, Green, Blue and NIR. On board GNSS/IMU provides direct georeferencing minimizing the need for independent ground control points (GCPs). OSI also uses the ALS50-II LiDAR sensor. Data from both of these sensors is available to the NRA for extracting geospatial information and this research will evaluate their suitability to the noise mapping needs of the NRA.

The fusion of a Normalized Digital Surface Model (nDSM) generated by subtracting an extracted DTM (Digital Terrain Model) from a DSM (Digital Surface Model) combined with multispectral imagery is known to have applications in urban classification (Hill et al., 2002; Hodgson et al., 2003; Rottensteiner et al., 2005; Rottensteiner et al., 2007), building extraction (Haala and Brenner, 1999; Rottensteiner et al., 2005) and potentially in the extraction of objects adjacent to national roads.

The high spatial resolution of ADS imagery has significantly enhanced information content compared to space born data and the availability of NIR data facilitates land cover classification. However, traditional pixel-based approaches are unable to deliver high accuracy, robustness and automation in the object extraction process. For this reason, the focus has now been shifted from pixel-based statistical methods to knowledge and object based-classification approaches (Hodgson et al., 2003; Taubenböck et al., 2006). Moreover, it is not possible to discriminate between vegetation and buildings using only the NIR band because of shadows and spectral variations caused by apparent differences in roof composition. For the extraction of ground surface type attribute, it is necessary to classify trees and low level vegetation such as grass. Input from another sensor is required which can provide the height information that the aerial images lack, though this information may also be generated from stereo aerial images, if available.

LiDAR has proved its potential in generating a DSM with high vertical accuracy and has almost become an industry standard for capturing height information. Accuracy of LiDAR data is a function of the flying height, laser beam diameter (system dependent), the quality of the GNSS/IMU data and post-processing procedures. New sensors claim vertical accuracies in the range of 5 cm which are very difficult to achieve by digital photogrammetry. Modern LiDAR sensors can also record multiple returns of the reflected single pulse as well as the intensity of the returning pulse. With the advances in technology, pulse rates of LiDAR systems have also increased from a few Hertz to 200 kHz such as Leica ALS60 sensor, providing a dense point cloud. The potential for the automated determination of roadside objects from the fusion of the two airborne data sources available to the NRA is a significant motivation behind this research.

LiDAR and aerial images can be captured at different times, resulting in a mis-registration between both. Mis-registration needs to be considered, even if both data sets are captured at the same time, because errors in calibration might cause the same effects. This element of the research will help to assess the direct georeferencing capability of the ADS40 and ALS50-II sensors used routinely by the OSI for mapping in Ireland. If direct georeferencing can be used, the need for GCPs can be minimized for many applications including the collection of data for noise mapping.

High density point clouds may be generated by multi-ray image matching on imagery taken with multiple overlaps and of high radiometric quality provided by sensors such as the Leica ADS40 (Haala, 2009). The potential of this technique to eliminate the need for LiDAR data acquisition will be explored.

Apart from airborne sensors, ground based laser scanning systems, TLS and MLS are also growing in popularity for high density data acquisition from a different geometrical perspective for mapping the road environment. Helicopter LiDAR would provide possibilities to map such smaller scale objects, but it is very expensive. Objects difficult to extract via airborne LiDAR data can be extracted using these ground based systems. Building façade, façade type, poles, road markings and footpaths have been extracted successfully using these systems (Kukko et al., 2009). However; the utilization of ground based laser scanning systems in extracting noise barriers is still largely unexplored. MLS offers this possibility but is hampered by moving and standing objects or features (e.g. cars, trees) in front of the noise barriers. The issues of registration between MLS and ALS data for achieving better fusion results also need further investigation.

It is, therefore, a motivating factor for this research to assess the detection of vertical planes in MLS data to map noise barriers which are thin and continuous along the road that cannot be extracted in the routinely available airborne sensor data. This will be approached by applying airborne LiDAR point cloud processing algorithms to the ground based sensors or developing new algorithms and evaluating their performance.

In addition, noise maps need to be updated every five years which means that changes occurring during this time period need to be monitored and incorporated in the subsequent noise maps. A change detection methodology is therefore also required, that is capable of detecting changes in subsequently captured data and eliminating the need for object re-extraction.

1.5 Research Hypothesis and Aims

It is hypothesized that objects and features important for noise modelling can be extracted using multispectral aerial images, LiDAR and ground based MLS sensors or by the fusion of these, with a high degree of automation.

The principal aim of this research is to design and evaluate a method to extract objects and features important for noise modelling with a high degree of automation using nationally available sources of data. The study aims to achieve the above in the context of the spatial data needs of the NRA in meeting its obligations under the European Noise Directive.

1.6 Specific Objectives of the Research

The utilization of nationally available datasets for extracting objects or features important for noise modelling by the NRA rather than using specialized or customized data capturing systems, is a key element of this research. This will make the research findings more easily and economically implementable in the Republic of Ireland (ROI). The NRA has already taken appropriate actions for the acquisition of LiDAR data of all the roads for which noise maps have to be prepared.

The following specific objectives are to be met in the course of this research.

1. Devise a method using knowledge-based and object-based classification techniques for automatic or semi-automatic object extraction from airborne sources.
2. Test the method objectively using separate development and test areas.
3. Strive for a high degree of accuracy and robustness in the object extraction method that is verified by experiments.

4. Evaluate factors influencing the performance of the method such as:
   a. Optimal classification parameters for buildings, trees, vegetation and roads.
   b. Registration issues between LiDAR and aerial images.
   c. Evaluating performance of different object extraction softwares such as Terra Solid, Erdas Imagine, E-Cognition and LiDAR Analyst available for processing LiDAR and aerial images with respect to the effective fusion of data and quality of the results.
5. Explore the potential of high density image matching for the generation of point clouds as an alternative to LiDAR.
6. Explore the potential of incorporating MLS data in the extraction process, particularly in relation to the detection of noise barriers.
7. Devise and evaluate methods for detecting changes in roadside objects.
8. Make recommendations for the best application of available airborne and MLS sensor data and existing GIS data to noise modelling.

1.7 Available Data

Airborne sensors' data include LiDAR and aerial images provided by OSI for two sites in the ROI using ALS50-II and ADS40 sensors. Object extraction method was developed using portion of the data from one project site called the development area which was later tested independently in two test areas (Test Area-1 and Test Area-2). For one project site MLS data was also available. Sensor and captured data characteristics, project sites' location, the development and the test areas are described in detail in chapter 3.

Reference vector data for checking the accuracy of the object extraction method was also provided by OSI. Ground truth data was also collected for the two project sites to check direct georeferencing quality of airborne sensors and compare the height of extracted buildings to the heights measured in the field.

1.8 Method Outline

The broad outline of the method evaluated in this research, aimed at extracting object and terrain features for noise mapping by fusing LiDAR and aerial images, is provided in Figure 1. The detailed methods for extracting each object of interest are presented in their respective sections. This includes development of an object extraction work flow using the development area and testing the method in two other independent test areas of similar characteristics and covered by the same airborne sensors. The object extraction method consists of two phases.

In the first phase, direct georeferencing quality of ADS40 and ALS50-II sensors was evaluated using GCPs. It was important to check the quality of the direct georeferencing as it can minimize the need for independent ground control points, making the whole process simpler, faster and economically feasible. ADS40 panchromatic stereo images were used to generate a DSM using Leica Photogrammetric Suite (LPS) from Leica GeoSystems and Match-T from Inpho using image matching techniques. The point clouds and subsequently generated DSMs from image matching and LiDAR were also compared with the independent ground control points acquired using Network RTK GPS survey to check the vertical accuracy. The DSM obtained from image matching was also evaluated using LiDAR DSM to check its suitability as a replacement to LiDAR.

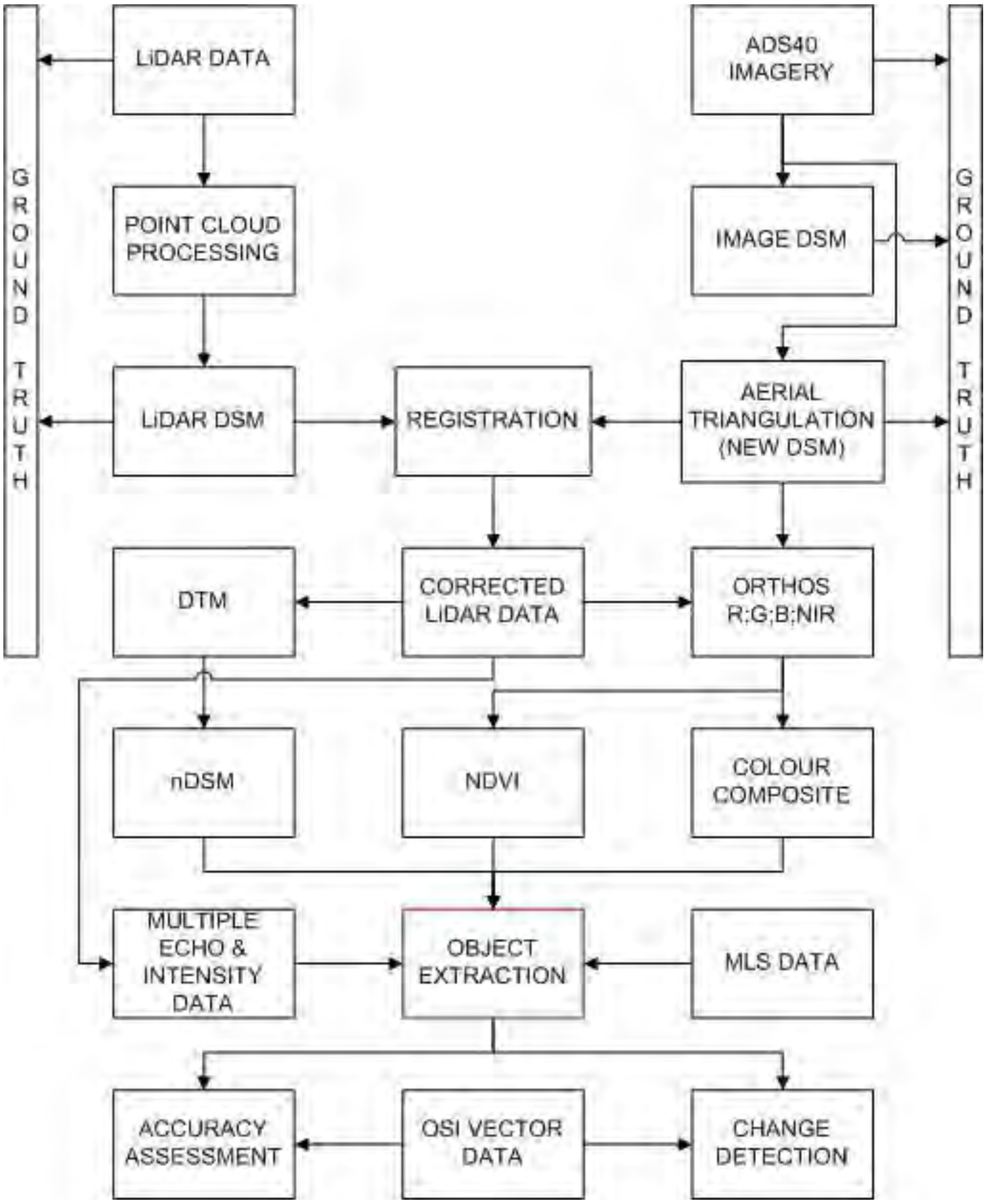

Figure 1: Object Extraction Method Outline

Triangulation of ADS40 sensor data was also performed using GCPs visible in the overlapping images. The main purpose behind this was to generate high quality reference data which could later be compared with LiDAR sensor data to evaluate its planimetric accuracy. A co-registration test was carried out between the LiDAR DSM and the image

DSM. LiDAR DSM was transformed to fit the image DSM using the developed method as explained in chapter 4 (section 4.7). These datasets were acquired at different times. However; had they been acquired simultaneously there would still be a need to evaluate the quality of correspondence between them before the actual extraction process, and therefore this step is a part of the proposed strategy.

After evaluating the used airborne sensor data for its horizontal and vertical accuracy, the second phase of object extraction began. Orthophotos were generated from the ADS40 sensor data using the RGB and NIR images. The DSM from LiDAR was preferred for generating orthophotos because of its better quality as compared to the DSM obtained from image matching using panchromatic aerial images.

NDVI (Normalized Difference Vegetation Index) and other indexes were calculated from the orthophotos and combined with nDSM calculated by subtracting DTM from LiDAR DSM. This DTM was generated from the LiDAR data employing Terrasolid software. Morphological reconstruction techniques were also investigated initially but were not found to be as useful.

These generated datasets along with multiple echoes were used in pixel-based, object oriented and knowledge-based classification techniques for extracting objects. The quality of the extraction process was determined using 2D vector data available from the OSI and ground truth surveys in the development area and the independent test areas.

Extraction of noise barriers and building façades, which are required for noise modelling, can be difficult and sometimes even impossible using airborne data. Hence, MLS data was examined for the extraction of such noise barriers and building façades. Previously extracted objects such as buildings were used to separate building façades from any of the extracted noise barriers.

In addition, methods for change detection were developed for incorporating the changes occurring in the project area. This process highlights and guides the operator to those regions where changes might have occurred over time, instead of inspecting the whole project area.

1.9 Structure of the Dissertation

This section briefly describes the organization of the dissertation. In chapter 2, a review of different data capturing technologies is provided with a particular emphasis on those sensors that are used by the OSI. In addition, different object extraction techniques using LiDAR and aerial images, their fusion and different measures used to evaluate the success of the developed algorithm are discussed at length.

Chapter 3 describes the project areas and related issues. It gives a detailed description of the available data from airborne and ground based sensors, flight characteristics during acquisition, vector data from the OSI and ground truth data acquired by the ground surveys.

Different steps involved in the processing of data, direct georeferencing quality assessment of airborne sensors data, evaluation of DSM generated by image matching techniques, aerial triangulation of ADS40 images to ensure proper registration of LiDAR data are explained in detail in chapter 4.

In chapter 5 the methods developed for the extraction of building boundary and height, single trees, hedges, tree clusters, ground surface type, roads and longitudinal road gradient have been explained. Three methods used for evaluating the success of the extracted objects using the OSI vector data have also been discussed towards the end.

The extracted objects and their accuracy assessment results for the development and the test areas are presented in chapter 6.

A detailed analysis of the object extraction results is presented in chapter 7. These have been addressed in context of the objectives set at the beginning of this research and the extent to which these were achieved in due course.

Chapter 8 provides a conclusion to this dissertation and highlights the innovative aspects of this research. It also provides recommendations for implementing the developed method for noise modelling and sets potential directions for future research.

2 Literature Review

A review is provided for different ground and air-based geodata capturing technologies with a special emphasis on sensors whose data is available from OSI and other local organizations. Techniques for extracting objects of interest within the context of noise modelling using a single data source or by data fusion have also been discussed. Different data acquisition techniques have been compared and object classification techniques have also been categorized. Parameters used in the previous research to determine the accuracy of object extraction have also been discussed using different methods. In the end, different change detection techniques for updating noise models have also been summarized.

2.1 Available Data Sources in ROI

OSI is the main government body responsible for spatial data acquisition, processing and updating and has Leica ADS40 and ALS50-II sensors for acquiring multispectral aerial and LiDAR data. OSI also provide a Network RTK service for rapid, high accuracy GNSS measurements. Apart from these, ground-based data acquisition systems such as MLS, video and digital cameras mounted on vehicle have been developed for road surveys by NUI at Maynooth, Ireland in cooperation with other private partners (NCG, 2008; NCG, 2010).

On 14th April 2010, NRA launched a research project for road environment modelling and asset management by fusing LiDAR data (2 points/m^2) and TLS data. This suggests a high need of spatial information required for noise modelling, road safety and asset management purposes.

In this research the focus was object extraction important for noise modelling using locally available datasets. A brief overview of research and development in these sensors technology is provided in the coming sections.

2.2 Digital Airborne Cameras

Leading commercially available large format imaging sensors are ADS (ADS40, ADS80) from Leica Geosystems (Sandau et al., 2000; Fricker, 2007), DMC from Intergraph (Hinz et al., 2001; Rosengarten, 2007), and UltraCam (UltraCamD, UltraCamX, UltraCamXp) from Microsoft (Leberl and Gruber, 2003).

These systems have replaced analogue frame cameras (Read and Graham, 2002) for topographic mapping and by the end of 2008, approximately 300 systems were in operational use worldwide (Honkavaara et al., 2009). The general design principles of these sensors includes a calibrated geometry with sub-pixel accuracy potential of up to 1 cm, a GSD (Ground Sampling Distance) potential of up to 2 cm, accurate stereoscopic data, an image width of more than 10,000 pixels, multi-spectral imagery in the Red, Green, Blue and NIR regions of the electromagnetic spectrum, and radiometry with linear response, large dynamic range, high resolution, and suitable for visual and quantitative applications (Fricker et al., 1999; Spiller, 1999; Honkavaara et al., 2009).

The ADS40 is a pushbroom line scanner while the DMC and UltraCam are multi-head frame sensors (Figure 2). DMC is good for photogrammetric and engineering applications whereas the ADS40 provides large image strips covering more area, effectively reducing operator time and effort, which is good for applications such as road surveys for noise modelling.

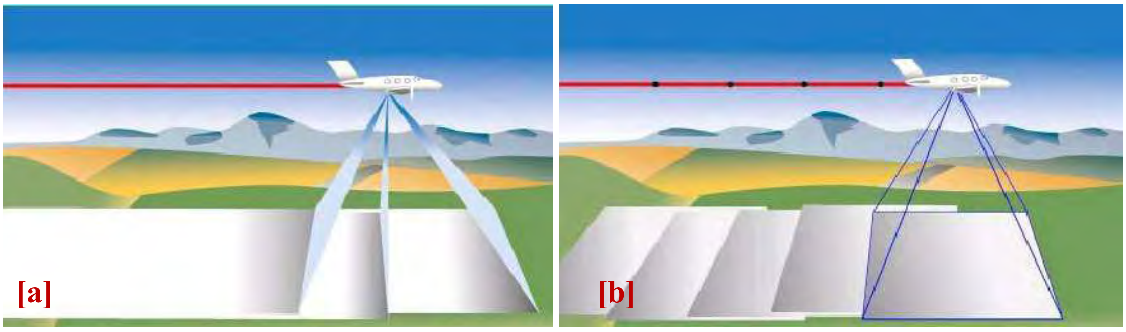

Figure 2: Different Image Capturing Techniques (a) Line Based Imaging (© LH Systems, 2000) and (b) Frame Based Imaging

The GSD of the multispectral channels of the DMC is 3 to 4 times larger than the nominal GSD of the panchromatic channels. ADS40 sensor has one CCD array for recording R, G, B and NIR images but two staggered pixel arrays with a difference of 0.5 pixel to record panchromatic images (Figure 3, (Tempelmann et al., 2000)) . This increases the spatial resolution by a factor of 2 (Reulke et al., 2006). The panchromatic channels are set at an angle to provide the stereoscopic view with high forward overlap.

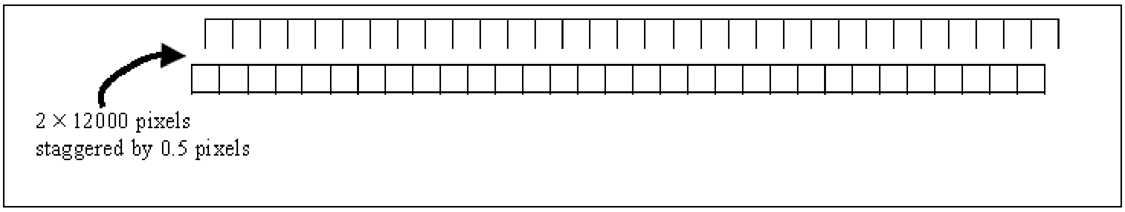

Figure 3: ADS40 Panchromatic Line Design

The radiometric resolution of the ADS40 is 12-bit, but it is reduced to 8-bit using a lossy compression due to the data storage speed limitations in practical situations or subsequent processing in image processing softwares. This reduces the radiometric quality important for DSM generation using image matching techniques. The desirable situation is to have 16-bit radiometric resolution (Honkavaara et al., 2009). Haala (2009) compared DSMs generated from digital frame camera data using digital image matching techniques and ALS50 LiDAR sensor data against independent ground control points. The vertical accuracy of the DSM generated using modern digital cameras was (RMS ± 3.9 cm) comparable to LiDAR (RMS ± 3.4 cm) using imagery with a GSD of 8 cm. This accuracy is possible because of the improvements in radiometric resolution of digital cameras as compared to the traditional analogue frame cameras such as the Zeiss RMK-Top15. However, digital image matching is affected by shadows and occlusions which is not the case with LiDAR as it is an active remote sensing sensor with much smaller swath width as compared to aerial images.

GSD is limited by flying height, flight speed, illumination conditions, frame rate and the smallest possible integration time and speed of data storage in the case of the ADS40 sensor. The minimum practically possible GSD is approximately 5 cm (Honkavaara et al., 2009). A GSD of 10-20 cm is considered appropriate for urban feature mapping by various geospatial data capturing companies and same is the case with OSI (Lemmens, 2010). The geometric performance of various commercially available frame and push-broom digital camera systems was investigated by Cramer and Haala (2009). Horizontal accuracy in the range of 0.25 of pixel and better was achieved both for image blocks with 8 cm and 20 cm GSD. The vertical component resulted in an accuracy of 0.5 pixel and better.

2.3 Airborne Laser Scanning (LiDAR) Systems

LiDAR systems have become the most important geospatial data acquisition technology that has been marketed since the late 1990’s (Axelsson, 1999). Installed on airborne and ground based platforms, these systems can collect explicit 3D data in large volumes at an unprecedented accuracy. LiDAR systems utilize pulsed, single wavelength laser light to obtain the topographic information. They transmit very short pulses in the near infrared part of the electromagnetic spectrum for range measurement. 3D object position is determined with the help of an onboard GNSS/IMU unit. The accuracy of the range measuring instrument is very high but overall system accuracy decreases because of inter alia, the errors introduced during the georeferencing of the point cloud using GNSS/IMU data. The complexity of the required processing of the measured laser data is relatively modest, which has fueled the rapid proliferation of this technology to a variety of applications (Shan and Toth, 2008) .

Three main commercial suppliers of LiDAR systems are Optech International Inc., Leica Geosystems and Riegel. Amongst these, Optech and Leica are the major suppliers in terms of volume and their data has been used extensively for research (Shan and Toth, 2008). Optech ALTM and Leica ALS both have similar scanning patterns and yield height accuracies of ± 15 cm at a flying height of 1200 m. Typically, a project area is covered in multiple strips by flying in opposite directions. Figure 4 shows a fixed wing aircraft capturing topographic details using LiDAR technology.

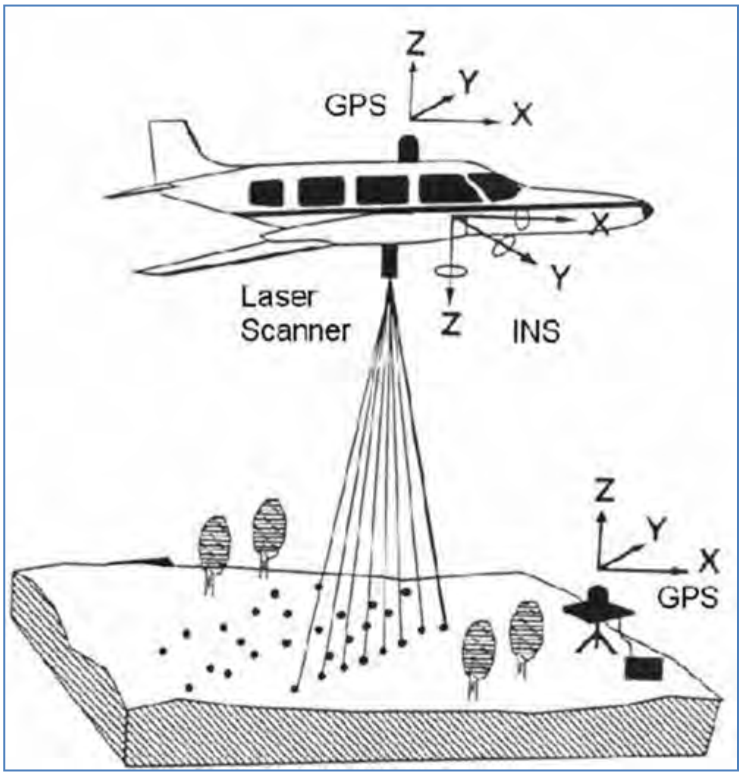

Figure 4: Airborne Laser Scanning System (Kao et al., 2005)

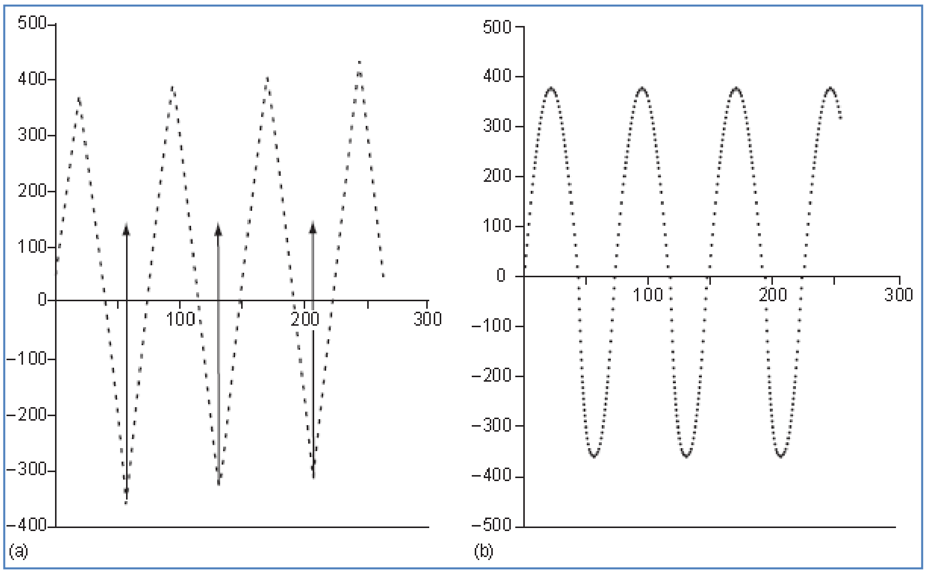

Figure 5: Ground Pattern of Point Cloud from Different LiDAR Systems

Figure 5 (a) shows the saw-toothed pattern over the ground that is produced by the Optech ALTM series of laser scanners; and (b) shows the sinusoidal pattern produced by the Leica ALS laser scanners (Shan and Toth, 2008). In both cases, oscillating mirrors are used as the scanning mechanism. Rotating mirror (Palmer scan) and fiber optic sensors (TopoSys) producing different scanning patterns have also been developed (Shan and Toth, 2008).

The Optech ALTM Gemini, latest in the ALTM series, and ALS50-II, latest in the ALS series from Leica Geosystems, both use multiple pulses in air to achieve a pulse rate of 167 KHz and 150 KHz respectively. As the technology has advanced, the horizontal accuracy of LiDAR has also steadily improved from 1/1000 of the flying height (H) to 1/5500 H (Shan and Toth, 2008).

Most commercial systems can record multiple echoes from a single laser pulse, together with intensity information, which delivers detailed information about the reflectance characteristics of the surface in the laser wavelength. Steinle and Vögtle (2000) explain the effects of different laser scanning modes on the accuracy of extracted building boundaries with respect to their size and this is because of the divergence of laser beams. First and last pulse data had been classified separately for building extraction and later compared with the reference models to determine planimetric and vertical accuracy (Vögtle and Steinle, 2005). First and last pulse data had been useful in separating vegetation from buildings as difference between first and last pulse elevation is less over buildings when compared to vegetation but this is not true for building boundary regions.

LiDAR return intensity which provides another classification cue used for buildings and road extraction depends on the range and scan angles of the laser beam. Changes in flying height and topography of the scanned surface and scattering and absorption of laser photons in the atmosphere, mean that the return energy attenuated and cannot be used to precisely describe the scanned surface (Ahokas et al., 2006; Höfle and Pfeifer, 2007; Kaasalainen et al., 2009). Radiometric calibration of LiDAR systems has also been performed using ground targets, similar to digital cameras which facilitate the feature classification using intensity information (Kaasalainen et al., 2007). As an outcome of this research, EuroSDR initiated a research project to develop a practical LiDAR intensity calibration method, using natural targets in field or laboratory or by portable laser instruments during a laser scanner flight (EuroSDR, 2010).

Modern LiDAR sensors are often also equipped with medium format digital cameras. This greatly helps in the manual classification of the captured point cloud or checking the accuracy of automatic and semi-automatic point classification techniques available in LiDAR data processing software.

Laser pulse-based LiDAR systems capture multiple pulse reflections but commercial systems are now available that can digitize and record the received signal of the reflected laser energy, which allows for the so-called full-waveform analysis (Shan and Toth, 2008). This offers the possibility of analyzing the waveform off line using digital signal processing methods in order to extract different surface attributes from the received signal based on the shape of the returning pulses. Figure 6 shows the shape of the complete waveform of the returned (reflected) pulse that can be used for further analysis.

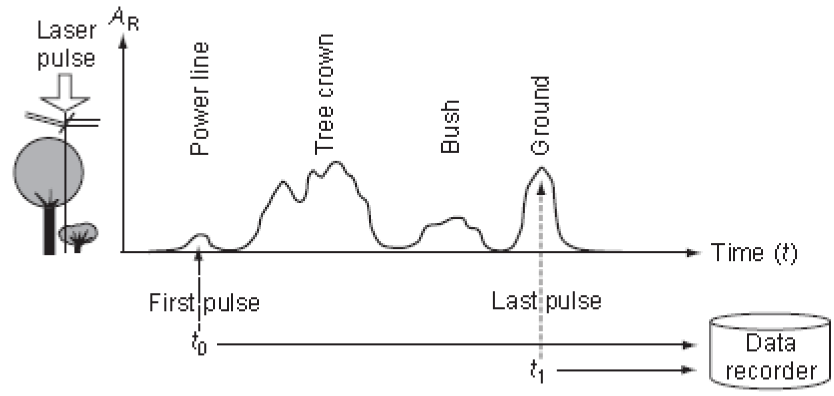

Figure 6: Full Waveform Laser Pulse Reflection (Shan and Toth, 2008)

The contribution of full-waveform data is less obvious in urban feature extraction than in woodlands since multiple pulses only appear when the laser beam hits building edges (Mallet and Bretar, 2009). However; this could be useful in removing vegetation segments from classified aerial images which is a big hindrance to successful building extraction.

Apart from commercial laser scanning systems as discussed earlier, some service providers have developed their own custom-built laser scanning system such as the Fast Laser Imaging Mobile Airborne Platform (FLI-MAP). FLI-MAP is the name given to a series of airborne laser scanning systems produced in-house by the Fugro surveying and mapping company (Fugro, 2010). FLI-MAP 400 is the latest in this series, and these systems are meant for low altitude corridor mapping as they are helicopter mounted. FLI-MAP 400 has a scan frequency of 150 KHz, can be used up to an altitude of 350 m and can record 4 returns per emitted pulse. It features twin small format digital still cameras, each producing images of the ground that are 11 megapixels in terms of their format size. FLI-MAP 400 also records the intensity information of the returning pulse. Figure 7 shows a helicopter equipped with a FLI-MAP system, which is mounted on the frame that is attached to the underside of the aircraft; note also the two outrigger pylons, each supporting a GPS antenna (Shan and Toth, 2008).

NRA in the ROI had to model the road environment on either side of roads and for this reason the corridor mapping systems were not considered economical, especially for urban areas, although, they provide high point density which is not achievable using fixed wing mounted LiDAR systems. For road safety and asset management helicopter-based systems are useful, especially if they are combined with MLS, data for extracting building façades, noise barriers etc. (Rutzinger et al., 2009).

Figure 7: Fugro FLI-MAP 400 Laser Scanning System (© Fugro)

2.4 Mobile Laser Scanning Systems

Mobile laser scanning has emerged as a new technology for capturing detailed road and rail track information. Speed of data acquisition and recording direct georeferencing, increased efficiency and productivity and accuracy of the resulting data which can be verified very quickly on site are the major advantages associated with this technology. These systems can be mounted on a variety of platforms, including cars, trucks, railroad vehicles and even boats (ILMF, 2010).

Noise barriers, important for noise modelling are difficult to extract from aerial imagery and LiDAR datasets but may be more easily and reliably using MLS. MLS has advantage over airborne sensors because of different representation of objects but in some cases they may also complement each other (Figure 8 (Riain and McCarthy, 2009)). For example building roofs not visible from street level can only be captured using airborne sensors.

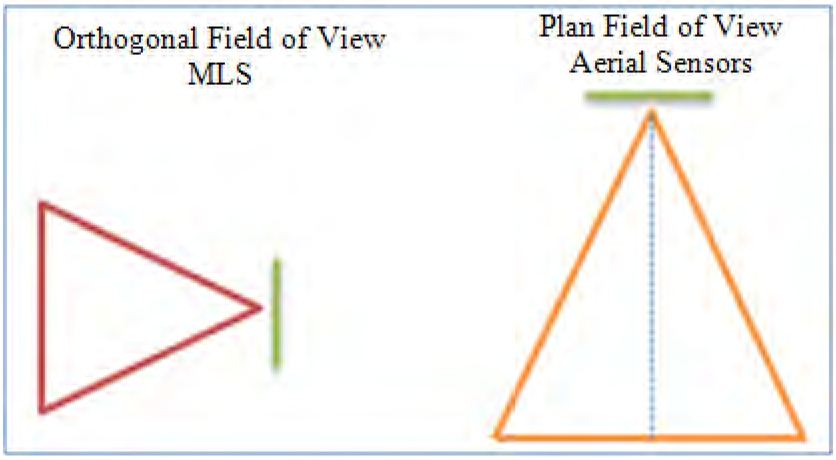

Figure 8: Oblique and Vertical Views of Road Environment

Road markings, edges, surface type (concrete or bitumen), footpath, traffic, electricity and light poles have been extracted using these mobile system's data (Brenner, 2009; Kukko et al., 2009). These systems provide 3D point cloud, intensity of the returning pulse and terrestrial images captured at the same time, providing rich information for object extraction.

Commercial mobile laser scanning systems are available from inter alia Riegl USA (VMX-250), Optech Inc. Canada (Lynx Mobile MapperTM) and StreetMapper Inc. UK

(StreetMapper 360). Figure 9 (a) shows a StreetMapper system mounted on a vehicle, (b) a scene from the video camera and (c) the laser scanner intensity data.

Figure 9: StreetMapper MLS (Kremer and Hunter, 2007)

Barber et al. (2008) estimated the planimetric (0.10 m) and vertical accuracy (0.03 m) of the StreetMapper system specifically for the national road mapping agencies by using check points measured using conventional surveying techniques and recommended its use for numerical modelling and decision making. Custom built mobile laser scanner systems have also been developed by Universities and research institutes such as NUI, Maynooth Ireland (Hunter, 2009), Finish Geodetic Institute (ROAMER MLS) (Kukko et al., 2009) and the National Geographic Institute, France (Soheilian et al., 2007).

Building façade type information is important for noise mapping and this can only be extracted using ground based systems. Limitations of these MLS data for road applications might occur due to parked vehicles on the road side, road users and vegetation in front of buildings and noise barriers.

Building footprints and vertical walls have been successfully extracted from MLS data (Hammoudi et al., 2009; Rutzinger et al., 2009) and this provides impetus for its use to detect noise barriers in this research.

2.5 LiDAR vs. Photogrammetry

High density LiDAR data provide explicit geometrical information of topographic objects and multispectral aerial images provide spectral information with high spatial and spectral resolutions. The human eye can easily recognize features and discontinuities in a point cloud (intensity and height visualization) and aerial images which is not the case with computers. However; manual extraction of this information is expensive and time consuming. Weidner and Förstner (1995) predicted the ever increasing demand of 3D GIS data and since then automatic or semi automatic object extraction is still a topic of significant research.

To explore the potential of both LiDAR and multispectral image datasets, it is important to identify the advantages and disadvantages of both and their complimentary nature, which is discussed in the following sections (Baltsavias, 1999; Schenk and Csatho, 2002).

2.5.1 DSM Quality

LiDAR provides dense 3D point clouds for DSM generation, which can also be generated using image matching techniques. The quality of the DSM generated using image matching techniques is poor because of object occlusions, shadows and matching errors especially over trees. However, LiDAR can penetrate trees and is not affected by shadows. Image or point cloud processing techniques used for DTM extraction from the generated point cloud are the same for LiDAR and photogrammetry.

2.5.2 Surface and Geometric Properties

Object texture such as roughness, variance of surface normals and geometric attributes such as local range variation, Gaussian and mean curvature are an important classification cue for classifying buildings and trees in LiDAR data (Maas and Vosselman, 1999; Vögtle and Steinle, 2000; 2003). However; classification in aerial images is based on spectral signature. If both datasets are available then cues obtained from LiDAR can be used to improve image classification results.

2.5.3 Edge Extraction

Edges extracted from aerial images are sharp as compared to LiDAR. This is because of LiDAR points not necessarily covering object edges uniformly at all places. Interpolation is generally performed for DSM generation to apply image processing techniques, which also results in rough edges.

2.5.4 Georeferencing Quality

LiDAR and airborne digital line sensors, both rely on direct georeferencing. However; LiDAR has high vertical and low planimetric accuracy as compared to line sensors.

Information extracted from both sensors data can be used for the extraction of roads, buildings, trees and other object of interests.

2.6 Object Extraction

Algorithms for object extraction combine more than one cue to classify objects of interest. Different object classification and extraction techniques can be categorized as (Shan and Toth, 2008).

1. **Rule or Knowledge-Based Classification**

   Based on expert knowledge about the appearance of certain object classes in the data that are used to define rules by which the classes can be separated.

2. **Fuzzy Logic**

   Fuzzy logic can be used to model vague knowledge about class assignment in order to avoid hard thresholds as in rule-based algorithms. This requires the definition of membership functions for all shape cues and all classes, and their parameters have to be determined in a training phase. In a second step, these membership values are combined to obtain a final decision (Vögtle and Steinle, 2003).

3. **Unsupervised Classification such as ISODATA or K-Means Clustering**

   Aim at the detection of distinct clusters in feature space that correspond to objects having similar properties, without assigning these clusters to semantic classes such as building or tree. This assignment has to be done in a separate classification and is sometimes carried out interactively (Haala and Brenner, 1999; Shan and Toth, 2008).

4. **Probabilistic Reasoning**

Probabilistic reasoning aims at assigning an object, s, to a class, C, of a given set of classes, θ, given the feature vector X_s of s. The optimum class C_{opt} is chosen as the class maximizing the a posteriori conditional probability $P(C_i|X_s)$ of C_i given the data vector X_s. These conditional probabilities are computed using the theorem of Bayes (Gorte, 1999).

The Dempster-Shafer theory of evidence was introduced as an expansion of the probabilistic approach that can also handle imprecise and incomplete information as well as conflict within the data (Lee et al., 1987; Klein, 1999).

These techniques can be applied either to each pixel of the DSM, to each LiDAR point, or to each candidate region (Brunn, 2001; Walter, 2004; Bartels and Wei, 2006). The classification technique used is highly influenced by the type of data available and the definition of object classes (Pfeifer et al., 2007).

The following sections provide a review of the application of above mentioned techniques for extracting objects from images (satellite or aerial) and LiDAR or by the fusion of both. These have been discussed in an order of top to bottom with respect to height (buildings, trees and then roads). Techniques targeted at the extraction of above-terrain features have to distinguish between buildings and trees. The latter is extracted as a byproduct or vice versa.

2.6.1 Methods for Building Extraction

2.6.1.1 Building Extraction from Aerial Images

Extraction of buildings from single aerial or indeed satellite, images presents considerable difficulty because of occlusion, complex building geometry, vegetation and lack of height information (Huertas et al., 1993; Shufelt and McKeown, 1993; Lin et al., 1994; Nevatia et al., 1997; Zhang, 1999; Muller and Zaum, 2005). Multiple overlapping images have been used for the classification of buildings by many researchers for estimating building heights using data-driven and model-driven approaches highlighting the necessity of third dimension (Fischer et al., 1998; Fradkin et al., 2001).

Waser et al. (2010) assessed the value of digital image data for semi-automatic analysis of classified land cover and tree species and was carried out in the framework of theDGPF-project. Sensor specific strengths of ADS40-2nd, Quattro DigiCAM, DMC, JAS-150, Ultracam-X, and RMK-Top15 cameras and weakness for classification purposes were presented and shortly discussed. The first approach was based on a maximum likelihood method in combination with a decision tree and produces 13 land cover classes. The second approach was based on logistic regression models and produces eight tree species classes. The accuracy assessment reveals that in both approaches similar classification results are obtained by all sensors. Some variations in the classification results are due to phenological differences and different illumination and atmospheric conditions since the image data was acquired at different dates.

DSM's generation using image matching techniques has been researched for its usefulness for building extraction (Brunn and Weidner, 1997; Vosselman, 1999; Nardinocchi, 2001) but results have been limited by the quality of image matching algorithms or shortcomings in aerial data such as shadows, poor quality of DSM over trees and several overlapping images were required.

2.6.1.2 Building Extraction from LiDAR

The detection of buildings from LiDAR is normally done is three steps.

1. DTM extraction from DSM to generate nDSM.
2. Detection of building candidate regions.
3. Evaluation of building candidate regions.

LiDAR data shows the topographic details from which the laser pulse is reflected and represents its non selective nature. For object extraction, it is important to extract the ground which is also one of the most desired outputs of LiDAR and the first step in building extraction.

The quality of DTM from LiDAR is comparable to those generated using terrestrial surveying and better than aerial photogrammetry, especially under the trees. For this reason, LiDAR has almost become an industry standard to generate high quality DTM. Extracting the ground manually is time consuming and expensive. Generally the time taken to classify a point cloud takes about 85% of the total project time (O'Neill, 2009). Different techniques have been used from time to time, to extract the ground points automatically (Kilian et al., 1996; Kraus and Pfeifer, 1998; Vosselman, 2000). A surface is interpolated using different techniques such as Kriging, inverse distance weighting, nearest neighbour, minimum curvature, polynomial regression and moving average to apply the image processing techniques to the point cloud for DTM extraction.

Different operations of gray scale mathematical morphology have been used to extract the terrain in the past research (Haala and Brenner, 1999; Morgan and Habib, 2002). Two basic operations are erosion and dilation and all others are built using these. These operations were previously built for binary images but have also been extended for gray scale images. Dilation and erosion are often used in combination. For example, the definition of a morphological opening of an image is erosion followed by dilation, using the same structuring element for both operations. The related operation, morphological closing of an image, is the reverse. It consists of dilation followed by an erosion with the same structuring element (MathWorks, 2010).

The selection of the shape and size of the structural element is crucial. It should be larger than the size of the biggest building in the area. If a large sized building exists in undulating terrain, this would result in some small hills being classified as buildings. That is why a coarse-to-fine strategy is required for terrain classification.

Haala and Brenner (1999), Rottensteiner and Briese (2002) and Rottensteiner et al.(2005) used a rule-based algorithm to identify large buildings in the area after each morphological process. These building regions were retained for the next iteration and the process was repeated until the minimum size structural element was reached.

Arefi and Hahn (2005) used geodesic dilation (morphological reconstruction) to separate terrain and off-terrain points. It has certain unique properties as compared to the traditional morphological image processing (MathWorks, 2010).

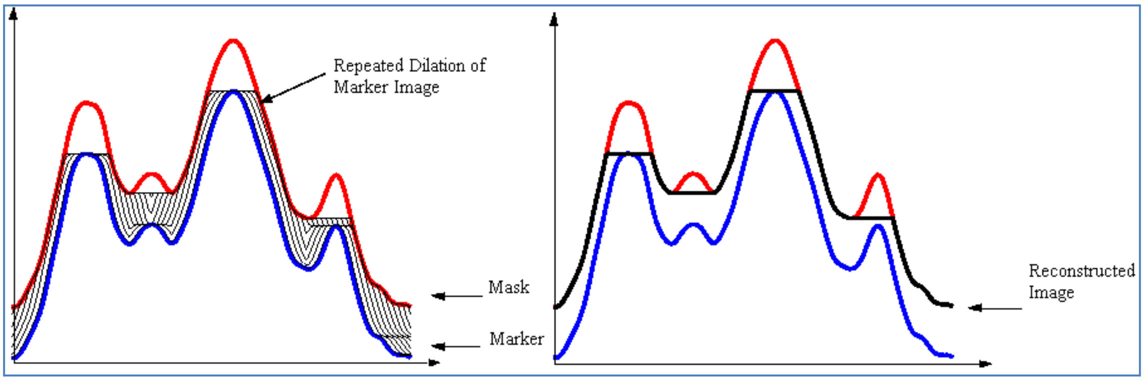

Figure 10: Repeated Dilations of Marker Image, Constrained by Mask

1. The processing is based on two images, a marker and a mask, rather than one image and a structuring element.
2. The processing repeats until stability; i.e., the image no longer changes.

3. The processing is based on the concept of connectivity, rather than a structuring element.

Arefi and Hahn (2005) required a proper height threshold to classify all off-terrain points from non-terrain points. It was difficult to estimate in the hilly terrains. A few marker images were created with different thresholds to overcome this difficulty. The off-terrain objects were separated using local range variation (difference of local maximum and minimum) and area thresholds in each resultant image (Mask - dilated Marker image). The classification technique again depends upon the knowledge of the operator about the project area.

Bartels et al.,(2006) developed a novel approach based on an unsupervised segmentation algorithm and skewness balancing to separate object and ground points efficiently from high resolution LiDAR point clouds using statistical moments. Instead of converting the point cloud to a grid, original point cloud was used.

A comparison of different filtering algorithms for extracting DTM was provided by Sithole and Vosselman (2004) and Keqi et al. (2005). The studies concluded that the success of terrain extraction algorithm varies depending upon the complexity of the scene, point density, steep slopes, discontinuities, very small and large objects, trees and buildings on slopes and objects connected to the Earth (bridges).

To find the actual height of the objects, a DTM has to be generated first and its elevations subtracted from DSM elevations. This new (normalized) surface model is called nDSM which represents the height of the objects relative to the terrain (Weidner and Förstner, 1995).

In the second step of building extraction from LiDAR data, buildings segments are generated using a height threshold value to separate low level objects. Standalone pixels and loosely connected pixels are removed using morphological operations. However; successive applications of the morphological operations can significantly alter the segment size and shape.

The last step for building extraction is the classification of buildings and trees using the mean values of the classification cues in the candidate regions, such as surface roughness, height variation, intensity etc. in combination with geometric attributes (size, shape, roundness etc) (Rottensteiner and Briese, 2002; Lu et al., 2006).

LiDAR sensors can record multiple returns, and first and last pulse data has also been explored for differentiating between buildings and vegetation segments. However, large differences in first and last pulse data can also occur at the edges of the buildings.

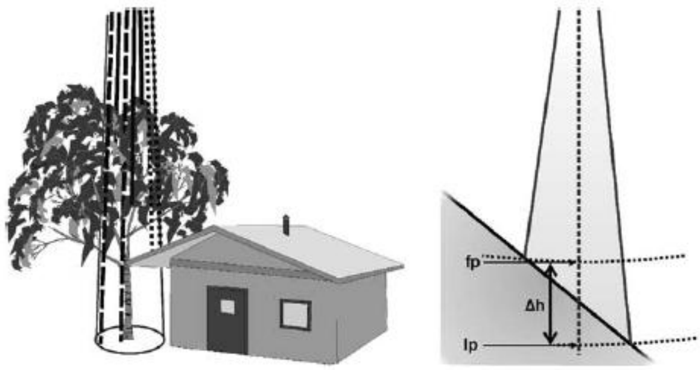

Figure 11: Laser Beam Interaction with Objects (Vögtle and Steinle, 2005)

Figure 11 shows how a laser beam covers a tree standing beside a house. Dashed lines represent those parts of the laser signal that penetrate the tree. Dotted lines show reflections at the roof of the building while solid lines indicate reflections at leaves and branches (Vögtle and Steinle, 2005). This illustrates the complex return scenarios that can occur during the interaction of the laser beam with topographic features. For DTM extraction, only last pulse data is used with an assumption that it generally belongs to the ground (Sithole and Vosselman, 2004). Depending upon the pulse used for object extraction, object size varies because of beam divergence.

Intensity of the LiDAR sensor which is in the NIR region of the electromagnetic spectrum has also been used as additional information for the classification of buildings, roads and trees (Höfle and Pfeifer, 2007; Kaasalainen et al., 2009). Spherical loss, topographic and atmospheric effects influenced the backscatter of the emitted laser power in these studies, which led to a noticeably heterogeneous representation of the received power.

2.6.1.3 Building Extraction by Data Fusion

To complement the short comings in LiDAR data, multispectral images are used for fusion. Colour infrared imagery (Haala and Brenner, 1999) and NDVI (Yi Hui Lu et al., 2006) have been applied for discriminating vegetation. Building shadows and water bodies where there is no reflection in LiDAR can be masked out using NDWI (Normalized Difference Water index) (Chen et al., 2009), where

$$\mathrm{NDWI} = (\mathrm{G} - \mathrm{NIR})/(\mathrm{G} + \mathrm{NIR})$$

In addition to these data sources, additional shape parameters such as size, compactness and parallelism of long segment contour lines have been used for classification purposes (Vögtle and Steinle, 2003; Arefi, 2009).

A height threshold is normally applied to an nDSM for removing small objects such as cars and low vegetation in order to improve building classification. It is similar to the application of a height threshold to LiDAR data as has been explained in the preceding section. A rule-based technique which requires operator knowledge of the area and manual selection of many thresholds was used by Forlani et al. (2006). In order to avoid hard thresholds, fuzzy logic or adaptive boosting algorithm (AdaBoost) for the automated identification of classification rules was used by Zingaretti et al. (2007).

The Dempster-Shafer theory of evidence (Shafer, 1976) for fusion has been used by Rottensteiner et al.(2004; 2005; 2007) and Lu et al. (2006). Rottensteiner et al.(2004; 2005; 2007) combined different classification cues obtained from LiDAR and aerial images using Dempster-Shafer theory for densely built up areas in order to extract buildings. It was concluded that considering only large sized buildings considerably improves the accuracy of the extraction process. Pfeifer et al. (2007) compared the Dempster-Shafer theory of evidence and a rule based classification technique developed in an open source GIS tool, and provided an overview of different building extraction algorithms from LiDAR data. It was concluded that an accuracy of 80% is achievable however; no method is fully automatic.

Khoshelham et al. (2010) compared different building classification techniques namely Bayesian, Dempster-Shafer and AdaBoost, based on the fusion of LiDAR and multispectral images on two different sites. By fusing multi sensor information, an overall accuracy of 90% was considered possible however; the accuracy varied depending upon the topographic details.

Mayer (2008) provided a review of the different state- of-the-art techniques for automatic object detection. Mayer emphasized that there are only a few practically successful systems in the market. The review concludes that the practical success of an automated objected extraction method must be backed up a theoretically informed background, statistical modeling, testing to clarify which approach will best suit a particular scenario and how useful it will be for praxis and efficient user interaction. Drawing from the above, much needs to be done to make any automatic process acceptable to the industry.

After the identification of building regions, building roofs are in most cases modelled using LiDAR data (Brunn and Weidner, 1997; Haala and Brenner, 1999; Maas and Vosselman, 1999; Rottensteiner and Briese, 2002; Suveg and Vosselman, 2004; Samadzadegan et al., 2005; Madhavan et al., 2006).

Shan and Toth (2008) explained methods for the extraction of building boundaries and roof reconstruction using data and model driven approaches to create prismatic and polyhedral models. Prismatic model as required by noise modelling was created in three steps: (1) building detection; (2) linear feature extraction; and (3) BSP-Tree (Binary Space Partitioning Tree).

For noise modelling, a level of detail comprising a building boundary with a single height value is required. This equates to the LoD1 designation as part of the OGC CityGML specification (Kolbe, 2008). Brenner (2005) compared different semi-automatic and automatic techniques for building reconstruction using LiDAR and aerial images. It was concluded that since the topic has been researched immensely over the last twenty years but still there are no fully automatic systems around.

Vögtle and Steinle (2000) determined the planimetric (± 0.2-0.3 m) and height accuracy (± 0.05-0.10 m) of the extracted building models using LiDAR and multispectral images, and these are within the acceptable limit of noise modeling i.e. within one metre of the referenced 3D models.

2.7 Methods for Trees Extraction

Trees are part of a DSM and must be classified in any case for the extraction of buildings and DTM. This also fuelled the research in vegetation studies using LiDAR data. Penetration of LiDAR through trees has made it possible to generate a DTM in forest areas which is not possible from photogrammetric and image matching techniques (Kraus and Pfeifer, 1998; Juha et al., 2000).

EuroSDR conducted a research project evaluating the quality, accuracy and feasibility of automatic or semi-automatic tree extraction methods using high density laser scanner data and aerial images (Kaartinen and Hyyppä, 2008). Data sets from two sites were delivered to twelve participants and the results were analyzed with respect to tree location, tree height, crown base height and crown delineation accuracy.

Participants either used LiDAR or aerial images and very few used both datasets. The results showed that the extraction method was the main factor on the achieved accuracy. When the laser point density increased from 2 points to 8 points per m^2, the improvement in crown base height and crown delineation accuracy was marginal, but in some methods the accuracy of the tree location and especially the tree height determination improved.

Only two participants had used the hybrid methods, where the height was obtained from laser data and crown delineation (and species) from aerial images. It was impossible to give a well grounded conclusion, if and by how much the results can be improved by integrating laser scanner data and aerial data. However; it was concluded that more emphasis should be put on the process, integrating features from laser scanning and aerial images. On the other hand, full waveform LiDAR data capturing sensors are also gaining popularity for vegetation studies.

NRA, Ireland is not interested in trees and vegetation extraction as these have no effect on noise propagation. However; these objects need to be classified for successful building extraction and are a byproduct of the extraction process which can be very useful for many other applications.

2.8 Methods for Road Extraction

2.8.1 Road Extraction from Images

Mayer et al. (2006) presented a review of different road extraction techniques used on the aerial and satellite images provided by EuroSDR in a collaborative research project. They assert that as per industry standards, the quality in terms of correctness and completeness should be more than 70% and 85% respectively to render any automatic approach acceptable. If a method or developed algorithm does not meet these accuracy measures, extensive manual work is required. In such a case, it might be preferable to digitize the objects manually. The study found that the road recognition and reconstruction results vary considerably depending upon the complexity of the scene. Meyer and colleagues conclude that it is possible to extract roads with the required accuracy measures in terms of completeness and correctness which can be useful for practical applications. However; this is achievable only for scenes with a limited complexity.

Gerke (2006) developed a geometric-topologic relationship model for roads and their surrounding objects (context objects, such as rows of trees) to support the quality assessment of road vector data as they may explain gaps in road extraction. The extraction and explicit incorporation of those context objects contributed to an efficient assessment of a given road database. Ravanbakhsh and Fraser (2009) extracted roundabouts using existing topographical databases and active contour model (such as ziplock snakes) from high resolution aerial images. Baumgartner et al. (2002) presented a system for semi-automatic road extraction and study its efficiency compared to manual plotting. The system employs a road tracking algorithm based on profile matching. Only 50% reduction in the plotting time was possible for rural scenes where as the developed tool was not feasible for complex urban scenes.

With the increase in spatial resolution of aerial and satellite images, roads are no longer represented as a line feature. For many applications such as car navigation both edges of the roads are needed. Aerial photogrammetry has the inherent problem of shadow, occlusions due to trees and buildings and parked cars etc. The automatic extraction of roads is a challenging task particularly for the high resolution data and a lot still needs to be done to be able to generate acceptable results.

2.8.2 **Road Extraction from LiDAR**

Road extraction only from LiDAR is still in its infancy. However; LiDAR DSM generated at a point spacing of 1 m is considered suitable for the extraction of road borders (Shan and Toth, 2008). LiDAR data is not affected by shadows and occlusions and can penetrate trees. A DTM built using this data in forest areas is comparable in accuracy to a DTM prepared by field surveying. Roads are part of the DTM which is used for road borders and center line extraction along with the intensity information.

Clode et al. (2007) used a phase coded disk approach to extract 2D roads from classified road pixels. The algorithm achieved a topological completeness of 87% and a topological correctness of 73%. Lane markings, intersections and roundabouts present additional challenges for road extraction in complex scenes.

Vector data has also been used in combination with LiDAR or aerial imagery for extracting road geometry and updating the database (Hatger and Brenner, 2003; Zhang, 2004).

2.8.3 Road Extraction by Data Fusion

LiDAR data has been used as supplementary information for road extraction from aerial images (Fortier et al., 1999; Hu et al., 2004). Roads have very specific reflectance properties in the wavelength of a LiDAR pulse because of the uniform and consistent nature of road material which is not the case with buildings. A road surface is defined by means of a homogeneity measure and break lines are described as linear structures that show discontinuities perpendicular to their shape (Brügelmann, 2000). Classification cues and techniques used for roads are mostly the same as used for buildings such as using NDVI for building and roads classification. Specific geometric parameters of roads have made shape parameters highly appropriate for road reconstruction. Multispectral images are also used to detect cars in the parking lots which will help in differentiating roads from parking areas as both have the same intensity and surface characteristics but varying shape parameters (length to width ratio).

2.8.4 Road Extraction from Ground Sensors

Extraction of road parameters which are important from a car navigation and a noise perspective has been done using ground based laser scanning systems in the recent years. These sensors provide detailed 3D information from an orthogonal perspective not available from airborne sensors.

Tao et al. (1998) carried out automatic reconstruction of road centerlines from mobile mapping image sequences. National Center for Geocomputation (NCG) at the NUI, Maynooth in cooperation with private partners had also developed such a system for asset management, road safety and other applications (NCG, 2008). Each object is digitized or identified manually and its position and other related attributes are stored in a GeoDatabase. Large numbers of terrestrial images are required to cover the area on both sides of the roads. Automatic object extraction from these stereoscopic images is also fuddled by the rich information content of these images.

Road centerline extraction is not an objective of this research as this is already available from OSI. These centerlines represent the position of the source of noise pollution. Additional attributes are also added to these lines such as traffic flow information and the type of traffic that can use this road. In multilane or dual carriage way each lane is modelled separately. The mentioned geospatial data capturing technologies have the potential to extract road surface type, road geometric parameters and model the road environment.

2.9 Accuracy Assessment

Methods used for the accuracy assessment of object extraction techniques vary and are of fundamental importance in the evaluation of the developed algorithms. The same applies to this research making it necessary to thoroughly evaluate the results before deeming them acceptable.

Accuracy assessment method can be pixel or object-based depending upon the data (available a priori or self generated) for verification. Rutzinger et al. (2009) utilized different classification accuracy assessment methods such as pixel-based, building centroid and building overlap to evaluate the success of different building extraction algorithms. Completeness and correctness parameters were determined using a method developed by Heipke et al. (1997). It was found that the results can vary up to 30% depending upon the method used and that different evaluation methods should be used simultaneously (Pfeifer et al., 2007; Rutzinger et al., 2009). These parameters have also been used to evaluate other object extraction algorithms developed for roads and trees. The accuracy method used to compare the extracted and reference objects can vary slightly however; the parameters used for reference i.e. completeness and correctness, generally remain the same.

The completeness is the percentage of the reference data which is explained by the extracted data. The correctness is the percentage of the extraction, which is in accordance with the reference.

Other measures such as quality, rank distance and branching factor have also been used in the research to show the success of object extraction. These are basically derived from completeness (compl) and correctness (corr) as can be seen from the formulae below.

$$Quality = \frac{Compl * Corr}{Compl - Compl * Corr + Corr}$$

$$Rank\ Distance = \sqrt{\frac{Compl^2 + Corr^2}{2}}$$

$$Branching\ Factor = \frac{Compl - 2 * Compl * Corr + Corr}{Compl * Corr}$$

Correct registration of extracted objects and reference data is very important when using pixel based accuracy assessment as compared to area overlap or building centroid methods. In the area overlap method, different classes of reference objects are identified depending upon the percentage overlap with respect to the extracted buildings. To call the extraction successful the percentage overlap must be above a preset threshold of 70% (generally). In the building centroid method, the centroid can lie outside the building and needs to be corrected before comparing it with the reference data.

2.10 Change Detection

There is a requirement under the noise directive that the noise maps be updated every five years. It is not feasible for NRA Ireland to acquire, process and analyze new data every five years for noise modelling. A method is required that can automatically identify the changes by comparing the new dataset with the previously acquired datasets or comparing previously extracted objects with the new dataset. Jensen (2007) analyzed various change detection algorithms and summarized their compositions. It was concluded that the use of expert systems to detect change automatically in an image with very little human interaction is still in its infancy.

Champion et al. (2009) reported the outcomes of a EuroSDR test undertaken to find out the building change detection approaches and their success rates using three different types of datasets i.e. satellite images, aerial images and LiDAR. It was concluded that change detection methods can be influenced by the methodology used, type and spatial resolution of input data and the complexity of the scene.

A simple difference between two DSMs acquired at two different times can show where changes might have occurred (Murakami et al., 1999). However; it will also reflect changes that occurred because of vegetation growth which might not be of interest to the NRA. The same is also true for simple image differences or comparing different spectral bands with one reference image for change detection. The cross correlation method requires classified objects, extracted from the data acquired on date 1 to be compared with the data acquired at date 2, without classifying it. Change detection accuracy will then be dependent upon the accuracy of the classified objects in data set pertaining to date 1.

3 Data

In order to assist in the development and testing of an efficient object extraction method, airborne sensor (image and LiDAR) data was provided by the OSI initially for the Sligo area and later for Maynooth and Leixlip towns and the road connecting (R148) them. Sligo is located in the north west of the ROI (Figure 12). The site of the second data set lies at a distance of 25 km from Dublin (Figure 13) which is on the east coast. The study areas are so selected as both aerial and LiDAR data should be available.

Figure 12: Data Set Locations in the ROI

Figure 13: Second Data Set Location

The Sligo data covers the town centre, which features a river flowing through it, a coastal area, residential and industrial buildings, a national highway, a number of bridges, trees, forest patches and low vegetation with terrain height variation of approximately 65 m. The second data set also comprises similar characteristics, however; it also includes the MLS data available for the road connecting the towns of Maynooth and Leixlip.

The details of the characteristics of the available airborne and ground based sensor data, areas of interest and other data sets available or acquired during the course of this research are given below.

3.1 Aerial Images

3.1.1 Sligo Area

Coverage Extent	6.5 km * 4.5 km
Nadir CCD Lines	Red, Green, Blue
Panchromatic	Forward and Backward Looking (28°,-14°)
NIR	Forward Looking (18°)
Sensor Pixel Size	0.0065 mm
Focal Length	62.7 mm
Number of Strips	3
Flying Height	1447 m
Ground Sampling Distance	0.15 m

Table 1: Characteristics of ADS40 Sensor during Sligo Data Acquisition

High resolution, multispectral aerial images were captured by the OSI using Leica ADS40 second generation sensor in the last week of March 2007. Flight characteristics are listed in Table 1.

The ADS40 sensor is configured with individual CCD lines for recording R, G, B and NIR data. It also has two staggered CCD lines for recording panchromatic data with a displacement of 0.5 pixels, therefore reducing the ground sampling distance to half as compared to other channels (Sandau et al., 2000). However; the OSI used only one CCD line data as part of their workflow. The second CCD line data was either not used or might have been permanently switched off.

The coordinate reference system used throughout this research was ITM (Irish Transverse Mercator) and its parameters are listed in Table 2 (Morgan and Bray, 2000). As a result, all extracted objects can easily be incorporated into other OSI databases and in the spatial analysis software used for noise modelling.

Projection	Transverse Mercator
False Easting	600,000.000 m
False Northing	750,000.000 m
Central Meridian	8° West Longitude
Scale Factor	0.999820
Latitude of Origin	53.5° North Latitude
Linear Unit	1 metre
Datum	ETRS89

Table 2: Coordinate Reference System Used Throughout the Research Project

Two areas were selected from the Sligo data which are referred to as the development and Test Area-1 in this research. These areas are marked in Figure 14 showing the full extent of available aerial images for Sligo. Each area covers approximately 3 km^2 and the Test Area-1 includes parts of all the three image strips. The development area was used for developing the object extraction method which was later tested objectively in the Test Area-1 to evaluate its performance.

Figure 14: Sligo Project Area

3.1.2 Test Area-2 (Maynooth and Leixlip)

The second project site which includes the towns of Maynooth and Leixlip and the road connecting them is designated Test Area-2 from here onwards. The developed method was retested here as was done in Test Area-1. The Figure 15 shows a single strip of aerial images (RGB) available for the Test Area-2 acquired using ADS40 sensor in June 2009. The flight characteristics are similar to the Sligo dataset (Table 1) but lack NIR imagery. The red polygon in Figure 15 shows the area (10 km^2) for which LiDAR data is also available. It covers 500 m on either side of the road (R148), a necessary condition required for noise modelling. This presents a more realistic scenario as compared to the development and the Test Area-1. The data was captured in June 2009 and provided to the DIT in March 2010 for testing the developed method.

Figure 15: Test Area-2 ADS40 Data

3.2 LiDAR Data

3.2.1 Sligo Area

The LiDAR data was captured by the OSI in May 2007 using a Leica ALS50-II sensor. The flight characteristics of the ALS50-II sensor data used in the Sligo area are listed in Table 3. High resolution data is only acquired when it is specifically needed such as for mapping transmission lines and fences but such data was not available for the Sligo area. ALS50-II sensor records multiple returns if the difference in elevation between them is more than 3.5 m. It also records the intensity of the returning pulses (single and multiple) with a radiometric resolution of 8-bit. Eight flight strips covered the entire project area. Raw LiDAR data was provided in ITM with orthometric height above the Malin Head datum.

Figure 16 shows the full extent of available LiDAR data for Sligo, two selected tiles for processing and the flight trajectories. Figure 17 shows a subsection of aerial images overlaid by the LiDAR DSM tiles.

Specification	**Data**
Flight Altitude	1242 m
Pulse Frequency	69 Hz
Wavelength of the Laser	1064nm (near infrared)
Measurement Density	$\simeq$ 1 to 1.5 points per m^2
Swath Width	800 m
Scan Rate	39.4 Hz
Field of View (FOV)	36°

Table 3: ALS50-II Sensor Flight Characteristics

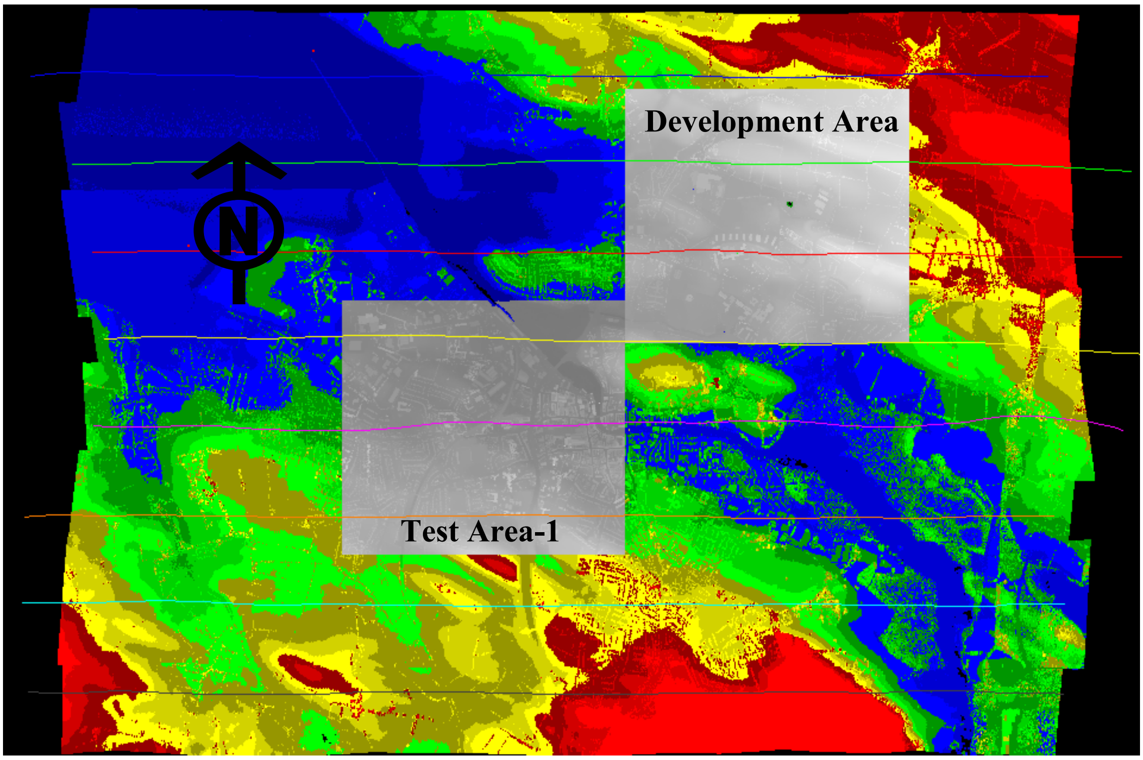

Figure 16: LiDAR Strips and Tiles Selected for Processing

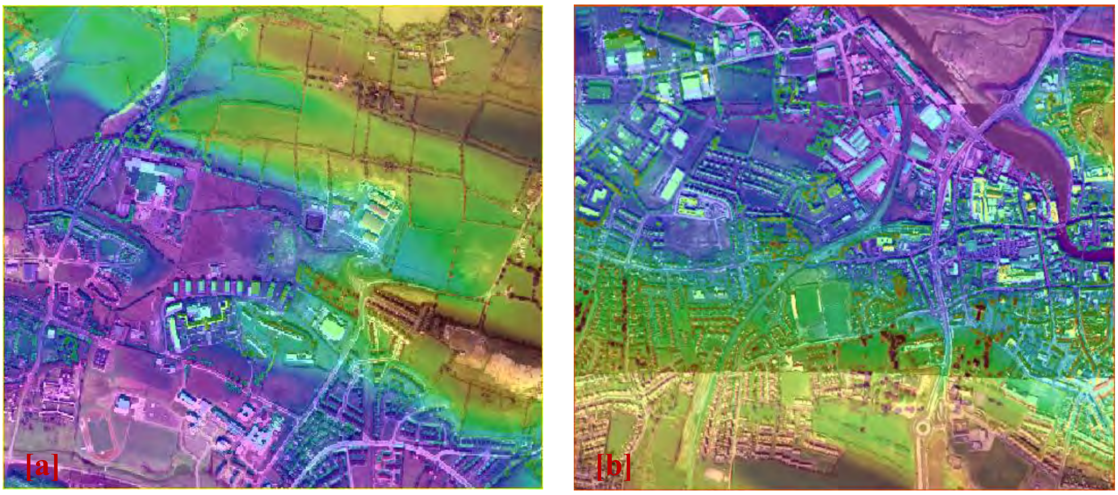

Figure 17: (a) Development and (b) Test Area-1(DSM Overlaying Imagery)

3.2.2 **Test Area-2**

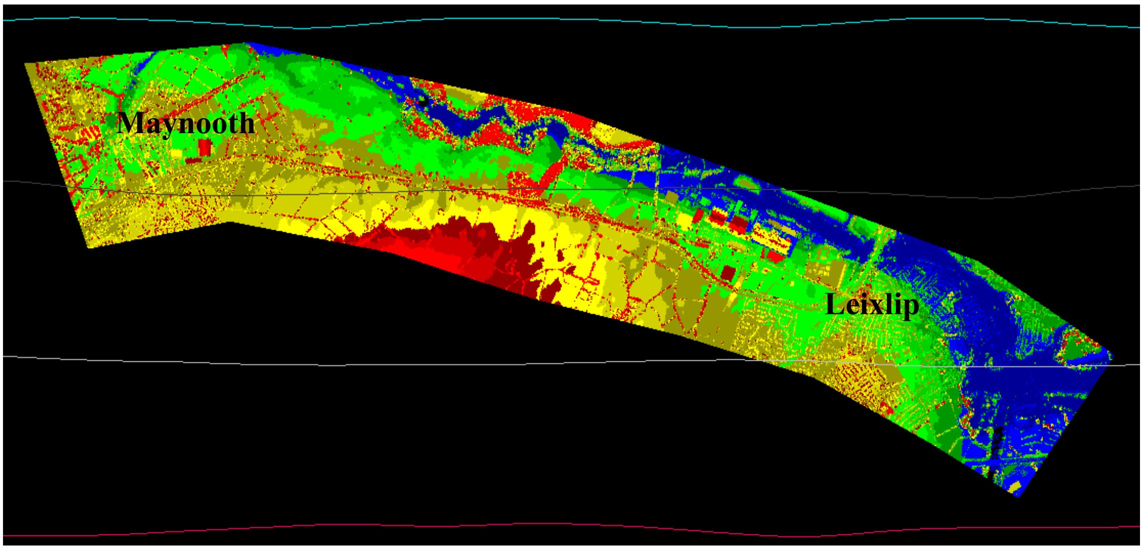

Figure 18: Four LiDAR Strips Covering Test Area-2

Figure 18 shows available LiDAR data and flight trajectories for the Test Area-2, acquired in July 2009. Figure 19 shows a subset of aerial images overlaid by the LiDAR DSM selected for further processing.

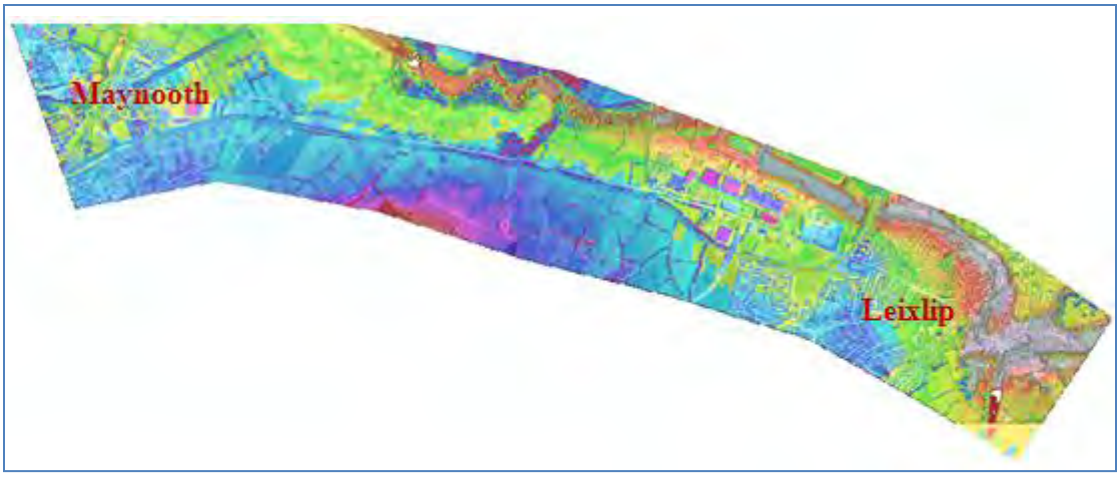

Figure 19: LiDAR DSM Overlaying Aerial Images (Test Area-2)

3.3 MLS (Mobile Laser Scanning) Data

The MLS data is only available for the national road (R148) connecting Maynooth and Leixlip in the Test Area-2. The data was acquired in both directions (Maynooth to Leixlip and back) by an experimental MLS system (XP-1) developed by the NUI, Maynooth. The density of the data is approximately 100 points/m^2 which happens to be greater in the areas with overlapping point clouds. The onboard Riegel LiDAR sensor also records the intensity of the reflected laser pulse.

There is a mismatch between the data acquired in either direction because of calibration issues between the vehicle and the mounted sensors (Figure 21). This makes it difficult to utilize the data captured in both directions simultaneously. For this reason, only the data captured from Maynooth to Leixlip has been used in this research as far as the Test Area-2 is concerned. The data captured from Leixlip to Maynooth was disregarded because it lacked objects of interest (boundary walls).

Figure 20: MLS Data (Test Area-2)

Figure 20 shows MLS data overlaying aerial images for the road (R148) between two roundabouts close to Tesco and Intel.

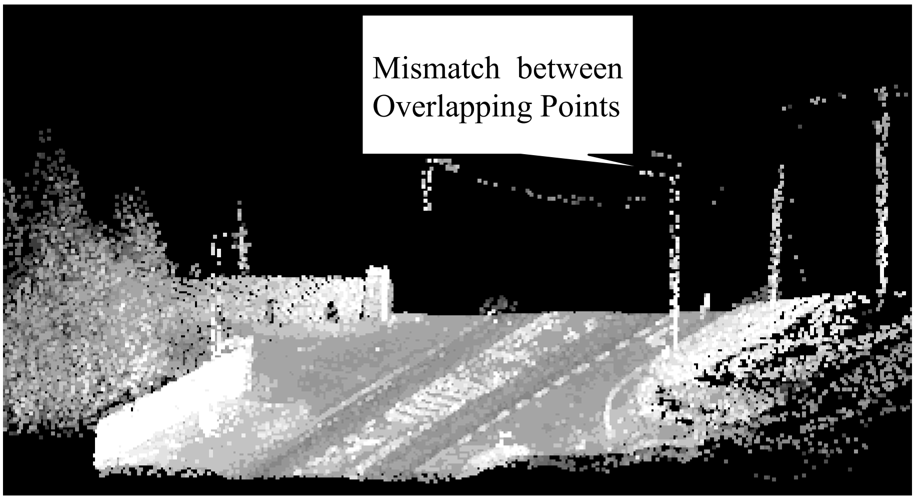

Figure 21: MLS Data (Intensity Image)

3.4 Ground Truth Data

3.4.1 Sligo Area

The ground truth data was acquired in two stages. In the first stage, static GPS technique (2 base stations plus rover) was used while in the second stage, Network RTK system was employed to acquire independent GCPs. The network RTK provides a real-time solution and is much faster. The points acquired in the static GPS survey were so selected that these were also identifiable in the aerial images and distributed over the whole project area. These points were used for determining the direct georeferencing quality of the aerial images and later for aerial triangulation. These points were also used to determine the height accuracy of the LiDAR DSM and the DSM generated from image matching.

A large number of 3D points were acquired using Network RTK system. These points were used for determining the accuracy of LiDAR point cloud and setting the orientation of the reflectorless Total Station used for measuring building heights. These building heights were later compared with the extracted building heights.

3.4.2 Test Area-2

GCPs were also acquired in Test Area-2 using the Network RTK system and building heights were measured using Total Station as was done in Sligo. These points were used for the vertical accuracy assessment of LiDAR point cloud and the measured building heights were compared with the extracted ones.

3.5 OSI Vector Data

Vector data was also provided by the OSI for the Sligo project area to check the accuracy of the developed object extraction method. This vector data included, buildings, road centreline and the road edges. This data corresponded to the year 2009, whereas the aerial and LiDAR data corresponded to the year 2007. The vector data was subjected to manual editing to make it similar to the aerial images from 2007, before using it for accuracy assessment. However; the vector data was used as such in the area overlap method for change detection. This was done by comparing it with the extracted objects from the airborne data. It highlights those features which are new or were modified or demolished in two years time.

The buildings were digitized as line features in the OSI vector data. Whereas extracted buildings were polygons. Multipart digitized building boundaries in the OSI data were merged together to create a single building polygon.

The vector data was also available for the Test Area-2 to reconfirm the accuracy of the developed method. Since the LiDAR and aerial images were also captured in the same year i.e. 2009, no significant differences were found.

4 Preliminary Data Processing and Accuracy Assessment

The steps performed in the processing of raw LiDAR and multispectral data acquired using ALS50-II and ADS40 sensors are discussed in detail in this chapter. The expected accuracies as per sensor specifications for particular flight characteristics are evaluated using independent GCPs, acquired at different stages during the course of this research. The DSMs generated using image matching techniques are compared with the LiDAR DSM to evaluate its potential for DTM extraction, orthophoto generation, object extraction or as a replacement for LiDAR. A method is suggested using common points in the LiDAR DSM and the new DSM generated by image matching after aerial triangulation to ensure proper registration in case the data from different airborne sensors is required to be fused.

4.1 Surveyed Reference Data

Performance Specifications	Accuracy
Static	Horizontal: 3 mm + 0.5 ppm (x baseline length)
	Vertical: 5 mm + 0.5 ppm (x base length)
RTK	Horizontal: 10 mm + 1.0 ppm
	Vertical: 15 mm + 1.0 ppm

Table 4: TOPCON System Specifications

To check the direct georeferencing quality of LiDAR and aerial images and to execute aerial triangulation, it was considered necessary to acquire GCPs having an accuracy higher than both datasets. In order to achieve that, a survey was planned for Sligo to acquire 12 static GCPs which were also visible in the available ADS40 aerial images. A TOPCON system was used which employs both GPS and GLONASS to determine the 3D coordinates of a point. The horizontal and vertical accuracies of TOPCON system in the static and Network RTK mode are listed in Table 4.

4.1.1 **Ground Control Points**

The survey was conducted on a day (14th November, 2008) when there were at least 6 satellites available at all times during the data acquisition (Figure 22).

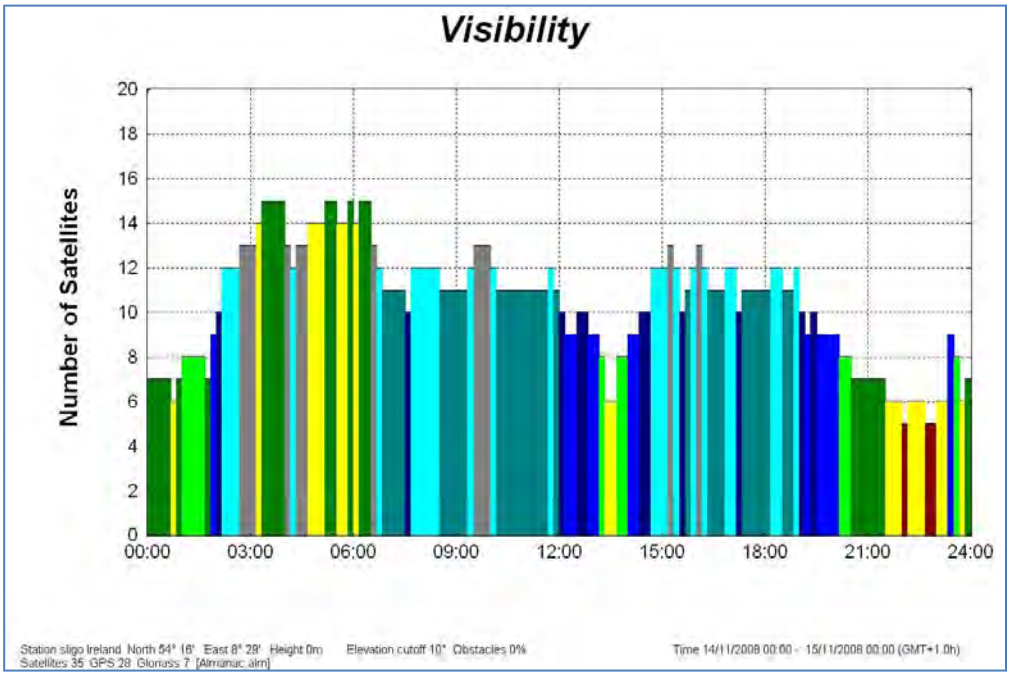

Figure 22: Satellite Availability

The base station was set up at an already known point, fixed by the OSI. A second, active station, point also exists in the project area at a distance of 555 m from the base station. The active station continuously acquires data which is available for download at hourly bases from the OSI website. Since the length of the base line was very small, it was considered necessary for the horizontal and the vertical accuracies to lie approximately in the range of 3 to 5 mm. The data was collected at each point for a duration of 15 minutes. Adjustment of the acquired data was performed by using the known coordinates of the base station. The coordinates of other acquired points were computed using Topcon software (Table 6). The coordinates of the known OSI active station were also compared with the resulting coordinates and these are presented in Table 5.

Base Length Stations		Easting (m)	Northing (m)	Height (m)
Base Station	Fixed	569322.817	836027.232	15.217
OSI Active Station	Known (1)	569830.044	836248.600	48.359
	Computed (2)	569830.044	836248.603	48.384
	Difference (2-1)	0	-0.003	-0.025

Table 5: Comparison of Active GPS Coordinates

No.	GCPs Information	Easting (m)	Northing (m)	Ortho. Height (m)
1	OSI Active Station	569830.044	836248.603	48.384
2	Base Station	569322.817	836027.232	15.217
3	GCP	569943.600	836644.749	3.341
4	GCP	569901.017	836682.820	3.658
5	GCP	570474.601	837218.653	30.020
6	GCP	569612.802	837569.547	11.210
7	GCP	569525.948	837455.615	13.275
8	GCP	567393.578	836575.852	6.035
9	GCP	566440.196	836253.136	7.437
10	GCP	567314.060	835335.233	31.616
11	GCP	568402.124	834739.729	33.359
12	GCP	568963.228	834940.388	31.061
13	GCP	569382.672	835562.79	17.854
14	GCP	569591.253	835727.047	9.651

Table 6: Computed Coordinates of Acquired GCPs in the Sligo Area

Figure 23: Ground Control Points Location

Another survey was conducted on 24th February 2010 to acquire more GCPs to verify the LiDAR point cloud quality over flat areas such as parking lots and to measure building heights using reflector less total station (Leica 1200). A mobile phone featuring Bluetooth was used as a medium of communication between the receiver and the remote server. The remote server constantly acquires RTK data from the active stations fixed by the OSI. The coordinates are computed and transferred back to the man held receiver. Figure 24 shows the basic components of Network-RTK technology. The planimetric and vertical accuracies of this system as reported by the OSI are 3 cm and 7 cm respectively (Bray, 2004). These were achieved in the said survey, using the TOPCON system. At the time of the first survey, the DIT did not have the Network RTK system available to them, otherwise more points would have been acquired the first time.

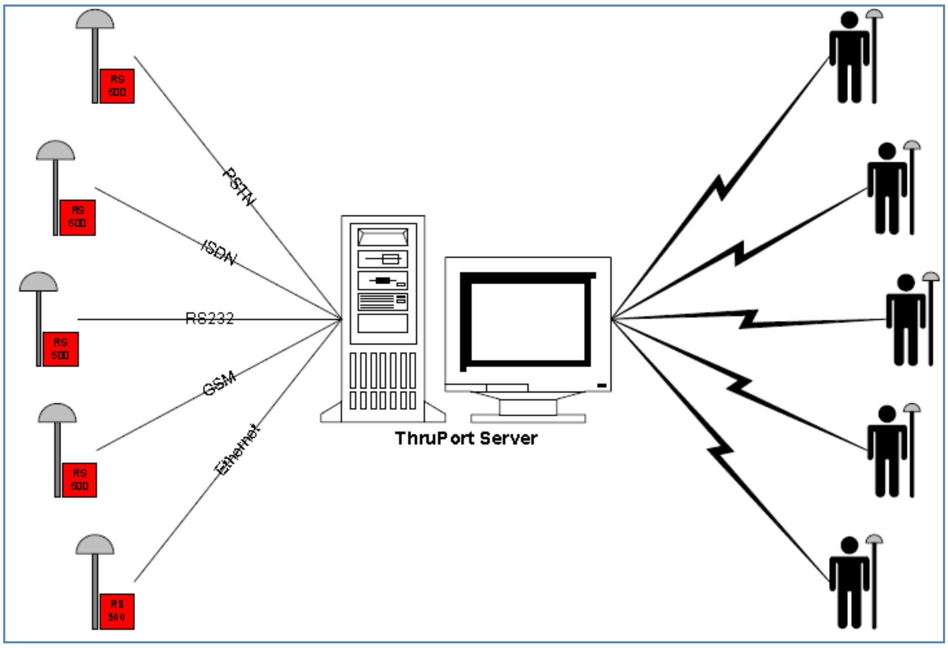

Figure 24: Network-RTK Configuration (Bray, 2004)

GPS Points	Mode	Coordinates			ΔE	ΔN	ΔH
		E (m)	N (m)	H (m)			
1	Static	569943.600	836644.749	3.341	-0.008	-0.001	-0.067
	Network-RTK	569943.608	836644.750	3.408			
2	Static	569901.017	836682.820	3.658	0.022	0.017	-0.049
	Network-RTK	569900.995	836682.803	3.707			
3	Static	570474.601	837218.653	30.020	-0.004	0.012	-0.043
	Network-RTK	570474.605	837218.641	30.063			
4	Static	569525.948	837455.615	13.275	0.016	0.015	-0.07
	Network-RTK	569525.932	837455.600	13.345			

Table 7: Accuracy Comparison of GCPs Acquisition Techniques

Four points were measured using the Network RTK system for which the coordinates were also available from the previous survey. These points were used to compare Network RTK with the static method of surveying. Table 7 shows the difference between the GCP coordinates determined in the two surveys. The maximum error in Easting, Northing and Height is 2, 1 and 7 cm respectively. This provides necessary confidence in measuring spot heights using the Network RTK system at many locations. It takes a couple of seconds to measure the coordinates once the Network RTK system is properly setup. Whereas, the static method of surveying requires two base stations to be set up and the time required at each location surpasses at least 10 minutes.

4.1.2 **Reference Building Height Data**

The orientation of total station for building height measurement was also done using point coordinates measured by the Network RTK system. Points were measured below the building roofs to calculate building heights. The measured heights (Table 8) were used to analyze the estimated building heights using the developed method of building extraction. The analysis of estimated and measured building heights is provided in chapter 7.

Building	Roof Ridge Height (m) (1)	Ground Height (m) (2)	Building Height (m) (1-2)
1	17.83	8.96	8.87
2	21.13	9.09	12.04
3	19.16	11.20	7.96
4	15.79	4.39	11.40
5	13.63	3.60	10.04
6	18.20	10.14	8.07
7	18.67	10.44	8.23
8	19.13	10.45	8.68
9	18.11	10.32	7.79
10	18.09	9.98	8.11

Table 8: Building Heights in the Development Area

4.2 LiDAR Data Processing

TerraScan and TerraMatch software from Terrasolid Inc. were used to process eight LiDAR aerial strips. The process starts by detecting low points or below surface points and points in the air using TerraScan. Flight trajectories were used in TerraMatch to find the differences between overlapping point clouds in adjacent strips over areas where the slope was high or in opposite directions. Such differences occur because of the interpolation required to geo-reference LiDAR point cloud using GPS/INS. These observed differences are translated into correction values for heading, roll and pitch which apply for the whole data set (Soininen, 2004).

Corrections	**Value**
Heading Shift	-0.031
Roll Shift	-0.0141
Pitch Shift	0.00277
Mirror Scale	0.00057

Table 9: LiDAR Strip Adjustment

Table 9 shows the correction values determined from the whole Sligo LiDAR data. After applying these corrections, differences in height values (dz) were computed at the overlapping point cloud in the adjacent LiDAR strips to identify any errors that remained after the adjustment process. Expected height and planimetric accuracies from ALS50-II sensor data are shown in Figure 25, which are dependent upon the flying height and the position of the point with respect to nadir (Leica Geosystems, 2007). The maximum error in dz was ± 0.025 m for strip 4 and 5 which is well below the sensor specification for the used flying height (Figure 26). This shows that all the strips matched perfectly. Overlapping points were deleted by restricting the FoV (Field of View) to 16° to ensure uniform point densities.

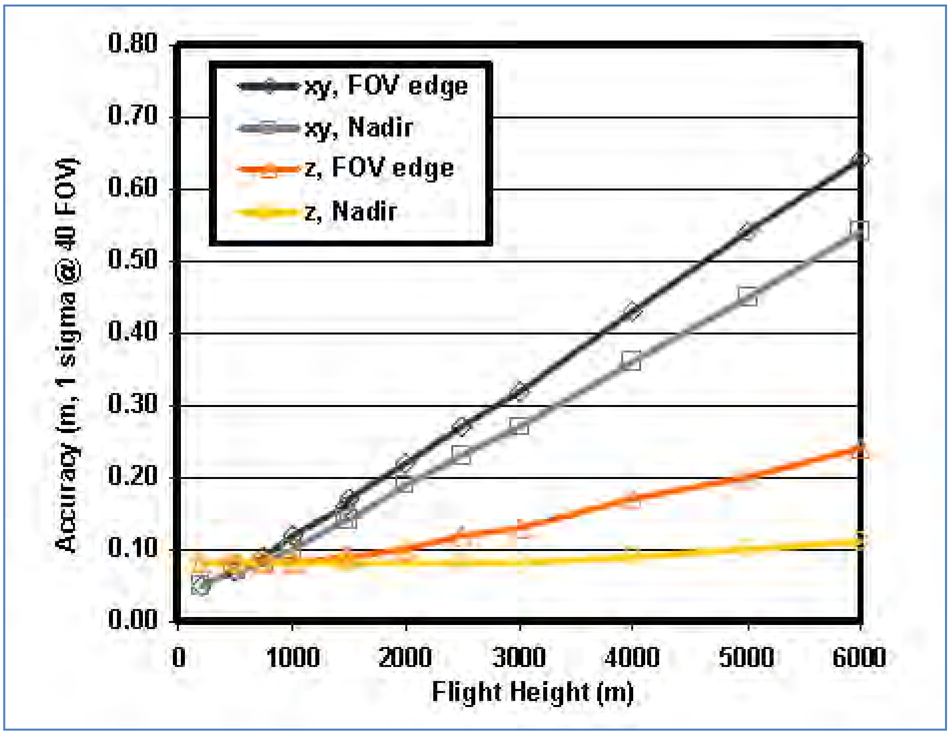

Figure 25: Leica ALS50-II Product Specifications

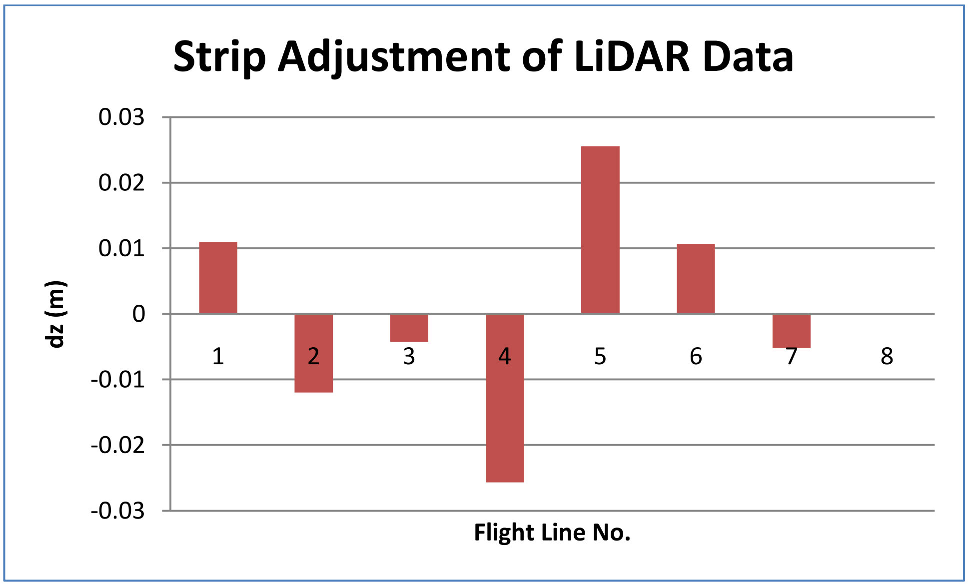

Figure 26: Height Shifts Computed in Adjacent LiDAR Strips

LiDAR data provided for the Test Area-2 was already pre-processed. Therefore, no strip adjustment was performed. However; the points overlapping in the adjacent strips were filtered using flight trajectories in TerraScan to ensure uniform point density.

4.2.1 DTM and nDSM Generation

The DSM contains ground and non-ground objects and these must be separated in order to extract a DTM which is used subsequently for nDSM (DSM-DTM) generation. Before starting the ground extraction process, it is important to detect and remove errors in the point cloud such as very low points (water bodies) or reflections in the air (birds or dust particles). TerraScan software was used to remove such points.

a. Low points (negative height): For each point a neighbourhood is considered and the low points are the points with a height value less than a pre-defined threshold below all other points within a given xy distance. However; this routine can also search for groups of low points where the whole group is lower than other points in the vicinity.
b. High points: A point is classified as high points, if there are less than the given number of neighbouring points (1-5) within a 3D search radius (2-10 m).

After removing low and high points, DSMs were generated for the development and the Test Area-1 & 2 using linear interpolation, which applies the first-order polynomials for each triangle area. The maximum TIN (Triangulated Irregular Network) linking distance was specified at this stage. A higher value will fill small gaps where either no LiDAR data is available because of the earlier filtration process or the LiDAR pulse is absorbed, such as in water bodies. Sampling was done using the nearest neighbour method. The pixel size selected for each DSM was 0.5 m.

DTM was extracted using TerraScan software which has almost become an industry standard. Figure 27 shows the inputs required for DTM extraction which are explained in the following paragraphs.

The maximum building size is required in the tile selected for processing which defines a starting grid size. Low points in these grids define the seed points for terrain extraction. Triangles in this initial model are mostly below the ground with only the vertices touching the ground. The routine then starts moulding the model upwards by iteratively adding new laser points to it. Each added point makes the model follow the ground surface more closely (Soininen, 2010).

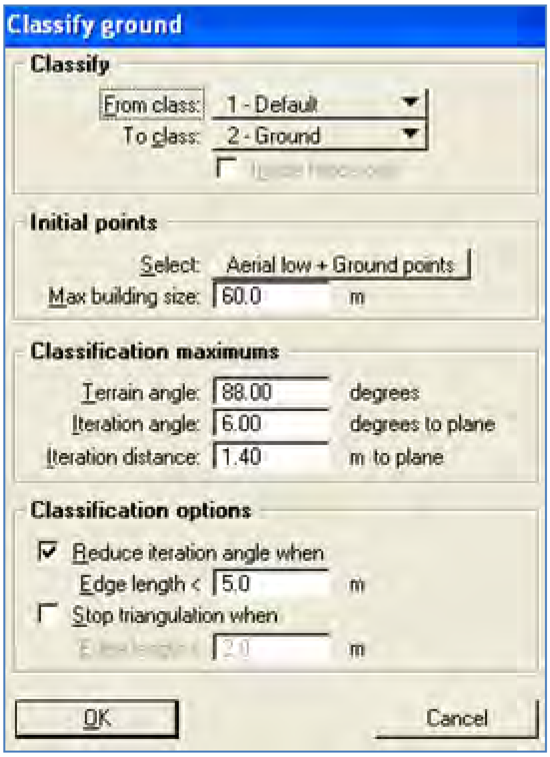

Figure 27: Parameters used for Terrain Extraction in TerraScan

Iteration parameters (for classification maximums in Figure 27) determine how close a point must be to a triangle plane for being acceptable as a ground point and added to the model. Terrain angle parameter restricts the maximum allowed angle in the generated

DTM. Iteration angle is the maximum angle between a point, it's projection on triangle plane and the closest triangle vertex. Iteration distance parameter makes sure that the iteration does not make big jumps upwards when triangles are large. This helps to keep low buildings out of the model (Soininen, 2010). Figure 29 and Figure 30 show the extracted DTMs and nDSMs in the selected development and the Test Area-1 and 2.

Negative heights in the DSM and DTM occurred due to interpolation were set to zero. MATLAB "$imfill$" operation was used to fill holes of any size by interpolating height from the neighbouring pixels in the generated DSM and DTM.

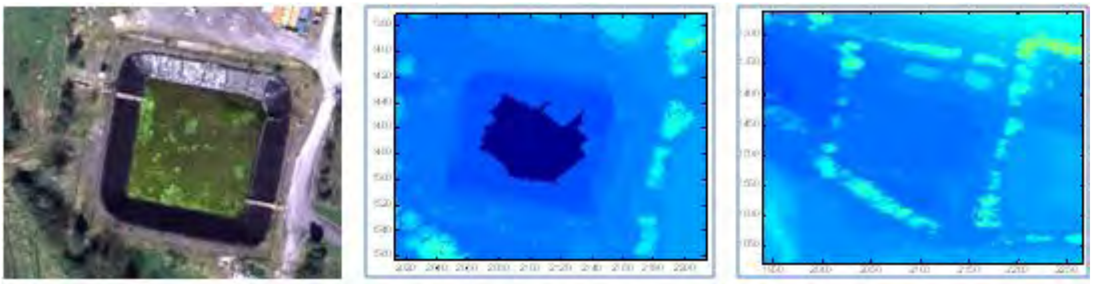

Figure 28: Results of MATLAB Hole Filling Operation (a) RGB Image (b) Hole in the DSM Before (c) After Filling

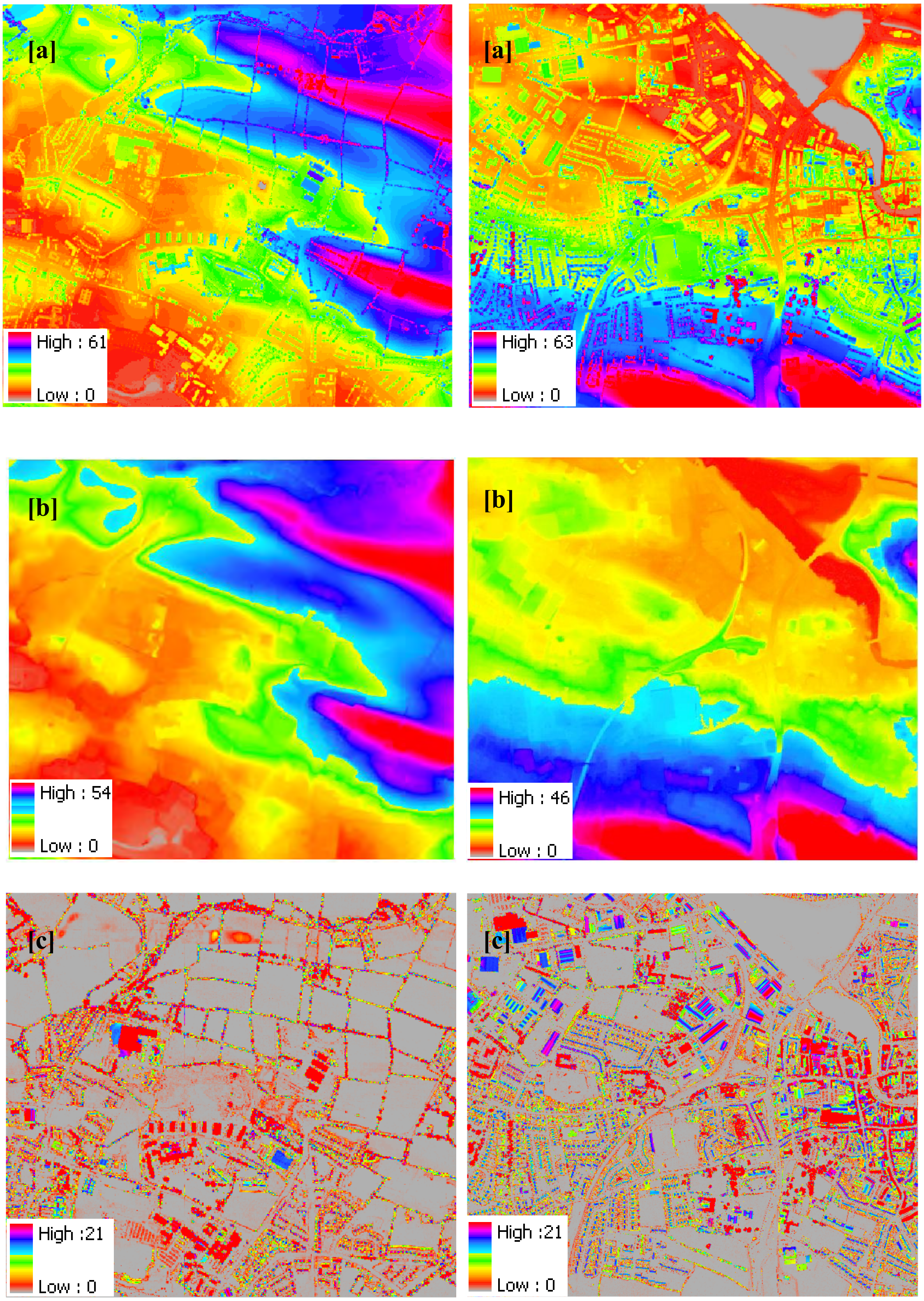

Figure 29: (a) Interpolated DSMs (b) Extracted DTMs and (c) nDSMs in Development (Left) and Test Area-1 (Right) Respectively

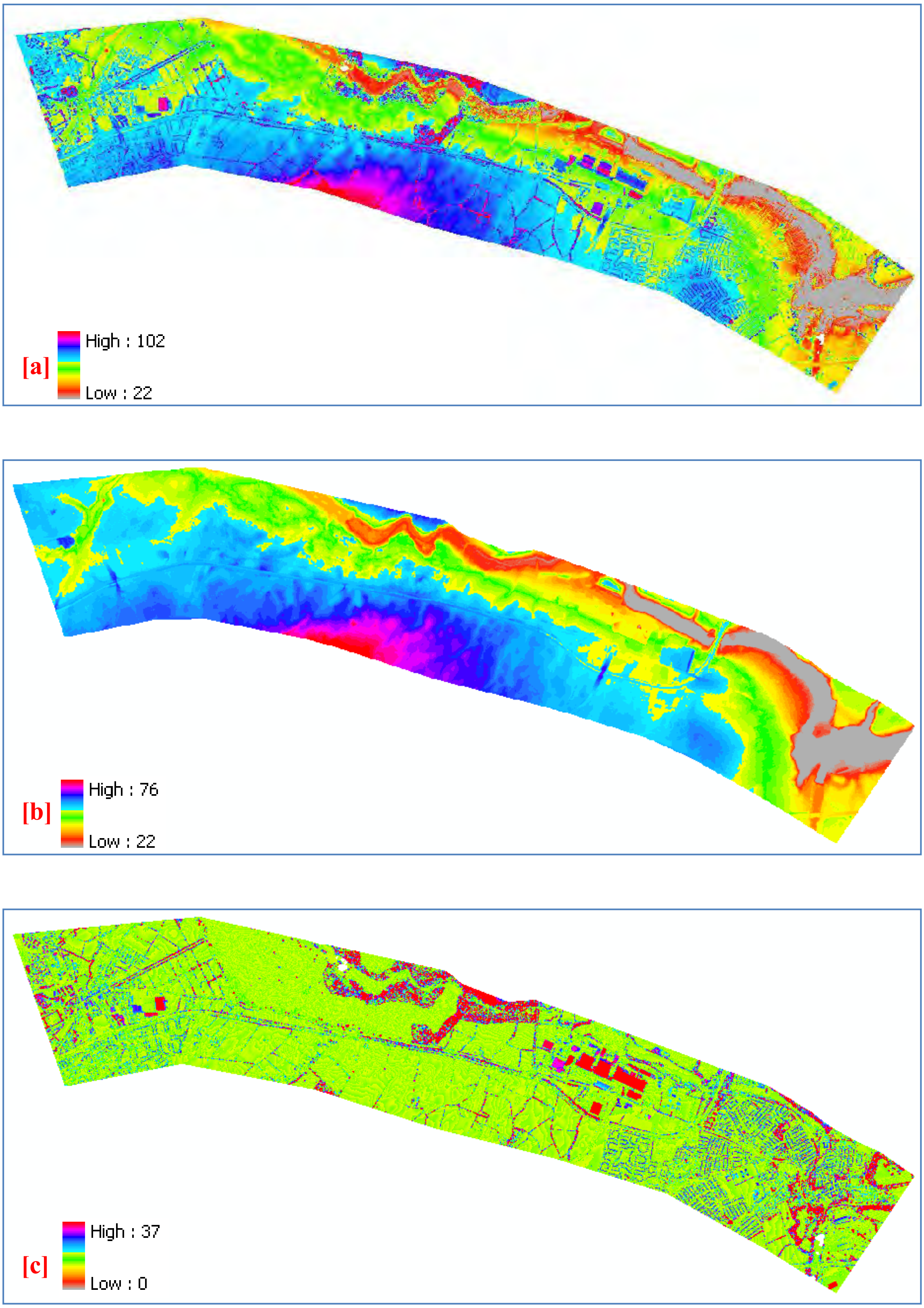

Figure 30: (a) Interpolated DSM (b) Extracted DTM and (c) nDSM in the Test Area-2

4.3 ADS40 Data Processing

Figure 31 illustrates the process involved in the acquisition and processing of ADS40 sensor data. GPro software from Leica Geosystems is used by the OSI for processing ADS40 data. It is a step by step procedure which should be followed to generate L1 (plane rectified) images from L0 (raw) images. Planimetric and vertical accuracies depend upon the accuracy achieved in the processing of GPS/INS. This is only acceptable for projects requiring medium accuracy. In order to achieve higher accuracies, triangulation of the acquired image strips with GCPs is necessary.

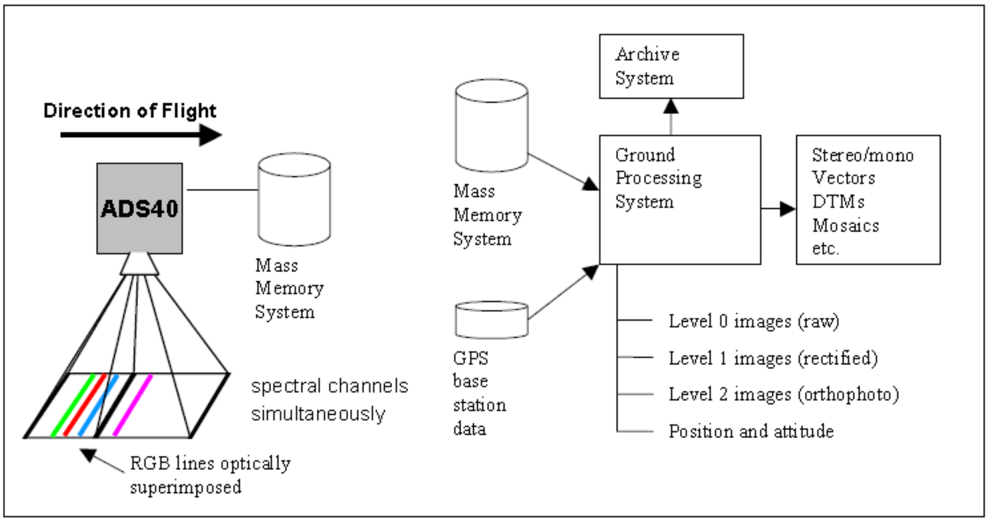

Figure 31: Direct Digital Workflow (Tempelmann et al., 2000)

The GPS and INS data, which is measured at high rates during image acquisition, yields a continuous position and attitude of the ADS40 sensor. During the triangulation process, this continuous stream of data is updated based on the principles of least squares bundle adjustment (ORIMA). "Orientation fixes" at regular intervals along the flight path of the push broom scanner are used (Figure 32 (a)) (Hinsken et al., 2002) . The colinearity equations, which describe the relationship between a point in the ground coordinate system and in the corresponding image, are generalised such that every point in the ground system falls between the two orientation fixes (Figure 32 (b)).

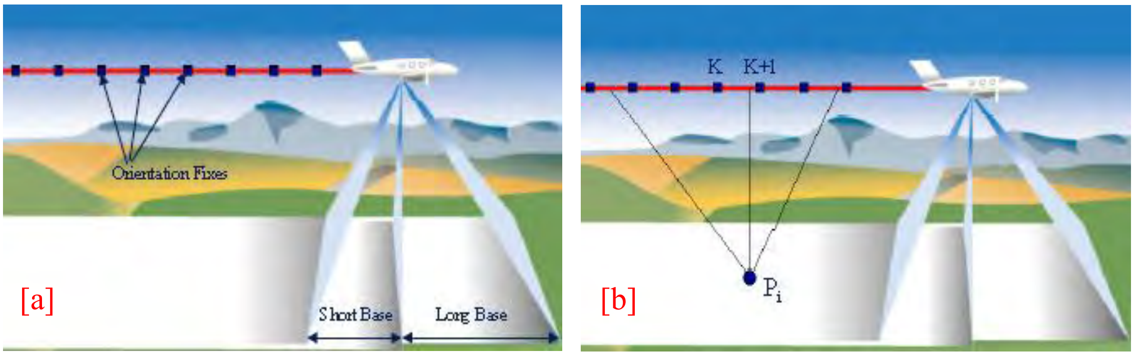

Figure 32: Orientation Fixes of GPS/INS Data (Line Scanning Camera)

$$x_i = F(X_i, Y_i, Z_i, X_k, Y_k, Z_k, \omega_\kappa, \varphi_\kappa, \kappa_\kappa, X_{\kappa+1}, Y_{k+1}, Z_{\kappa+1}, \omega_{\kappa+1}, \varphi_{\kappa+1}, \kappa_{\kappa+1})$$

$$y_i = G(X_i, Y_i, Z_i, X_k, Y_k, Z_k, \omega_\kappa, \varphi_\kappa, \kappa_\kappa, X_{\kappa+1}, Y_{k+1}, Z_{\kappa+1}, \omega_{\kappa+1}, \varphi_{\kappa+1}, \kappa_{\kappa+1})$$

Given above are the generalized co-linearity equations for image coordinates x, y of point i. F is the focal length of the camera and G is the GSD which varies with flying speed. These equations are a function of the orientation fixes k and k+1.

Raw ADS40 sensor data of the Sligo project area which consists of three flying strips was processed in-house using GPro to utilize the NIR channel which is not processed as part of the OSI workflow. It also provided the opportunity to assess the direct georeferencing quality and later to perform aerial triangulation on ADS40 sensor data. However; for the Test Area-2, only the pre processed single aerial strip was provided which lacked the NIR channel because of the earlier mentioned reason. This also made it unusable to assess direct georeferencing quality.

4.4 Accuracy Assessment of ADS40 Images and Triangulation

The captured GCPs, easily identifiable in stereoscopic panchromatic images were used for evaluating the horizontal as well as the vertical accuracy of ADS40 images. LiDAR has a high vertical and a low planimetric accuracy. Whereas, the case is opposite for ADS40 digital sensor. It is therefore considered necessary to evaluate the data from both airborne sensors prior to object extraction, especially when both data sets need to be fused. The GCPs were marked manually in the aerial images using LPS software and their corresponding ground coordinates were recorded and compared with the coordinates measured during the field survey (Table 10).

	Coordinates from Imagery (m)			Coordinates by GPS (m)					
No.	Easting	Northing	Height	Easting	Northing	Height	ΔE	ΔN	ΔH
1	569829.949	836248.469	48.443	569830.044	836248.603	48.384	-0.095	-0.134	0.059
2	569943.408	836644.769	3.365	569943.6	836644.749	3.341	-0.192	0.020	0.024
3	569901.017	836682.927	3.623	569901.017	836682.82	3.658	0.000	0.107	-0.035
4	570474.891	837218.421	30.113	570474.601	837218.653	30.02	0.290	-0.232	0.093
5	569526.085	837455.614	12.910	569525.948	837455.615	13.275	0.137	-0.001	-0.365
6	567393.524	836575.756	5.999	567393.578	836575.852	6.035	-0.054	-0.096	-0.036
7	566439.530	836253.464	6.244	566440.196	836253.136	7.437	-0.666	0.328	-1.193
8	567314.029	835335.439	31.594	567314.06	835335.233	31.616	-0.031	0.206	-0.022
9	568402.001	834739.174	32.828	568402.124	834739.729	33.359	-0.123	-0.555	-0.531
10	568963.623	834939.936	30.537	568963.228	834940.388	31.061	0.395	-0.452	-0.524
11	569382.611	835562.984	17.810	569382.672	835562.79	17.854	-0.061	0.194	-0.044

Table 10: Difference between 3D Image and GPS Coordinates

Table 11 shows the RMSE, Mean and standard deviation of 11 points used for comparison. Planimetric and vertical accuracy is about 0.30 and 0.45 m respectively which is still acceptable for projects requiring medium accuracy as well as for noise modelling and lie within the sensor specification limits of the used flying height (Geosystems, 2007). In the second run, 8 GCPs were used to calculate RMSE value at 3 check points and σ_0 using ORIMA. Three image strips were divided automatically into 72 images depending upon the GPS/INS position fixing in three flight profiles. Standard deviation allowed in GCPs' measurement was set to 0.005 m for E, N and H. The RMSE for check point differences is tabulated in Table 12.

The achieved planimetric and vertical accuracy was less than 5 cm after aerial triangulation was performed. This value is suitable for projects requiring a high accuracy.

	ΔE (m)	ΔN (m)	ΔH (m)
RMSE	0.265	0.268	0.440
Mean	-0.037	-0.056	-0.234
St. Dev	0.291	0.294	0.445

Table 11: Accuracy Assessment of ADS40 Data without GCPs

Image Block	**#GCPs/ChP**	**ChP differences / RMSE [m]**			σ_0
ADS40		**ΔE**	**ΔN**	**ΔH**	**μm**
GSD=15cm	8 / 3	0.04	0.05	0.02	4

Table 12: Empirical Accuracy for ADS40 Line Scanning System

4.5 DSM Generation by Image Matching

The DSMs were generated from stereoscopic ADS40 panchromatic images for the development and the Test Area-1 using image matching techniques in LPS and Match-T softwares before and after aerial triangulation or bundle block adjustment. Former was used for vertical accuracy assessment using GCPs and its comparison with the LiDAR DSM and latter was used for checking registration (planimetric accuracy) of LiDAR data.

In LPS, DSM is generated as an image and there is no option to have an output in the form of point cloud. This however; is not the case with Match-T. The resolution of the DSMs was 0.5 m which corresponds to a point density of 4 Points/m^2. This is the minimum requirement for extracting building roof shapes (Fritsch, 2010). The type of terrain (flat, undulating or mountainous) and terrain model required (DSM or DTM) are the two major inputs for appropriate image matching. Other inputs such as, smoothing, feature density (number of pixels to be used) and parallax threshold should also be selected appropriately, depending upon the intended use of the generated surfaces. The option that allows the detection of gross and minor errors in the generated point cloud, (Match-T only) should be enabled to automatically detect bad points. Break lines and spot heights can also be used during image matching to improve the quality of the generated surface.

The process of image matching can be problematic because methods are prone to failure in certain areas (Baltsavias, 1999). Area-based matching matches small areas or patches in each digital image using cross-correlation or least-squares matching techniques. Area-based techniques have difficulty in regions with monotonous uniform textures, such as man-made features or areas of sudden elevation change.

Feature-based matching identifies objects such as the edges of buildings, roads, etc., which are visible in both images. Feature-based techniques suffer in monotonous regions with few features. In order to overcome these problems the software packages offer different strategies and a variety of post-processing tools, for example, interpolation and filtering algorithms.

In LPS (9.1) there are eight predefined scanning strategies which all differ in search and correlation window size and the correlation coefficient limit, but also in the amount of DSM filtering, the topography, and surface type. Search window size, correlation window size, and correlation coefficient limit can be adjusted automatically if the corresponding checkbox is enabled in the strategy parameter dialog window.

If adaptive change is selected, LPS computes and analyzes the terrain features after each pyramid and determines the strategy parameters accordingly. Once the correlation coefficient has been computed for each set of possible matching image points, various statistical tests are used within LPS to determine the final set of image points associated with a ground point on the surface of the Earth. After the final set of image points has been recorded, the 3D coordinates associated with the ground feature are computed. The resulting computation creates a DSM mass point. A mass point is a discrete point, located within the overlap portion of at least one image pair, the 3D ground coordinates of which are known. A space forward intersection is used to compute the 3D coordinates associated with a mass point (Eckert and Hollands, 2010).

Gehrke et al.(2008) presented a DSM derivation approach based on Semi-Global Matching (SGM) for ADS line scanner images (Hirschmuller, 2005). It was found that the SGM derived surfaces strongly agrees with the LiDAR points. Based on high resolution ADS imagery, the increased point density reveals fine detail that may be difficult for LiDAR to capture. There are, however, significant differences inherent to the respective method. Generally around trees and vegetation, where LiDAR in contrast to image based SGM has the ability to penetrate to the ground, or measure the top more consistently.

Lemaire (2008) explained MATCH-T DSM method for the automatic measurement of an extremely large number of irregularly distributed surface points. The point extraction is on computation units. Each computation unit chooses the best suited image pairs.

Each image pair delivers a point cloud. The combined point clouds are filtered by a robust analysis. INPHO calls this extraction method sequential multi-matching.

In order to improve the matching precision, LSM can be optionally selected in the new MATCH-T DSM (5.2) software. The improvement in height accuracy of the raster is about 20%, but computation time increases by a factor of two, thus LSM is optional. The user can decide himself if the 20% accuracy improvement is worth spending that extra time. The selection of the best suited image pairs is based on the analysis of the DSM slope. The algorithm chooses images that have the best viewing angle of the matching unit. The algorithm allows a limitation of the number of models which are used for the DSM extraction in one matching unit (Lemaire, 2008).

Eckert and Hollands (2010) compared four different softwares for creating DSM in urban area. It was concluded that a little can be optimized by the user to achieve a more detailed and accurate DSM using automatic DSM generation methodologies.

DSM generated using Match-T software is better than LPS when inspected visually. Poor matching occurs in both, especially over building roofs where one side is shadowed. Although, there have been significant improvements in radiometric and spatial resolution of large format line scanners, DSM generated using LiDAR still has an edge over DSM generated using image matching techniques for tree extraction and roof modelling. Figure 33 and Figure 34 show DSMs generated using image matching techniques and their difference with respect to LiDAR DSM to highlight areas of large variation.

For noise modelling, the DTM should be accurate to 1 m. In view of this requirement, the pixels in difference images (LiDAR DSM minus DSM generated using image matching) were categorized into two classes to assess the suitability of the DSM generated using image matching techniques for the purpose of noise modelling.

Table 13 shows the percentage of pixels in the DSMs generated in Match-T and LPS, whose difference with respect to the reference (LiDAR DSM) lay in the range of ± 1 and ± 2 m. The results show the superiority of the image matching algorithm used in Match-T over LPS for generating DSMs. This is because the percentage of pixels with a difference of less than 1m with respect to the reference pixels is greater in Match-T DSM. The results are approximately the same for the development and the Test Area-1 using Match-T software. However; large variations occurred with the LPS software although the same method was used for both areas.

Height Difference	Development Area		Test Area-1	
	LPS	Match-T	LPS	Match-T
± 1 m	64.18	67.14	45.11	61.53
± 2 m	74.72	81.57	67.24	80.11

Table 13: Evaluation of Image Matching Algorithms for DSM Generation

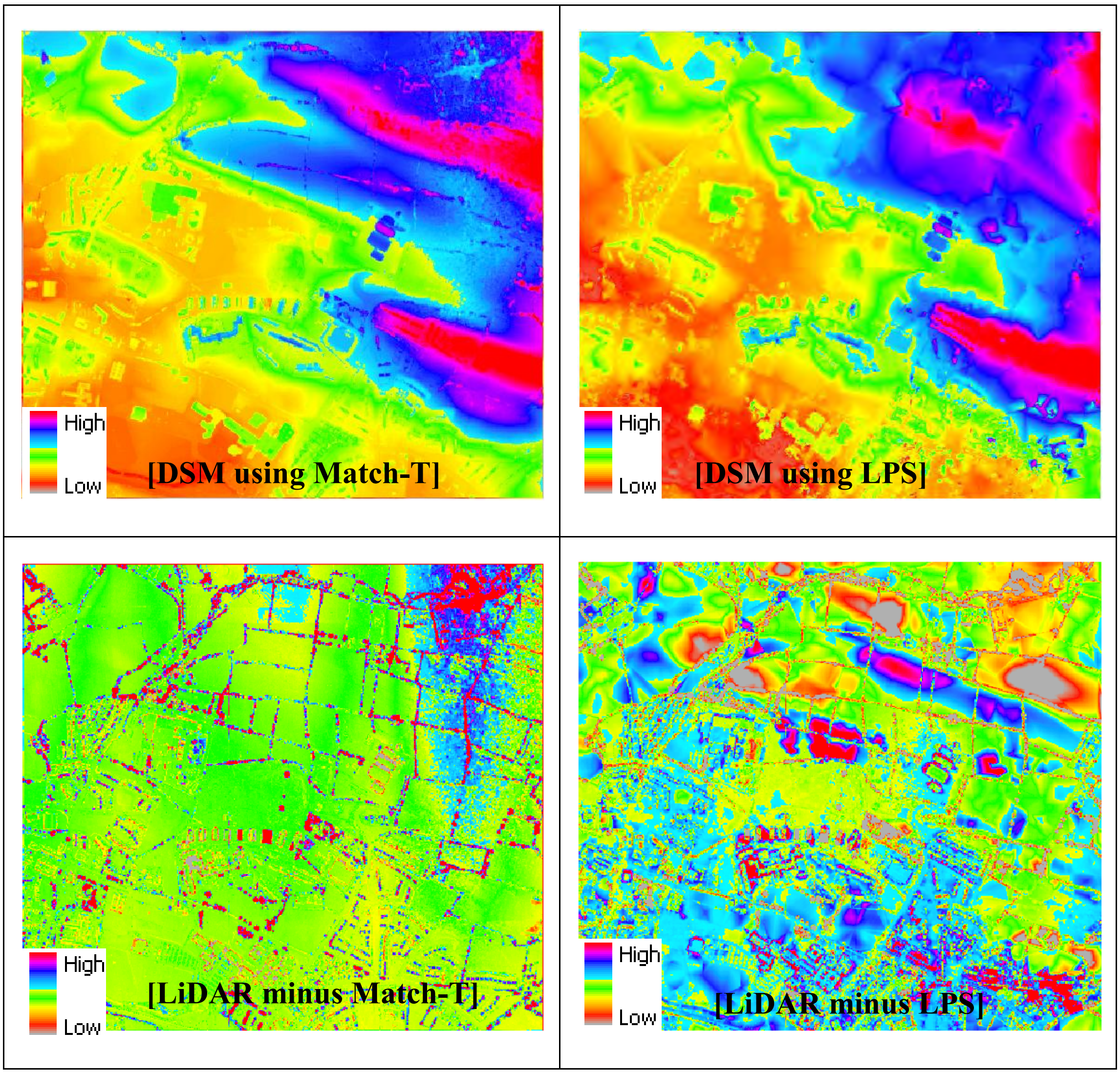

Figure 33: DSMs Generated using Match-T and LPS in the Development Area and their Difference to LiDAR DSM

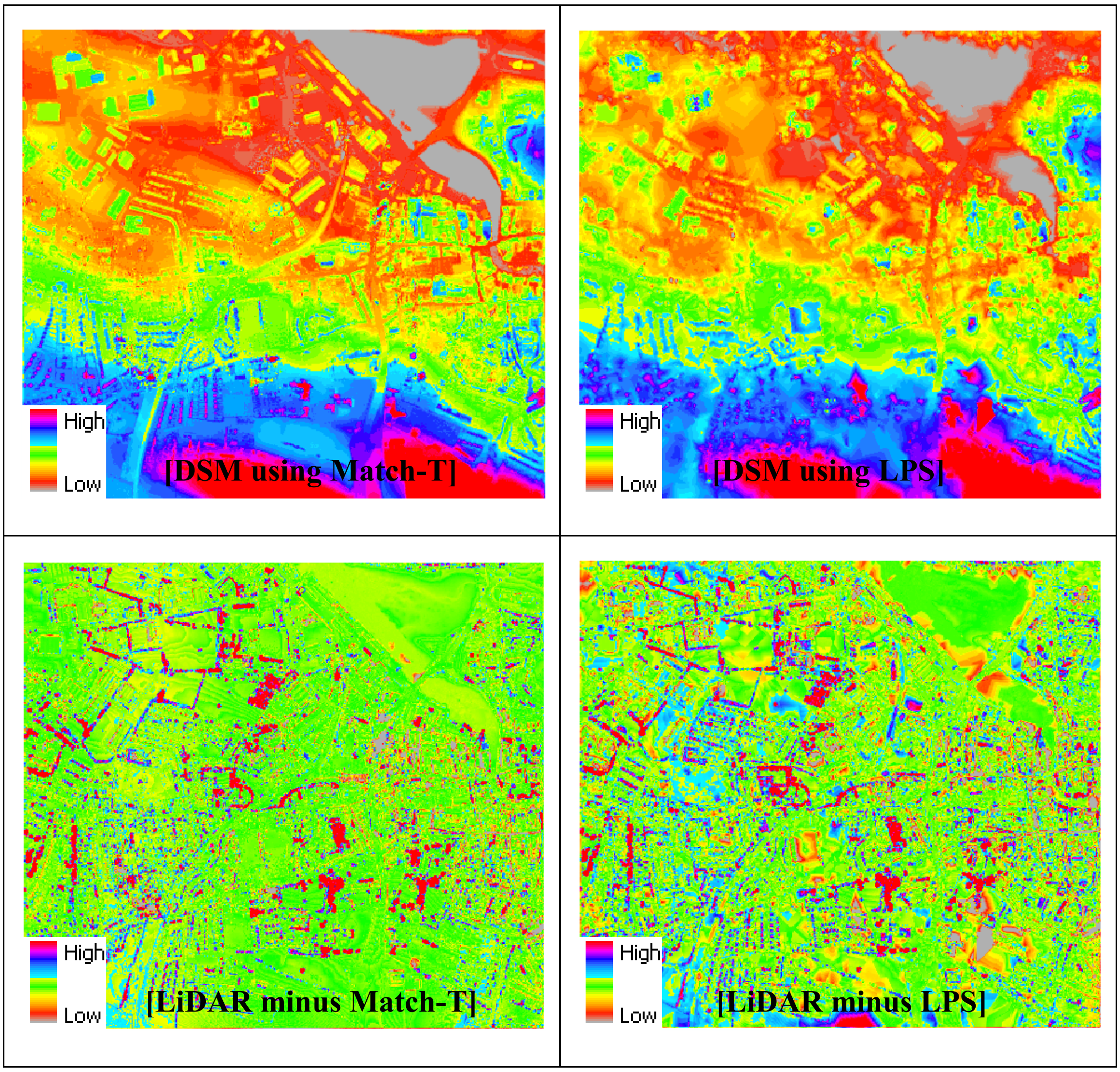

Figure 34: DSM Generated using Match-T and LPS in the Test Area-1 and their Difference to LiDAR DSM

4.6 Accuracy Assessment of LiDAR and Image DSMs

4.6.1 Vertical Accuracy of DSMs using GCPs (Static GPS Survey)

The LiDAR DSM and the DSM generated using image matching techniques have been evaluated for their vertical accuracies using the GCPs. These GCPs were collected in the static GPS survey and can also be identified in the aerial images.

Vertical Accuracy	
Difference from reference data	Δh
Number of tested points	n
Root Mean Square Error	RMSE = $\text{sqrt}(\sum \Delta h^2/n)$
Maximum Difference	$\lvert \Delta h_{max} \rvert$
Definition of a blunder (threshold)	S>3*RMSE
Number of blunders	N
Number of points without blunders	$n' = n - N$
Mean	$\mu = \sum \Delta h/n'$
Standard Deviation	$\sigma = \text{sqrt}\left(\sum(\Delta h-\mu)^2/(n'-1)\right)$
Horizontal Accuracy	$\sigma_p = \sqrt{(\sigma^2_x + \sigma^2_y)}$

Table 14: Vertical and Horizontal Accuracy Measures

It is not possible to identify the exact points in the DSMs. Therefore, the heights were computed using bilinear interpolation at the measured locations. These heights were later compared with the heights of the GCPs.

The method used to assess the vertical accuracy and remove blunder points was adopted from Höhle and Potuckova (2006) and is explained in detail in Table 14. The GCPs which were called blunder points do not mean that these were not acquired properly. In fact, they represented an error in DSMs. These points were removed from the subsequent calculation as these were few in number but significantly altered the final results. This made it difficult to predict the true picture of the available data height quality.

All GCPs were located on roads, footpaths or flat surfaces such as car parking lots. Detailed calculations are shown in Appendix-I.

DSM Generation Method	Points Observed	Blunders	RMSE (m)	Mean (m)	Standard Deviation (m)
LPS	13	3	0.489	-0.102	0.200
Match-T	10	2	0.321	-0.001	0.160
LiDAR	14	5	0.444	-0.035	0.109

Table 15: Vertical Accuracy Assessment of DSMs

The greatest vertical accuracy (standard deviation of 10 cm) was achieved using LiDAR for DSM generation. Vertical accuracy is dependent on the flying height and position of the point with respect to nadir. The expected vertical accuracy from the available ALS50-II LiDAR data is around 10 cm which is similar to the estimated vertical accuracy as shown in Table 15. This suggests that LiDAR generated DSMs are superior to the ones generated using image matching techniques (area, feature based or together).

For a typical photogrammetric project, $\sigma_h = 0.02 - 0.03\%$ of the flying height (Höhle and Potuckova, 2006). ADS40 stereoscopic panchromatic images of Sligo were captured at a flying height (H) of 1,447 m with an expected $\sigma_h = 0.29 - 0.44$ m. Both image matching softwares generated good quality DSM in flat areas where most of the acquired GCPs were located. This also resulted in achieving good vertical accuracies as can be seen from Table 15.

Number of blunder points was higher in LiDAR DSM as compared to the other DSMs. However; this is due to the low RMSE value of LiDAR which results in a tighter threshold to filter blunder points. As a subsequent result of this, more points were eliminated. However; this shows how close the LiDAR measurements match with the heights of the acquired GCPs (precision). The comparison of height interpolated at each GCP location from three different DSMs is shown in Figure 35. The points which were eliminated as a result of not meeting the threshold value in any of the DSMs show zero height difference such as point 8, which was identified as a blunder point in all DSMs.

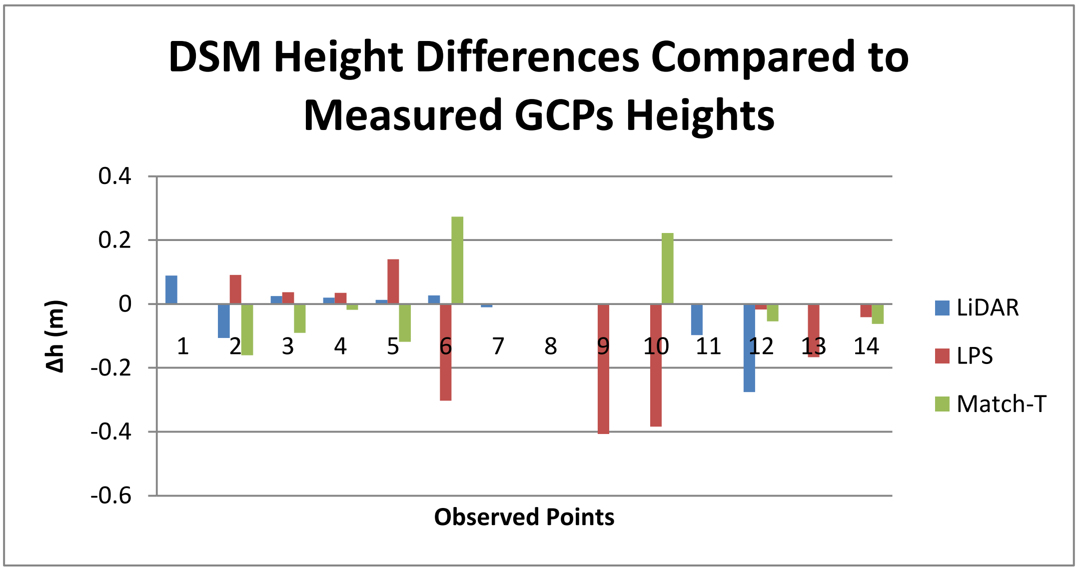

Figure 35: Height Difference Comparison in the Generated DSMs

4.6.2 Vertical Accuracy of DSMs using GCPs (Network RTK)

A total of 165 points were captured in the second round using Network RTK system (Appendix-V). Figure 36 shows the location and characteristics of 5 selected areas for data acquisition. The previous DSM evaluation using 14 GCPs was not considered sufficient enough to quantitatively determine the DSM quality. An approach similar to the previous one was used with the new GPS points with small modifications because of large Δh values. These mostly occur in DSMs generated using LPS. A threshold of ± 1 m was used initially, prior to the determination of RMSE in order to remove all points having Δh values greater than the selected threshold. The DSMs from LPS, LiDAR and Match-T were used for vertical height accuracy assessment.

Figure 36: Five Surveyed Sites in Development Area (Sligo)

After removing the blunder points, RMSE was calculated, followed by mean and standard deviation as has been done in the previous section. Table 16 shows the number of points removed as blunders, the total points finally used in the assessment and the standard deviations. The standard deviation values are on the higher side for LPS and Match-T generated DSMs when compared to using only 14 points for assessment as was done previously. However, vertical accuracy of LiDAR DSM is still close to the anticipated value of 10 cm.

Parameters	LPS	LiDAR	Match-T
Points Available	165	165	165
$\Delta h > \pm 1\ m$	49	4	0
RMSE (m)	0.400	0.153	0.405
$S > 3\ RMSE$	1.201	0.459	1.215
New Blunders	0	5	0
Final Points Used	116	156	165
Mean (m)	-0.212	-0.074	-0.024
σ_v (m)	0.340	0.083	0.329

Table 16: Vertical Accuracy Assessment Using GCPs Acquired by using Network RTK System

The blunder points were very close to the buildings and trees (Figure 36, Area-3 &5) where matching is poor in overlapping images. The blunder points can also occur because of the interpolation required for DSM generation. That is why it was considered important to evaluate the vertical accuracy of point cloud using independent GCPs and not the generated DSMs.

4.6.3 Vertical Accuracy of Point Cloud using GCPs (Network RTK)

Five areas (Figure 36) for which GCPs were acquired using the Network RTK system were used again to determine the vertical accuracy of the point cloud produced using LiDAR and image matching techniques. This was done without converting them to a surface model. However; the DSM obtained from LPS was converted to a point cloud using the elevation value at the pixel centre. This was done because LPS cannot produce a point cloud as an output.

TerraScan provides a routine to compare the ground points against the control points. It scans through the 3D point cloud and loads points within a given search radius from any of the known points. It then creates a small triangulated surface model from the points around each known point. The elevation for each known point location is then computed from the triangulated surface model. This effectively interpolates the elevation from the points which were closest to a known point. A report is generated as an output (Table 17) listing the interpolated elevations at a known location from the point cloud and the difference with respect to the actual measured value in the field (Soininen, 2010). If the determined elevation shift is more than the expected (determined from sensor specification for a particular height), it can be applied to the available data.

Table 17 shows that the available LiDAR data and the point cloud obtained using Match-T software have a high vertical accuracy. However; the results obtained from the LPS point cloud show the short comings of the matching software in the regions surrounded by buildings and trees. This results in a large number of blunder points and high standard deviation values especially in the Area-3 (Figure 36).

Figure 37 shows the standard deviations in elevations obtained from three different point clouds with respect to the measured values in an independent ground truth survey. The high accuracy of LiDAR point cloud makes it more suitable for object extraction rather than creating it from stereoscopic images. The quality of the point cloud obtained from image matching techniques especially from Match-T is good for applications that require terrain model to be accurate up to 1 m. However; this is not the case with LPS which requires considerable improvements.

Area	No. of Points	DSM	Mean (m)	Standard Deviation (m)	RMSE (m)	Average (m)	Min. dz (m)	Max. dz (m)
1	37	LiDAR	0.097	0.129	0.088	-0.096	-0.410	0.020
		Match-T	0.120	0.129	0.140	0.056	0.292	0.230
		LPS	0.468	0.265	0.524	-0.454	-1.063	0.231
2	17	LiDAR	0.123	0.131	0.045	-0.123	-0.177	-0.016
		Match-T	0.085	0.068	0.102	0.078	-0.031	0.190
		LPS	0.140	0.220	0.221	-0.057	-0.701	0.238
3	37	LiDAR	0.219	0.234	0.085	-0.219	-0.500	-0.122
		Match-T	0.712	0.151	0.728	-0.713	-0.931	-0.312
		LPS	5.925	3.897	7.058	5.925	1.501	13.88
4	29	LiDAR	0.054	0.071	0.072	-0.004	-0.140	0.204
		Match-T	0.033	0.038	0.040	0.014	0.073	0.097
		LPS	0.189	0.323	0.319	0.037	0.594	1.014
5	44	LiDAR	0.122	0.128	0.039	-0.122	-0.196	-0.025
		Match-T	0.363	0.252	0.380	-0.289	-0.502	0.447
		LPS	0.769	1.586	1.576	0.195	-0.593	8.539

Table 17: Vertical Accuracy Assessment of Point Cloud Obtained using LiDAR and Image Matching Techniques with Respect to Independent GCPs

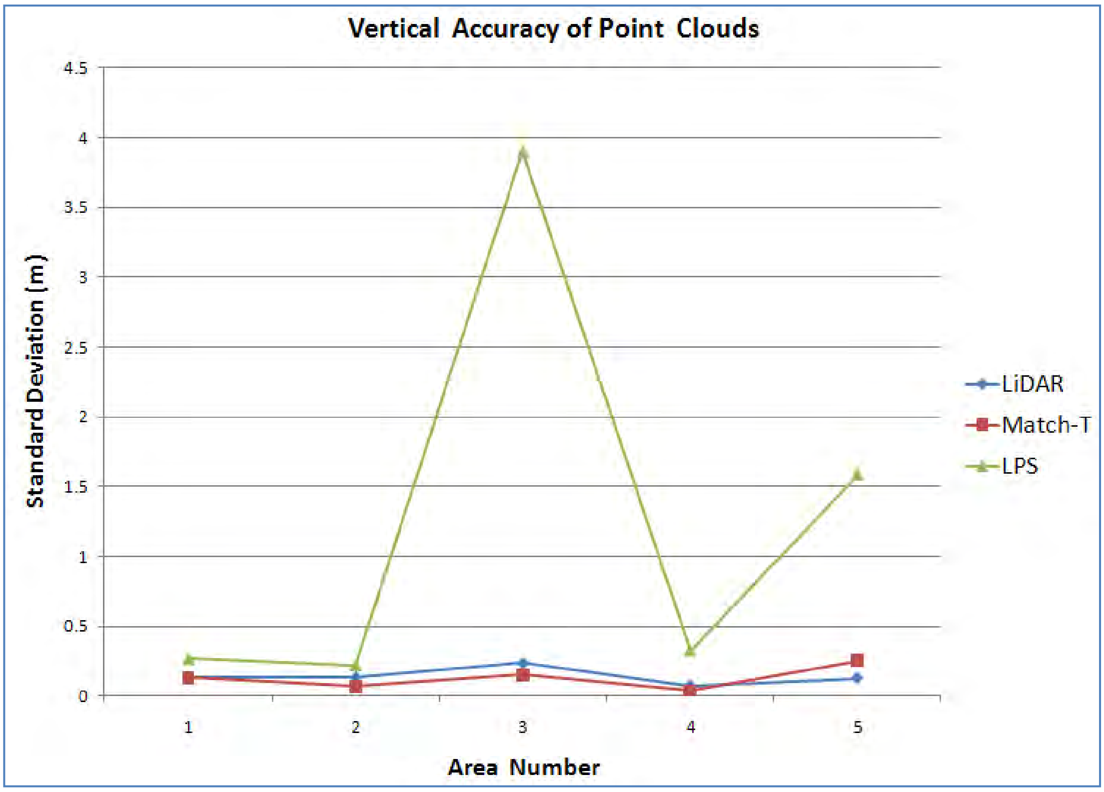

Figure 37: Standard Deviation of Interpolated and Measured Height Values

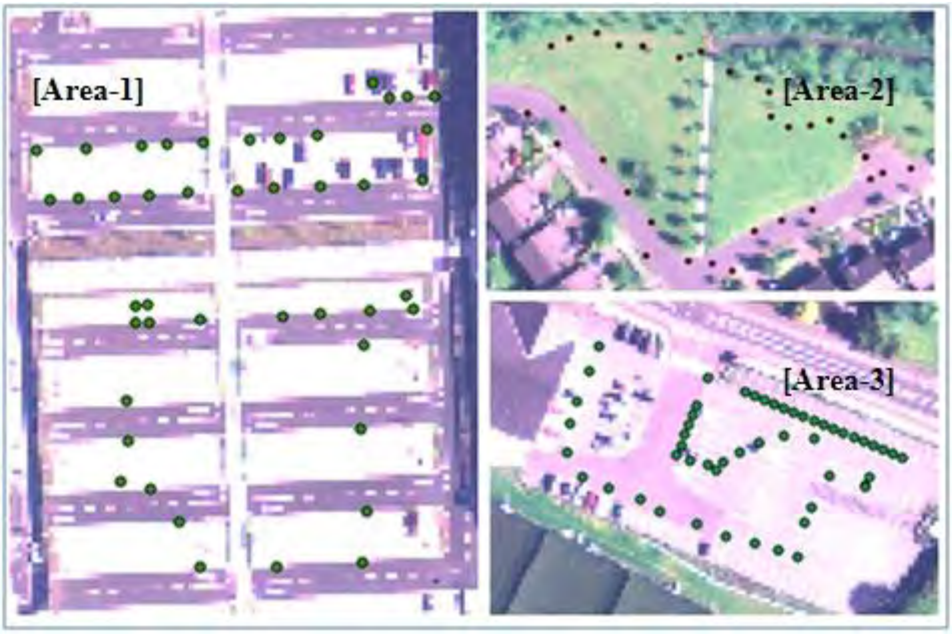

Figure 38: Three Surveyed Sites in Test Area-2 (Maynooth-Leixlip) using Network RTK System

Area	No. of Points	DTM (Source)	Mean (m)	Standard Deviation (m)	RMSE (m)	Average (m)	Min. dz (m)	Max. dz (m)
1	44	LiDAR	0.200	0.076	0.212	0.198	-0.038	0.352
2	35	LiDAR	0.132	0.094	0.151	0.118	0.095	0.329
3	52	LiDAR	0.036	0.042	0.044	0.016	-0.141	0.105

Table 18: Vertical Accuracy of Generated DTM using TerraScan Software in the Test Area-2

Figure 38 shows three areas in the Test Area-2 where GCPs (Appendix-VI) were acquired in a field survey to determine the accuracy of ground extraction from the available LiDAR data using TerraScan. The points were acquired on a hard surface such as car parking lots (Figure 38: Area-1 & Area-3) as well as on soft ground (Figure 38: Area-2) surrounded by vegetation and buildings.

The standard deviation (Figure 36) of the measured heights (GCPs) and the heights interpolated from the extracted ground (LiDAR) for these known locations is very low and approximately the same as achieved in the Sligo Area. However; in the Test Area-2 the extracted filtered ground was evaluated rather than the full point cloud to evaluate the quality of the generated DTM (Table 18).

4.7 DSM Registration

The proper registration of LiDAR and aerial images is a necessary prerequisite for any process combining the two data sources (data fusion). Both LiDAR ALS50-II and ADS40 sensors rely on direct georeferencing, which needs to be verified to ensure proper registration.

Point features are the principal sources of control for photogrammetric triangulation although extracted linear features and planar patches have also been used in the past research for registering LiDAR and aerial images (Habib and Schenk, 1999; Habib et al., 2004; Mitishita et al., 2008). The accuracy of LiDAR systems has improved greatly in the recent years which is why LiDAR data is considered as a viable source for photogrammetric control (Mitishita et al., 2008). Locating a single image point that corresponds to a particular laser point in the LiDAR set is either very difficult or impossible (Baltsavias, 1999). Building boundaries, roof ridges and break-lines extracted from the aerial imagery and LiDAR are useful for registering both data sets.

Ressl et al. (2008) used DEM in the overlapping LiDAR strips for checking the quality of the relative orientation. A roughness mask was calculated for each strip to consider only smooth surfaces. If the differences are above expectations, a deeper analysis of the two slightly shifted grids was done using least square matching. This is because, the height differences between pairs of overlapping strips show the summed effect of all errors from GNSS/IMU and laser. This total effect should be split into its parts in X, Y and Z.

Kager (2004) used corresponding tie planes in the overlapping LiDAR strips and flight trajectory for LiDAR strip adjustment to correct internal systematic errors and to improve the relative orientation of the strips. This was done by minimizing the residuals at corresponding planes in the overlapping LiDAR strips. The absolute orientation of the LiDAR data was corrected using ground control planes. These were provided from terrestrial measurements or measured during aerial triangulation. These control planes can then be used simultaneously in the strip adjustment, together with the tie planes. Using this approach the entire LiDAR strip adjustment can be compared with block adjustment by integrated sensor orientation as in the case of aerial images.

In case of conventional aerial images or modern digital cameras with central projection for each captured image, normal collinearity equations are applicable for transforming object coordinates in LiDAR to image space. ADS40 data is a continuous array of pixels in the flight direction, directly georeferenced using an on board GPS/INS. GPS/INS positions are fixed at different intervals. The position and orientation for each array of pixels is then interpolated between these fixed intervals.

Most photogrammetric projects are carried out in a configuration that provides a 3D stereoscopic model of the project area. However; in this research, high radiometric resolutions of modern large format digital cameras were utilized in order to make the registration process simple and quick. High quality GCPs were used for the aerial triangulation of ADS40 strips to generate a reference dataset that can be used for registering LiDAR data. The available LiDAR data was already evaluated for its vertical accuracy in the DSM and point cloud forms prior to this.

The DSMs were created from overlapping images using image matching techniques. This process eliminates the need of extracting common features in data sets and their matching. A fully automatic extraction process with high robustness and accuracy is still not available which further obstructs the registration process. DSMs obtained from LiDAR and by image matching using Match-T after aerial triangulation were used to register LiDAR data with aerial images. Two approaches have been considered which are explained in the following sections.

4.7.1 **First Approach**

Common points were identified in LiDAR and image DSMs. A 2D conformal transformation (translation, scale and rotation) was then used to determine the transformation parameters and applied to the whole LiDAR point cloud.

The 2D conformal transformation equations that were used are as follows:

$$X = ax - by + C_X$$

$$Y = bx + ay + C_Y$$

The above transformation was applied about the origin of the coordinate reference system.

4.7.1.1 Sligo Project Area

Parameters	Panchromatic Images	
	Development Area	Test Area
a	1.001611	0.9999799
b	0.000640	0.001044
C_x	-381.097	987.467
C_y	-1709.745	-425.613
$RMSE\ X$	0.75 pixel (0.39m)	0.92 pixel (0.33m)
$RMSE\ Y$	0.67 pixel (0.35m)	0.65 pixel (0.29m)
Rotation* $(\theta = tan^{-1}(\frac{b}{a})$	0.000638	0.001044
Scale $\lambda = \sqrt{a^2 + b^2}$	1.001610	0.999799
X shift Mean (m)	-0.80	-0.28
Y shift Mean (m)	0.20	-0.27

Table 19: Transformation Parameters for ALS50-II LiDAR sensor data in Sligo Project Area

DSMs from LiDAR and aerial images were created with a resolution of 0.5 m. Transformation parameters (Table 19) were determined using eight common points to transform LiDAR ALS50-II point cloud before fusing it with the multispectral data.

The values for X shift Mean and Y shift Mean were calculated from the 8 points used in the matching process. Georeferencing can be an issue while implementing the developed method for extracting objects important from a noise modelling perspective and this simple method can be used to rectify such problems.

4.7.1.2 EuroSDR Project

EuroSDR started a research project whose aim was to evaluate the techniques used for registering LiDAR with aerial images. DIT also participated in this project as it provided an opportunity to evaluate the method that was developed in house, on the data from other sensors. DMC aerial images, ALS50-II and Optech ALTM 3100 data were provided by the EuroSDR to the participants. Artificial shifts and rotations were purposely introduced by the project organizer in the LiDAR data.

The developed method was tested during this project. Match-T was used to generate DSMs from the panchromatic and the coloured stereoscopic aerial images captured using the DMC camera for registering ALS50-II and Optech LiDAR data.

Panchromatic and colour orthophotos were created using the generated DSM from image matching. This was done to make sure that the provided interior and exterior orientation parameters were properly setup using the GCPs. The GCPs were also provided by the EuroSDR as a part of the dataset.

The NIR band was provided at a later stage, by the EuroSDR because of the large vegetation cover, hindering automatic building extraction from the aerial images. However; this has not been used in the developed method.

Figure 39 shows the used DSMs generated from ALS50-II and Optech LiDAR sensors, DSMs from image matching using Match-T and orthophotos.

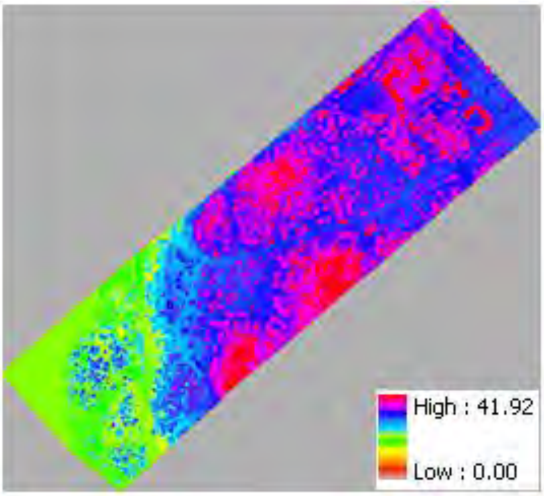

ALS50-II DSM

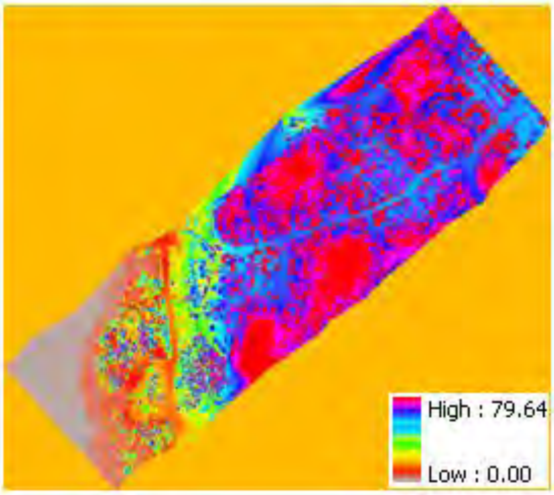

Optech ALTM 3100 DSM

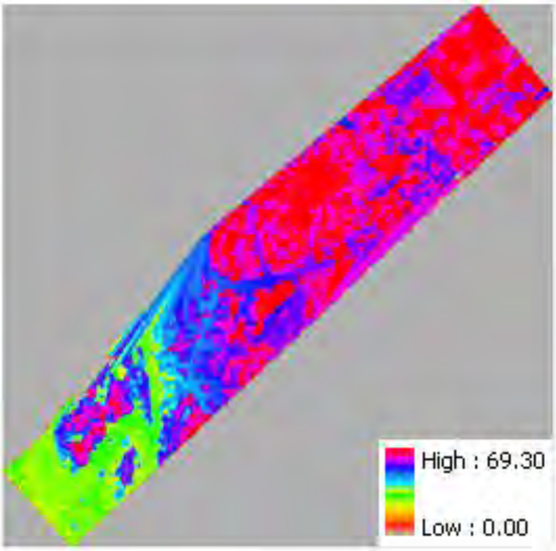

DSM from Pan Images

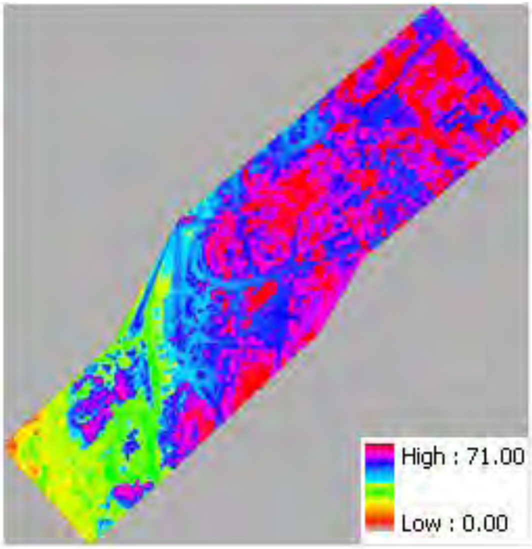

DSM from RGB Image

RGB Orthophoto

Panchromatic Orthophoto

Figure 39: Data Processing Steps in the EuroSDR Project

The quality of the DSM generated from the panchromatic aerial images was much better as compared to the DSM produced from the multi-spectral images. The reason for this is that the DMC sensor has 4 panchromatic CCD lens modules. The four panchromatic images from these converging cameras are mosaiced digitally to form a single high resolution image as compared to four independent channels for capturing multispectral information. This results in a reduced ground resolution (Hinz et al., 2001). Computed parameters of the transformation for registering LiDAR with aerial images are listed in Table 20.

Parameters	Panchromatic Images		RGB Images	
	Optech ALTM 3100	ALS50-II	Optech ALTM 3100	ALS50-II
a	1.000508	0.999846	0.999819	0.9999493
b	-0.001018	-0.00111	-0.00114	-0.000082
C_x	-6953.95	-7358.28	-7499.45	-377.89
C_y	-3029.81	1415.07	1610.74	3390.75
$RMSE\ X$	0.8 pixel (0.39m)	0.7 pixel (0.33m)	0.23 pixel (0.05m)	0.4 pixel (0.2m)
$RMSE\ Y$	0.7 pixel (0.35m)	0.6 pixel (0.29m)	0.5 Pixel (0.25m)	0.5 pixel (0.25m)
Rotation* $(\theta = tan^{-1}(\frac{b}{a})$	-0.0010	-0.0011	-0.0011	-0.0001
Scale $\lambda = \sqrt{a^2 + b^2}$	1.0005	0.9998	0.9998	0.9995
X shift Mean (m)	24.06	-18.84	24.17	-18.09
Y shift Mean (m)	-17.89	-21.22	-17.39	-20.87
* Rotation θ is in Radians and about origin of the coordinate system				

Table 20: Computed Transformation Parameters

The shift parameters, C_X and C_Y were not indicative of the actual shifts between the LiDAR and images. Therefore, these were analysed separately, following the application of the transformation to the LiDAR data set, based on a sample of 1000 points. These are given as X shift Mean and Y shift mean in Table 20.

Preliminary results are available for the EuroSDR project (Rönnholm, 2010). The comparison was done using six local reference surfaces (distributed to different sides of laser scanning strips) that were created from additional terrestrial laser scanning (with expected accuracy of a couple of centimetres). Laser point clouds were registered with reference surfaces using ICP (iterative closest point) method. The total error budget includes errors from developed registration method as well as from internal geometrical errors of laser scanning data and image orientations.

The preliminary results relating to the accuracy of the registration method are discussed in chapter 7 along with the results obtained by the methods developed by other project participants.

4.7.2 Second Approach

Instead of identifying common points in the images, cross-correlation method was investigated by convolving LiDAR DSM over image DSM to reach a point where correlation reaches its peak value. This method has certain limits such as:

a. This method was limited to the determination of the shifts in X and Y directions.
b. An initial estimation pertaining to the amount of shift that occurs between the two datasets was required to set the convolution limits. This was particularly important for the EuroSDR project where large shifts were artificially induced.
c. The quality of the image DSM was poor as compared to the LiDAR DSM especially over vegetation, building roofs (shadows) and the regions occluded by high objects or shadowed.

However; this method can be easily automated, if the shifts are small and the quality of both DSMs is good. Two parameters i.e. the maximum shift allowed in X and Y directions are required to initiate the process. The process terminates by providing the output of the location where the maximum correlation is reached.

$$Cov_{ij} = \frac{\sum_{k=1}^{N}(Z_{ik} - \mu_i)(Z_{jk} - \mu_j)}{N - 1}$$

$$Corr_{ij} = \frac{Cov_{ij}}{\delta_i \delta_j}$$

Where,

Z - value of a cell

i,j – are image layers

μ- is the mean of a layer

N- is the number of cells

k - denotes a particular cell

δ_i and δ_j are standard deviations of image i and j

Cross correlation values are determined by moving LiDAR DSM over image DSM in a window of 5 m^2. The computed values are shown in Figure 40. As the shifts in the Sligo data were small, a high correlation value was achieved in the beginning of the process.

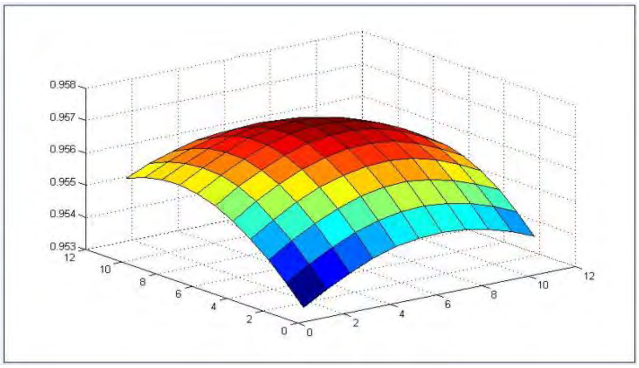

Figure 40: 3D Scatter Plot

The method is computationally intensive and not recommended for large areas. It was therefore not considered any further. The manual matching of common points is faster and more reliable however; it requires human intervention in the registration process.

Different issues related to LiDAR (ALS50-II) and ADS40 data processing were discussed in this chapter. This was done with a special emphasis on achievable accuracies using the data from these sensors which was verified by the ground truth data. Direct georeferencing quality was evaluated and in case of a mismatch, a solution was also suggested to register LiDAR data with stereoscopic aerial images. This is because a few GCPs are required for ADS40 aerial triangulation to achieve a reference data set with which LiDAR can be matched. In the next chapter a method has been developed for extracting objects of interest by fusing the information extracted from these two datasets.

5 Method Development

This chapter details the steps considered and implemented during the course of this research to fuse LiDAR and aerial images for the extraction of buildings, trees and roads. The object extraction strategy was developed in the area called the development area and later tested as such on the two test areas i.e. Test Area-1 and Test Area-2.

The extraction method used for each object of interest is explained in its respective section. The initial step was the generation of orthophotos to avoid a strategy based on co-linearity equations i.e. back projection of LiDAR data (or object segments) to the multi-spectral images. This was because of the non availability of nadir NIR image. Another reason for avoiding co-linearity equations was the fact that and each array of pixels in the push broom scanner has its own geo referencing as has been explained in the preceding chapter.

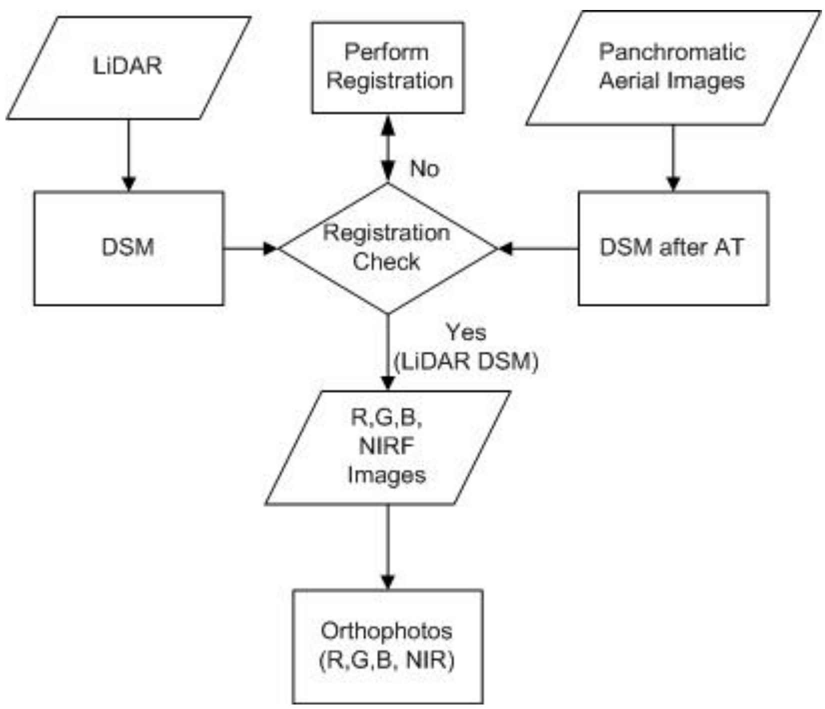

Figure 41: Orthophoto Generation

The steps undertaken for orthophoto generation can be seen at a glance in the following flow chart in Figure 41 and explained subsequently.

- Single return data from LiDAR was used for DSM generation. The DSM from the aerial images was also generated after aerial triangulation.
- The DSM from aerial images was used as a reference to check to eliminate any errors in the direct georeferencing of the LiDAR data, as has been explained in the previous chapter.
- The orthophotos from nadir R, G, B and forward looking NIR (18°) section of the electromagnetic spectrum were created using LPS.

Figure 42: (a) True Colour and (b) Colour Infrared Orthophotos

Figure 42 shows a combination of different spectral bands (a) R,G,B and (b) NIR,R,G that have been further exploited to extract useful information for object extraction such as NDVI and NDWI (Normalized Difference Water Index) indices.

Proper thresholding of these calculated indices is necessary to extract desired objects and different methods have been considered in order to achieve this. The building segments were generated from thresholded NDVI and binary nDSM (DSM-DTM) and further classified to remove remaining vegetation segments using cues obtained from LiDAR. Building extraction is generally hindered by the presence of vegetation. Although NRA is not interested in vegetation, however; it should be separated for successful building extraction.

A method was developed for the generation of vegetation segments (Figure 70) and classification of building segments in vegetation, left after the NDVI thresholding. The vegetation was further classified into trees and hedges using a shape parameter. A method for tree crown extraction was also developed (Figure 78). Singles trees were separated from tree clusters using a distance matrix.

Roads are generally part of DTM and were separated from grass and barren surfaces using LiDAR intensity and NDVI images (Figure 83). The holes were filled in the resulting road segments. The road gradient was also determined.

The MLS data was only available for a section of road connecting the towns of Maynooth and Leixlip (Test Area-2) and is used in this research for noise barrier extraction.

In the following sections, the details of methods developed for extracting each object of interest (building, tree, road and noise barrier) and the steps taken to address different issues have been explained. In the end, accuracy assessment methods that have been used for determining the success of the developed methods using reference data from the OSI have been explained.

5.1 Building Extraction

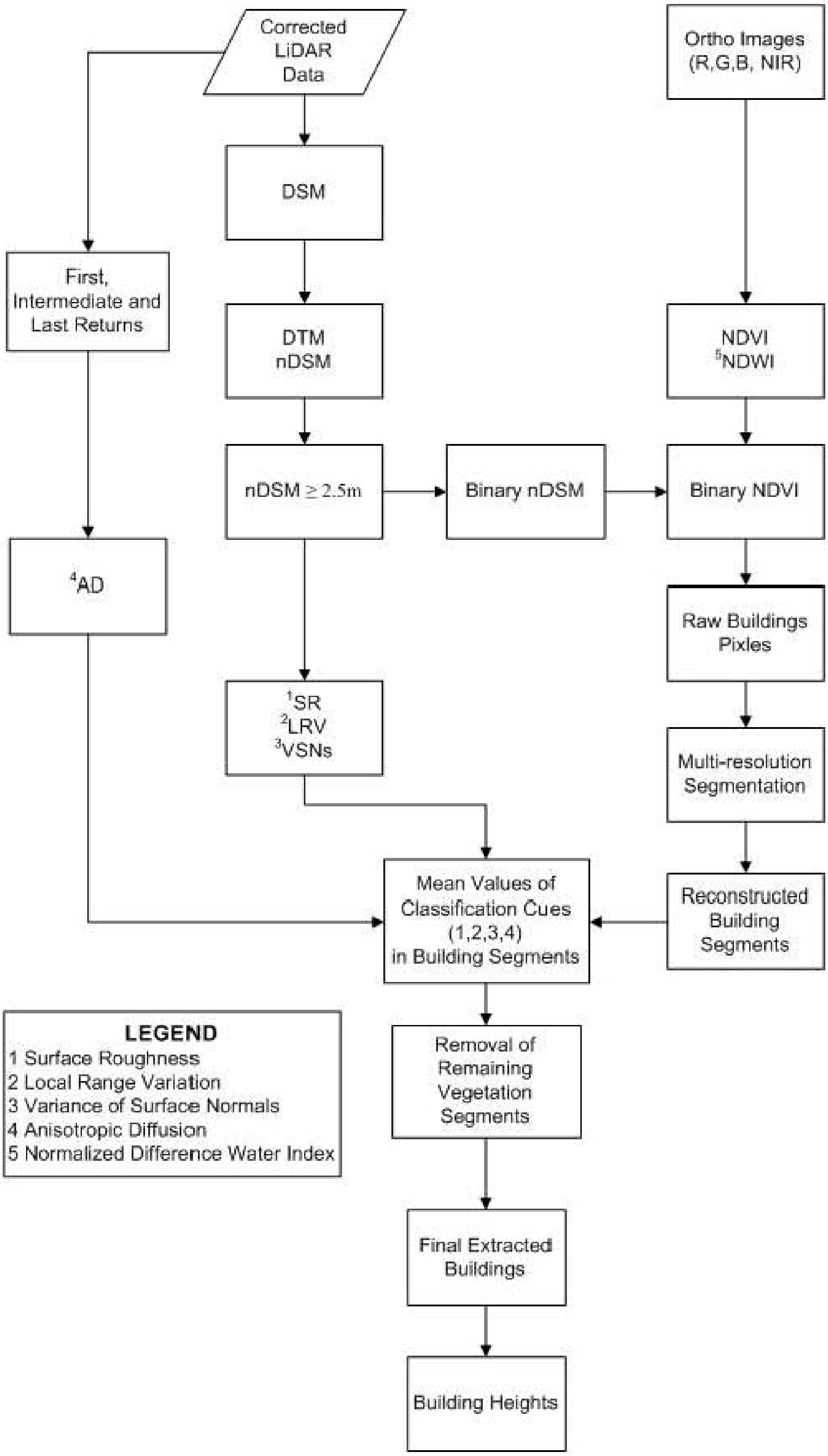

Figure 43: Method for Building Extraction

Figure 43 shows the developed method for building extraction after the initial registration check as shown in the Figure 41.

5.1.1 NDVI

The first product created from orthophotos for object extraction was NDVI for separating vegetation from other objects such as roads and buildings. NDVI is defined as:

$$NDVI = \frac{NIR - R}{NIR + R}$$

ADS40 camera has a radiometric resolution of 12-bit whereas the captured images were stored as 16-bit images during processing in GPro. These were then used for NDVI calculation. However; for thresholding and further processing these were converted to 8-bit images. This is because the images having a high spatial resolution and covering large areas cannot be processed in Definiens Ecognition software if smaller sized segments (consisting of 2 or 3 pixels) are required from multi-resolution segmentation. LiDAR intensity, object texture and geometric information extracted from LiDAR was also stored in 8-bit format. It was considered appropriate to use a single radiometric resolution throughout the extraction process.

A threshold is necessary for separating vegetation from other objects in the NDVI image. It is not a unique value and varies because the amount of radiation arriving at a passive sensor depends on many factors. Some of them are characteristic for the sensor or the object, but there are also geometrical ones, namely the direction of the sun, the sensor viewing direction, and the normal vectors of the illuminated surfaces. A slope facing the sun will appear brighter than a slope pointing away from the sun (Rottensteiner et al., 2007). Parameters such as the position of the sun at the time of data capturing or training areas have also been used to determine appropriate thresholds for NDVI image by others (Hejmanowska, 1998; Rottensteiner et al., 2007). On most occasions, date and time at which the data was acquired is not available to the operator and to avoid selection of training areas, only those techniques were considered in this research, that have the potential of making the process automatic or minimize operator involvement and knowledge of the area. Figure 44 shows ground and building regions showing different characteristics, making multi-spectral information very difficult to be thresholded.

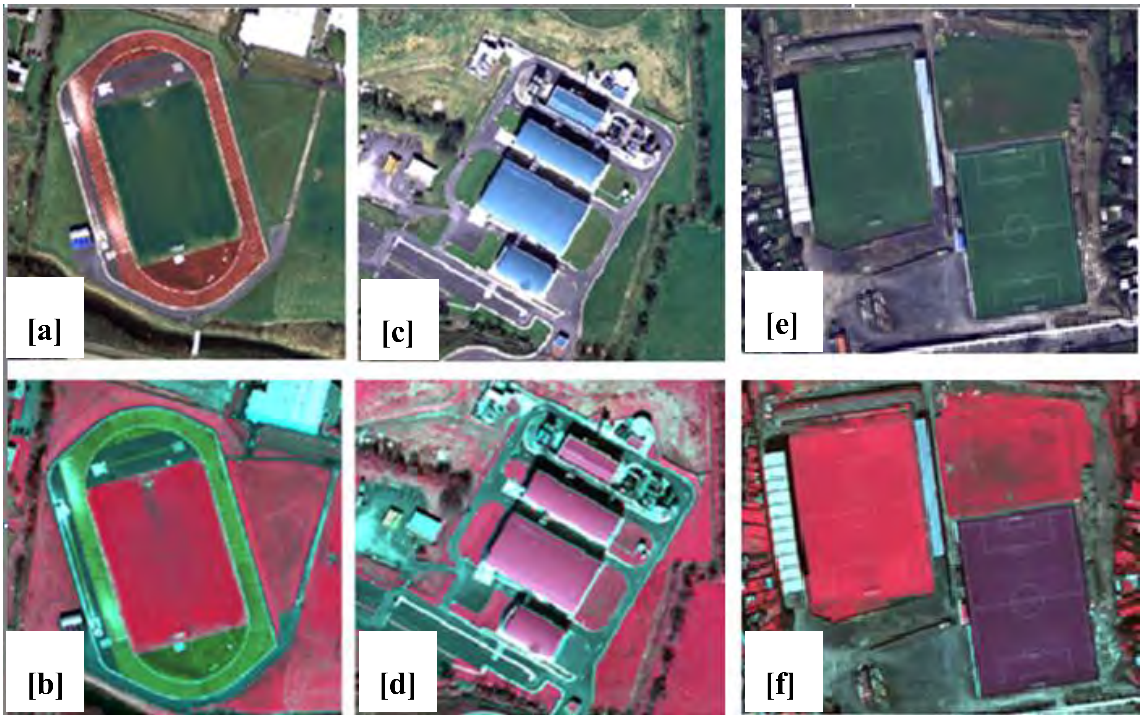

Figure 44: Spectral Heterogeneity of Ground and Buildings

Figure 44 (a), (c) and (e) show the true colour ortho image sections and (b), (d) and (f) show their representation in CIR imagery. Figure 44 (a) and (b) show how CIR imagery can be helpful in successfully separating vegetation from other image objects. Figure 44 (c) and (d) show a typical large industrial building with its representation closer to vegetation and lastly Figure 44 (e) and (f) show variation within CIR image to separate two different grass fields. One of these could be a grass field while the other could be Austro

Turf. Such objects were retrieved during vegetation extraction using the same classification cues as were used during the extraction of buildings for classifying vegetation that remained amongst the building segments.

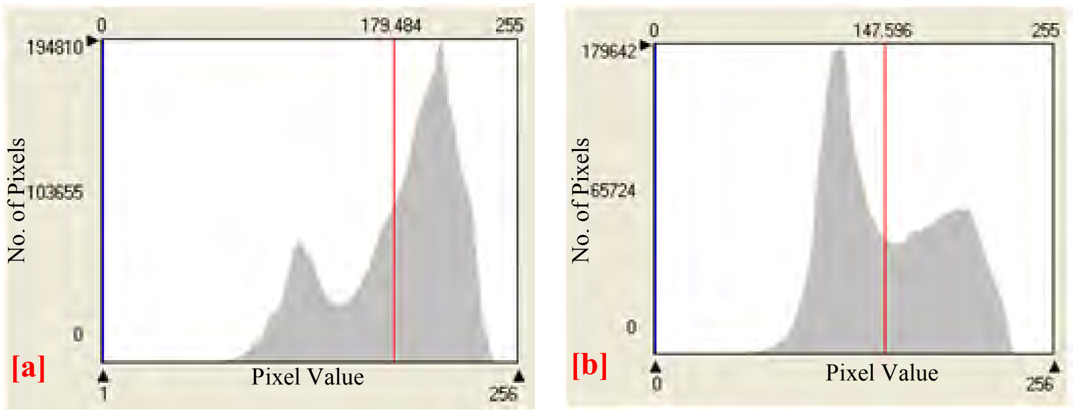

Figure 45: Histogram Variation of NDVI Images

The red line in Figure 45 shows the separation between vegetation and other non natural objects based on the histogram mean value i.e. 179.484 (Figure 45 (a) Development Area) and 147.596 (Figure 45(b) Test Area-1) in Sligo. The valley between the first two peaks also provided a rough idea for selecting a threshold for NDVI image and was compared later with the values determined using global thresholding methods.

5.1.2 **Image Thresholds**

If the image consists of predominantly two objects then a histogram based threshold can be used (Figure 45). The thresholded image $g(x,y)$ is defined as

$$g(x,y) = \begin{cases} 1 & if\ f(x,y) \geq T \\ 0 & if\ f(x,y) < T \end{cases}$$

Then any point (x,y) for which $f(x,y)\ \geq T$ is called an object point; otherwise, the point is called a background point. Pixels labelled 1 correspond to objects, where as pixels labelled 0 correspond to the background. When T is a constant, this approach is called global thresholding (Gonzalez et al., 2004).

5.1.2.1 Threshold by method of Gonzalez:

To automatically select a threshold, a method developed by Gonzalez et al.(2004) was investigated. The steps involved in this method were implemented in MATLAB and are explained below.

1. Select an initial estimate for T. (A suggested initial estimate is the midpoint between the minimum and maximum intensity values in the image).
2. Segment the image using T. This will produce two groups of pixels: G_1, consisting of all pixels with intensity values $\geq T$, and G_2, consisting of pixels with values $< T$.
3. Compute the average intensity values $\mu_1$and μ_2 for the pixels in groups G_1 and G_2.
4. Compute a new threshold value:

$$T = \frac{(\mu_1 + \mu_2)}{2}$$

5. Repeat steps 2 through 4 until the difference in T in successive iterations is smaller than a predefined parameter $T_{\circ}$ which is 0.5, for the purpose of this research.

5.1.2.2 Threshold by Method of Otsu

Another method for automatically selecting threshold provided in MATLAB is Otsu's method (Otsu, 1975).

$$T = graythresh\ (f)$$

Otsu's method is a histogram based method which chooses a threshold value that maximizes the variance between two classes. The threshold is returned as a normalized value between 0.0 and 1.0 (Gonzalez et al., 2004).

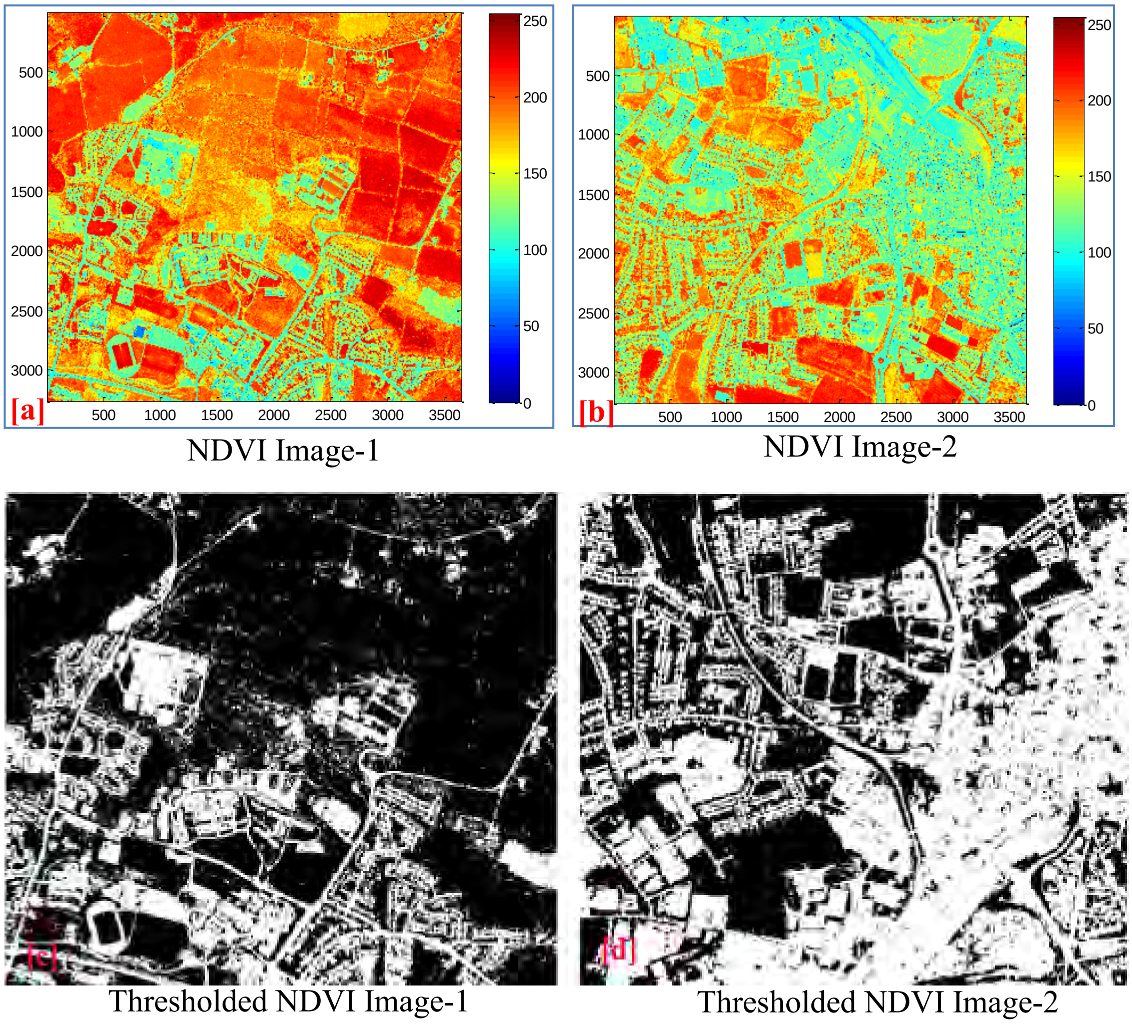

Figure 46: (a, b) NDVI Images and (c, d) Thresholded Images

Global thresholding may fail when the background is not uniform. It is also affected by illumination. The common practice is to compensate illumination before applying global thresholding. Morphological top hat operator (opening) combined with MATLAB graythresh function can be used to compensate non-uniform background problems but this does not appear to be an issue with the available data.

Figure 46 upper half (a & b) show two NDVI images while the lower half shows their corresponding binary images (c & d) using Gonzalez et al. (2004) method, where, white pixels correspond to buildings and roads and black pixels correspond to vegetation.

Thresholding Method	NDVI Image-1	NDVI Image-2
(Gonzalez et al., 2004)	163.910	152.742
(Otsu, 1975)	164.633	152.601
Histogram Analysis (Mean)	179.484	147.596
Histogram Valley	146.573	154.604

Table 21: Global Thresholds for NDVI Images

Image thresholding values from the two used methods (Table 21) were not very close to the values determined using histogram. However; the lowest value between two histogram peeks for NDVI Image-2 (Figure 46 (b)) was close to the first two thresholding methods. One possibility is to select this low value for thresholding or use either of the Gonzalez or Otsu method for automatic thresholding. Gonzalez method was used in this research for thresholding NDVI image. Visual inspection of binary NDVI images revealed that building roof parts under shadows were retained but industrial buildings in Figure 44 (c) were considered as vegetation.

5.1.3 NDWI

NDWI index have been used previously to delineate open water features from satellite and high resolution aerial images (McFeeters, 1996; Chen et al., 2009). NDWI is defined as

$$NDWI = \frac{G - NIR}{G + NIR}$$

This is important for road extraction as these features remain part of the thresholded NDVI image retained for building as well as road extraction.

A LiDAR sensor records no data over water bodies because LiDAR beams are absorbed in water. However; a few points could be recorded if water level is low. Regions with negative height values or no values were investigated to mask out such areas but did not prove successful because of low water levels, wavy conditions and small boats, resulting in LiDAR reflections from the river. These reflections from water bodies need to be removed as these regions later became part of the generated DTM. However; this is not applicable to buildings as these water bodies were separated from the thresholded NDVI image using height threshold.

Figure 47: Thresholded Binary NDWI Images

After determining NDWI, all proposed methods of image thresholding to separate water areas were tested. Thresholding results in the removal of vegetation and dark areas removal instead of the actual water bodies. Although, water channel in Figure 47 (a) is narrow and small however; the NDWI index also failed to mask out the river in Figure 47 (b). The manual investigation of pixel values to select an appropriate threshold was also not very conclusive in separating these regions. Water bodies in both areas have been masked out manually.

5.1.4 nDSM Processing

Single return data from LiDAR was used to create DSM and DTM after removing low and very high points using Terrasolid as has been explained in chapter 3. However, multiple reflections were utilized to determine another classification cue (Anisotropic Diffusion (AD)) which is explained at a later stage in this chapter. The DTM was subtracted from the DSM to obtain actual object heights (nDSM). A height threshold of 2.5 m was used for the purpose of separating low height objects in nDSM and a binary image was generated (Figure 48).

Figure 48: Binary nDSM with Height Threshold ($\geq 2.5\ m$)

A morphological operation such as opening of a 3 x 3 matrix was used once to eliminate the stand alone single pixels. Care must be taken in using morphological operations (matrix size and iterations) as these significantly change the size and shape parameters of the extracted objects. Figure 49 shows the effectiveness of the morphological operation (opening) in removing a single white pixel (object pixel) and separating loosely connected pixels.

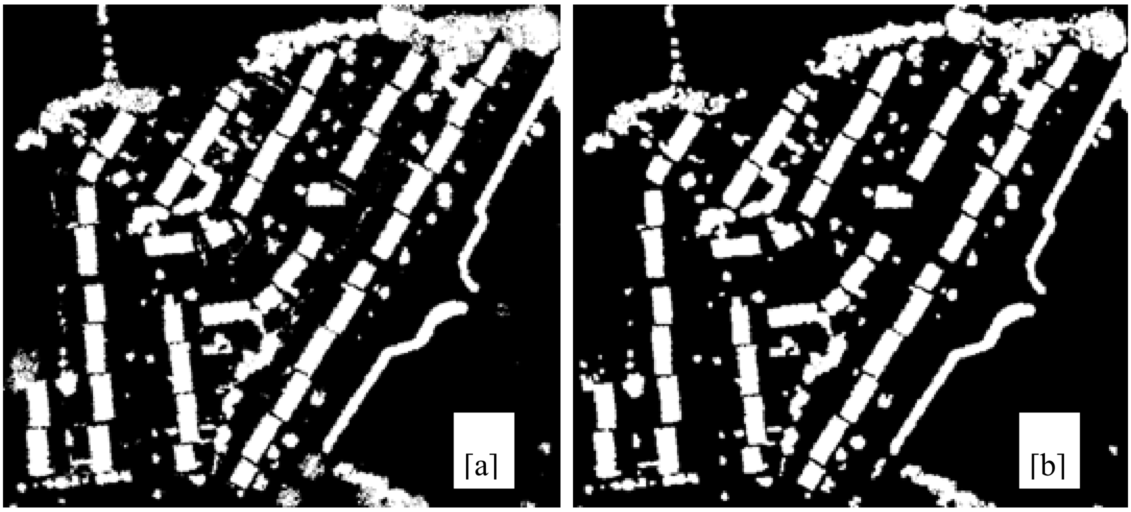

Figure 49: Morphological Operation (Opening) Results (a) Before (b) After

The resulting binary nDSM image now contains two objects i.e. building and trees which were separated using thresholded NDVI image.

5.1.5 **Raw Buildings**

Two iterations of morphological operation opening were used with the thresholded binary NDVI image (Figure 46 (c) Development area) showing buildings and other man-made objects with white pixels.

This generated binary image (Figure 50 (b)) was than combined with the previously generated binary nDSM image using conditional and Boolean functions.

$$Raw\ Buildings = Either\ 1\ if(Both\ nDSM\ and\ NDVI = 1) or\ 0\ otherwise$$

Figure 50: Results of Morphological Operation (Opening) on NDVI Image (a) Before (b) After

The extracted raw buildings (Figure 51) need further processing to generate building regions without holes which is explained in the next section.

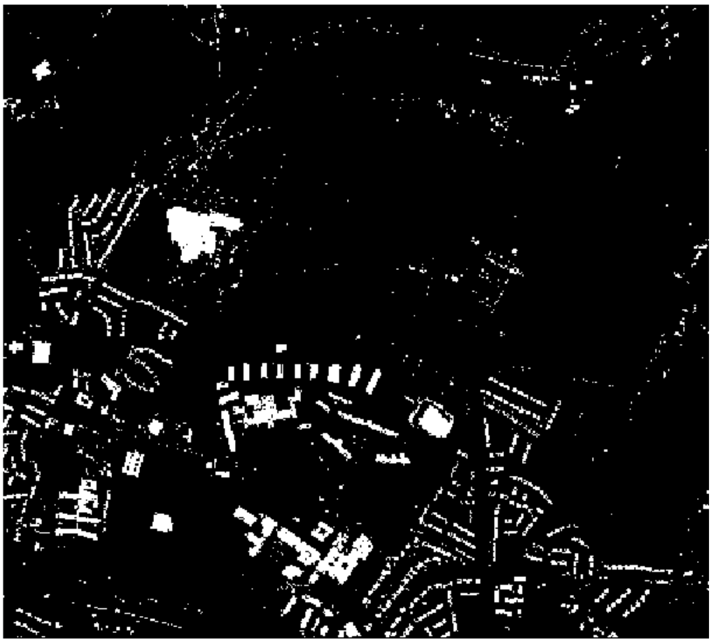

Figure 51: Raw Building Boundaries

5.1.6 **Building Reconstruction**

The raw extracted building regions need reconstruction to fill the gaps within, which occurred during NDVI thresholding or artefacts ,which occurred during orthophoto generation. Instead of using morphological operation to fill these gaps, the relative border between the small gaps (black image segments) and the building pixels (white image segments) was used. This way those object shapes were retained which would be altered had morphological operations been used.

Object oriented analysis was carried out using Ecognition to fill holes in building regions without filling the real open spaces between them. Multi-resolution segmentation was used to generate small segments. These, when combined after filling gaps, reproduced objects not very different from the actual objects in the raw building image in terms of their size and shape. Figure 52 shows a dialogue box from Ecognition that allows one to set multi-resolution segmentation parameters.

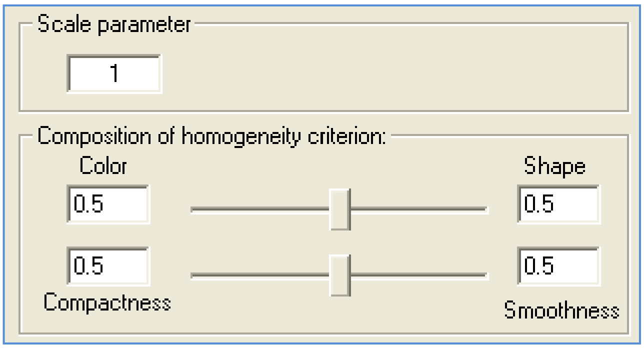

Figure 52: Object Segmentation Parameters in Ecognition

The scale value should be kept low and proper weights should be assigned for colour, shape compactness and smoothness. The shown values in Figure 52 were used for segmenting raw building image.

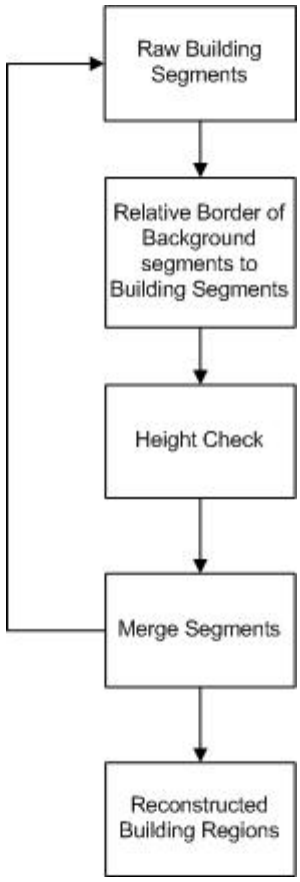

Figure 53: Flow Chart for Building Objects Reconstruction

The relative border of background segments with building segments (white) was determined. The object merging started by using relative border value of 100% to first incorporate small segments (black) completely surrounded by building segments (white). These segments were then merged to generate building regions. After the first cycle, the process was repeated with lower relative border value. In this manner, more gaps were filled (Figure 53). The minimum value used for relative border was 75%. The heights of identified segments fulfilling this criteria were checked from the binary nDSM before merging them into building regions. This was so done to avoid filling the space between buildings which might be very close to each other. This process also filled small gaps in tree regions caused during orthophoto generation or due to LiDAR penetration, resulting in large height variations within the tree regions in the generated DSM.

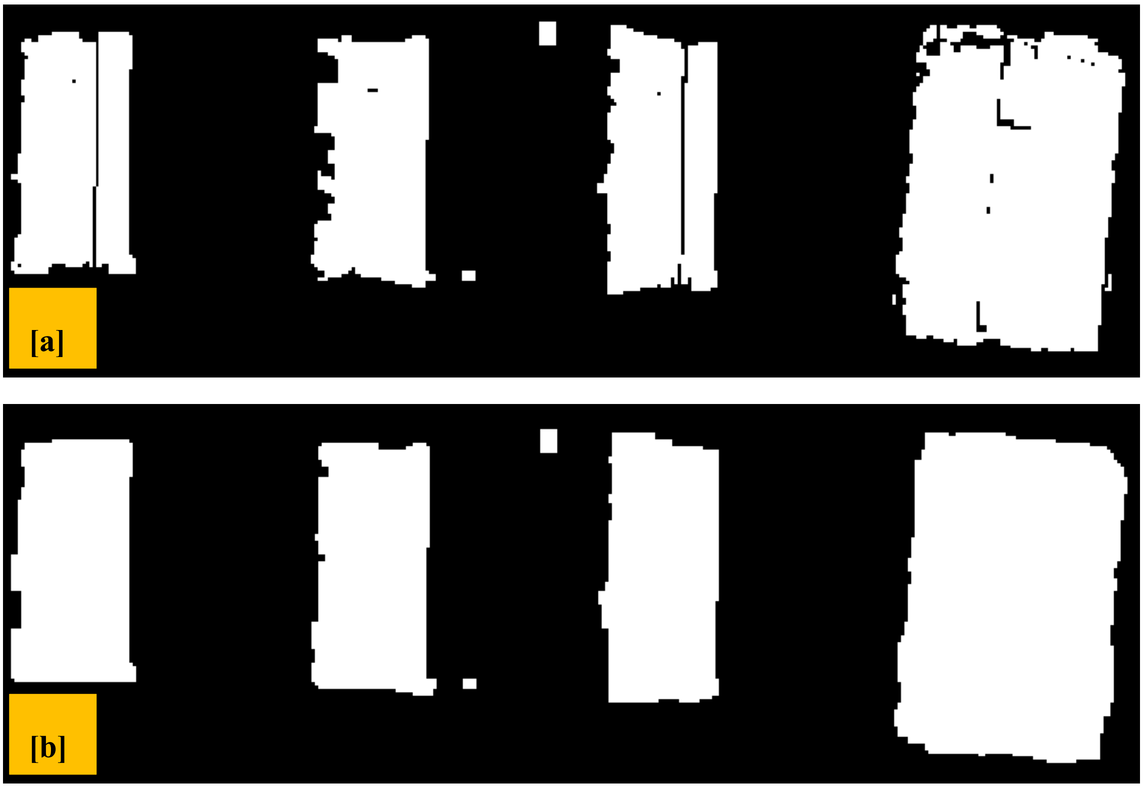

Figure 54: Reconstructed Building Regions (a) Before (b) After

Figure 54 shows the reconstructed building regions before and after the application of the reconstruction method shown in Figure 53. After reconstruction, these building regions were further classified using parameters obtained from the LiDAR data (Variance of Surface Normals, Surface Roughness, Local Range Variation and Anisotropic Diffusion) to remove those vegetation segments which were not separated using NDVI thresholding and still existed amongst building regions. These classification parameters are explained in the following section. The mean value of each of these stated parameters was determined in the reconstructed building regions and analysed to extract the final building regions.

5.1.7 **Classification Cues from LiDAR**

5.1.7.1 Variance of Surface Normals (VSNs)

The surface normal is a vector perpendicular to a surface. Surface normals show large variations over trees as compared to the buildings (Figure 55). The point density was low in the available LiDAR data. This resulted in small flat areas over the building roofs when DSM was interpolated (Figure 55) and affect the quality of the surface normal. The variance of the surface is defined as:

$$variance = \frac{\sum(x_{ij} - M)^2}{n - 1}$$

Where:

x_{ij} = Digital Number (DN) of pixel (i, j)

n = number of pixels in a window

M = Mean of the moving window, where:

$$Mean = \frac{\sum x_{ij}}{n}$$

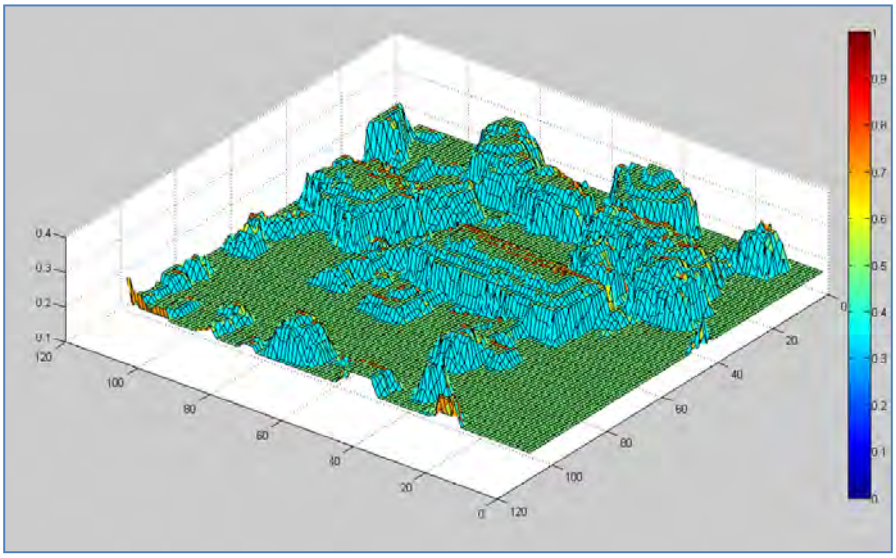

Figure 55: Subset of 3D Surface Normal Plot in Development Area

The variance of surface normals was computed for the generated nDSM with a height threshold of 2.5 m using a 3 x 3 matrix. The mean variance value was calculated for each object in the reconstructed building image.

Figure 56 shows a surface generated using normal vector values at each pixel and Figure 57 shows the corresponding variance of the surface normals, both gray scale (8-bit).

5.1.7.2 Local Range Variation (LRV)

Local range variation is a height based classification cue used for separating buildings and trees from other small objects such as cars, bushes etc (Arefi, 2009). Large height variations occur in small areas especially for trees as compared to buildings. However; this does not apply to small buildings.

LRV was calculated by subtracting local maximum and minimum obtained by convolving the nDSM by a 3 x 3 matrix. Mean LRV value in building segments was used for classifying remaining trees (false positive). This operation is simple and can also be very useful, if only buildings and tree boundaries are required from LiDAR, or to refine extracted building edges.

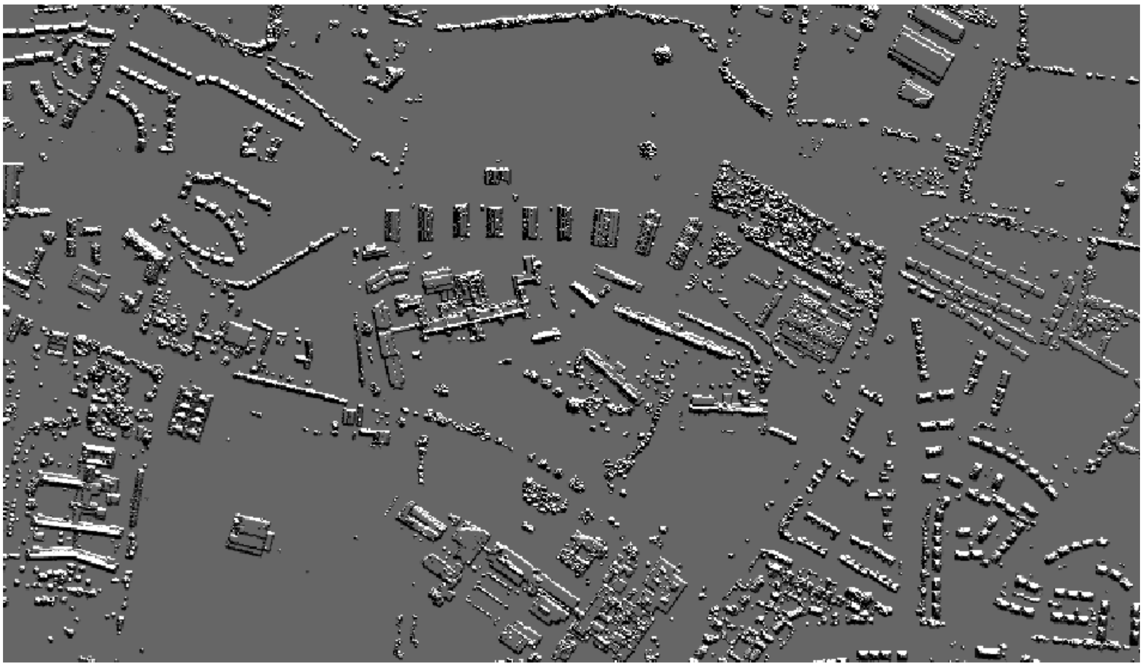

Figure 56: Subset of Surface Normal Image (Development Area)

Figure 57: Subset of Variance of Surface Normals Image (Development Area)

Figure 58 shows LRV image (gray scale, (8-bit)) for a portion of the development area. The mean variance value was low for building regions whereas it was higher for trees.

Figure 58: Subset of Local Range Variation Image (Development Area)

5.1.7.3 Surface Roughness

In the DSM image, there is a significant height change between ground and non-ground objects. Whereas, the height change within a single object such as a building will be much smaller compared to large trees. The second derivative of nDSM was used to separate trees amongst building regions. The Laplacian is a generalization of the second derivative taken in two dimensions. It has the effect of enhancing changes (Myler and Weeks, 1993). When there is a significant height change, the sign of second derivative reverses.It however remains constant if the object has a smooth surface. Figure 59 shows a section of the nDSM (Figure 59 (a)) revealing the surface roughness value over a tree and a building (Figure 59 (b)). For trees it changes abruptly from negative to positive as LiDAR penetrates the vegetation but this is not the case with the buildings resulting in lower mean values compared to trees. However; it is not applicable to building edges.

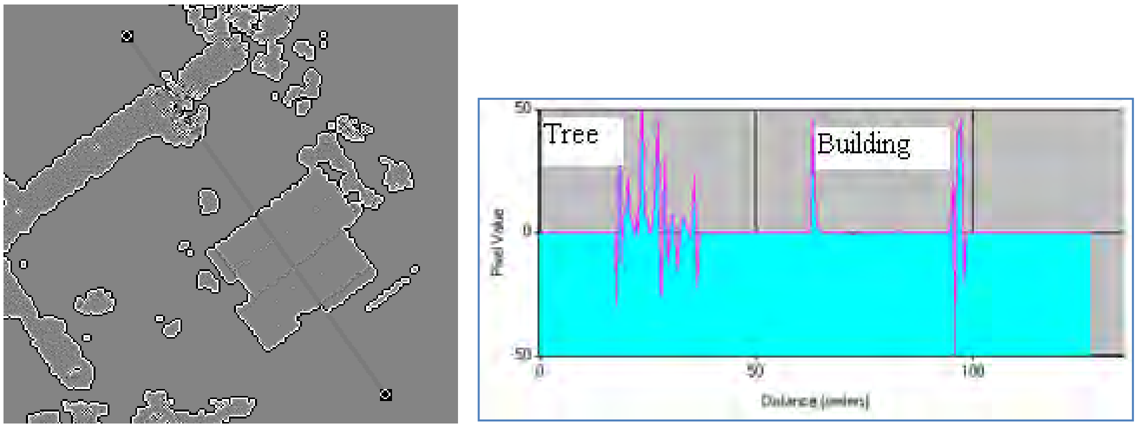

Figure 59: Cross Section of nDSM Showing Surface Roughness

0	-1	0
-1	4	-1
0	-1	0

Table 22: Laplace Filter for Surface Roughness

-1	-1	-1	-1	-1
-1	-1	-1	-1	-1
-1	-1	24	-1	-1
-1	-1	-1	-1	-1
-1	-1	-1	-1	-1

Table 23: Smoothed Laplace Filter for Surface Roughness

Laplace filter was used to determine the surface roughness parameter. It can be used alone (Table 22) or in combination with Gaussian smoothing (Table 23).

Figure 60 shows the results achieved after convolving the thresholded nDSM with the two previously defined matrices. Small variations over buildings roofs were smoothed using Laplacian filter combined with Gaussian which helps in the better classification of tree and building segments.

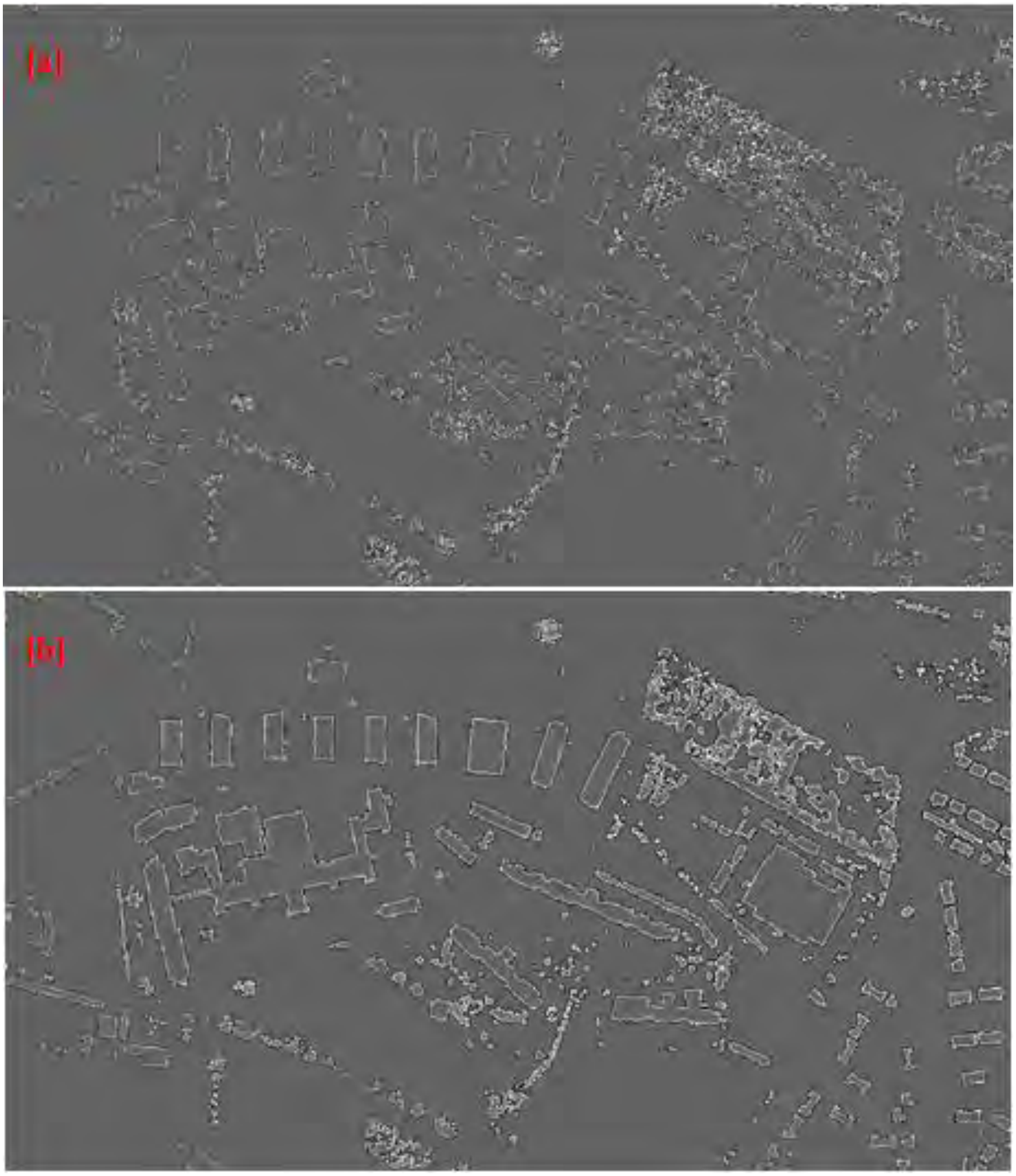

Figure 60: Subset Gray Scale (8-bit) Surface Roughness Image (a) Laplace (3*3) (b) Smoothed Laplace (5*5) (Development Area)

Many researchers also performed segmentation of DSM using Gaussian and mean curvature for building roof extraction by identifying different surface types instead of Laplace filter (Besl and Jain, 1988). Using surface curvature signs, a surface type image was determined for each pixel. In the second stage, an iterative region growing was performed using variable order surface fitting. The output of the second stage consists of a region label image, which contains all region definitions in one image, and a list of coefficient vectors, one for each region. These regions were also used for classifying buildings and trees in the range images.

5.1.7.4 Anisotropic Diffusion

Object extraction techniques are dependent upon the characteristics of the available data. For example, Optech ALTM sensor can record two returns per emitted pulse. That is why; it is possible to create two separate range and intensity images from a single scan. Normalized Difference (ND) is a LiDAR based vegetation index to separate trees from buildings using the first pulse and the last pulse, especially for the Optech sensor data. Equation for ND is defined as (Arefi et al., 2003).

$$ND = \frac{First\ pulse - Last\ Pulse}{First\ pulse + Last\ Pulse}$$

Once a major part of vegetation is removed, building regions can be refined using the previously stated classification cues obtained from the LiDAR data.

Multiple returns from ALS50-II data area were not dense, except where there are clusters of trees or big trees (Figure 61). These multiple returns, because of their very low density, cannot be interpolated. It was not possible to classify these returns on the basis of height to find those echoes which were reflected from the ground or building corners, because of the complex urban environment as shown in Figure 62.

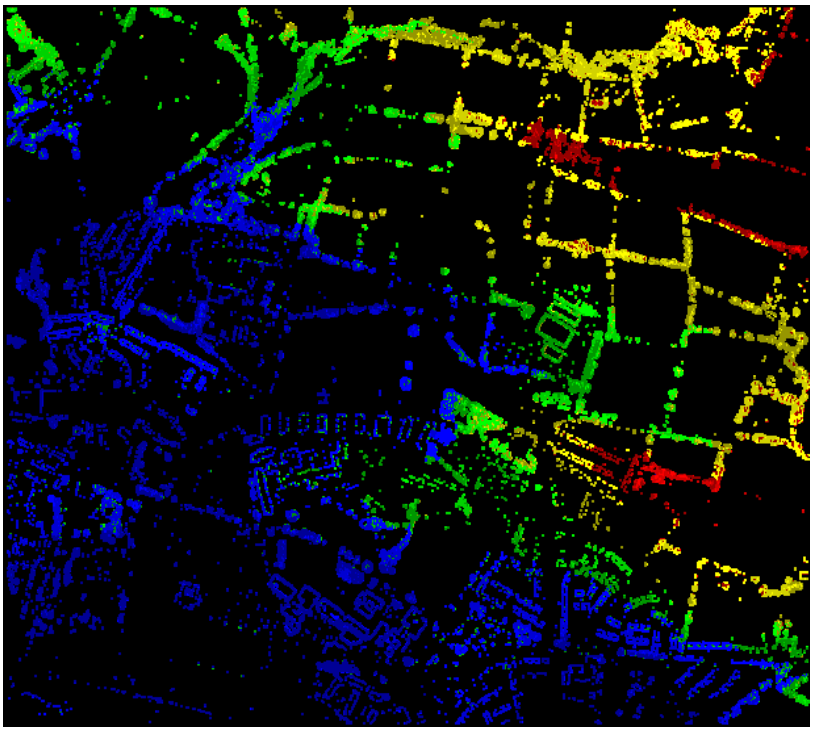

Figure 61: Multiple Return Range Image from ALS50-II Sensor

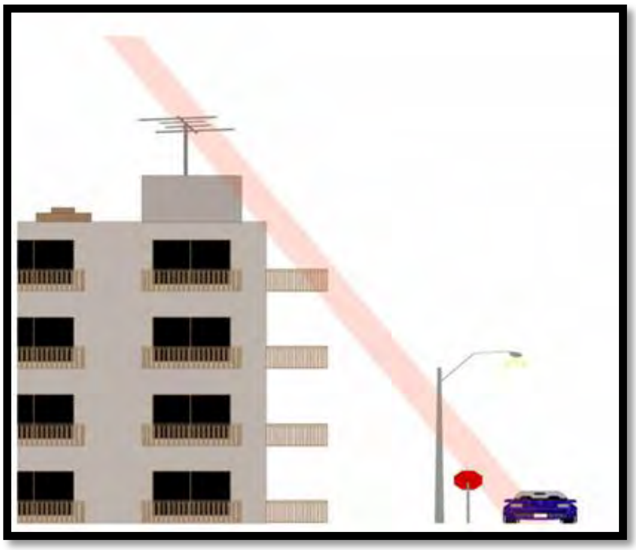

Figure 62: Complex Urban Environment Side View (Jenkins, 2006)

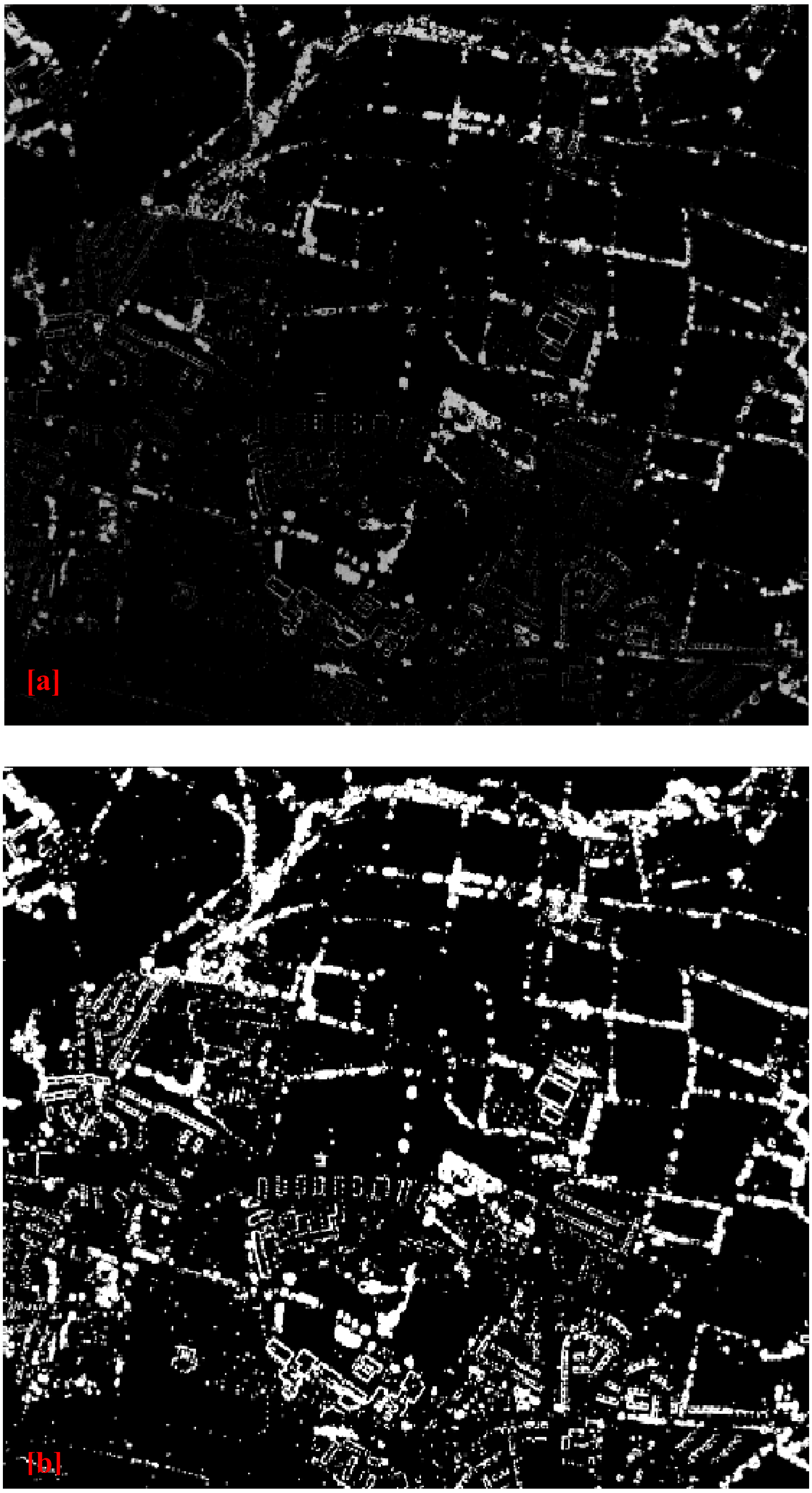

Figure 63: Effect of Anisotropic Diffusion (a) Multiple Returns Image Before (from TerraScan) (b) Resulting Diffused Image

The density of multiple returns was greater over trees as compared to the buildings. These were exported as a height image (gray scale) using TerraScan (Figure 63 (a)). The multiple returns were combined using AD to utilize them for building and tree classification. This process smoothes the regions while preserving and enhancing, the contrast at sharp intensity gradients (Figure 63 (b)). A 2D network structure of 8 neighbouring nodes was considered for diffusion conduction (Perona and Malik, 1990; Kovesi, 2007).

5.1.8 LiDAR Classification Cue Analysis

The classification cues obtained from LiDAR (VSNs, LRV, SR and AD), whose mean values were determined in the reconstructed building regions to remove remaining trees, require thresholding. This was done using QQ plot to select appropriate thresholding values. It has two forms, a normal QQ (Quantile - Quantile) plot and a general QQ plot which are explained below.

5.1.8.1 Normal QQ plot

Normal QQ plots are graphs on which quantiles from two distributions are plotted relative to each other. Distribution of the data is compared to a standard normal distribution, providing another measure of the normality of the data. The closer the points are to the straight line in the graph, the closer the sample data follows a normal distribution (ESRI, 2007).

5.1.8.2 General QQ plot

The general QQ plot is used to assess the similarity of the distribution of the two datasets. A general QQ plot is created by plotting data values for two datasets where their cumulative distributions are equal (ESRI, 2007).

Normal QQ plot technique was used in ArcGIS after exporting building polygons from Ecognition (raster to vector conversion) with four attributes to select appropriate thresholds for classifying the remaining trees amongst them. Only the buildings greater than or equal to 30 m^2 were considered. This was done to eliminate small structures (such as huts and sheds) especially in the back yards which could possibly have been extracted as buildings.

The general QQ plot is useful for comparing the classification cues. However; this has been done later by using the confidence matrix to examine the number of trees removed by each classification cue that have also been classified by other cues. This shows how effective each classification parameter is in removing trees.

Figure 64 to Figure 67 show the normal QQ plot of mean values for each of the four classification cues. Where the plotted classification cue object value deviates from the straight line, it is an indication of possible tree objects and was selected as a threshold to separate them from buildings. By selecting the plotted values in the graph (red ellipse) corresponding objects were highlighted in ArcGIS. The minimum value of the selected objects for a particular classification cue was set as a threshold. The Normal QQ plot reveals the heterogeneous behaviour of the parameters better than histogram especially highlighting each single object which varies greatly from the other objects. The buildings have low mean VSNs, LRV, SR and AD values as compared to the trees.

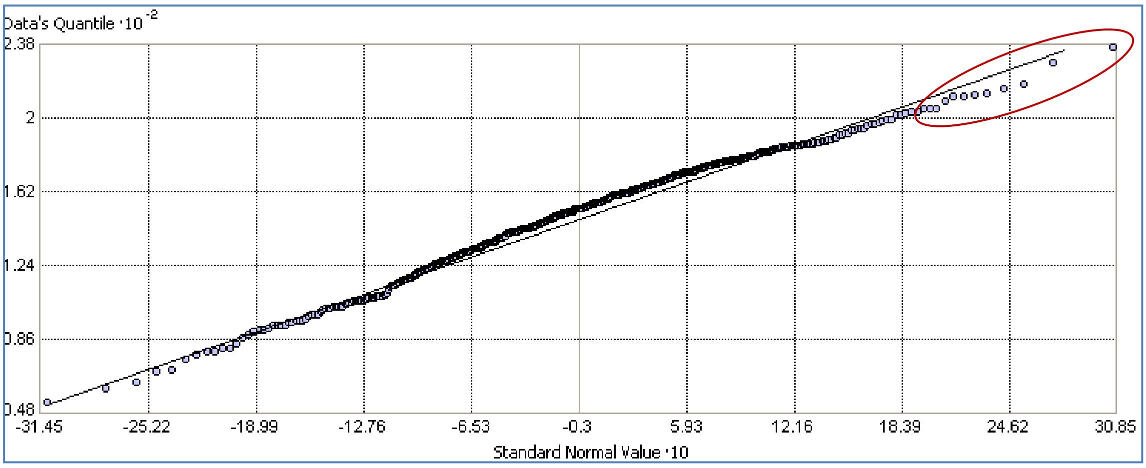

Figure 64: Variance of Surface Normals QQ Plot

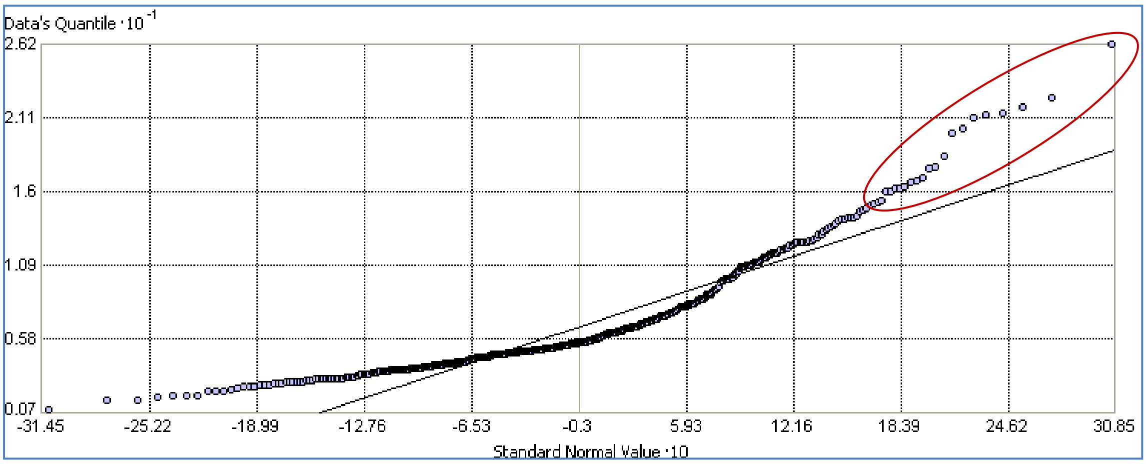

Figure 65: LRV Normal QQ Plot

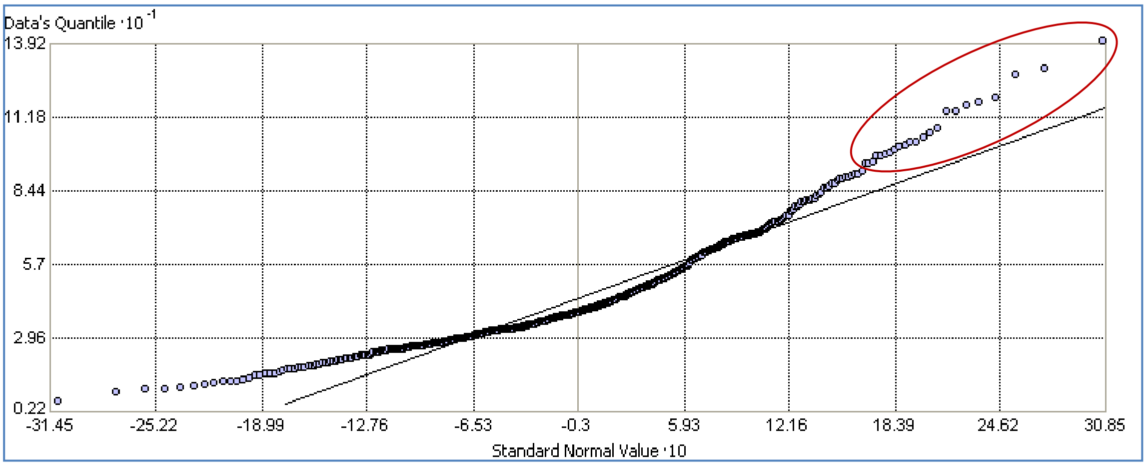

Figure 66: Surface Roughness Normal QQ Plot

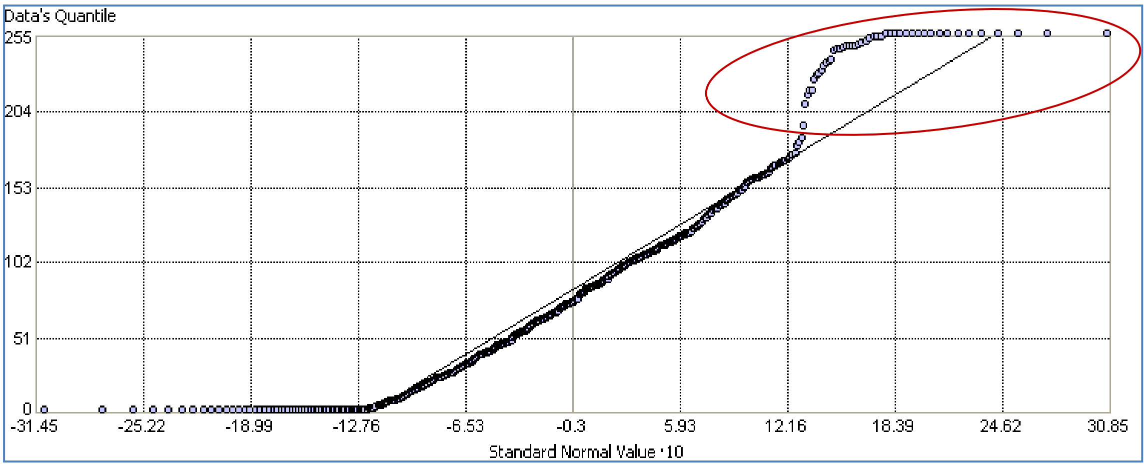

Figure 67: Anisotropic Diffusion Normal QQ Plot

5.1.9 LiDAR Parameter Analysis without NDVI

If only ALS50-II sensor data with three multiple returns was available for object extraction without multi spectral images, it would be difficult to classify buildings and trees in the thresholded nDSM. All classification cues were analyzed using normal QQ plot to select appropriate thresholds for the classification of buildings and trees. The task becomes tedious because of a large number of objects. There were more than 1,233 objects in the LiDAR data in the development area which were reduced to less than 500 when using NDVI. This makes parameter analysis and the extraction process easier.

5.1.10 Final Extracted Buildings

Thresholds determined using Normal QQ Plots were applied to the reconstructed building objects to remove remaining trees. The determined mean building object values for classification are given in Table 24 .

Parameter	**≤ Thresholds**
Surface Roughness	90
LRV	15
Variance of Surface Normals	203
Anisotropic Diffusion	192

Table 24: Thresholds Determined from LiDAR Parameters

In order to avoid harsh thresholding, a technique similar to multi-agent based modelling was utilized, which softened the effect of the applied thresholds. This was done by adding an additional object attribute using four classification cues. For example, if an object has been classified as a tree by three classification cues but not so by the fourth one, its score is 3 out of 4 (75%). Another way is to assign weights to each attribute. However; in this research only the first technique was used. An object to be classified as a tree should score at least 75%.

	SR	LRV	VSN	AD
SR	24	11	4	13
LRV	11	19	3	11
VSN	4	3	12	5
AD	13	11	5	46

Table 25: Confidence Matrix (Development Area)

A matrix was developed to see which classification cue has classified most objects as trees and what the extent of overlap between different cues is. For example, 24 objects were classified as trees that exist in the reconstructed building layer using SR threshold. Out of these 24 objects, 11, 4 and 13 objects have also been classified using LRV, VSNs and AD respectively. This suggests that a single parameter was not sufficient for proper classification.

Anisotropic diffusion was the best one amongst the selected classification cues as can be seen from Table 25. It classified 46 objects as trees which were previously classified as buildings.

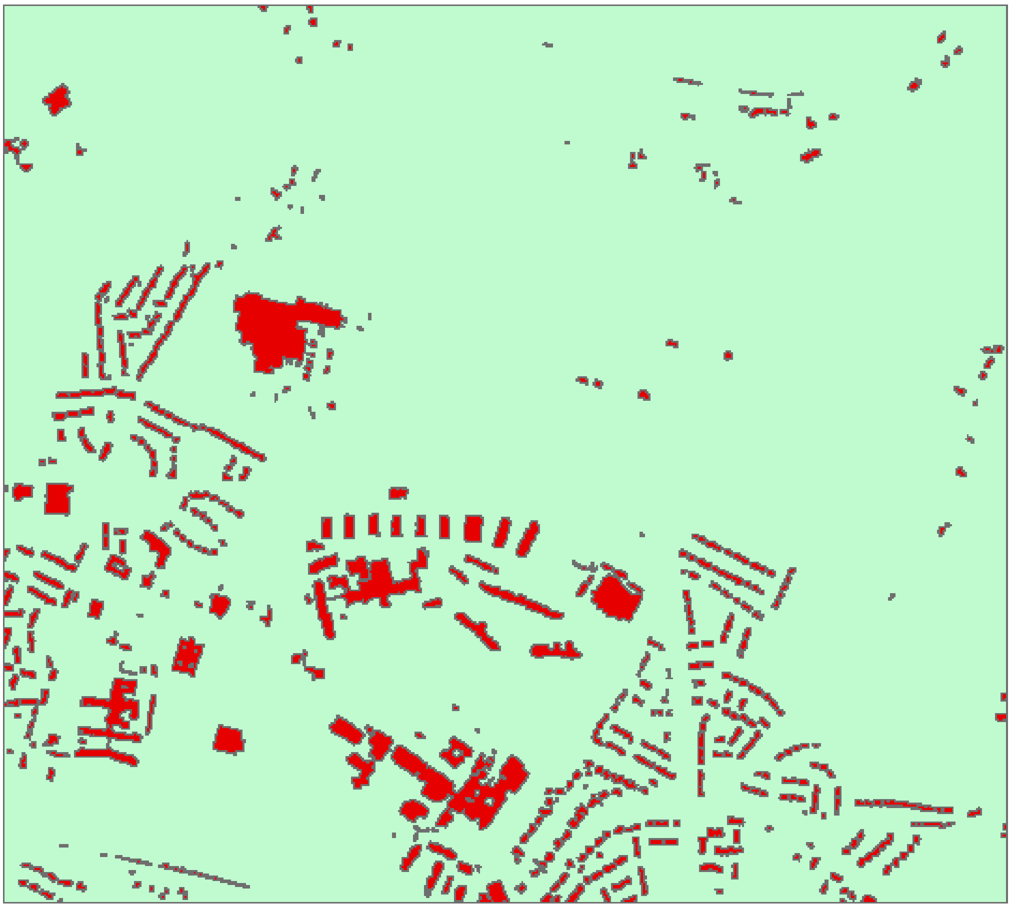

Figure 68: Final Extracted Buildings

Figure 68 shows the final extracted buildings in the development area using NDVI, nDSM and the four classification cues determined from LiDAR. The buildings with an area greater than or equal to 30 m^2 are shown. Buildings smaller than 30 m^2 are generally sheds outside main buildings and in open fields. Such structures are even not part of the OSI vector data. These small regions also occur from vegetation without leaves. In every building extraction technique a size threshold has been used to get rid of stand-alone pixels or segments (Rottensteiner et al., 2007; Matikainen et al., 2009).

5.2 Building Heights

Extracted building have to be assigned with appropriate height attribute necessary for generating 3D building model, an important requirement of noise mapping. Most of the National mapping agencies are facing challenges to extract and store this information along with 2D buildings model. After extracting building outlines, two methods have been evaluated to determine building heights.

5.2.1 Building Centroid

Building polygons centroid were determined and heights at these centroids were determined from nDSMs using bilinear interpolation. These building heights were evaluated by a ground truth survey using reflectorless total station (Leica 1200).

5.2.2 Descriptive Statistics

Instead of computing centroid from extracted building outline, three heights i.e. maximum and average and median had been determined from nDSM. Figure 69 shows how height varies along (a) and across (b) the roof in the nDSM.

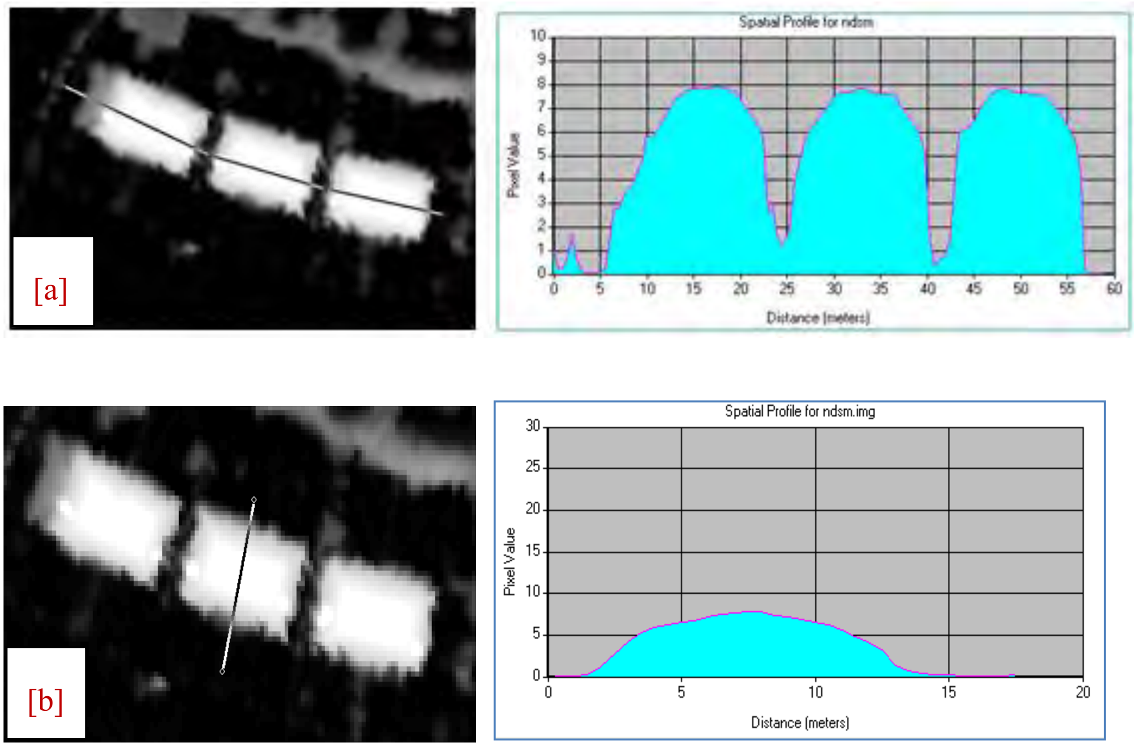

Figure 69: Cross Section Showing Building Roof Height Variation

5.3 Vegetation Extraction

The buildings and not trees are an important component of a noise model. The trees therefore need to be masked out for successful building extraction. However, trees are an important component of every 3D city model. All green areas extracted using the method given in Figure 70 were referred to as vegetation. After the vegetation was extracted, it was further classified into single trees, tree clusters and hedges' depending upon the shape attributes and distance from the nearest tree peaks.

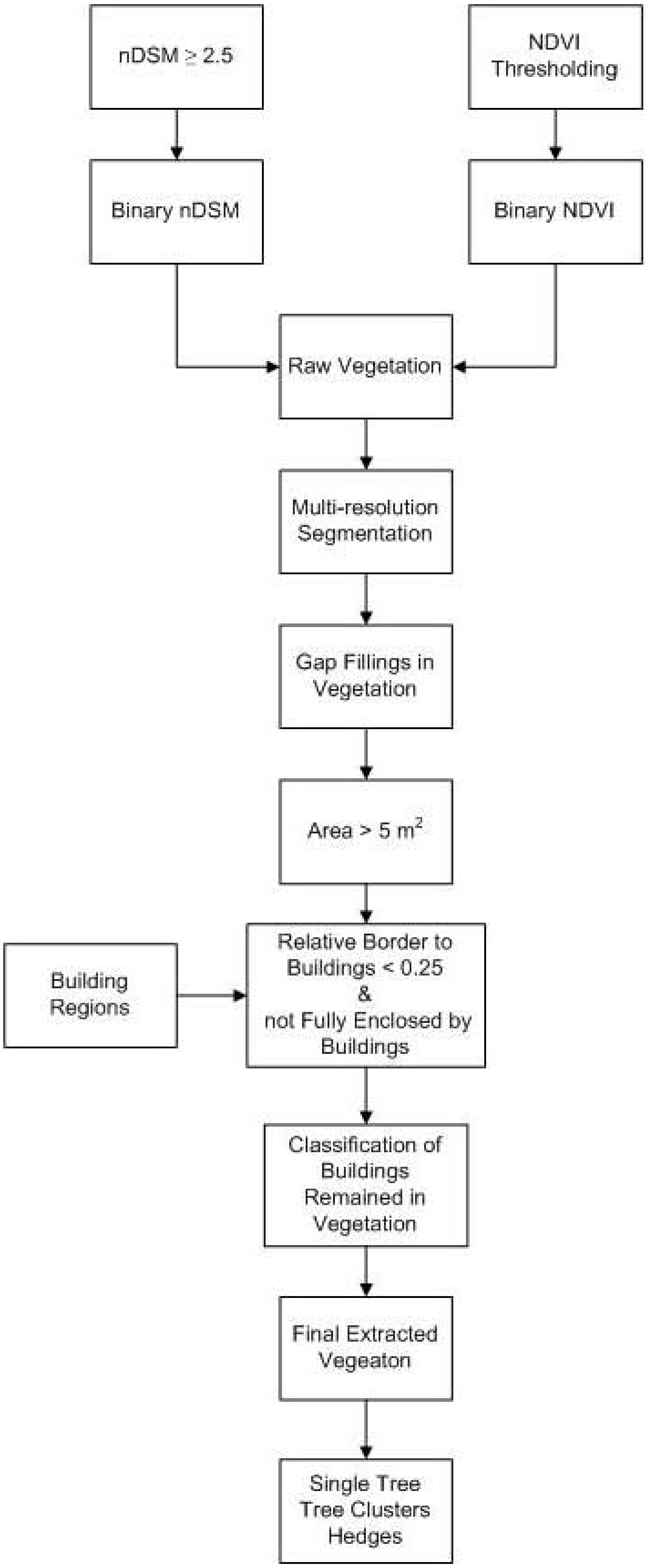

Figure 70: Vegetation Extraction Method

5.3.1 **NDVI Image**

The process of vegetation extraction initiated with the same threshold value as was used for building separation from NDVI. However; at this instance, the values above the threshold were retained. This was so because after the application of the threshold, the NDVI Image mostly contained vegetation and those buildings having spectral characteristics similar to vegetation (Figure 71). A threshold of 2.5 m on nDSM was also retained for vegetation extraction. The binary raw vegetation image was created using binary nDSM and binary thresholded NDVI. This image represents those pixels where vegetation was present in the nDSM (Figure 72).

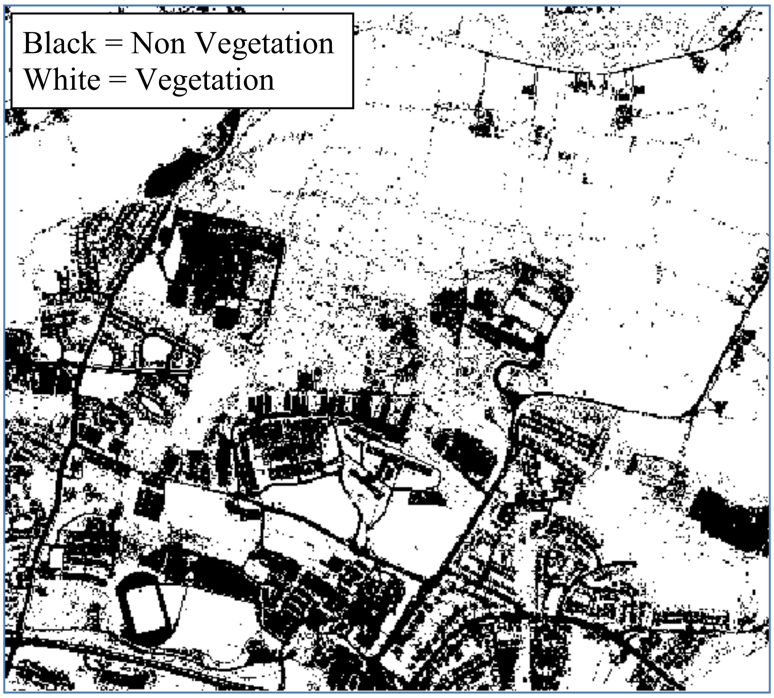

Figure 71: Binary Thresholded NDVI Image for Vegetation Extraction

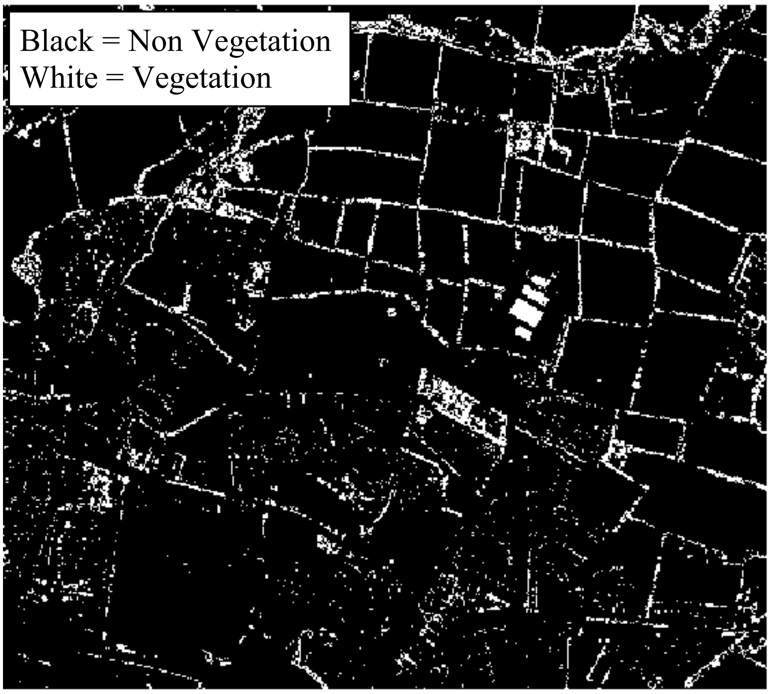

Figure 72: Binary Raw Vegetation Image

5.3.2 **Gap Filling in Vegetation**

It was necessary to fill small gaps among the vegetation pixels due to artefacts that occurred especially over the vegetation during orthophoto generation. Figure 73 (a) shows the captured RGB image having a pixel size and radiometric resolution of 15 cm and 16-bit respectively. Figure 73 (b) shows the generated orthophoto at a reduced spatial and radiometric resolution (50 cm & 8-bit). Tree trunks can be seen for some of the trees which were tilting away from the projection centre suggesting that these trees did not have a lot of leaves. However; in the generated orthophoto, tree structures were destroyed and it seems that the tree shadows are overlying the trees. This results in a low NDVI value which subsequently results in gaps/holes in the vegetation segments after the thresholding of the NDVI image.

Figure 73: Subset of RGB Image in Development Area (a) RGB Image (b) Ortho RGB Image

Multiresolution image segmentation was used to divide the binary raw vegetation image (Figure 72) into small segments. The ratio of the relative border of non vegetation segment was used as a criteria to merge them with the vegetation segments, similar to the method used during building reconstruction process. Vegetation smaller than 5 m^2 was also ignored. The vegetation segments that were fully enclosed by extracted buildings or around edges need to be removed. This is because of the forward looking NIR (18°) band and nadir Red band combination for calculating NDVI after orthophoto generation using LiDAR DSM (pixel size 0.5 m). This results in some distortions around building edges and ridges especially for high buildings. Figure 74 (a) shows a high building in the development area and Figure 74 (b) shows a subset of the corresponding raw binary vegetation image (Figure 72).

A threshold was used to extract vegetation having a border of less than 0.25 relative to the buildings and not completely surrounded by building boundaries (Figure 75).

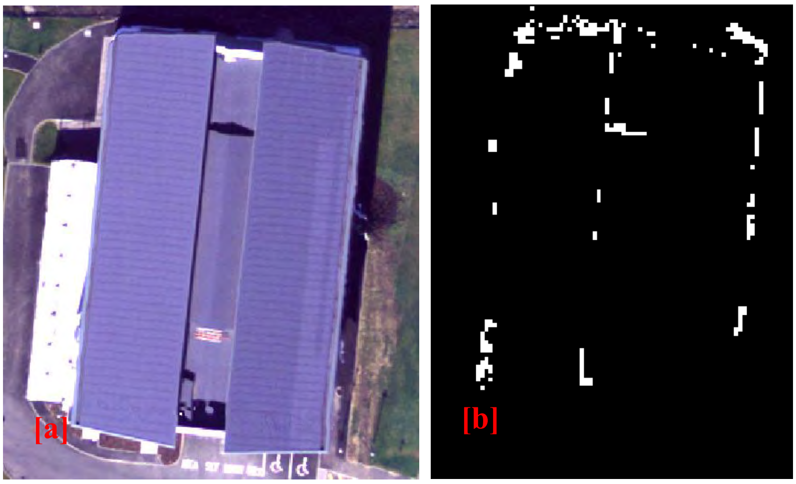

Figure 74: (a) Ortho RGB Image (b) Vegetation Segments on Building Roof and Around Edges

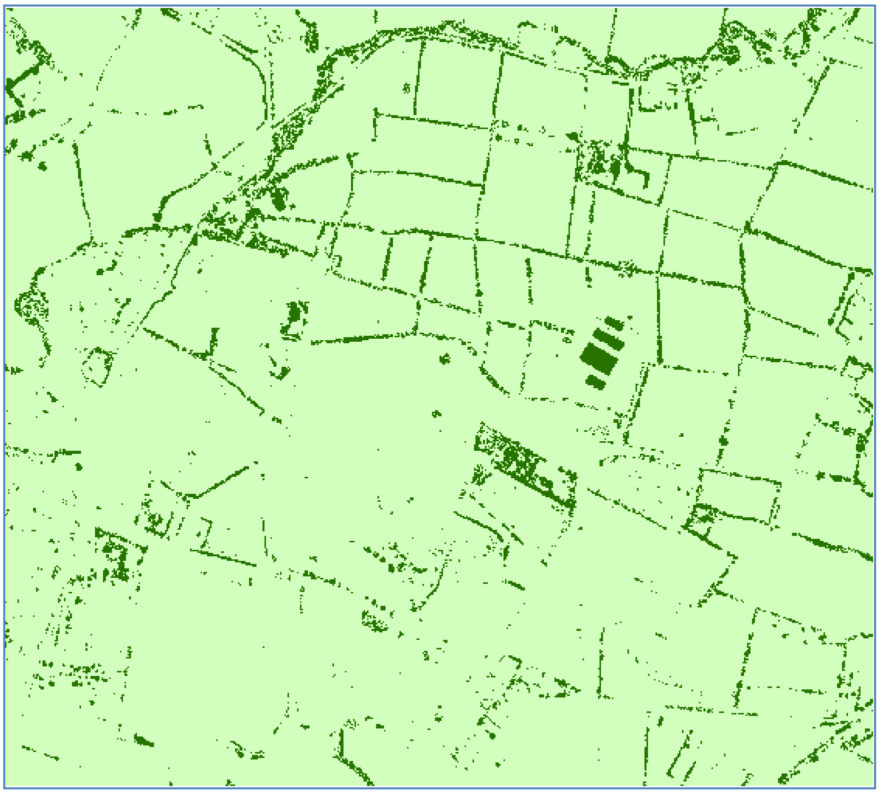

Figure 75: Extracted Vegetation (Development Area)

5.3.3 **Extraction of Non-Vegetation Objects**

After filling the gaps and removing artefacts created at the time of orhtophoto generation, the potential vegetation areas (Figure 75) were searched for the buildings that were present amongst vegetaion (Figure 76). The shape parameters such as rectangularity, compactness, roundness and shape index were analysed to separate the buildings from vegetation but without success. However; combining these with the four classification cues (VSNs, LRV, SR and AD) used previously for spearating trees that existed in classified buildings proved useful in separating buildings from vegetation. Same thresholds values were used for classification cues obtained from LiDAR as listed in Table 24. The used shape parameters were rectangularity (>0.85), compactness (>1) and shape index (>1).

An additonal parameter (classification cue) was also generated from the used classifiation cues as was done perviously for building extraction to soften the effect of stringent thresholdings. This included the four cues from LiDAR and three cues from shape analysis. Building candidate region scoring at least 6 out of 7 (85%) were finally selected and separated from vegetation.

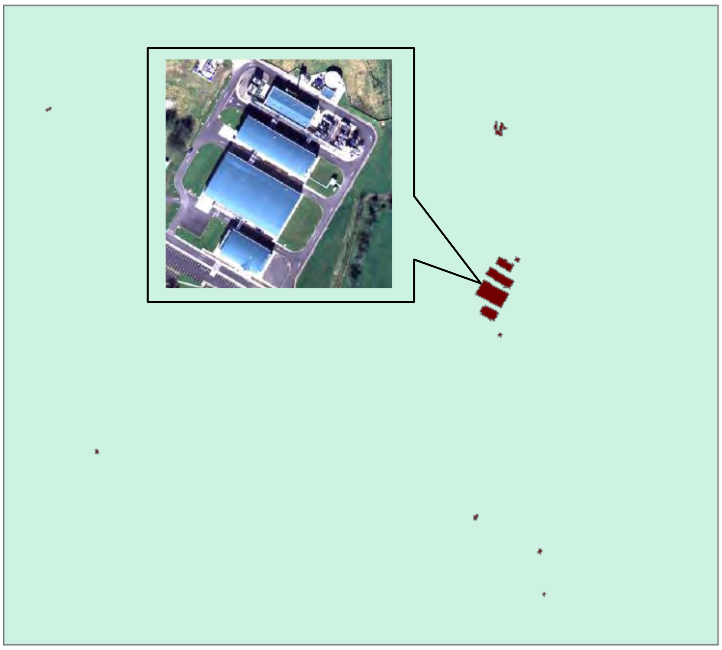

Figure 76: Buildings Separated from Vegetation (Development Area)

Figure 76 shows the buildings that exist amongst vegetation because of NDVI values in the range used for vegetation extraction. These were successfully separated using the explained methodology and added back to the buildings that were extracted previously.

5.3.4 **Hedge Extraction**

The hedges along roads and around dwellings and fields were separated from the extracted vegetation using a shape parameter i.e. length to width ratio (>5). The extracted hedges are shown in Figure 77 overlaying the ortho RGB image.

Figure 77: Extracted Hedges in the Development Area

5.3.5 **Single Tree Extraction**

A pixel based analysis was carried out for extracting single trees or tree clusters from the extracted vegetation using pixel height values. The vegetation pixel height was reversed, so the high points (tree peaks) became the lowest points (ditches) and vice versa. Hydrological analysis was performed to segment out pixels representing ditches (tree peaks), where the flow accumulated from the neighbouring pixels. The steps performed in the extraction of single trees can be seen from the flowchart in Figure 78. These segments were extracted and finally converted to the points representing tree peaks (Figure 79).

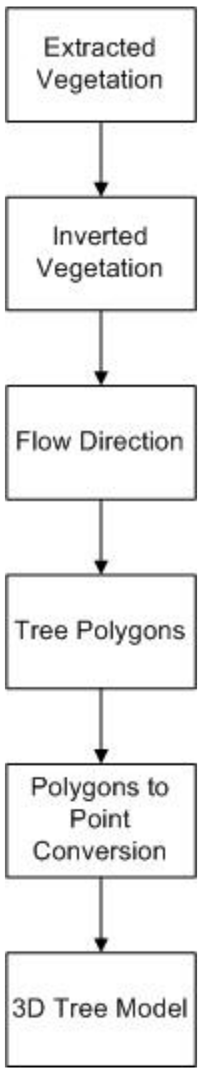

Figure 78: Method for Single Tree Extraction

Figure 79: Extracted Tree Peaks Overlaying Ortho RGB Image

5.3.6 Tree Clusters

In order to extract tree clusters, a distance matrix was calculated representing the distance of each single point (tree crown) from all the other points (trees). In this way, the distance between each individual tree and its 7 closest neighbouring trees was calculated. Finally, all those trees placed at a distance of less than 3 m from their neighbours were selected and categorized as tree clusters (Figure 80). The number of neighbours and the distance between the tree clusters may vary. However; it is not fundamentally important as the purpose here is to provide a workable solution for extracting tree clusters, if required.

Figure 80: Extracted Tree Clusters Overlaying RGB Image

5.4 Road Extraction

It is important to identify different surface types for effective noise modelling. It is so because the extent of noise reflection varies with the change in surface material thus affecting noise propagation. Road surfaces are either made up of asphalt or concrete with varying sound reflection properties.

Aerial images are always captured during daytime, when there are maximum road users. These road users, different types of road markings, overarching trees and the similarity of road surface to building roofs present the biggest challenges in road classification. With the help of the LiDAR sensor, the detailed road geometry can be captured during night time. The height information from LiDAR can be used to separate roads from building roofs. However; the problem of large trees overarching the roads remains. These trees can affect the quality of the generated DTM, especially if the point cloud density is low.

The roads were part of the extracted DTM as has been explained in chapter 4, along with other surface objects such as grass, drive ways, footpaths and paved or unpaved surfaces. If DTM has to be used then the holes in it, which occurred due to above-terrain object filtration, should not be filled with the interpolated value from their neighbours. The pixel value of these holes should be set to 0. However; it is preferable to use inverted binary nDSM where the value 1 represents the ground having zero height as shown in Figure 81.

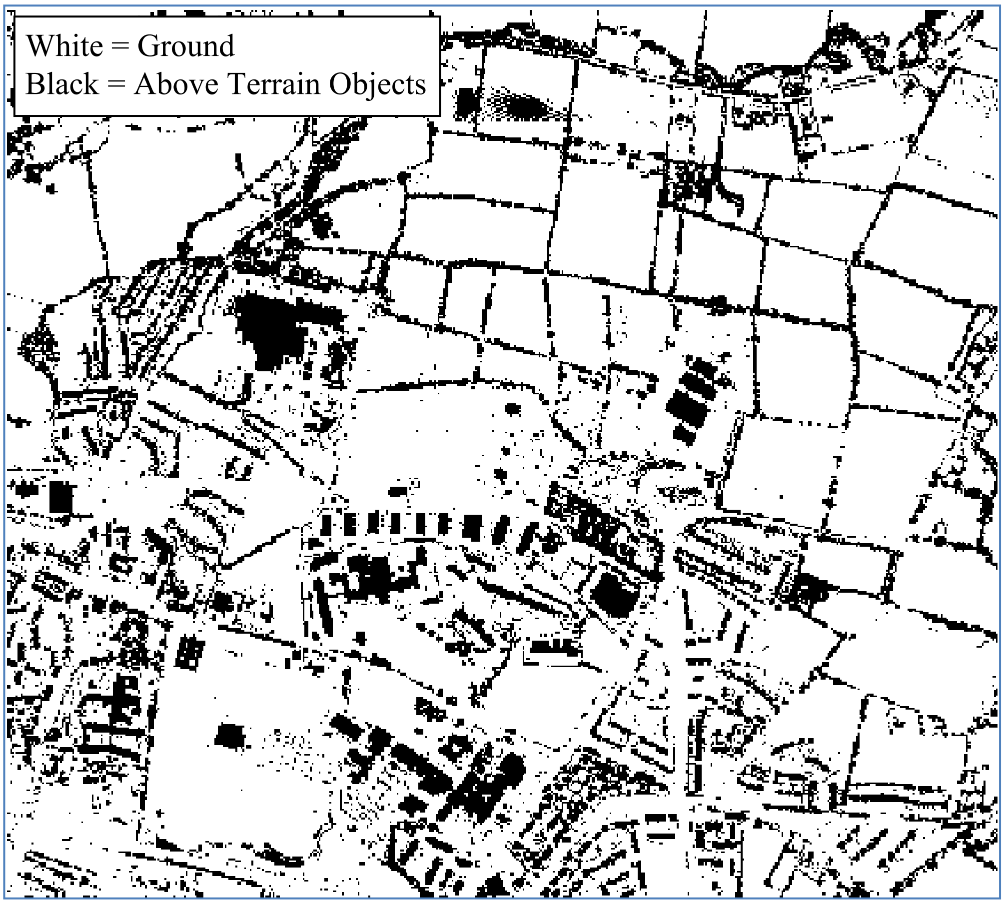

Figure 81: Inverted Binary nDSM (Development Area)

Roads are generally part of the ground surface with the exception of bridges. These were extracted by fusing LiDAR intensity and NDVI images. The ground has been classified into three surface types i.e. roads including car parking lots, grass covered surfaces and barren or ploughed surfaces as shown in Figure 82. The method for road extraction is shown in Figure 83.

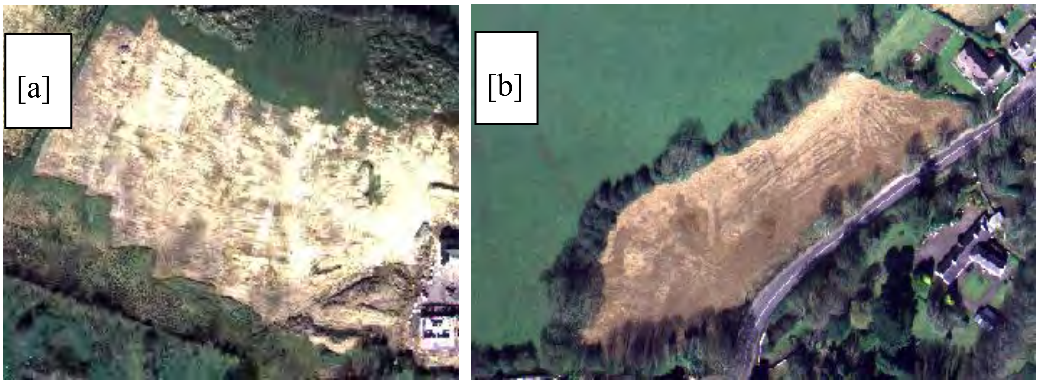

Figure 82: Different Ground Surface Types (a) Barren Surface/Construction site (b) Ploughed Ground

LiDAR intensity information was uniform over the roads. It was used to separate roads especially from the barren surface/ploughed ground in combination with the previously thresholded NDVI image, used for building extraction.

Multi-resolution segmentation was used to generate small segments which when combined after classification do not alter object boundaries a lot as was the requirement during building extraction. Parameters used for multi-resolution segmentation are shown in Figure 84.

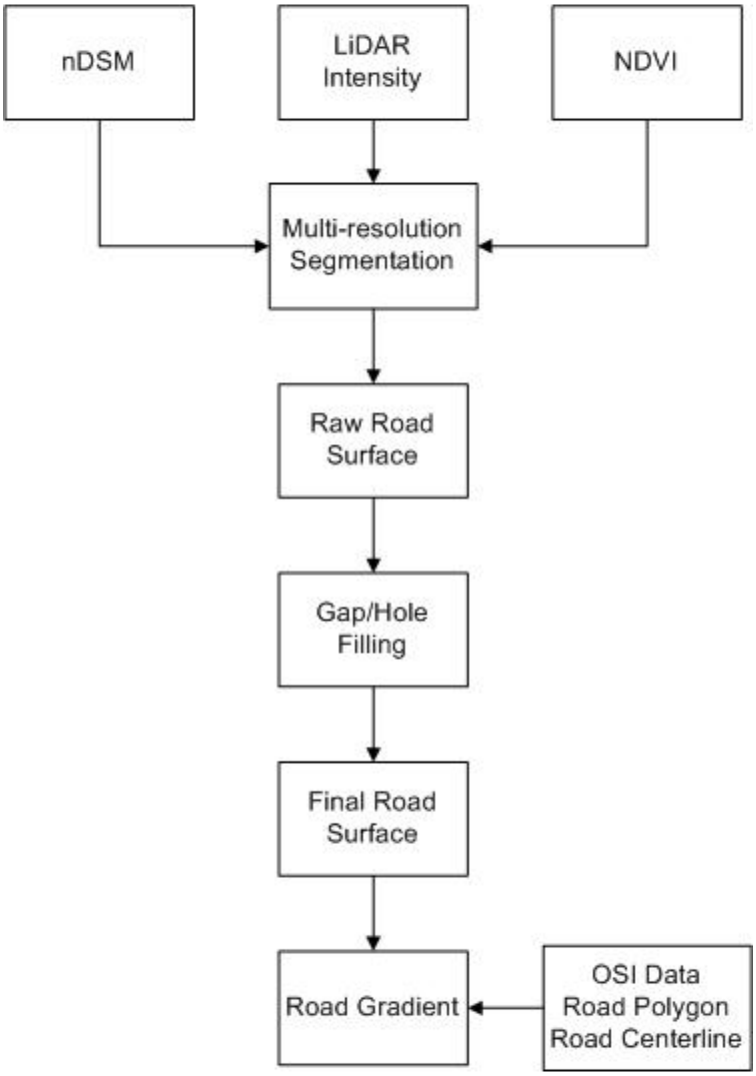

Figure 83: Road Extraction Method

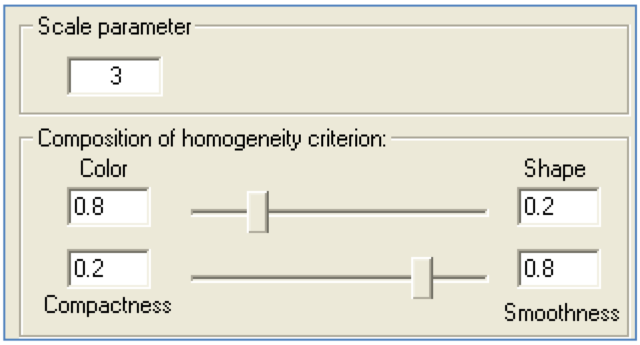

Figure 84: Multi-resolution Parameters used for Road Extraction

A scale parameter equal to 3 was used to generate small segments. Reducing it further generates segments equal to the pixel size (0.5m). In addition it utilizes considerable memory resulting in software crashes. More weight was assigned to colour rather than the shape in order to use LiDAR intensity and NDVI values for segmentation. Compactness and smoothness depend upon the shape value (0.2) which was set low for road extraction to generate long thin segments better representing the road boundaries.

The raw road surface was extracted by selecting NDVI and LiDAR intensity values below 146. The values were selected by investigating the mean values of these two parameters over a few road segments. The reason for calling it a raw surface the presence of holes in it. These might have occurred due to road users, overarching trees or trees in between a dual carriage way, partitioning barrier etc. These holes need to be filled. This is of particular importance if the road centre line has to be extracted. A new method was developed to fill such holes.

Holes in the raw road surfaces were filled by reversing the extracted raw road binary image. By doing so, small gaps appeared as noise. These gaps were filled by using morphological operation opening. Figure 85 (a) shows a subset binary image of the raw road surface (white pixels) in the development area before the hole filling operation and Figure 85 (b) shows the resulting final road surface.

Figure 86 shows the extracted road surface. Roads or hard surfaces covering an area less than 250 m^2 as well as long narrow roads in the open country can be ignored as per the recommendations of the working group and have been listed in chapter 1. The extraction of road segments provide the initial input required for extracting road vector data such as centre line, longitudinal and cross sectional slope etc. In order to extract road centre line, the maximum road width in the project area needs to be known before hand.

This helps in separating drive ways and car parking areas from the main road. However; the extraction of road centreline is not possible for those road segments which are under dense vegetation as shown in Figure 86 (red polygon). The object-oriented techniques for processing vector data extend the determined road centreline on both sides of the gaps depending upon the maximum allowable limit as set by the operator. However; the results were not good in cases when the roads are at a curve or in the case of large gaps.

Road centrelines and edges have already been digitized by the OSI as line features. These are available to the NRA and were not further researched. The developed method will help in incorporating different man made surfaces into the noise model which have reflection properties different from natural surfaces.

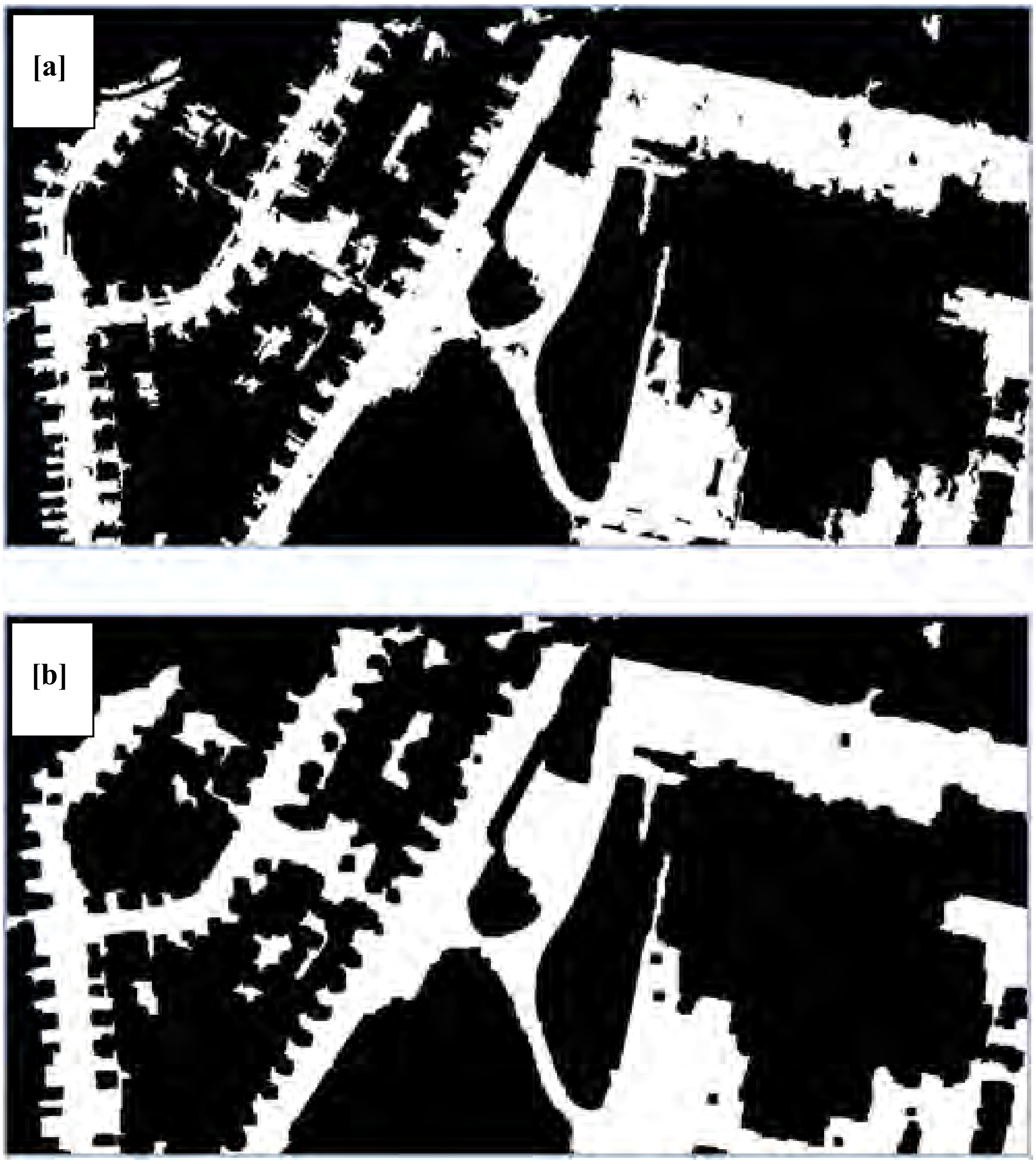

Figure 85: Morphological Operation (Opening) for Holes Filling (a) Raw Road Surface (Before) (b) Final Road Surface (After)

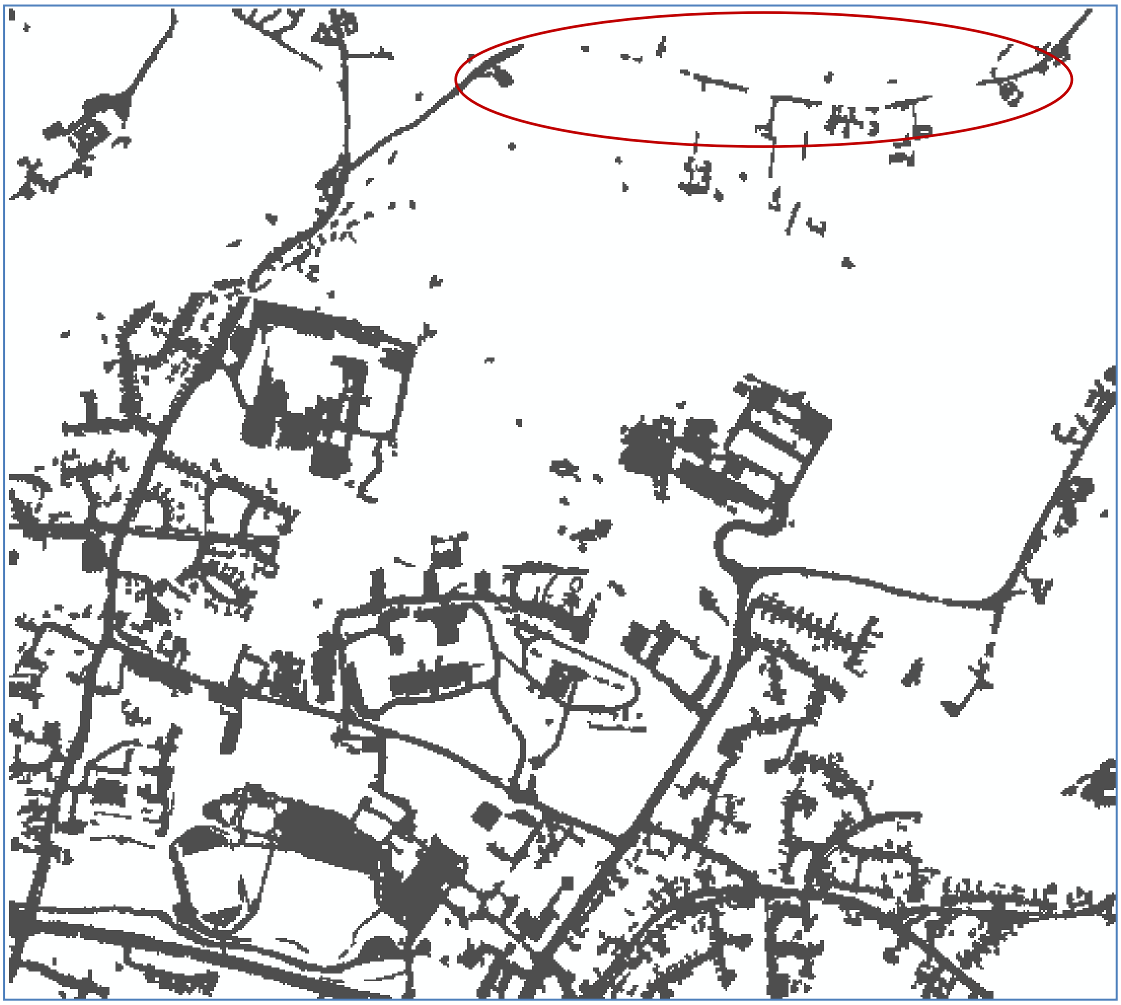

Figure 86: Extracted Road Surface (Development Area)

Ploughed, barren or construction site surfaces were also extracted using the same methodology as was used for road surface extraction with an additional input i.e. the extracted road surface itself. Appropriate thresholds were selected for NDVI (110 <NDVI< 163) and LiDAR (>135) intensity after inspecting some segmented regions. The extracted segments were checked against previously extracted roads to insure that they don’t overlap. Extracted surfaces are shown in Figure 87.

Figure 87: Extracted Ploughed, Barren or Construction Site Surfaces Different from Natural Ground and Roads and Greater than 250 m^2

5.4.1 Longitudinal Road Gradient

Gradient is an important parameter as traffic noise increases at sharp slopes. It was stored as an additional attribute along with the road centreline. Gradient is defined as

$$Gradient = \frac{\Delta h}{L}$$

Gradient was calculated using Hawth's tool in ArcGIS (Beyer, 2004). The generated DTM was used to determine the slope of the area. The length weighted mean (Figure 88) and standard deviation (Figure 89) were then determined for each section of the road centre line. Length weighted mean shows the slope mean value over the course of each road section. However; if there is a sharp change in slope in a particular road section, this can be better identified using standard deviation. It also eliminates the need of digitising these sections as a separate new line. Figure 89 shows that in the development area there are very few sections where there is a sharp change in the road slope.

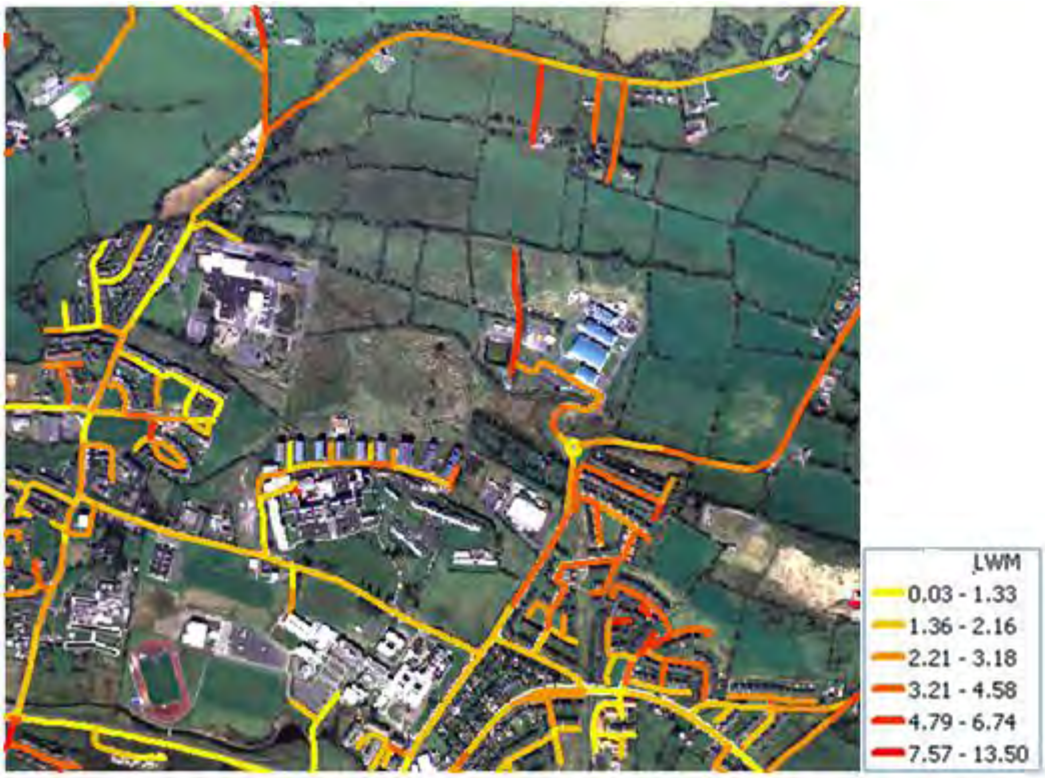

Figure 88: Road Length Weighted Mean Gradient

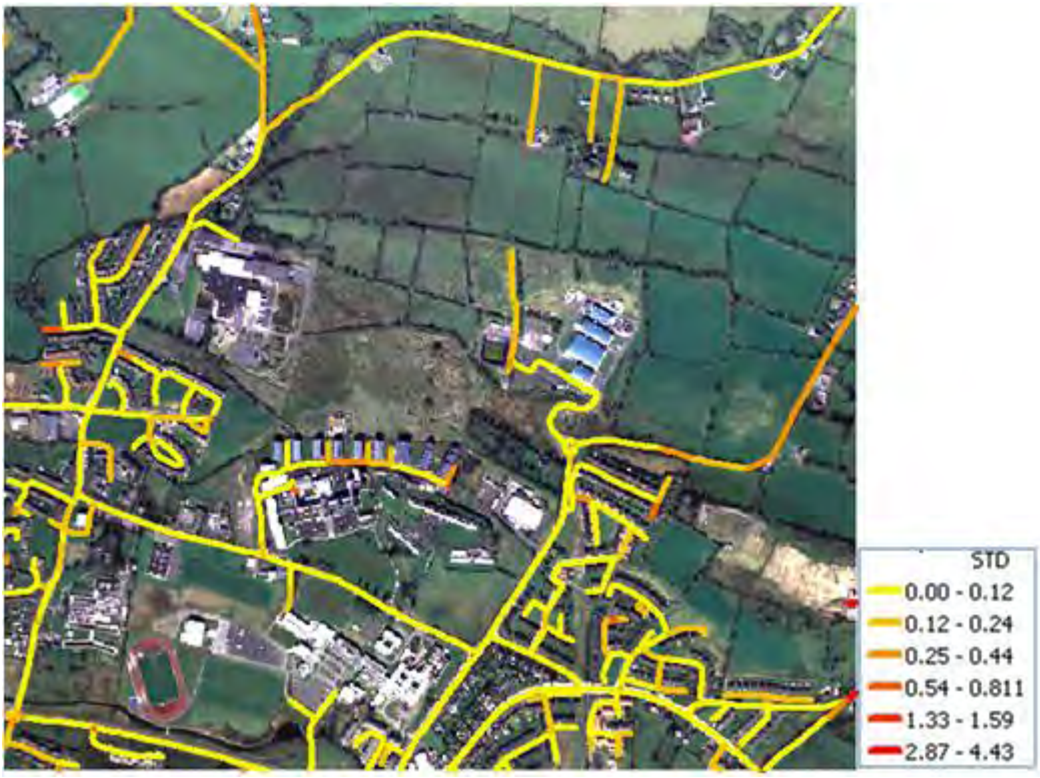

Figure 89: Road Length Weighted Standard Deviation

5.5 Noise Barrier Extraction

Noise barriers are an important component of any noise model. These are built specifically closer to the source of sound to dampen the noise before it propagates. These barriers are thin (Figure 90 (a)) and continuous along the road (Figure 90 (b)).

Figure 90: Example of a Highway Noise Barrier

Any noise barrier should be at least as tall as the line-of-sight between the noise source and the receiver, plus 30%. Therefore, if the line-of-sight is 3 m high, then the barrier should be at least 4 m tall for optimal performance (Sound Fighter Systems, 2010). These noise barriers because of their geometry are not visible in the low density LiDAR data, especially if these are perpendicular to the flight direction. The developed methods of object extraction (buildings and roads) using airborne sensor data were able to extract hedges along the road and dwellings. However; these were not able to extract boundary walls because of their thickness i.e. 15 cm. This is the same as the GSD of the available ADS40 sensor data. The orthophotos were used for object extraction with a reduced spatial resolution (0.5 m) further dropping the chances of a wall or noise barrier extraction.

5.5.1 **Noise Barrier Extraction Method**

5.5.2 **Point Cloud Classification**

Mobile Laser Scanner (MLS) data was only available for the Test Area-2 and has been described in chapter 3 (section 3.3). A method was developed for the semi-automatic extraction of noise barriers using the trajectory of the MLS. As explained in the chapter 3, no purpose built noise barrier existed in the area. However; a continuous wall along the road connecting Maynooth and Leixlip towns was considered as a possible noise barrier.

The process starts by extracting the ground points from MLS data or using classified ground points from airborne LiDAR extracted for DTM. Ground is needed to extract those points which are in the height range of 0.5 to 4 m (possible noise barrier height as mentioned earlier) from the ground to narrow down the object search space. The points below 0.5 m were not considered as these could be because of small vegetation in front of the noise barrier.

A second classification cue was used calculated using MLS trajectory during the data acquisition. The perpendicular distance of previously filtered point (0 - 4 m) from the trajectory was calculated. The perpendicular distance from a point (m, n) to the line $Ax + By + C = 0$ is given by:

$$d = \frac{|Am + Bn + C|}{\sqrt{A^2 + B^2}}$$

This formula is applicable to straight road stretches. However; if they lie on curves, small road stretches should be used to minimize the deviation of the noise barrier from the sensor trajectory. On the other hand it is not practical to process all MLS data at one time, necessitating the need to sub divide it into several smaller subsections. These sub-sections can be so selected that the road segment is straight in each section. Purpose built noise barriers generally have a constant distance from the road centreline or MLS trajectory. However; this is not applicable to walls.

Moreover, depending upon the type of material they are made of, the noise barriers have unique reflectance properties recorded as intensity of the returning pulse. However; it is quite possible that over time these get covered by vegetation (plants that grow as vines) resulting in variable intensity values.

5.5.3 **Principal Component Analysis**

The classification cues (perpendicular distance from the road trajectory and intensity) were analysed using Principal Component Analysis (PCA) for the filtered point cloud. PCA is a technique that takes a collection of data and transforms it such that the new data has certain given statistical properties. The statistical properties are chosen such that the transformation highlights the importance of data elements. Thus, the transformed data can be used for classification by observing the important components of the data (Nixon and Aguado, 2002).

The first and second principal components were determined in MATLAB and were thresholded to extract those points that belong to the noise barrier. Different weights can also be assigned to these classification cues in PCA, if the intensity is not uniform or if the barrier is not parallel to the sensor trajectory. However; in this research no weights were used for classification cues. This was mainly due to the fact that the versatility of the data was limited by only a single wall making it difficult to run various scenarios.

5.5.4 Line Fitting

Robust Least squares fitting method was used to fit a straight line into the points classified as a noise barrier because of the sensitivity of linear least squares to outliers. Outliers have a large influence on the fit because squaring the residuals magnifies the effects of these extreme data points. MATLAB curve fitting toolbox provides these two robust regression methods:

Least Absolute Residuals (LAR): The method finds a curve that minimizes the absolute difference of the residuals, rather than the squared differences. Therefore, extreme values have a lesser influence on the fit.

Bisquare Weights: This method minimizes a weighted sum of squares, where the weight given to each data point depends on how far the point is from the fitted line. Points near the line get full weight. Points farther from the line get reduced weight. Points that are farther from the line than would be expected by random chance get zero weight.

For most cases, the Bisquare weight method is preferred over LAR because it simultaneously seeks to find a curve that fits the bulk of the data using the usual least squares approach, and it minimizes the effect of outliers (MathWorks, 2010).

The polyfit and polyval commands in MATLAB were used initially for a regular linear fit to the candidate points after PCA. To fit a line (n = 1) through the data (x, y), the corresponding MATLAB command is

$$\mathrm{pcoeff} = \mathrm{plyfit}(x, y, 1)$$

The output of this function call is a vector pcoeff which includes the coefficients a_1 and a_0 of the line fit $p_1(x) = a_1 x + a_0$. To evaluate and plot this line, values of x must be chosen. The polyval command uses the coefficients generated from polyfit to generate the y values of the polynomial fit at the desired values of x. After determining the initial fit (regular linear fit), Bisquare weights method was used for robust least squares fitting. The process continues until the fit converges.

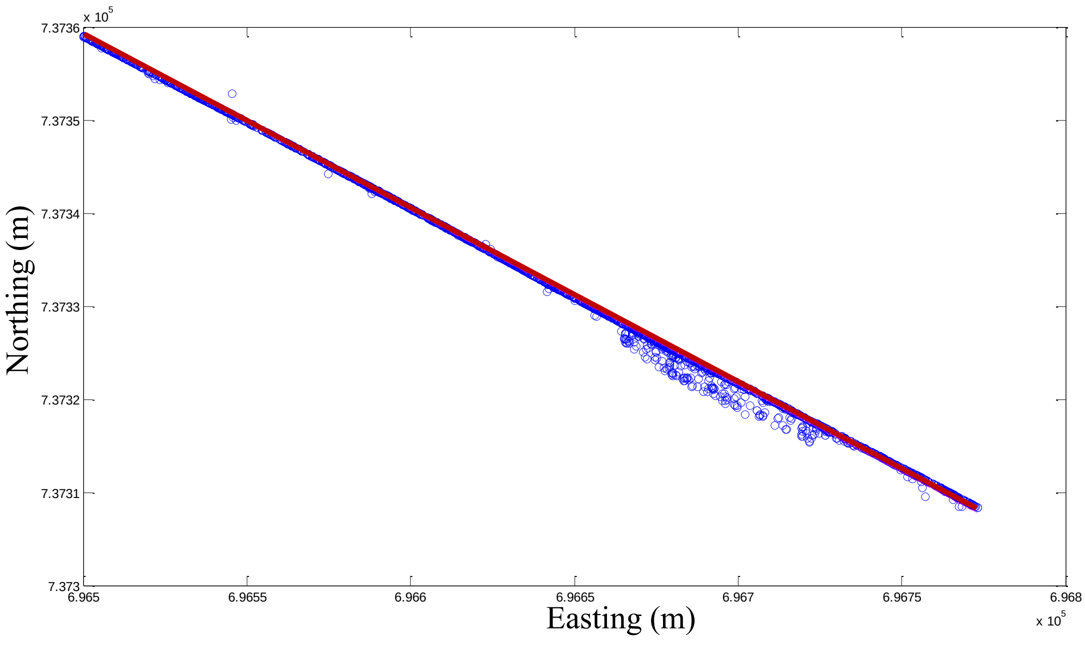

Figure 91: Extracted Noise Barrier

Figure 91 shows a section of the road for which a continuous wall along the road was extracted. This wall was tested against the previously extracted building boundaries to make sure that the two do not overlap (especially building façade) and that it is an independent structure with in the road neighbourhood. The developed method for noise barrier extraction is summarized in Figure 92.

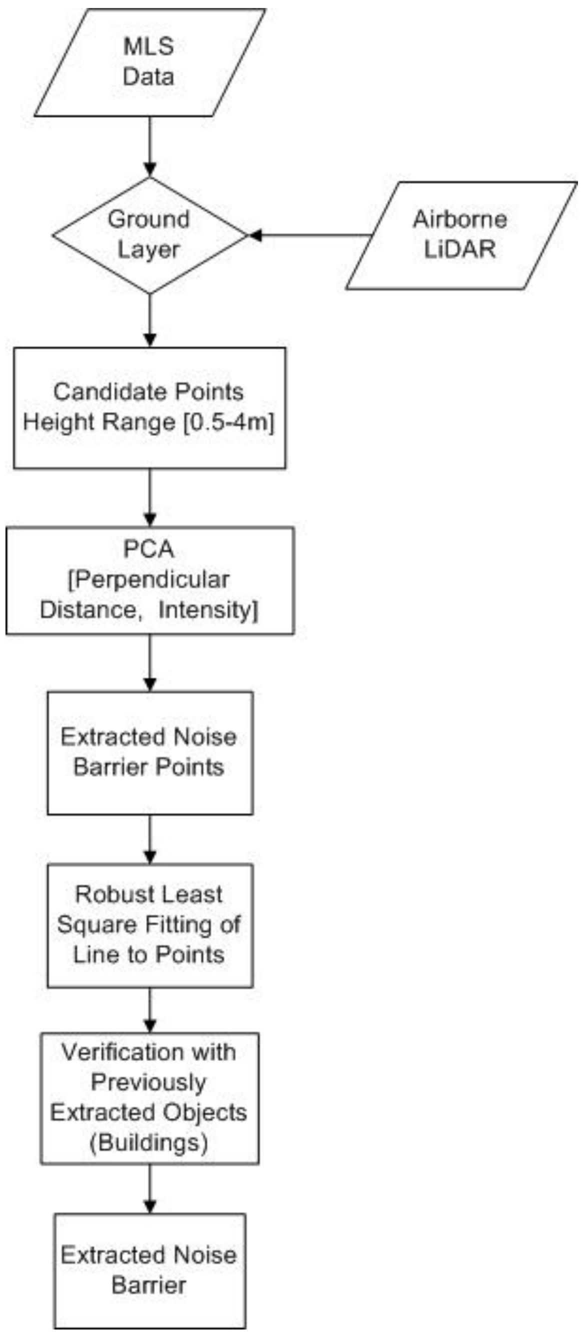

Figure 92: Noise Barrier Extraction Method

5.6 Accuracy Assessment

To evaluate the accuracy of extracted objects (buildings, trees and roads) using the developed method, the OSI vector data was used as a reference. The reason for choosing the OSI data was to examine the accuracy in real world rather than digitizing the objects in house using orthophotos or Digital Photogrammetric Work Station. Three different methods used for estimating building extraction accuracy are explained in the following sections. These have been discussed here from the perspective of buildings. This is so because, later on, only the pixel-based method and the area overlap method were used for the extraction of roads and vegetation respectively. This is because of the non availability of reference data for vegetation and the nature of extracted road objects.

Accuracy measures such as completeness, correctness and quality were calculated to determine the success of the extraction method (Heipke et al., 1997).

$$completeness = \frac{Tp}{Tp + Fn}$$

$$correctness = \frac{Tp}{Tp + Fp}$$

$$quality = \frac{Tp}{Tp + Fp + Fn}$$

$completeness, correctness$ & $quality$ are generally expressed in percentage.

An entity classified as an object that also corresponds to an object in the reference is called a True Positive (T_p). A False Negative (F_n) is an entity corresponding to an object in the reference that is classified as background. A false Positive (F_p) is an entity classified as an object that does not correspond to an object in the reference.

5.6.1 **Building Centroid**

In building centroid method, building polygons were used and their centroids were calculated. These centroids might lie outside the building regions and need to be corrected. Building representation in the provided OSI data and our extracted buildings is very different. The buildings with common roofs were extracted as one whereas they exist as separate buildings in the OSI data as has been touched upon earlier in chapter 3 (section 3.5). Internal borderlines not visible from the top were marked through the ground survey. Moreover, the operator also used his own judgment in marking the borders between buildings having common roofs with the help of back or front garden walls between the buildings. This method requires a lot of manual work with the extracted or reference data to make both datasets correspond before beginning the actual comparison process.

Figure 93: Different Building Representations (a) Ortho RGB Image (b) OSI Vector (c) Extracted Buildings

Figure 93 (a) shows buildings in RGB orthophoto (b) shows OSI vector and (c) shows the extracted building boundaries. The buildings which are very close have been extracted as single buildings (Figure 93 (c)). Instead of comparing the building centroids, the extracted buildings that intersect with the OSI buildings were considered as a successful extraction (true positive). That is why this method has been referred to as building intersection from here onwards.

The analysis was based on the number of buildings in the OSI data and the extracted buildings; intersecting buildings in both datasets (T_p); the number of buildings missed that exist in the OSI data (F_n); and the extracted buildings that do not exist in the OSI data (F_p). Table 26 shows the details of building intersection method based on extracted and reference object intersection in the development area.

OSI Building Vector	No. of Buildings
Area > 30 m^2	1074
Area (15 to 30) m^2	72
Area < 15 m^2	190
Total OSI Buildings	1336
Building $\geq$ 30 m^2 Overlapping Extracted Buildings (T_p)	1017
Missed Large Buildings	1074-1017=57
New Buildings in 2009 Vector Data	6
Buildings Missing in OSI Data	1
Total Missed Buildings (F_n)	57-6-1=50
Extracted Buildings not Matching OSI (F_p)	74

Table 26: T_p, F_n *and* F_p Determination Based on Building Intersection Method (Development Area)

The number of buildings in the OSI vector data was far more than the extracted buildings because of the marked internal boundaries. 57 extracted buildings did not match with the buildings in the OSI data. This was due to some vegetation been extracted as buildings and different definitions of buildings in the OSI data. The OSI data did not include some temporary structures or industrial installations which were extracted as buildings. The containers placed outside the loading bay at construction sites were also detected. The buildings with an area more than 30 m^2 were considered as a threshold in the extraction process, however; there were only 10 buildings that were extracted overlapping the OSI building vector with an area between 15 and 30 m^2. The building size threshold can be reduced to 15 m^2 but it would increase the noise in the extraction process resulting in a reduced overall accuracy.

Large trees overarching building roofs or buildings surrounded by high dense vegetation reduce the accuracy of the extraction process. However; these buildings were digitized in the OSI vector data (Figure 94) by the operator. Figure 94 (a) shows buildings in ortho photo and (b) shows the OSI building vectors and the extracted building polygons.

Figure 94: Trees Overhanging Building Roofs (a) Ortho RGB Image (b) Extracted Buildings (Blue) and OSI Vector (Red)

Figure 95: (a) and (b) are New Buildings and (c) Missing Buildings in OSI Data

The OSI vector data corresponds to the year 2009 whereas the images and LiDAR data were captured in 2007. Some new buildings were constructed in the mean time. Figure 95 (a) and (b) show these new buildings whereas (c) shows an extracted building that was not present in the OSI data. This building has either not been digitized or has been demolished. Such buildings were removed from the OSI building vector and the extracted buildings.

5.6.2 Pixel-Based

In the pixel-based accuracy assessment method, each pixel in the extracted building is compared with the reference building, generated by converting the OSI building vector to raster. This requires good registration of the reference and the extracted buildings, and is a prerequisite for using this method.

The pixel based method for accuracy assessment is more stringent than the building intersection method as each pixel in the reference image (OSI) is compared with the extracted building image. Figure 96, Figure 97 and Figure 98 show the determined T_p F_n, and F_p images in the development area using the pixel-based method. The number of white pixels in each of these images was computed to calculate the accuracy measures (completeness, correctness and quality).

Spaces between the buildings were filled because of morphological operations or because of relative border criteria used to fill gaps in the building segments resulting in white pixels around building edges in F_n, and F_p. Since the OSI vector data was converted to raster, this also results in rough object edges.

Figure 96: Successfully Extracted Building Pixels (T_p)

Figure 97: Building Pixels Missed by the Extraction Process (F_n)

Figure 98: Non Building Pixels Extracted by the Developed Method (F_p)

The pixel-based method was also used to measure road extraction accuracy.

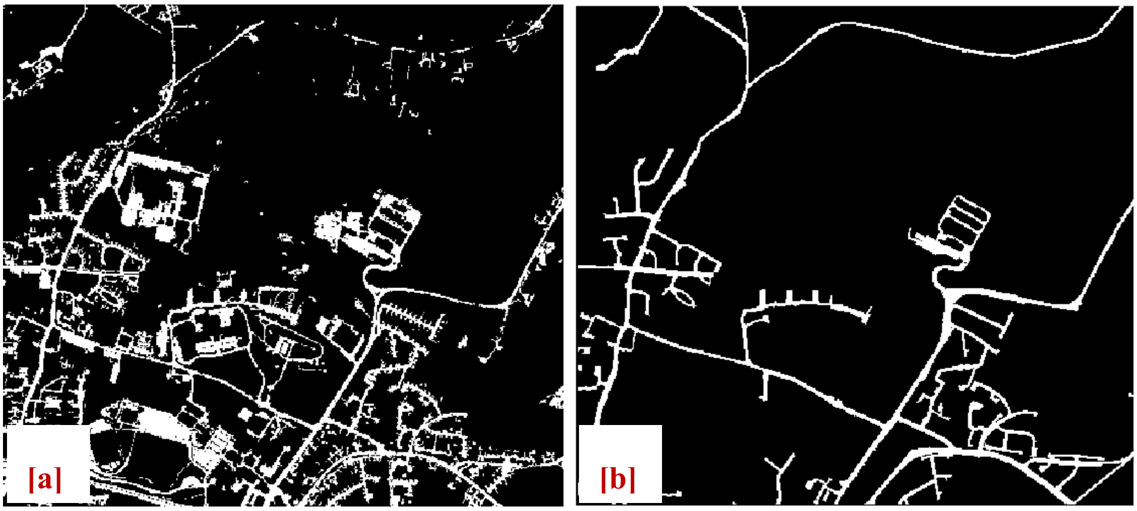

Figure 99: (a) Extracted Roads and (b) OSI Roads

Figure 99 (a) shows the extracted roads using the developed method and the Figure 99 (b) shows the data available from the OSI for accuracy assessment. The OSI data does not include all surfaces having reflectance similar to roads.

Figure 100 shows the pixel-based comparison of reference and extracted roads. Figure 100 (a) shows that most of the road pixels were successfully extracted (white pixels). However; the method fails to extract the road under overarching trees resulting in gaps Figure 100 (b). Figure 100 (c) shows the hard ground surface extracted using the developed method and was not digitized as road in the OSI data. However; these areas are important for noise modelling.

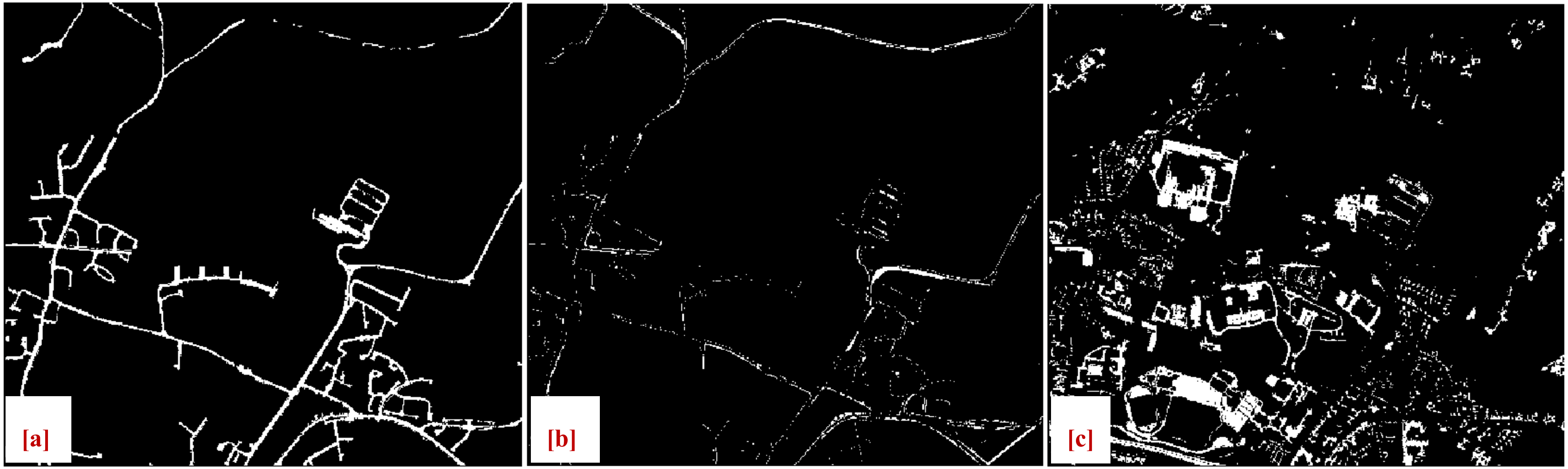

Figure 100: T_p, F_n and F_p Binary Images for Accuracy Assessment (Development Area)

5.6.3 **Area Overlap**

A third method was used to determine the percentage overlap of the extracted and the OSI buildings. A threshold has to be selected based on the percentage overlap to determine the buildings that were extracted successfully.

T_p was determined using OSI building polygons and calculating the area it covers in the corresponding extracted building polygons and then summing up all these areas. For F_n, the calculated total overlapping area was subtracted from the total OSI building area. F_p was determined from the area overlapped by the OSI building vector minus the total area of the extracted building. The percentage overlap of each of the OSI building vector with the extracted building polygon was calculated.

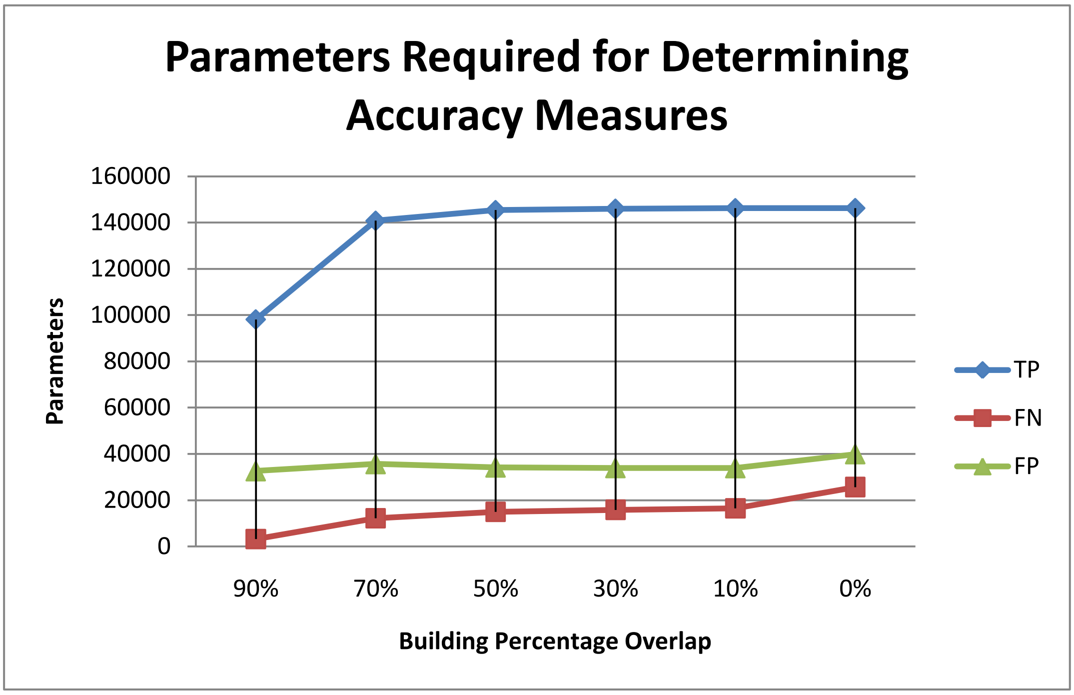

Figure 101: T_p F_n, and F_p using Area Overlap Method

The percentage overlap threshold that should be considered to identify T_p extraction is again debatable. That is why different overlap percentages have been considered for accuracy assessment in the development and the test areas. Figure 101 shows the three parameter values determined by considering different percentage overlaps as successful extraction. Considering 90% area overlap to be regarded as a successful extraction is not very realistic, given that there are many small buildings in the area. However; 70 or 50% area overlap can be considered as a suitable threshold to separate those objects that have been extracted successfully.

6 Results

The results of object extraction in the development area and the two test areas are presented (3D model) using the methods developed in the previous chapter. The chapter also shows the results obtained for each object in its corresponding section. These results are analysed in depth in the following chapter.

6.1 Development Area

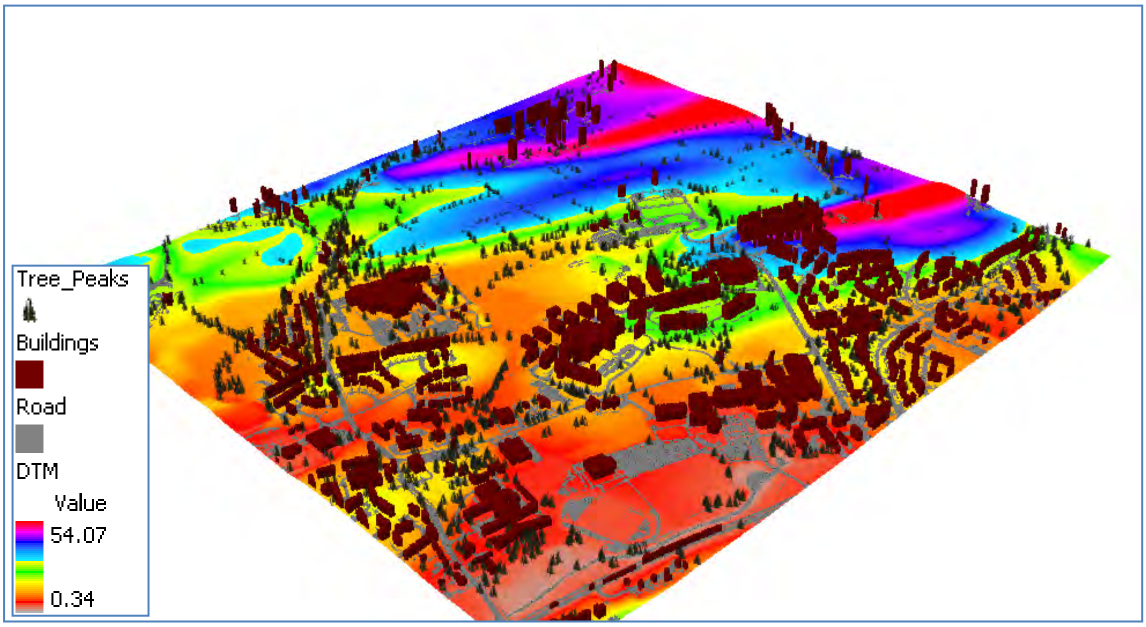

Figure 102: 3D Model of Development Area

The model extracted as a result of the object extraction method developed in chapter 5 is shown in Figure 102. The model shows buildings with individual heights, trees and roads overlaying the DTM. The steps for extracting each object of interest in the development area and the intermediate results were presented in chapter 5. Therefore, only the final 3D model has been presented here. Building height is an important attribute of noise modelling. The selected height is compared with the actual building heights measured using ground survey in chapter 7.

6.2 Test Area-1

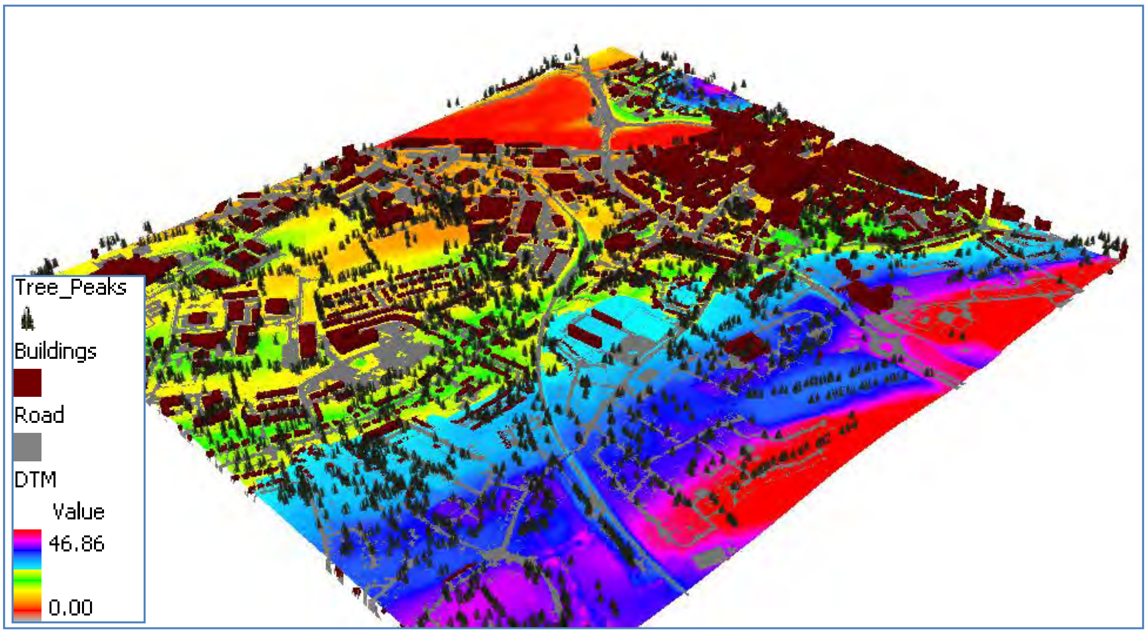

Figure 103: 3D Model Sligo (Test Area-1)

	SR	LRV	VSNs	AD
SR	33	10	8	6
LRV	10	64	7	27
VSNs	8	7	20	3
AD	6	27	3	30

Table 27: Confidence Matrix (Test Area-1)

The developed method was also tested objectively in Test Area-1 using the available Sligo data. Table 27 shows the developed confidence matrix to examine the effectiveness of each classification cue obtained from the LiDAR data for the extraction of final buildings. These classification cues were thresholded using the Normal QQ plot in ArcGIS. Figure 103 shows the final generated 3D model for Test Area-1. Intermediate results are shown in Annexure-II.

6.3 Test Area-2

In the Test Area-2, ADS40 and LiDAR data were available to test the developed method of object extraction along a road connecting Maynooth and Leixlip towns. NIR band was not available for Test Area-2 and is compensated by using returned LiDAR pulse intensity value for NDVI determination.

A continuous wall along the road was extracted as a noise barrier using MLS data in Test Area-2 using the method explained in chapter 5. Intermediate results are shown in Annexure-III.

	AD	SR	LRV	VSNs
AD	2918	528	180	33
SR	528	1119	70	157
LRV	180	70	514	145
VSNs	33	157	145	169

Table 28: Confidence Matrix (Test Area-2)

Vegetation segmentation in the reconstructed buildings was removed again using cues obtained from LiDAR. Table 28 shows how helpful these classification cues. Figure 104 shows the final 3D model for the Test Area-2 covering 500 m on either side of the road. Figure 105 shows the continuous wall extracted along the road, using MLS data.

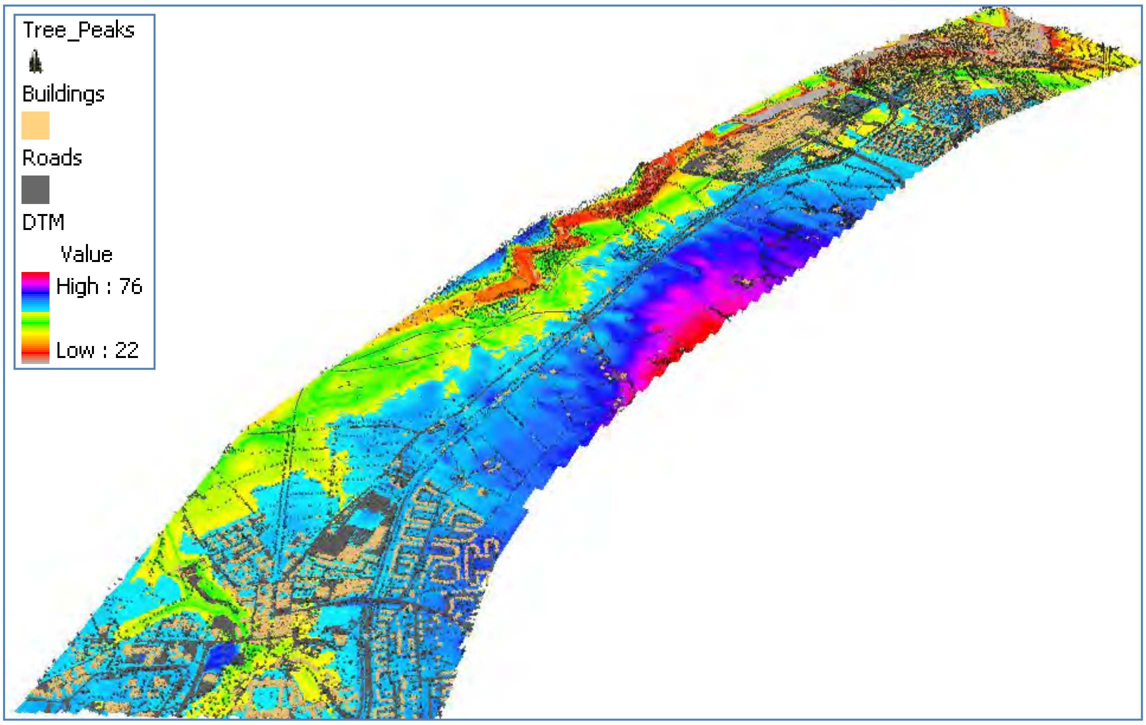

Figure 104: 3D Model (Test Area-2)

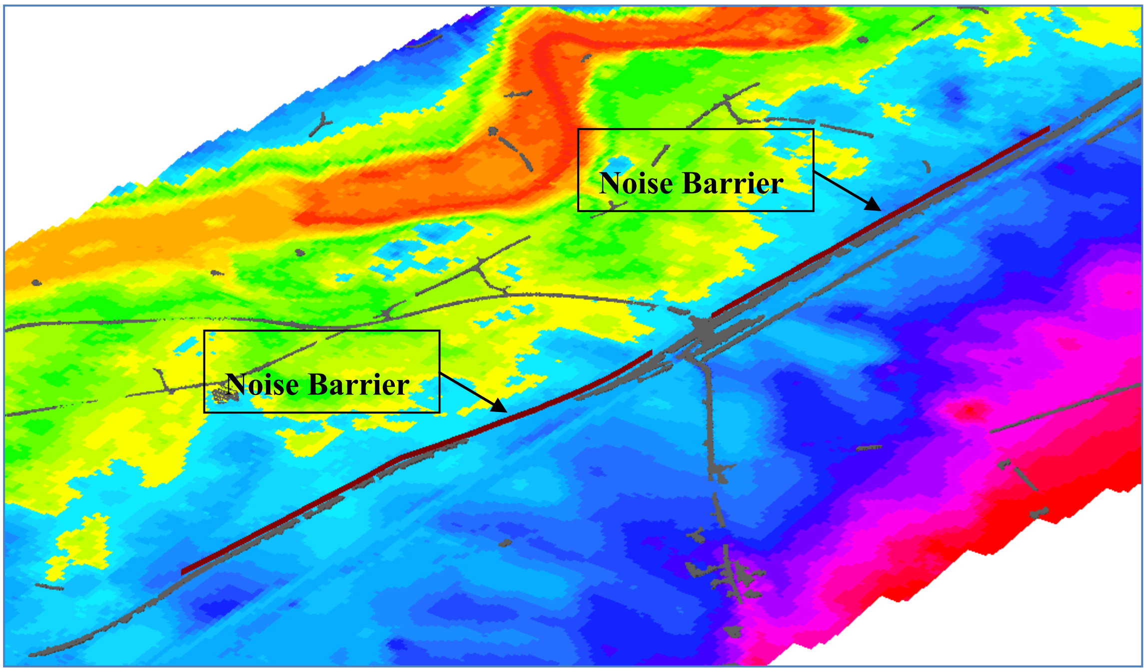

Figure 105: Extracted Noise Barrier (Wall along Maynooth Leixlip Road (R148))

6.4 Accuracy Assessment for Extracted Buildings

6.4.1 Building Intersection

Table 29 shows the accuracy assessment based on the building intersection method for the development and the test areas.

Area	Completeness	Correctness	Quality
Development Area	95.31	93.21	90.48
Test Area-1	97.26	96.91	94.34
Test Area-2	89.18	69.44	64.05

Table 29: Accuracy Assessment Based on Building Intersection Method

6.4.2 Pixel-based

Table 30 shows the obtained results in the development and the test areas using the pixel-based method of accuracy assessment.

Area	Completeness	Correctness	Quality
Development Area	88.28	76.81	69.70
Test Area-1	87.65	82.52	73.92
Test Area-2	81.77	70.93	61.24

Table 30: Accuracy Assessment Based on Pixel-based Method

6.4.3 **Area Overlap**

Table 31 and the graphs in Figure 106 show the accuracy assessment results obtained using the area overlap method. Different area overlaps were considered to (0 to 90%) for the selection of an appropriate threshold to draw a line between successful extraction and failure using the developed method for building extraction.

% Overlap >	Development Area			Test Area-1			Test Area-2		
	Completeness	Correctness	Quality	Completeness	Correctness	Quality	Completeness	Correctness	Quality
90	57.03	52.66	37.70	59.54	56.55	40.85	60.67	51.35	38.52
70	81.87	75.60	64.76	79.82	75.81	63.62	79.94	67.65	57.83
50	84.44	77.97	68.18	82.83	78.67	67.64	83.35	70.54	61.83
30	84.75	78.26	68.60	83.49	79.29	68.54	83.81	70.93	62.38
10	84.88	78.38	68.78	83.96	79.74	69.20	83.91	71.01	62.50
0	84.89	78.39	68.79	84.04	79.81	69.30	83.92	71.02	62.52

Table 31: Accuracy Assessment Considering Different Percentage Overlap

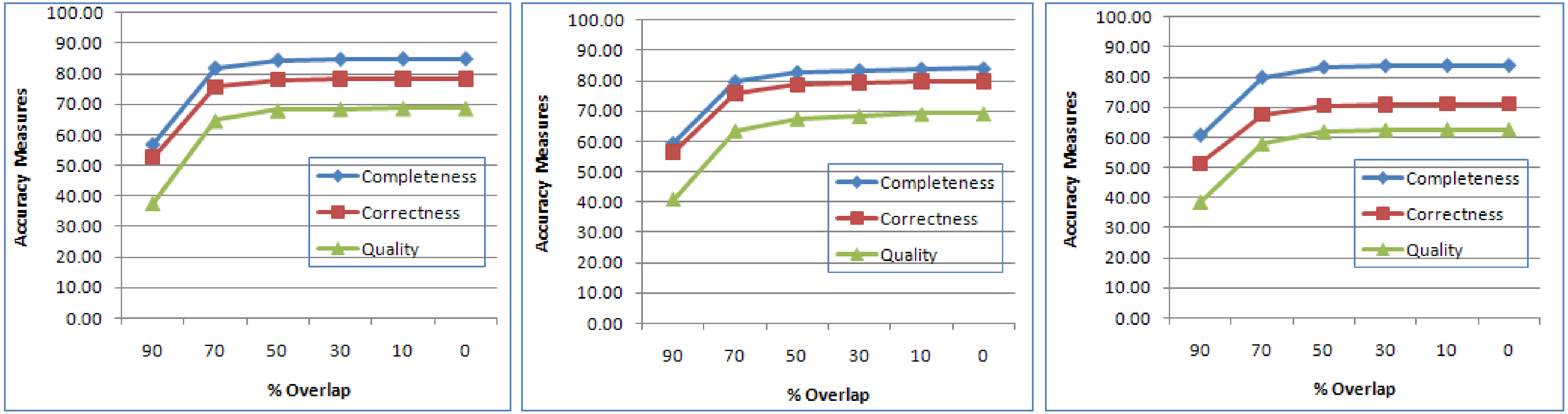

Development Area Test Area-1 Test Area-2

Figure 106: Graphs Representing Accuracy Measures using Area Overlap Method

6.5 Building Heights

Table 32 and Table 33 shows the comparison of the measured building heights during ground truth survey and the heights computed using the building centroid (bilinear interpolation) and descriptive statistical measures in the building regions.

In the Test Area-2 it was not possible to measure ground height close to the building (private housing) as was done in the development area. The orthometric height of the building roof was subtracted from the ground height (DTM) to obtain the actual building height.

6.6 Vegetation Extraction

Vegetation is not required by the NRA and nothing is mentioned about it in the report (Assessment of Exposure to Noise) prepared by the European working group. However; vegetation needs to be separated in order to extract buildings. Therefore, these are generated as a by product useful for many other applications.

The buildings that appeared in the extracted vegetation were considered as an error in vegetation extraction. The overlapping areas of the OSI building vector and the extracted vegetation were calculated. The correctness measure of accuracy assessment was determined indirectly by the area overlap method using the OSI building vector and the extracted vegetation. The completeness and quality measures were not possible to measure because of the non availability of the reference vegetation data. Table 34 shows the perecentage success in separating vegetation from the buildings in the development and the test areas.

Buildings	Roof Ridge Height (1)	Ground Height (2)	Building Height (3)	Centroid Height (4)	Max. Height (5)	Avg. Height (6)	Median Height (7)	Difference (m)			
								[3-4]	[3-5]	[3-6]	[3-7]
1	17.83	8.96	8.87	8.33	8.58	6.32	6.56	0.54	0.29	2.55	2.31
2	21.13	9.09	12.04	11.73	11.84	9.53	10.08	0.31	0.20	2.51	1.96
3	19.16	11.20	7.96	7.55	7.92	6.17	6.56	0.41	0.04	1.80	1.40
4	15.79	4.39	11.40	10.88	12.09	9.19	9.84	0.52	-0.69	2.21	1.56
5	13.63	3.60	10.04	9.56	10.07	8.04	9.50	0.47	-0.03	2.00	0.54
6	18.20	10.14	8.07	7.61	11.07	7.12	7.06	0.46	-3.00	0.95	1.00
7	18.67	10.44	8.23	7.65	7.71	6.62	6.69	0.59	0.52	1.61	1.54
8	19.13	10.45	8.68	7.73	7.91	5.11	6.04	0.95	0.77	3.57	2.64
9	18.11	10.32	7.79	6.77	8.12	5.64	6.69	1.03	-0.33	2.15	1.10
10	18.09	9.98	8.11	7.10	10.29	6.98	7.35	1.01	-2.18	1.13	0.76

Table 32: Building Height Determination (Development Area)

Buildings	Orthometric Height (1)	DTM Height (2)	Building Height (3)	Centroid Height (4)	Max. Height (5)	Avg. Height (6)	Median Height (7)	Difference (m)			
								[3-4]	[3-5]	[3-6]	[3-7]
1	48.91	40.23	8.68	8.69	8.79	6.37	6.71	-0.01	-0.11	2.31	1.96
2	48.70	40.51	8.19	8.42	8.65	6.35	6.69	-0.23	-0.46	1.84	1.49
3	48.75	40.82	7.92	7.34	11.85	6.36	6.82	0.58	-3.93	1.57	1.10
4	48.93	41.11	7.83	7.56	8.50	6.45	6.75	0.27	-0.67	1.37	1.08
5	49.11	41.35	7.76	7.85	8.10	6.38	6.56	-0.09	-0.34	1.38	1.20
6	49.63	41.52	8.10	8.52	8.66	6.34	6.65	-0.42	-0.56	1.76	1.46
7	50.23	42.01	8.21	7.90	9.08	6.62	7.00	0.31	-0.87	1.59	1.21

Table 33: Building Height Determination (Test Area-2)

Accuracy Assessment	Correctness %
Development Area	98.92
Test Area-1	97.84
Test Area-2	99.42

Table 34: Accuracy Assessment of Extracted Vegetation Using Area Overlap Method

6.7 Road Extraction

The used OSI vector data includes road boundaries. However; parking lots, carpeted drive ways and other surfaces which are part of DTM having reflectance properties very similar to a road, were not available. Accuracy measure completeness was only possible. It was considered appropriate to determine the extent to which the extracted information matches with the available data (completeness). If a method extracts most of the objects, it can be improved to achieve better classification. However; if a method fails in identifying the potential road areas altogether, then it does not leave a possibility for improvement.

The pixel-based method of accuracy assessment was used for road extraction and the results are shown in Table 35.

Area	Completeness
Development Area	81.29
Test Area-1	79.45
Test Area-2	65.92

Table 35: Road Accuracy Assessment Results

7 Analysis

This chapter weighs the final results of this research against the initial objectives set in chapter 1 (section 1.6). In doing so, it also looks at the various issues that were dealt with during the course of this study. The chapter is laid out to address and analyse each objective one by one in the light of the findings. It however; does not include the last objective which is related to making relevant recommendations. The potential recommendations that have transpired out of this research and are hoped to provide useful direction to future studies in the area are presented as a separate section in the following chapter.

7.1 Devise an automatic or semi-automatic approach using a combination of classification techniques for object extraction.

The initial efforts to devise a fully automatic process during this research did not prove potentially successful or practical. It was realized that it is not possible to establish a fully automatic system for each and every involved step.

This objective of the research was therefore accomplished by developing a method which is semi-automatic in its essence and requires operator inputs. The software used and the areas requiring operator input at different stages are listed in Appendix-IV. It is not possible to set a single value for a particular parameter or classification cue owing to the heterogeneous nature of objects and characteristics of the available datasets. For example, classification of DTM from LiDAR point cloud in TerraScan requires an input parameter of maximum building size in the project area.

It is a step by step procedure and needs to be followed as such, so that a macro can be developed. These macros can be created using Definiens Ecognition or the Expert classifier and Spatial modeller in Erdas Imagine. This enables the process to be automated to a large extent requiring minimal operator inputs at only a few points.

The developed method is a combination of different classification techniques namely knowledge-based, object-oriented, pixel-based and multi-agent (to avoid strict thresholds) based modelling. If it was possible to extract all objects using one technique then off the shelf solutions could have been available however; this is not the case. Depending upon the accuracy, details and the type of object required for a particular application, a combination of different techniques is more useful.

7.2 Test the method objectively using separate test and development areas and Strive for a high degree of accuracy and robustness in the object extraction method that is verified by experiments.

The second and third objectives have been discussed together primarily because it creates a logical flow and a better understanding by addressing the two side by side. These objectives were achieved by objectively testing the developed method in two areas and following a comprehensive approach to evaluate the accuracy of the results. Three methods were used to provide full confidence over the accuracy measures for buildings. However, in the case of vegetation and roads, accuracy assessment was carried out using only one method for a number of reasons which have been explained in detail in chapter 5 (section 5.6) . The extracted objects and their accuracy assessment results using the OSI vector data as presented in the previous chapter are analysed in the following sections.

7.2.1 Building Extraction

The results of the three accuracy assessment methods are summarized in Table 36. In the area overlap method, the minimum overlap of 50% was selected as a threshold to select T_p.

High accuracy results were achieved for the developed and the Test Area-1 using the building intersection method, however; this was not the case for the Test Area-2. This is because of a large number of F_p as the method relies only on the number of objects rather than the size or comparison of individual pixels. However; the correctness value remains the same for the Test Area-2 for all methods i.e. around 70%. This is due to the non availability of the NIR band as has been discussed in the preceding chapters.

The accuracy measures obtained using the pixel-based and the area overlapping methods are close. Both pixel-based and areal overlaping methods were affected by the artifacts in the building roofs created at the time of orthophoto generation. This is because of the single available aerial strip of NIR forward looking and nadir Red images which were used to create orthophotos and subsequently for NDVI. This and the related issues affecting the quality of the orthophotos and therefore necessitating a gap filling procedure to make up for errors, have already been explained in detail in chapter 5, during building and vegetation extraction.

The combination of the thresholded NDVI and nDSM image removed most of the vegetation. This greatly helps in analyzing the shape parameters and classification cues obtained from LiDAR to separate the remaining vegetation segments.

Anisotropic classificaiton cue developed and used in this research was extremly useful in removing trees as can be seen from the results of the confidence matrix in chapter 5 (section 5.1.8) and chapter 6 (section 6.1 and 6.2). This was particularly true for the trees the classified building regions especially in the Test Area-2 where the initial classfication was poor because of the non availability of the NIR band and coarse LiDAR intensity that was used.

Errors in building boundaries also occur when converting the OSI vector data to raster image and vice versa for the extracted building regions. Therefore, the ´simplify polygon´ option was used when converting objects from raster to vector in order to avoid a zigzag pattern in the building boundaries. This caused variation in the results obtained in the area overlap method and the pixel-based method. Theoretically, both should be the same for an overlap greater than zero, however; in this case they differ by 3 to 4 percent (Table 36).

The results indicate that there is quite a large variation in the accuracy assessment, depending upon the method used. It is important to clearly explain the method and any underlying assumptions one uses to determine the accuracy measures. The pixel-based method is easier to implement and gives a quick over view of the object extraction success. The results can vary up to 30%, depending upon the method used (Rutzinger et al., 2009).

Area	Building Intersection Method			Pixel-based Method			Area Overlap Method ≥ 50%		
	Completeness	Correctness	Quality	Completeness	Correctness	Quality	Completeness	Correctness	Quality
Development Area	96.31	93.21	90.48	88.28	76.81	69.70	84.44	77.97	68.18
Test Area-1	97.26	96.91	94.34	87.65	82.52	73.92	82.83	78.67	67.64
Test Area-2	89.18	69.44	64.05	81.77	70.93	61.24	83.35	70.54	61.83

Table 36: Summary of Accuracy Assessment Results (Building Extraction)

7.2.2 Building Height

Building attribute i.e. height is of utmost importance for noise modelling and extracted height is compared with that measured during the ground truth survey as has already been shown in Table 32 and Table 33 for the development and Test Area-2 respectively.

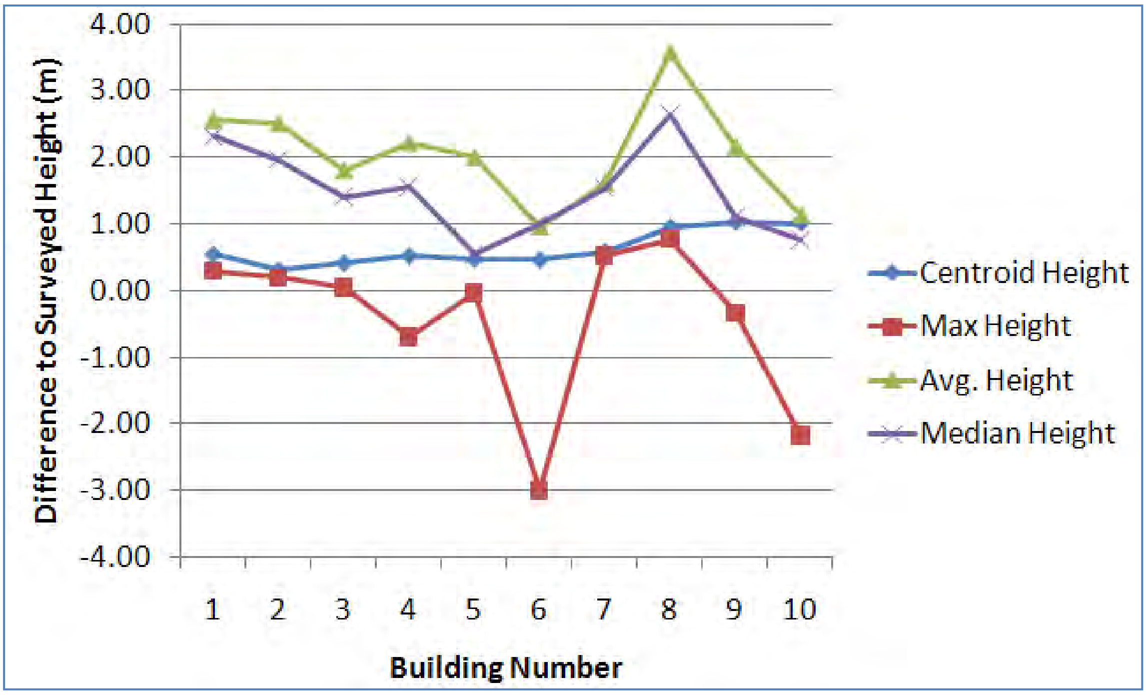

Figure 107: Height Difference with Reference to Surveyed Height (Development Area)

Overall, the building heights are determined within the permissible limit of noise mapping which is 1m (as per the guidelines provided by the European Working Group) by considering the centroid height. This can be seen from the blue line labelled centroid height in which stays in the permissible range for all the plotted buildings.

Figure 107 and Figure 108 shows the difference between the estimated heights using nDSM and the measured heights for each building. The maximum height value is very close to the height at the centroid of the polygon. However; this is not applicable to those buildings which are very close to the trees or in case of trees overarching a portion of the building roofs such as buildings 6 and 10 (Figure 107) and building 3 (Figure 108) . The centroid represents the centre of a minimum bounding rectangle that best fits the irregular building shapes. It is quite possible that the centroid might be outside the building region in which case it will require a correction. In such a case, a spatial query provided in ArcGIS makes it possible to identify all those buildings whose centroids lie outside and to subsequently correct them.

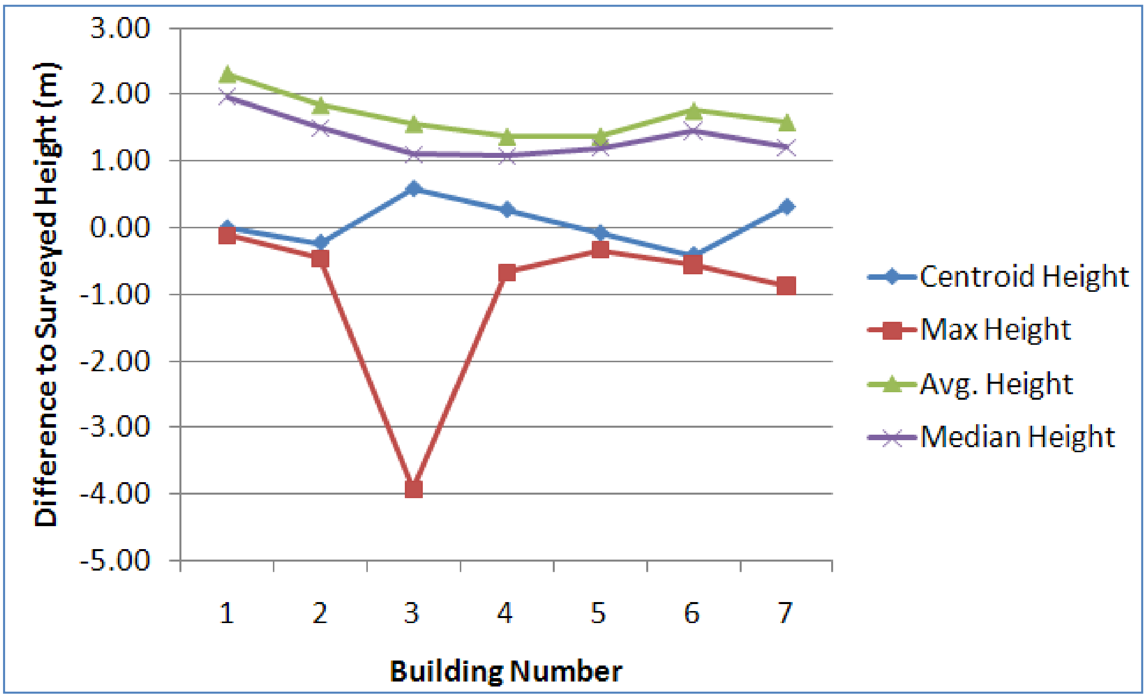

Figure 108: Height Difference with Reference to Surveyed Height (Test Area-2)

The average and median building height values have large differences with reference to the measured heights as compared to the maximum and the centroid heights. For noise modelling, it is recommended to be on the safer side by choosing those building heights which are slightly less than the actual (Avg. or Median Height) or centroid building heights.

7.2.3 Vegetation Extraction

Table 34 in the preceding chapter shows that the NDVI index was useful in separating vegetation from buildings in all areas that were part of the thresholded nDSM (≥ 2.5 m). This raises the question, why the accuracy of the results for building extraction was lower, had all the vegetation been separated successfully? This has been addressed in the following lines.

Only two to three percent of the extracted vegetation lies over the OSI building vectors, which suggests that most of the errors that occurred in building extraction were not because of trees but because of the wrongly classified pixels around the building edges. This could be because of two reasons:

1. Thresholding of the NDVI image
2. The quality of the orthophotos

The factors affecting the quality of orthophotos have been explained previously. The sections of the building roofs facing the sun have a different NDVI as compared to those under shadow as shown in Figure 109. This might result in some parts of the buildings being classified as vegetation. The thresholding of the NDVI image is a critical step in the developed method and necessary to achieve good results. That is the reason behind evaluating different methods. However; it is important to know that the thresholding criteria can vary with the content of the scene and flight characteristics.

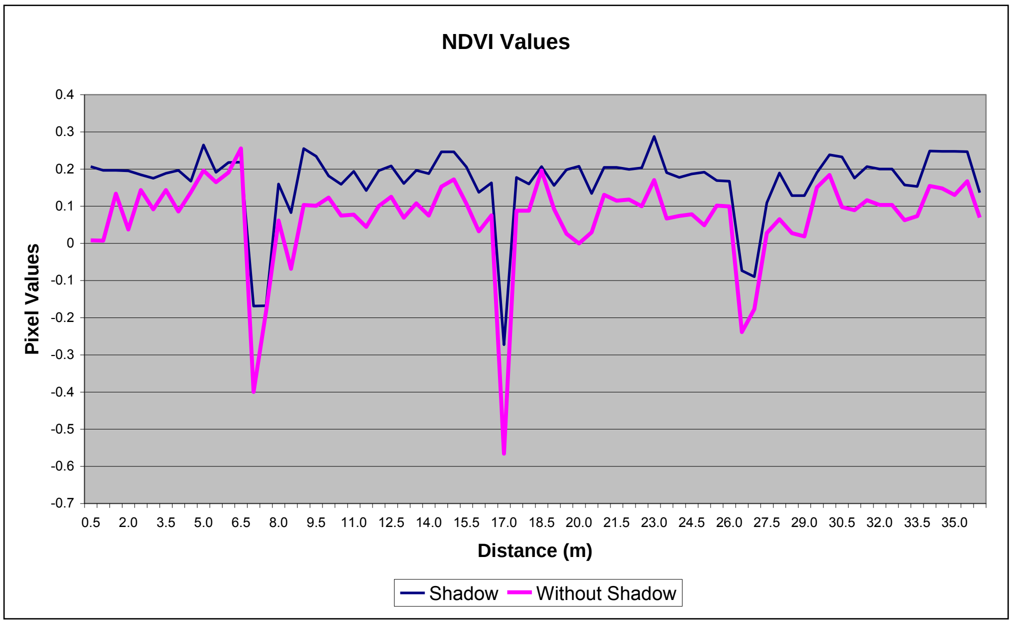

Figure 109: NDVI Thresholding

7.2.4 Road Extraction

A completeness value of approximately 80% was achieved using the developed method for the development and the Test Area-1 but not for the Test Area-2 (Table 35). The completeness is 65% for the Test Area-2 and this is attributed to the large number of trees overarching small roads in the towns of Maynooth and Leixlip and the road connecting them. In the developed method, LiDAR intensity information was used to separate these segments but for the Test Area-2 it was also used for NDVI calculation.

A high completeness value suggests that most of the roads were identified successfully. The correctness value is low because of parking lots, drive ways, footpaths and other surfaces which are not regarded as roads and were not part of the used reference data.

7.3 Evaluate factors influencing the performance of the method such as:

a. Optimal classification parameters for buildings, trees, vegetation and road classification.

b. Registration issues between LiDAR and aerial images for better fusion.

c. Performance of different object extraction softwares such as Terra Solid, Erdas Imagine, E-Cognition, LiDAR Analyst available for processing LiDAR and aerial images with respect to the effective fusion of data and quality of the results.

(a) The NDVI is very helpful in the initial separation of buildings and vegetation segments, however; some vegetation is classified as buildings and vice versa. This was corrected later using shape parameters and classification cues obtained from LiDAR. It is difficult to select one particular set of classification cues. Additional cues can also be used such as Gaussian and mean curvature, fitting plane to LiDAR point and the difference between the first pulse and the last pulse depending upon the density and characteristics of the used LiDAR sensor. However; the main issue is related to how these should be grouped together for extracting a particular object of interest.

(b) The registration of LiDAR and aerial images is important. In this research the DSM was used twice. Firstly, for orthophoto generation and secondly, for fusing nDSM with NDVI. To resolve the registration issue between LiDAR and the aerial images, a new method was developed. This method is applicable to line scanning and other image capturing sensors and the results are shown in chapter 4 (section 4.7) for the data used in this research and that of the EuroSDR project.

Figure 110 and Figure 111 show the planimetric and rotational accuracy of the developed registration method respectively for the EuroSDR project in comparison with contributions from other project partners against the reference data (TLS).

The developed method of transformation was based on the common points matched between the two DSMs i.e. the LiDAR DSM and the DSM from aerial images (using image matching techniques), each of which had a resolution of 0.5 m. The RMSE for transformation on matched points was of the order of 0.3 m. Therefore, the results indicated in the preliminary report are consistent with this (0.2 m).

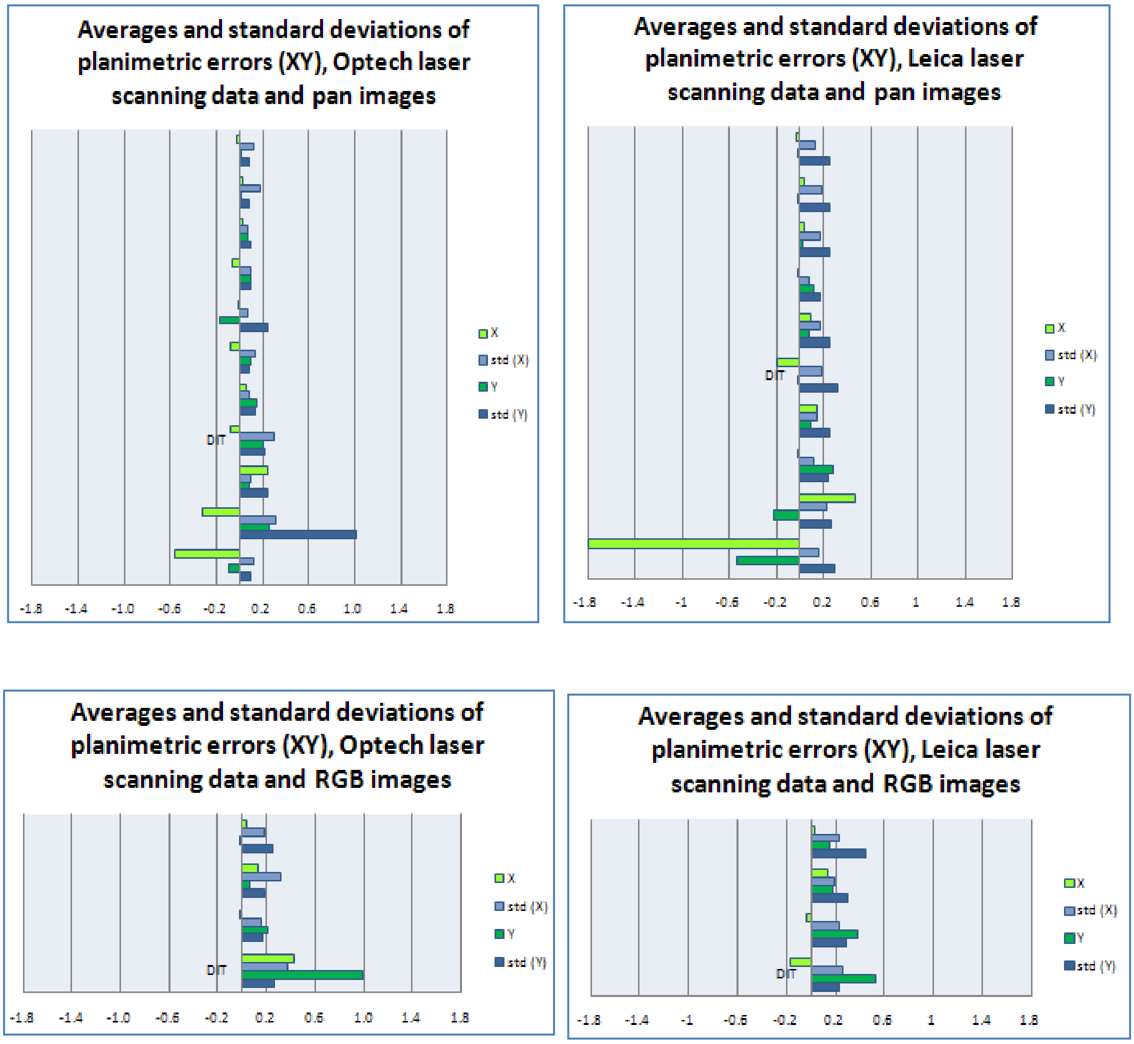

Figure 110: Planimetric Accuracy of the Developed Method for Registration

The correction values were also determined for the development and the Test Area-1 (chapter 4, section 4.7.2). The determined X mean shift (-0.80 m) for the development area was more than the pixel size of the used DSMs for registration. The registration accuracy of the developed method is in the range of ± 0.20 and ± 0.30 m. The determined transformation parameters were applied to correct the DSM from LiDAR, although the determined change in the shift values was very small.

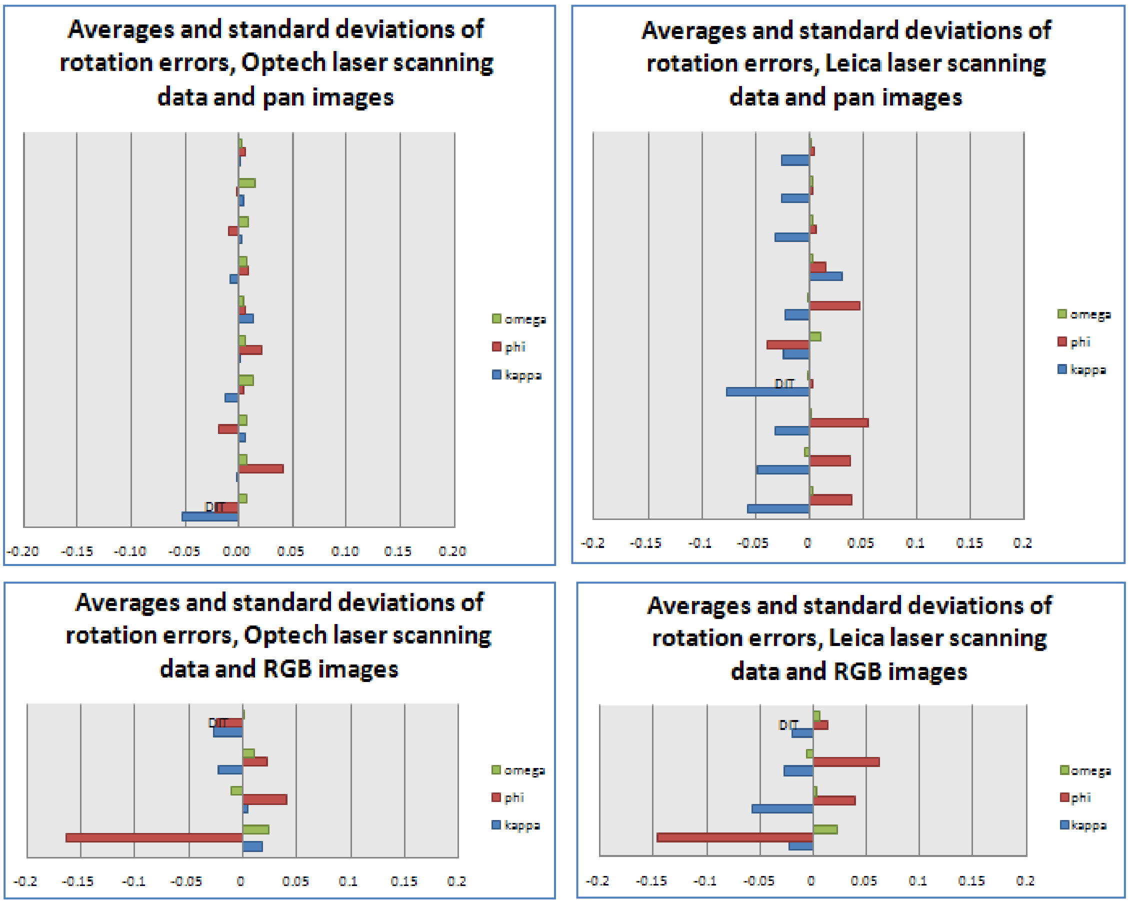

Figure 111: Rotation Accuracy of the Developed Method for Registration

(c) Till today, there is no single technique or software available that can extract objects of interest with highest accuracy and robustness. The softwares used in this research are listed in Appendix-IV and suggest that no single software is capable of performing all steps even semi-automatically. For example, the softwares used for image processing cannot handle LiDAR point cloud as efficiently as can be done using specialist software such as Terrasolid.

Terrasolid and LiDAR analyst extension of ArcGIS have the capability to extract DTM, buildings and trees only from LiDAR data. However; these results vary a lot because of the LiDAR density. For extracting building planes, the minimum required density is 4 points/m^2 (Fritsch, 2010).

Terrasolid and LiDAR analyst were tested with high density LiDAR data (16 points/m^2) from FLI-MAP corridor mapping system in the initial stages of this research. The purpose was to check the quality and automation of these specialist softwares. In Terrasolid, building roofs can be modelled semi-automatically by selecting LiDAR points that belong to the building roofs allowing the software to fit planes to these points. Operator intervention is required to remove wrongly detected planes or adjusting plane boundaries. If building foot prints are available then the step of roof points´ selection is eliminated.

Figure 112 shows a few buildings with LoD 2 (Level of Detail 2) according to OGC standard using high density LiDAR data. Such a detailed roof model is not a requirement of noise modelling and additionally, high density LiDAR data is expensive to acquire for 4,000 km of roads, 500 m on either side as per the requirement of noise modelling. Moreover, specialist routines are still not available to extract each object of interest automatically.

Figure 113 and Figure 114 show buildings, trees and forest patches` extraction using the same high density FLI-MAP data by LiDAR analyst, but tree clusters were still extracted as buildings. The results have not been analysed quantitatively because of the non availability of such data over a longer road stretch also covering the required area of interest on both sides of the road.

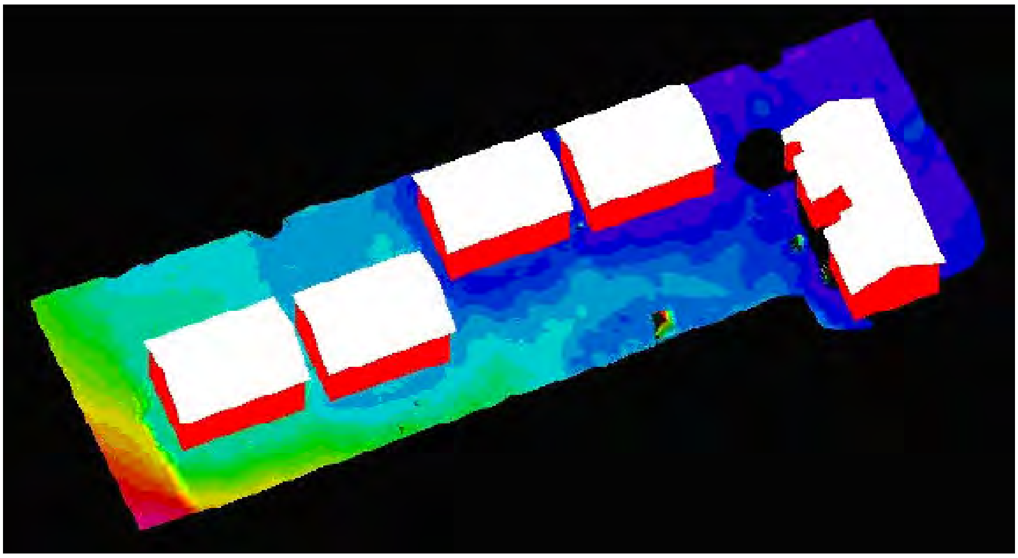

Figure 112: Building Roof Modelling in Terrasolid (Terrasolid)

Figure 113: Building Boundary Extraction Using LiDAR Analyst

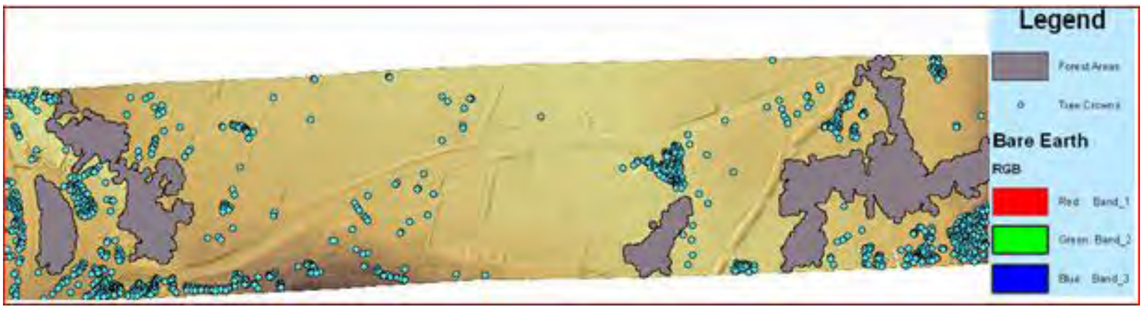

Figure 114: Tree and Forest Extraction Using LiDAR Analyst

Objective, an extension available in Erdas Imagine for object oriented analysis uses supervised or unsupervised classification to identify the initial object segments. After converting these to vector, it further classifies them into other objects of interest. However; object oriented analysis requires operator knowledge of the area, limiting its applicability for full automation. Apart from the height information, other object geometric attributes that can be derived from LiDAR data require new modules to be created in Erdas Imagine or E-Cognition. In this research, these attributes were mostly determined in MATLAB and were incorporated in these image processing softwares to improve object classification. This presents a potentially important hindrance in the fusion of LiDAR and aerial images.

7.4 Explore the potential of high density image matching for the generation of point clouds as an alternative to LiDAR.

Direct georeferencing quality of ADS40 sensor data was evaluated using GCPs and the results are presented in chapter 4 (section 4.4). These suggest its applicability to projects with planimetric accuracy requirement of ± 0.3 m and vertical accuracy of ± 0.5 m. However; the accuracy can be further improved by aerial triangulation even if 4 or 8 GCPs are available.

The quality of DSM obtained using image matching techniques is dependent upon the software used. Match-T and LPS were used for DSM generation and their vertical quality was accessed using GCPs along with the DSM from LiDAR (chapter 4, section 4.6). The vertical accuracy of DSMs from image matching is comparable to LiDAR DSM but the quality is poor (LPS), especially over the trees, buildings and regions that are under shadow or are occluded. The quantitative analysis (chapter 4, section 4.5) was performed using the simple difference between LiDAR DSM and image DSMs to find the percentage of points which are in the range of 1m to LiDAR DSM. This suggested the superiority of Match-T software over LPS. Building shape and height are an important component of noise model and quality of LiDAR DSM is better than the DSMs generated from image matching. However; DSM generated from image matching is good for DTM extraction in which objects above ground are filtered out.

Recently, EuroSDR has started a project "Benchmarking of image matching approaches for DSM computation" which suggests the importance of DSM generated by image matching rather than using another sensor data for its acquisition. The benchmarking study aims at highlighting the pros and cons of the considered image matching techniques. This will help in better understanding of the potential application ranges of these techniques.

The German society of photogrammetry, remote sensing and Geoinformation (DGPF) also initiated a research project to analyse the performance of new photogrammetric digital airborne cameras for generating DSM and subsequently DTM using image matching (Haala, 2009). The results were promising but require multiple overlapping images. This makes it unsuitable for noise modelling where roads and their environment (500 m) are of major interest. Instead of capturing multiple overlapping images, fusion of LiDAR and aerial images available from the OSI is a good alternative.

7.5 *Explore the potential of incorporating MLS data in the extraction process, particularly in relation to the detection of noise barriers.*

Noise barriers are purposely constructed close to the roads for sound dampening. No purpose built noise barrier exists in the project areas. Walls may also be considered as noise barriers as they also have a significant impact on noise propagation. The thickness of outer boundary walls is generally 45 cm which is much higher than the noise barrier (15 cm). No walls were detected because of the low resolution of LiDAR data and subsequently generated orthophotos (50 cm) which makes it difficult to extract such structures. The minimum required resolution to detect these walls is 8 points/m^2 (O'Neill, 2009).

A vertical wall was extracted in the Test Area-2 using MLS data even when arched by trees and covered with vines using the method explained in chapter 5 (section 5.5). This suggests the applicability of MLS to extract objects in road environment that are difficult or impossible through airborne sensor data.

The developed method is only applicable in situations where walls and barriers are parallel, have a uniform intensity and are of a certain height. If any of these classification cues vary the weighted PCA as suggested in the chapter 5 (section 5.5) should be employed as an alternative to achieve better results.

7.6 *Devise and evaluate a method for detecting changes in roadside objects.*

Three possible methods to update the noise model every five years are explained below. All three methods have the potential to identify the regions where changes have occurred depending upon the type of data available. Unfortunately, for both project areas, the aerial data acquired at different times was not available to check the stated methods.

7.6.1 DSM Difference

Changes can occur because of vegetation growth, new or demolished buildings and due to changes in the terrain because of new roads. A simple difference between the two DSMs from LiDAR at different times can highlight the changes. No such temporal LiDAR data was available for the development and the test areas and it was therefore decided to create an artificial one. Four buildings that exist in the development area were deleted from the DSM (Figure 115 (a)) and the difference between the original and the altered DSM highlighted the changes (Figure 115 (b)).

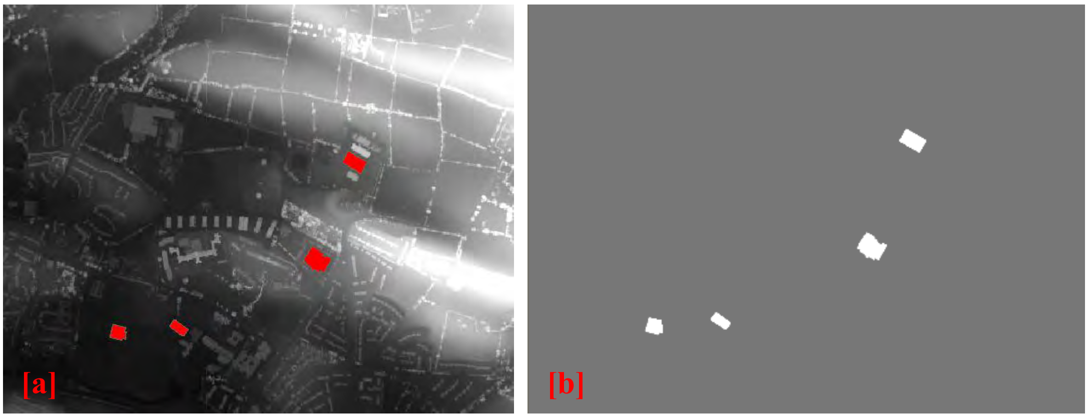

Figure 115: Simple Difference between Temporal DSMs for Change Detection

7.6.2 Cross Correlation

Cross correlation was used to determine changes in the two DSMs (original and altered) created for the first method.

$$Cov_{ij} = \frac{\sum_{k=1}^{N}(Z_{ik} - \mu_i)(Z_{jk} - \mu_j)}{N - 1}$$

$$Corr_{ij} = \frac{Cov_{ij}}{\delta_i \delta_j}$$

Where,

Z - value of a cell

i,j – are the two DSMs

μ- is the mean in a window of 3*3

N- is the number of cells (9)

k - denotes a particular cell

δ_i and δ_j are standard deviations in a window of 3*3

Mean and standard deviation were determined in the two DSMs for each pixel by convolution using a 3*3 matrix and the result is shown in Figure 116.

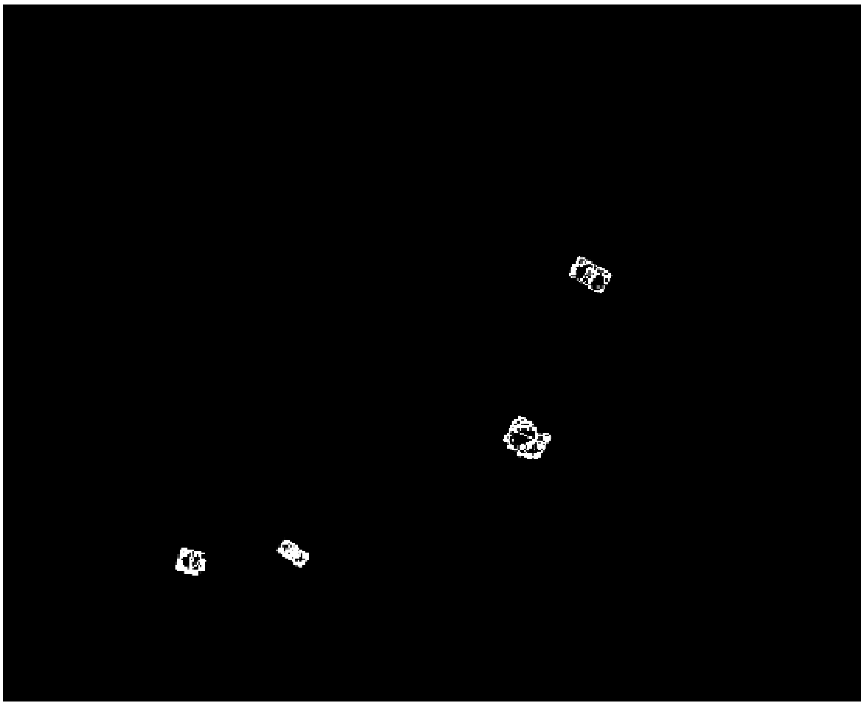

Figure 116: Change Detection using Cross Correlation

7.6.3 Using Vector Data

Instead of DSMs, this method used the extracted and the reference objects. The available OSI data corresponds to the year 2009 and the images and LiDAR data were captured in early 2007. Any changes that might have occurred during this time are updated in the OSI data but not in the objects extracted using the developed method.

The area overlap method used for accuracy assessment was used again for change detection by calculating the percentage overlap. If the buildings in the OSI data do not overlap the extracted buildings, the overlap value is zero, highlighting potential changes. Depending upon the percentage overlap, different classes can be made. For example new buildings, partially changed and demolished buildings (where an extracted building does not overlap any OSI building, then it might have been demolished).

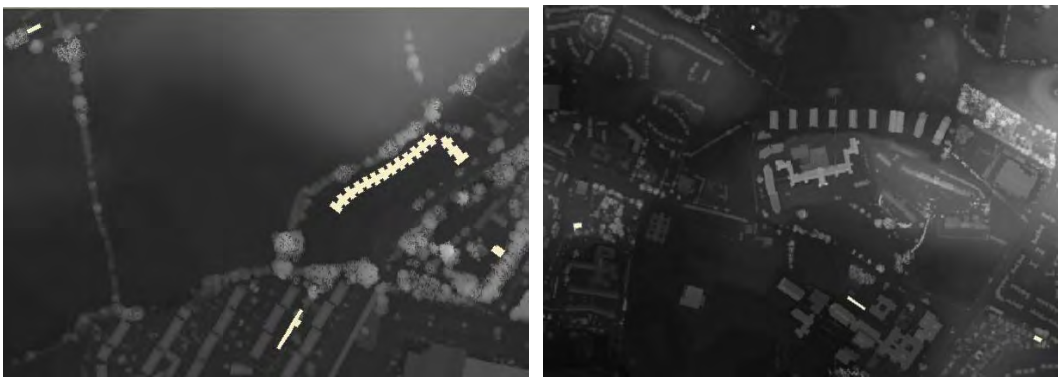

Figure 117: Change Detection using Area Overlap Method (New buildings in off-white colour)

A simple difference between two DSMs acquired at different times can identify the pixels where changes have occurred. However; it needs further investigation to identify those segments where changes have occurred in the buildings and not in the vegetation.

The cross correlation method requires temporal images. The objects classified in one dataset can then be compared with the other unclassified data. This eliminates the whole exercise of object extraction a second time. However; the change detection accuracy depends upon the accuracy of the previous classification.

The area overlap method of building change detection is appropriate where vector data is available from another source or extracted from the newly acquired dataset to identify changes. The newly acquired dataset should be of better or at least comparable quality to extract desired objects and later used for change detection.

The mentioned change detection techniques can guide the operator to those regions where changes are significant to make the data updating process faster and economical as concluded in the EuroSDR project (Champion and Everaerts, 2009).

8 Conclusion and Recommendations

The previous chapter analyzed the findings of this research in context of the set objectives. This chapter provides an overall conclusion of the study by highlighting the principal findings, discussing some limitations and providing potential recommendations for future research.

8.1 Conclusions

In order to provide an overall conclusion to this study, it makes sense to look at what has been achieved in context of the initial aims as were set in chapter 1 (section 1.5). The principal overarching aim of this research was to devise a method with a high degree of automation for the extraction of features and objects that are crucial to noise modelling. This research presented a semi automatic method for doing so that is based on a series of recommended steps which need to be followed as such for achieving optimal results. The reasons behind not pursuing a fully automatic approach beyond a certain point in this research are described in detail in chapter 7 (4^{th} objective). A related aim of this research was to make use of nationally available datasets so that a practical and an economical solution may be worked out. The datasets used in this study were provided by the OSI. The research aims also involved developing the said method in context of the spatial needs of the NRA which are detailed in chapter 1 (section 1.2). This research addresses these needs by proposing a developed method which provides information about the ground surface type, building heights and extents, vegetation and noise barriers in specific context of the requirements of the European Working Group.

Specific conclusions pertaining to this study are described in the following paragraphs.

High spatial and radiometric resolution of the multi-spectral images captured using ADS40 sensor was found to be insufficient on its own for urban classification. This was due to the uncertainty in discriminating between trees and grass, misclassification of buildings caused by diverse roof compositions, shadow effects and their spectral resemblance with roads and difficulty in distinguishing cars on the roads. Classification accuracy was not satisfactory even after the incorporation of NIR band for vegetation separation. Object height obtained from LiDAR nDSM and objects´ geometric attributes significantly improved the accuracy of the extraction process and estimation of building heights when fused with aerial images. Using available low density LiDAR data alone for object classification also proved unsuccessful in discriminating trees from buildings.

This research has simultaneously utilized knowledge, pixel and object-based classification techniques for object extraction. Using any of these techniques on its own will not have generated results to the desired level of accuracy.

The developed method is semi-automatic, however; the statistical methods used for thresholding can guide the operator to their appropriate values depending upon the project area.

Classification cues can vary depending upon the type and nature of data. For example, high density Optech sensor data provides two range images i.e. the first and the last pulse. The difference between these two range images can eliminate most of the vegetation as it can record large differences compared to buildings. Moreover, the plane fitting to LiDAR data can also be tested to filter out any remaining vegetation.

Proper registration of LiDAR and aerial images is a pre-requisite for the fusion of two datasets. In this research, it is crucial for generating orthophotos. The method used to ensure their proper registration provided results within the acceptable tolerances required for noise mapping as verified in the EuroSDR project and also by the ground truth surveys.

Creation of true orthophoto requires multiple overlaps and is not a viable option for NRA. However; in the ROI, buildings are also not high and the errors mostly occur at strip edges which might be beyond the noise mapping border, if aerial images are acquired specifically for the roads. Accuracy could have been better if true orthophotos were available.

Only buildings of size greater than or equal to 30 m^2 were considered in this study for the extraction because of certain reasons which are explained further. A size threshold is required to separate small identified building regions. These mostly occur because of temporary structures in the fields or small huts behind main buildings in the back yards. Such small regions can also occur because of previously mentioned reasons i.e. non availability of nadir NIR band and multiple overlapping images for orthophoto generation. Trees without leaves are also a source of possible noise. That is why classification cues obtained from LiDAR and geometric attributes were unable to separate these regions from buildings. However; accuracy of building extraction increases considerably by increasing the size threshold (Rutzinger et al., 2009). Most building extraction algorithms consider buildings which are greater than 30 m^2 (Rottensteiner et al., 2007). In noise modelling, buildings of all sizes should be incorporated to generate an accurate noise model. Considering buildings greater than 30 m^2 might result in an error of 1 to 3db in the estimated noise values (WG-AEN, 2006).

Noise barriers are not extractable from the available airborne sensor data. They were initially visible in the aerial images but not anymore after orthophoto generation having a spatial resolution of 0.5 m. The developed method for noise barrier extraction using MLS data has proven MLS potential for road side asset management and geometric modelling. This is because of different objects` representation and high density point cloud, not achievable using currently available airborne LiDAR sensors on a routine basis.

A new operator with a basic knowledge of remote sensing can be trained in a relatively short time to implement the developed method. The determination of the NDVI and classification cue thresholding as suggested in this research requires experience. However, this can be acquired in handful projects of similar nature. This applies to nearly every image classification software.

8.2 Innovation in the Proposed Method

A number of innovative aspects of this research are described as follows.

1. The utilization of airborne line scanner data (ADS40) and its fusion with LiDAR (ALS50-II) data for object extraction is not common. Most of the past international research has used digital frame cameras and Optech LiDAR sensor data.
2. Methodology development, implementation and testing were focused on a real-world application meeting specific needs of the NRA using only nationally available data sets. To the best knowledge of the researches, this study is the first of its kind in the ROI from the perspective of utilizing the available airborne sensor data and investigating its usefulness in terms of object extraction for noise modelling. Most international tests have focused on single object extraction e.g. roads, buildings or vegetation as mentioned in the literature review in the respective sections. Developed method is unique in extracting all three together and

with a specific end use in mind. The developed method is also not restricted to the ROI and noise modelling. It can be used for object classification using different sensors' data but the results might vary up to 30%. This is because of different sensors' specifications and flight characteristics used for acquiring LiDAR and aerial images.

3. The utilization of multiple echoes to improve building and tree classification.
4. Resolving registration problems between LiDAR and aerial images. A methodology has been developed for checking their co-registration and, where an anomaly exists, how it can be rectified. The developed method is applicable to line scanning and digital frame cameras. The method performs well compared to other methods used in Europe and is uniquely the only one to use the developed approach.
5. Accuracy assessment of DSMs generated using LiDAR and stereoscopic image matching techniques available in LPS and Match-T softwares using independent ground control points. This was done to check which one is superior and should be used for orthophoto generation and noise modelling.
6. The integration of MLS with airborne sensor data for the detection of noise barriers.
7. Providing potential solutions for updating noise models using change detection methods.

8.3 Recommendations

The final objective of this research is addressed in this section. The final objective was:

Make recommendations for the best application of airborne and MLS based sensor data and existing GIS data to noise modelling in the environment of Irish roads

It has been found out during the research that NIR band is not a part of the data processing chain of OSI and also not been archived. That is why no NIR data was available for the Test Area-2. However, the data has been downloaded and processed for the development and Test Area-1 upon request. NIR band has proven its potential in object classification, vegetation studies and should be at least archived for its potential usage in studies requiring temporal data.

If possible, simultaneous capturing of aerial images and LiDAR data should be preferred over separate acquisition or otherwise with minimum possible gap. Depending upon the type of objects to be extracted, data should be captured during such time of the day and year when maximum classification cues can be determined. For example, if roads are the object of interest then the LiDAR data should be captured at night, when there is minimum traffic on road and in late autumn or early spring, when trees are without leaves. This results in maximum reflections from ground. However, multispectral images cannot be captured at night and if required to be acquired separately from LiDAR, then the latter should be captured at night.

NRA Ireland is currently acquiring LiDAR data for roads with a minimum point density of 2 points/m^2. However, OSI is acquiring data with an intention to develop DTM with a resolution of 2 m accurate to 25 cm for urban areas and 5 to 10 m resolution for rural areas accurate to 50 cm. Integrating newly acquired LiDAR data from NRA will potentially improve the accuracy of the developed classification method.

Most LiDAR sensors are capable of capturing the intensity of the returned pulse which is in the near infra red range. This information is useful in separating different ground types i.e. bare earth, road, ploughed surface and cobble stone roads etc. when used alone or in combination with multi-spectral images. A project is ongoing in EuroSDR to develop a feasible, cost-effective technique for intensity calibration. The outcome of this project should be incorporated for the improvement of the object classification results, especially for the extraction of roads from LiDAR data which is still in its infancy (Shan and Toth, 2008).

Customization of available spatial data processing softwares is required to develop a system where new classification cues can be integrated and used for robust object extraction. This would be a leap forward towards the automation of the whole process.

References

Ahokas, E., Kaasalainen, S., Hyypp, J. and Suomlainen, J. (2006). Calibration of the Optech ALTM-3100 laser scanner intensity data using brightness targets. Marne-la-Vallee, France, In: The International Archives of the Photogrammetry, Remote Sensing and Spatial Information Sciences. Vol. 36, Part A1**:** 7.

Arefi, H. (2009). From LiDAR Point Clouds to 3D Building Models. Institut für Angewandte Informatik. München, Universität der Bundeswehr München. PhD.

Arefi, H. and Hahn, M. (2005). A morphological reconstruction algorithm for separating off-terrain points from terrain points in laser scanning data. Proceedings of the ISPRS Workshop "Laser scanning 2005", Enschede, the Netherlands.

Arefi, H., Hahn, M., Lindenberger, J. and TopScan, S. (2003). LIDAR data classification with remote sensing tools. ISPRS Joint Workshop on Challenges in Geospatial Analysis, Integration and Visualization II, Stuttgart, Germany 131–136.

Axelsson, P. (1999). Processing of laser scanner data--algorithms and applications. ISPRS Journal of Photogrammetry and Remote Sensing, 54(2-3): 138-147.

Baltsavias, E. P. (1999). A comparison between photogrammetry and laser scanning. ISPRS Journal of Photogrammetry and Remote Sensing, 54(2-3): 83-94.

Baltsavias, P. E. and Gruen, A. (2003). A comparison of aerial photos, LIDAR and IKONOS for monitoring cities. Remotely Sensed Cities, Taylor & Francis, London, 47-84.

Barber, D., Mills, J. and Smith-Voysey, S. (2008). Geometric validation of a ground-based mobile laser scanning system. ISPRS Journal of Photogrammetry and Remote Sensing, 63(1): 128-141.

Bartels, M. and Wei, H. (2006). Maximum Likelihood Classification of LIDAR Data incorporating multiple co-registered Bands. 4th International Workshop on Pattern Recognition in Remote Sensing in conjunction with the 18th International Conference on Pattern Recognition, Hong Kong: 17-20.

Bartels, M., Wei, H., Mason, D. C., Building, H. P. and Gate, E. (2006). DTM generation from LIDAR data using skewness balancing. 18th International Conference on Pattern Recognition, Hong Kong: 566–569.

Baumgartner, A., Hinz, S. and Wiedemann, C. (2002). Efficient methods and interfaces for road tracking. International Archives of Photogrammetry, Remote Sensing and Spatial Information Sciences,34: 28-31.

Besl, P. J. and Jain, R. C. (1988). Segmentation through variable-order surface fitting. Pattern Analysis and Machine Intelligence, IEEE Transactions on, 10(2): 167-192.

Beyer, H. L. (2004). Hawth's Analysis Tools for ArcGIS. Retrieved 25th July, 2010, from http://www.spatialecology.com/htools.

Bray, C. (2004). GPS „Network RTK' Solution for Ireland. GPS Positioning Infrastructure Retrieved 8th March, 2010, from www.fig.net/pub/cairo/papers/ts_08/ts08_01_craenenbroeck.pdf.

Brenner, C. (2005). Building Reconstruction from Images and Laser Scanning. International Journal of Applied Earth Observation and Geoinformation, 6: pp. 187-198.

Brenner, C. (2009). Extraction of features from mobile laser scanning data for future driver assistance systems. Advances in GIScience: 25-42.

Brügelmann, R. (2000). Automatic breakline detection from airborne laser range data. International Archives of Photogrammetry, Remote Sensing and Spatial Information Sciences, Amsterdam, The Netherlands, Vol. XXXIII, Part B3.: pp.109-116.

Brunn, A. (2001). Statistical interpretation of DEM and image data for building extraction. Automatic Extraction of Man-Made Objects from Aerial and Space Images (III),B. e. al.(eds), Monte Verita, Switzerland: 171–180.

Brunn, A. and Weidner, U. (1997). Extracting Buildings From Digital Surface Models. International Archives of Photogrammetry and Remote Sensing, Vol. XXXII(3–4W2)(27).

Champion, N. and Everaerts, J. (2009). The Euro SDR Test "Detection of unregistered buildings for updating 2D databases". European Spatial Data Research Official Publication Number 56: 9-40.

Champion, N., Rottensteiner, F., Matikainen, L., Liang, X., Hyyppä, J. and Olsen, B. P., Eds. (2009). A test of automatic change detection approaches. CMRT09. IAPRS. Paris, France.

Chen, Y., Su, W., Li, J. and Sun, Z. (2009). Hierarchical object oriented classification using very high resolution imagery and LIDAR data over urban areas. Advances in Space Research, 43(7): 1101-1110.

Clode, Simon, Rottensteiner, Franz, Kootsookos, Peter, Zelniker and Emanuel (2007). Detection and vectorization of roads from lidar dataBethesda, MD, ETATS-UNIS, American Society for Photogrammetry and Remote Sensing, 19.

Cramer, M. and Haala, N. (2009). DGPF-Project: Evaluation of digital Photogrammetric aerial based imaging systems – Overview and results from pilot center. ISPRS Workshop on High Resolution Earth Imaging for Geospatial Information, Leibniz Universität Hannover: digitally published on CD, 8 pages.

Eckert, S. and Hollands, T. (2010). Comparison of Automatic DSM Generation Modules by Processing IKONOS Stereo Data of an Urban Area. Selected Topics in Applied Earth Observations and Remote Sensing, IEEE Journal of, 3(2): 162-167.

ESRI. (2007). Normal QQ plot and general QQ plot. Retrieved 24 March, 2010, from http://webhelp.esri.com/arcgisdesktop/9.2/index.cfm?id=3286&pid=3279&topicname=Normal_QQ_plot_and_general_QQ_plot.

Europa. (2010). Transport- Looking for Sustainable Mobility. Retrieved 30 July 2010, from http://europa.eu/pol/trans/index_en.htm.

European Parliament, C. (2002). Deadlines relating to the Implementation of the Directive 2002/49/EC. from http://ec.europa.eu/environment/noise/pdf/deadlines_d2002_49.pdf.

European Parliament, C. (2002). Directive 2002/49/EC of the European Parliament and of the Council of 25 June 2002 relating to the assessment and management of environmental noise - Declaration by the Commission in the Conciliation Committee on the Directive relating to the assessment and management of environmental noise. Retrieved 11 April 2010, from http://ec.europa.eu/environment/noise/directive.htm.

EuroSDR. (2010). Radiometric Calibration of ALS Intensity Retrieved 16 April, 2010, from http://bono.hostireland.com/~eurosdr/start/index.php?option=com_content&task=view&id=35&Itemid=50.

Fischer, A., Kolbe, T. H., Lang, F., Cremers, A. B., Förstner, W., Plümer, L. and Steinhage, V. (1998). Extracting Buildings from Aerial Images Using Hierarchical Aggregation in 2D and 3D. Computer Vision and Image Understanding, 72(2): 185-203.

Forlani, G., Nardinocchi, C., Scaioni, M. and Zingaretti, P. (2006). Complete classification of raw LIDAR data and 3D reconstruction of buildings. Pattern Analysis & Applications, 8(4): 357-374.

Fortier, M., Ziou, D., Armenakis, C. and Wang, S. (1999). Survey of work on road extraction in aerial and satellite images. Center for Topographic Information Geomatics, Ontario, Canada. Technical Report, 241.

Fradkin, M., Maitre, H. and Roux, M. (2001). Building detection from multiple aerial images in dense urban areas. Computer Vision and Image Understanding, 82(3): 181-207.

Fricker, P. (2007). Raising the bar for milti-band, high resolution airborne imagery. Photogrammetric Week '07,D. E. Fritsh, Wichmann Verlag: 71-79.

Fricker, P., Sandau, R. and Walker, A. S. (1999). Digital photogrammetric cameras: possibilities and problems. In Photogrammetric Week '99,D. Fritsch, Spiller, R., Eds.;, Wichmann Verlag: 71-82.

Fritsch, D. (2010). Generation and Processing of 3D Topographic Landscape Models. 3D Digital Landscape Models - From 2D cartographic to 3D topographic data, Dublin, Ireland.

Fugro. (2010). FLI-MAP 400. Retrieved 16 April, 2010, from http://www.flimap.com/site47.php.

Gehrke, S., Morin, K., Downey, M., Boehrer, N. and Fuchs, T. (2008). Semi-Global Matching: An Alternative to LiDAR for DSM Generation. International Archives of Photogrammetry and Remote Sensing,XXXVIII, Part 1.

Geosystems, L. (2007). Leica ADS40 2nd Generation Airborne Digital Sensor. Retrieved 21 July, 2010, from http://nasher-eng.com/Products%20files/Geospatial%20Imaging/Airborne%20Sensors/ADS40_2ndGeneration_datasheet.pdf.

Geosystems, L. (2007). Leica ALS50-II Airborne Laser Scanner Product Specifications. Retrieved 18 July 2010, 2010, from http://www.aoc.co.za/resources/pdf/products/airborne_LiDAR/als50-ii.pdf.

Geosystems, L. (2010). Leica ADS80 Airborne Digital Sensor. Retrieved 11 July, 2010, from http://www.leica-geosystems.us/en/Leica-ADS80-Airborne-Digital-Sensor_57627.htm.

Gerke, M. (2006). Automatic Quality Assessment of Road Databases using Remotely Sensed Imagery. Hannover, Deutsche Geodätische Kommission bei der Bayerischen. PhD. Dissertation.

Gonzalez, R. C., Woods, R. E. and Eddins, S. L. (2004). Digital Image processing using MATLABUpper Saddle River, N.J., Pearson Prentice Hall, xiv, 609 p.

Gorte, B. (1999). Supervised image classification; Spatial Statistics for Remote Sensing;.Remote Sensing and Digital Image Processing, Springer Netherlands, 153-163.

Haala, N. (2009). Comeback of Digital Image Matching. In Photogrammetric Week '09, Wichmann Verlag.

Haala, N. and Brenner, C. (1999). Extraction of buildings and trees in urban environments. ISPRS Journal of Photogrammetry and Remote Sensing, 54(2-3): 130-137.

Habib, A., Ghanma, M. and Mitishita, E. (2004). Co-registration of photogrammetric and LIDAR data: Methodology and case study. Revista Brasileira de Cartografia, 56(1): 1-13.

Habib, A. and Schenk, T. (1999). A new approach for matching surfaces from laser scanners and optical sensors. International Archives of Photogrammetry and Remote Sensing. 32(3 ⁄ W14)**:** 55–61.

Hammoudi, K., Dornaika, F. and Paparoditis, N. (2009). Extracting building footprints from 3D point Clouds using terrestrial laser scanning at street level. IAPRS,CMRT09,R. F. In: Stilla U, Paparoditis N (Eds),Vol. XXXVIII, Part 3/W4, Paris, France.

Hatger, C. and Brenner, C. (2003). Extraction of road geometry parameters from laser scanning and existing databases. International Archives of the Photogrammetry, Remote Sensing and Spatial Information Sciences XXXIV (Pt. 3/W13).

Heipke, C., Mayer, H., Wiedemann, C. and Jamet, O. (1997). Evaluation of automatic road extraction. International Archives of Photogrammetry and Remote Sensing, 32(3 SECT 4W2): 151-160.

Hejmanowska, B. (1998). Removal of topographical effect from remote sensing data for thermal inertia modelling. International Archives of Photogrammetry and Remote Sensing, 32: 238-245.

Hill, R. A., Smith, G. M., Fuller, R. M. and Veitch, N. (2002). Landscape modelling using integrated airborne multi-spectral and laser scanning data. International Journal of Remote Sensing, 23(11): 2327-2334.

Hinsken, L., Miller, S., Tempelmann, U., Uebbing, R. and Walker, S. (2002). Triangulation of LH Systems' ADS40 imagery using Orima GPS/IMU. International Archive of Photogrammetry, Remote Sensing and Spatial Information Sciences, Commission III, WG III/1,Vol XXXIV Part 3A, Graz, Austria.

Hinz, A., Dörstel, C. and Heier, H. (2001). DMC - The digital senosor technology of Z/I-Imaging. In Photogrammetric Week 01',D. Fritsh and Spiller, R., Wichmann Verlag: 93-103.

Hirschmuller, H. (2005). Accurate and efficient stereo processing by semi-global matching and mutual information. Computer Vision and Pattern Recognition, 2005. CVPR 2005. IEEE Computer Society Conference on,2: 807-814 vol. 2.

Hodgson, M. E., Jensen, J. R., Tullis, J. A., Riordan, K. D. and Archer, C. M. (2003). Synergistic use of LIDAR and color aerial photography for mapping urban parcel imperviousness. Photogrammetry Engineering and Remote Sensing, 69(9): 973-980.

Höfle, B. and Pfeifer, N. (2007). Correction of laser scanning intensity data: Data and model-driven approaches. ISPRS Journal of Photogrammetry and Remote Sensing, 62(6): 415-433.

Höhle, J. and Potuckova, M. (2006). The EuroSDR Test "Checking and Improving of Digital Terrain Models". European Spatial Data Research, Official Publication Number 51: Pages 11-55.

Honkavaara, E., Arbiol, R., Markelin, L., Martinez, L., Cramer, M., Bovet, S. p., Chandelier, L., Ilves, R., Klonus, S., Marshal, P., Schläpfer, D., Tabor, M., Thom, C. and Veje, N. (2009). Digital Airborne Photogrammetry-”A New Tool for Quantitative Remote Sensing?-”A State-of-the-Art Review On Radiometric Aspects of Digital Photogrammetric Images. Remote Sensing, 1(3): 577-605.

Hu, X., Tao, C. V. and Hu, Y. (2004). Automatic road extraction from denser urban area by integrated processing of high resolution imagery and LiDAR data. ISPRS, Istanbul, Turkey.

Huertas, A., Lin, C. and Nevatia, R. (1993). Detection of buildings from monocular views of aerial scenes using perceptual organization and shadows. ARPA, Image Understanding Workshop, Washigto D.C. USA: 253-260.

Hunter, G. (2009). 3D Laser Mapping's futuristic mobile mapping GeoConnexion Retrieved 15 April, 2010, from http://www.geoconnexion.com/geouk_news_article/3D-Laser-Mappings-futuristic-mobile-mapping/5629.

ILMF. (2010). Mobile Laser Scanning. The International LiDAR 10 Mapping Forum Retrieved 15 April, 2010, from http://www.lidarmap.org/mobilemapping/.

Jenkins, J. (2006). Key Drivers in Determining LiDAR Sensor Selection. Promoting Land Administration and Good Governance, 5th FIG Regional Conference. Accra, Ghana.

Jensen, J. R. (2007). Introductory digital image processing a remote sensing perspective., Prentice Hall, USA.

Juha, M. H., Ulla, P., Hannu, H., Henrik, G. A. H. and Georg, S. R. (2000). Accuracy of laser scanning for DTM generation in forested areas,W. K. Gary, Upendra, N. S., Christian, W. and Vasyl, V. M.,4035, SPIE: 119-130.

Kaartinen, H. and Hyyppä, J. (2008). EuroSDR-Project „„Tree Extraction''. European Spatial Data Research Official Publication, Volume 53.

Kaasalainen, S., Hyyppä, J., Litkey, P., Hyyppä, H., Ahokas, E., Kukko, A. and Kaartinen, H. (2007). Radiometric calibration of ALS intensity. IAPRS Volume XXXVI, Part 3 / W52, 2007.

Kaasalainen, S., Vain, A., Krooks, A. and Kukko, A. (2009). Topographic and distance effects in laser scanner intensity correction. Laserscanning09,F. Bretar, Pierrot-Deseiligny, M. and Vosselman, G.,XXXVIII, Paris, France.

Kager, H. (2004). Discrepancies between overlapping laser scanner strips-simultaneous fitting of aerial laser scanner strips. International Archives of Photogrammetry, Remote Sensing and Spatial Information Sciences,35, B/1, Istanbul, Turkey: pp. 555-560.

Kao, D. L., Kramer, M. G., Love, A. L., Dungan, J. L. and Pang, A. T. (2005). Visualizing distributions from multi-return lidar data to understand forest structure. Cartographic Journal, The, 42(1): 35-47.

Keqi, Z., Whitman and Dean (2005). Comparison of three algorithms for filtering airborne lidar dataBethesda, MD, ETATS-UNIS, American Society for Photogrammetry and Remote Sensing, 12.

Khoshelham, K., Nardinocchi, C., Frontoni, E., Mancini, A. and Zingaretti, P. (2010). Performance evaluation of automated approaches to building detection in multi-source aerial data. ISPRS Journal of Photogrammetry and Remote Sensing, 65(1): 123-133.

Kilian, J., Haala, N. and English, M. (1996). Capture and evaluation of airborne laser scanner data. XVIIIth ISPRS Congress,IAPRS, XXXI, Part B3, Vienna, Austria,

: 383-388.

Klein, L. A. (1999). Sensor and data fusion concepts and applications, Society of Photo-Optical Instrumentation Engineers (SPIE) Bellingham, WA, USA,

Kolbe, T. H. (2008). Representing and exchanging 3D city models with CityGML; 3D Geo-Information Sciences.Lecture Notes in Geoinformation and Cartography, Springer Berlin Heidelberg, 15-31.

Kovesi, P. D. (2007). MATLAB implementation based on Peter Kovesi's anisotropic diffusion. MATLAB and Octave Functions for Computer Vision and Image Processing. Retrieved 24 March, 2010, from http://www.csse.uwa.edu.au/~pk/research/matlabfns/.

Kraus, K. and Pfeifer, N. (1998). Determination of terrain models in wooded areas with airborne laser scanner data. ISPRS Journal of Photogrammetry and Remote Sensing, 53(4): 193-203.

Kremer, J. and Hunter, G. (2007). Performance of the Streetmapper Mobile LIDAR Mapping System in „Real World' Projects. In Photogrammetric Week '07, Wichmann and Verlag: 215-225.

Kukko, A., Jaakkola, A., Lehtomaki, M., Kaartinen, H. and Chen, Y. (2009). Mobile mapping system and computing methods for modelling of road environment. Urban Remote Sensing Joint Event 1-6.

Leberl, F. and Gruber, M. (2003). Flying the new large format digital aerial camera Ultracam. Photogrammetric Week '03,D. Fritsch, Wichmann Verlag: 19-25.

Lee, T., Richards, J. A. and Swain, P. H. (1987). Probabilistic and evidential approaches for multisource data analysis. IEEE Transactions on Geoscience and Remote Sensing: 283-293.

Lemaire, C. (2008). Aspects of the DSM production with high resolution images. International Archives of the Photogrammetry, Remote Sensing and Spatial Information Sciences, 37: 1143-1146.

Lemmens, M. (2010). Georeferenced Data Products. GIM INTERNATIONAL, 24(04): 23.

Lin, C., Huertas, A. and Nevatia, R. (1994). Detection of buildings using perceptual grouping and shadows. IEEE Computer Society Conference on Computer Vision and Pattern Recognition, Proceedings CVPR '94.: 62-69.

Lu, Y. H., Trinder, J. C. and Kubik, K. (2006). Automatic building detection using the Dempster-Shafer algorithm. Photogrammetric Engineering and Remote Sensing, 72(4): 395.

Maas, H.-G. and Vosselman, G. (1999). Two algorithms for extracting building models from raw laser altimetry data. ISPRS Journal of Photogrammetry and Remote Sensing, 54(2-3): 153-163.

Madhavan, B. B., Wang, C., Tanahashi, H., Hirayu, H., Niwa, Y., Yamamoto, K., Tachibana, K. and Sasagawa, T. (2006). A computer vision based approach for 3D building modelling of airborne laser scanner DSM data. Computers, Environment and Urban Systems, 30(1): 54-77.

Mallet, C. and Bretar, F. (2009). Full-waveform topographic lidar: State-of-the-art. ISPRS Journal of Photogrammetry and Remote Sensing, 64(1): 1-16.

MathWorks. (2010). Curve Fitting Toolbox. Retrieved 9th October, 2010, from http://www.mathworks.com/help/toolbox/curvefit/bq_5ka6-1.html.

MathWorks. (2010). Morphological Reconstruction. Retrieved 11 March, 2010, from http://www.mathworks.com/access/helpdesk/help/toolbox/images/f18-16264.html.

MathWorks. (2010). Morphology Fundamentals: Dilation and Erosion. Retrieved 11 March, 2010, from http://www.mathworks.com/access/helpdesk/help/toolbox/images/f18-12508.html#f18-13322.

Matikainen, L., Hyyppä, J., Ahokas, E., Markelin, L. and Kaartinen, H. (2009). An improved approach for automatic detection of changes in buildings. Lasers scanning 2009,P.-D. M. In: Bretar F, Vosselman G (Eds),Vol. XXXVIII, Part 3/W8, Paris, France, IAPRS.

Mayer, H. (2008). Object extraction in photogrammetric computer vision. ISPRS Journal of Photogrammetry and Remote Sensing, 63(2): 213-222.

Mayer, H., Hinz, S., Bacher, U. and Baltsavias, E. (2006). A test of automatic road extraction approaches. Photogrammetric Computer Vision '06,W. Förstner and Steffen, R.,XXXVI, Bonn, Germany: 209-214.

McFeeters, G. (1996). The use of the Normalized Difference Water Index (NDWI) in the delineation of open water features. Abingdon, ROYAUME-UNI, Taylor and Francis. 17.

Mitishita, E., Habib, A., Centeno, J., Machado, A., Lay, J. and Wong, C. (2008). Photogrammetric and lidar data integration using the centroid of a rectangular roof as a control point. Photogrammetric Record, 23(121): 19.

Morgan, M. and Habib, A. (2002). Interpolation of LIDAR data and automatic building extraction. ACSM-ASPRS Annual conference proceedings, Washington, D.C. USA.

Morgan, R. and Bray, C. (2000). A new co-ordinate system for Ireland. Retrieved 13 April, 2010, from http://www.osi.ie/en/alist/osi-papers.aspx.

Muller, S. and Zaum, D. W. (2005). Robust building detection in aerial images. The International Archives of Photogrammetry, Remote Sensing, and Spatial Information Sciences, XXXVI (3/W24), Vienna, Austria.

Murakami, H., Nakagawa, K., Hasegawa, H., Shibata, T. and Iwanami, E. (1999). Change detection of buildings using an airborne laser scanner. ISPRS Journal of Photogrammetry and Remote Sensing, 54(2-3): 148-152.

Myler, H. R. and Weeks, A. R. (1993). The pocket handbook of imaging processing algorithms in CEnglewood Cliffs, N.J. London, PTR Prentice Hall; Prentice-Hall International, xi, 303 p.

Nardinocchi, C. (2001). Building detection and roof extraction in laser scanning data. Automatic extraction of man-made objects from aerial and space images (III),B. e. al.(eds), Monte Verita, Switzerland: 319.

NCG. (2008). Integration of Terrestrial and Aerial Image Mapping Systems for Noise Mapping. Retrieved 15 April, 2010, from http://ncg.nuim.ie/content/projectsold/mobilemapping/noisemapping/.

NCG. (2010). Spatially Encoded Digital Video. Retrieved 15 April, 2010, from http://ncg.nuim.ie/redir.php?action=projectsold/sedv.

Nevatia, R., Lin, C. and Huertas, A. (1997). A system for building detection from aerial images. Automatic Extraction of Man-Made Objects from Aerial and Space Images (II),E. P. Baltsavias and Henricsson, E. O., Ascona, Switzerland.

Nixon, M. S. and Aguado, A. S. (2002). Feature extraction and image processingOxford, Newnes, xii, 350 p.

NRA. (2004). Guidelines for the Treatment of Noise and Vibration in National Road Schemes. Retrieved 14 April, 2010, from http://www.nra.ie/Publications/DownloadableDocumentation/Environment/file,3482,en.PDF.

O'Neill, V. (2009). Airborne LiDAR in Ordnance Survey Ireland 3rd Annual Irish Earth Observation Symposium, Geological Survey of Ireland, Dublin.

Otsu, N. (1975). A threshold selection method from gray-level histograms. Automatica, 11: 285-296.

Perona, P. and Malik, J. (1990). Scale-space and edge detection using anisotropic diffusion. IEEE Transactions on pattern analysis and machine intelligence, 12(7): 629-639.

Pfeifer, N., Rutzinger, M., Rottensteiner, F., Muecke, W. and Hollaus, M. (2007). Extraction of building footprints from airborne laser scanning: Comparison and validation techniques. Urban Remote Sensing Joint Event, 2007: 1-9.

Ravanbakhsh, M. and Fraser, C. S. (2009). Road Roundabout Extraction from very High Resolution Aerial Imagery. CMRT09,(Eds:), UStilla, Rottensteiner, F. and Paparoditis, N.,Vol. XXXVIII, Part 3/W4, Paris, France.

Read, R. E. and Graham, R. W. (2002). Manual of Air Survey: Primary Data AcquisitionCaithness,Scotlank, UK, Whittles Publishing,

Ressl, C., Kager, H. and Mandlburger, G. (2008). Quality checking of ALS projects using statistics of strip differences. The International Archives of the Photogrammetry, Remote Sensing and Spatial Information Sciences,37: pp. 253-260.

Reulke, R., Becker, S., Haala, N. and Tempelmann, U. (2006). Determination and improvement of spatial resolution of the CCD-line-scanner system ADS40. ISPRS Journal of Photogrammetry and Remote Sensing, 60(2): 81-90.

Riain, G. Ó. and McCarthy, D. T. (2009). Spatial Video: Technology & Opportunities. 3rd Annual Irish Earth Observation Symposium, Geological Survey of Ireland, Dublin.

Rönnholm, P. (2010). Registration Quality Towards Integration of Laser Scanning and Photogrammetry. The 116th EuroSDR Science Committee Meeting. Frankfurt, Germany.

Rosengarten, H. (2007). Integraph's PhoWo Message. In Photogrammetric Week '07,D. Fritsch, Wichmann Verlag: 19-25.

Rottensteiner, F. and Briese, C. (2002). A new method for building extraction in urban areas from high-resolution LIDAR data. International Archives of the Photogrammetry, Remote Sensing and Spatial Information Sciences, vol. XXXIV(3A).

Rottensteiner, F., Trinder, J., Clode, S. and Kubik, K. (2005). Using the Dempster-Shafer method for the fusion of LIDAR data and multi-spectral images for building detection. Information Fusion, 6(4): 283-300.

Rottensteiner, F., Trinder, J., Clode, S. and Kubik, K. (2007). Building detection by fusion of airborne laser scanner data and multi-spectral images: Performance evaluation and sensitivity analysis. ISPRS Journal of Photogrammetry and Remote Sensing, 62(2): 135-149.

Rottensteiner, F., Trinder, J., Clode, S., Kubik, K. and Lovell, B. (2004). Building detection by Dempster-Shafer fusion of LIDAR data and multispectral aerial imagery. Proceedings of the 17th International Conference on Pattern Recognition, 2004.,2: 339-342.

Rutzinger, M., Oude, E., S. , Pu, S. and Vosselman, G. (2009). Automatic extraction of vertical walls from mobile and airborne laser scanning data. Laser scanning 2009, IAPRS, Vol. XXXVIII, Part 3/W8,P.-D. M. Bretar F, Vosselman G (Eds), Paris, France: 7-11.

Rutzinger, M., Rottensteiner, F. and Pfeifer, N. (2009). A Comparison of Evaluation Techniques for Building Extraction From Airborne Laser Scanning. Selected Topics in Applied Earth Observations and Remote Sensing, IEEE Journal of, 2(1): 11-20.

Samadzadegan, F., Azizi, A., Hahn, M. and Lucas, C. (2005). Automatic 3D object recognition and reconstruction based on neuro-fuzzy modelling. ISPRS Journal of Photogrammetry and Remote Sensing, 59(5): 255-277.

Sandau, R., Braunecker, B., Driescher, H., Eckardt, A., Hilbert, S., Hutton, J., Kirchhofer, W., Lithopoulos, E., Reulke, R. and Wicki, S. (2000). Design Principles of the LH systems ADS40 Airborne Digital Sensor. XIXth ISPRS Congress,Vol. XXXIII B1, Amsterdam, The Netherlands: 258-265.

Schenk, T. and Csatho, B. (2002). Fusion of Lidar data and aerial imagery for a more complete surface descriptor. IAPSIS, Vol XXXIV 3A: 310–317.

Shafer, G. (1976). A mathematical theory of evidence, Princeton university press Princeton, NJ,

Shan, J. and Toth, C. K. (2008). Topographic Laser Ranging and Scanning : Principles and Processing. London, Taylor and Francis.

Shufelt, J. A. and McKeown, D. M. (1993). Fusion of monocular cues to detect man-made structures in aerial imagery. CVGIP: Image Understanding, 57(3): 307-330.

Sithole, G. and Vosselman, G. (2004). Experimental comparison of filter algorithms for bare-Earth extraction from airborne laser scanning point clouds. ISPRS Journal of Photogrammetry and Remote Sensing, 59(1-2): 85-101.

Soheilian, B., Paparoditis, N., Boldo, D. and Rudant, J. P. (2007). Automatic 3D Extraction Of Rectangular Roadmarks With Centimeter Accuracy From Stereo-pairs Of A Ground-based Mobile Mapping System,vol. XXXVI, Part 5/C55, Padua, Italy: pp.22-27.

Soininen, A. (2004). TerraMatch User's Guide. Retrieved 6 August, 2010, from http://www.terrasolid.fi/system/files/tmatch.pdf.

Soininen, A. (2010). TerraScan User's Guide. Retrieved 5th May, 2010, from http://www.terrasolid.fi/system/files/tscan_1.pdf.

Sound Fighter Systems, L. L. C. (2010). Common Questions. Retrieved 25 July, 2010, from http://www.soundfighter.com/content.asp?page=7#q02.

Spiller, R. H. (1999). Z/I Imaging: A new system provider for photogrammetry and GIS. In Photogrammetric Week '99,D. Fritsch, Spiller, R., Wichmann Verlag: 35-42.

Steinle, E. and Vögtle, T. (2000). Effects of different laserscanning modes on the results of building recognition and reconstruction. XIXth ISPRS Congress,Vol. XXXII, Amsterdam, The Netherlands: 858– 865.

Suveg, I. and Vosselman, G. (2004). Reconstruction of 3D building models from aerial images and maps. ISPRS Journal of Photogrammetry and Remote Sensing, 58(3-4): 202-224.

Tao, C., Li, R. and Chapman, M. A. (1998). Automatic reconstruction of road center-lines from mobile mapping image sequences. Photogrammetric Engineering and Remote Sensing, 64(7): 709-716.

Taubenböck, H., Esch, T. and Roth, A. (2006). An urban classification approach based on an object-oriented analysis of high resoltion satellite imagery for a spatial structuring within urban areas. 1st EARSeL Workshop of the SIG Urban Remote Sensing. Humboldt-Universität zu Berlin.

Tempelmann, U., Börner, A., Chaplin, B., Hinsken, L., Mykhalevych, B., Miller, S., Recke, U., Reulke, R. and Uebbing, R. (2000). Photogrammetric software for the LH systems ADS40 Airborne Digital Sensor. Int. Arch. of Photogrammetry and Remote Sensing. Amsterdam, The Netherlands. Vol. 33, Part B2,pp. 552-559.

Vögtle, T. and Steinle, E. (2000). 3D Modelling of buildings using laser scanning and spectral information. Geoinformation for all, XIXth Congress of the ISPRS,Vol. XXXIII, Part B3, Amsterdam, The Netherlands: 927–934.

Vögtle, T. and Steinle, E. (2003). On the quality of object classification and automated building modeling based on laserscanning data. IAPRS. vol.XXXIV-3W13**:** 149-155.

Vögtle, T. and Steinle, E. (2005). Fusion of 3D building models derived from first and last pulse laserscanning data. Information Fusion, 6(4): 275-281.

Vosselman, G. (1999). Building reconstruction using planar faces in very high density height data. International Archives of Photogrammetry and Remote Sensing, 32(3; SECT 2W5): 87-94.

Vosselman, G. (2000). Slope based filtering of laser altimetry data. Geoinformation for all, XIXth Congress of the ISPRS,Vol. XXXIII, Amsterdam, The Netherlands.

Walter, V. (2004). Object-based classification of remote sensing data for change detection. ISPRS Journal of Photogrammetry and Remote Sensing, 58(3-4): 225-238.

Waser, L., Klonus, S., Ehlers, M., Küchler, M. and Jung, A. (2010). Potential of Digital Sensors for Land Cover and Tree Species Classifications A Case Study in the Framework of the DGPF-Project PFG Photogrammetrie, Fernerkundung, Geoinformation 2(2): pp. 141-156.

Weidner, U. and Förstner, W. (1995). Towards automatic building extraction from high-resolution digital elevation models. ISPRS Journal of Photogrammetry and Remote Sensing, 50(4): 38-49.

WG-AEN. (2006). Good Practice Guide for Strategic Noise Mapping and the Production of Associated Data on Noise Exposure. Assessment of Exposure to Noise Version 2.   Retrieved 2 January, 2010, from http://ec.europa.eu/environment/noise/pdf/wg_aen.pdf.

Yi Hui Lu, Trinder, J. C. and Kubik, K. (2006). Automatic building detection using the dempster-shafer algorithm.American Society for Photogrammetry and Remote Sensing Bethesda, MD, ETATS-UNIS9.

Zhang, C. (2004). Towards an operational system for automated updating of road databases by integration of imagery and geodata. ISPRS Journal of Photogrammetry and Remote Sensing, 58(3-4): 166-186.

Zhang, Y. (1999). Optimisation of building detection in satellite images by combining multispectral classification and texture filtering. ISPRS journal of photogrammetry and remote sensing, 54(1): 50-60.

Zingaretti, P., Frontoni, E., Forlani, G. and Nardinocchi, C. (2007). Automatic extraction of LIDAR data classification rules. 14th International Conference on Image Analysis and Processing, 2007. ICIAP 2007. : 273-278.

Appendix-I

LPS DSM

Image DSM Height (m)	GPS Z (m)	Δh (m)	Maximum Difference (m)	N (number of tested points)	RMSE (m)	Blunders Definition S>3*RMSE (m)	Maximum Difference * 3 (m)	Number of Blunders	Number of Points without Blunders	Δh without Blunders (m)	Mean (m)	Standard Deviation (m)
3.432	3.341	0.091	0.091	13	0.489	1.468	0.272	3	10	0.091	-0.102	0.200
3.695	3.658	0.037	0.037				0.112			0.037		
30.054	30.02	0.034	0.034				0.103			0.034		
11.350	11.21	0.140	0.140				0.420			0.140		
12.972	13.275	-0.303	0.303				0.910			-0.303		
4.876	6.035	-1.159	1.159				3.477			xxxx		
6.435	7.437	-1.002	1.002				3.007			xxxx		
31.209	31.616	-0.407	0.407				1.221			-0.407		
32.975	33.359	-0.384	0.384				1.152			-0.384		
30.512	31.061	-0.549	0.549				1.648			xxxx		
17.837	17.854	-0.017	0.017				0.051			-0.017		
9.485	9.651	-0.166	0.166				0.499			-0.166		
15.198	15.24	-0.042	0.042				0.125			-0.042		

Match-T DSM

Images DSM Height (m)	GPS Z (m)	Δh (1-3) (m)	Maximum Difference	N (number of tested points)	RMSE (m)	Blunders Definition S>3*RMSE (m)	Maximum Difference * 3 (m)	Number of Blunders	Number of Points without Blunders	Δh without Blunders (m)	Mean (m)	Standard Deviation (m)
3.502	3.341	-0.161	0.161	10	0.321	0.962	0.482	2	8	-0.161	-0.001	0.160
3.748	3.658	-0.090	0.090				0.270			-0.090		
30.038	30.02	-0.018	0.018				0.054			-0.018		
11.329	11.21	-0.119	0.119				0.356			-0.119		
13.002	13.275	0.273	0.273				0.820			0.273		
33.137	33.359	0.222	0.222				0.667			0.222		
30.511	31.061	0.550	0.550				1.650			xxxx		
17.908	17.854	-0.054	0.054				0.162			-0.054		
8.912	9.651	0.739	0.739				2.217			xxxx		
15.303	15.24	-0.063	0.063				0.188			-0.063		

LiDAR DSM

LiDAR DSM Height (m)	GPS Z (m)	∆h (1-3) (m)	Maximum Difference (m)	N (number of tested points)	RMSE (m)	Blunders Definition S>3*RMSE (m)	Maximum Difference * 3 (m)	Number of Blunders	Number of Points without Blunders	∆h without Blunders (m)	Mean (m)	Standard Deviation (m)
47.704	48.384	-0.680	0.680	14	0.444	1.333	2.039	5	9	xxxx	-0.035	0.109
3.824	3.341	0.483	0.483				1.448			xxxx		
3.747	3.658	0.089	0.089				0.267			0.089		
29.914	30.02	-0.106	0.106				0.318			-0.106		
11.234	11.21	0.024	0.024				0.073			0.024		
13.295	13.275	0.020	0.020				0.059			0.020		
6.048	6.035	0.013	0.013				0.039			0.013		
7.464	7.437	0.027	0.027				0.080			0.027		
31.606	31.616	-0.010	0.010				0.031			-0.010		
32.362	33.359	-0.997	0.997				2.990			xxxx		
31.781	31.061	0.720	0.720				2.161			xxxx		
18.525	17.854	0.671	0.671				2.012			xxxx		
9.553	9.651	-0.098	0.098				0.293			-0.098		
14.965	15.24	-0.275	0.275				0.826			-0.275		

Appendix-II


RGB Orthophoto

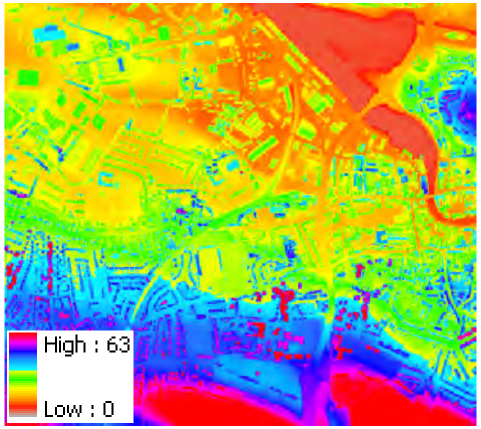

LiDAR DSM

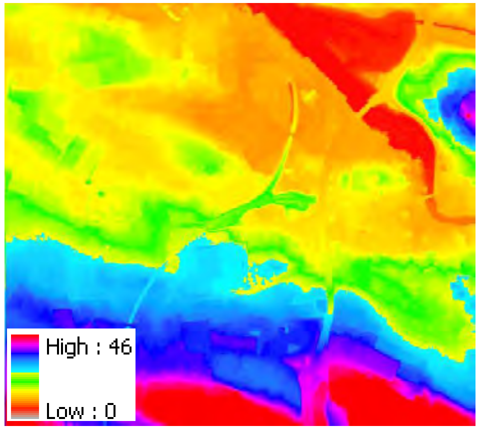

LiDAR DTM

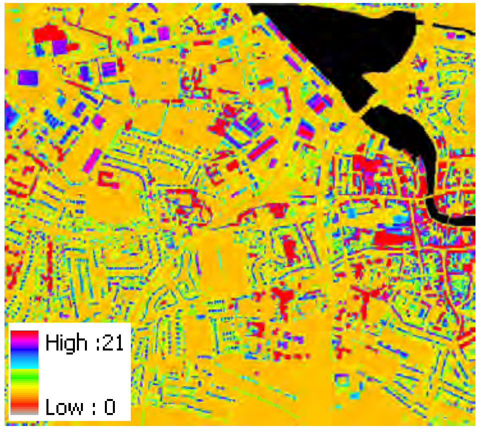

nDSM


nDSM ≥ 2.5m

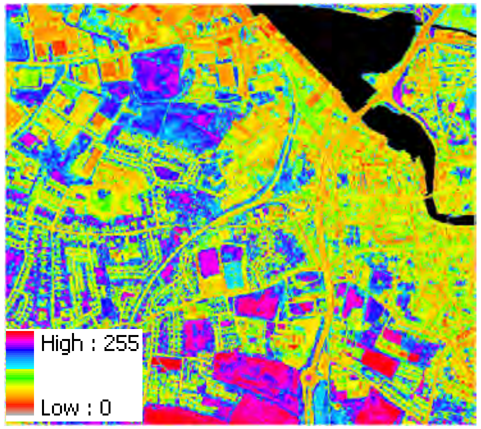

NDVI


NDVI ≤ 152.742

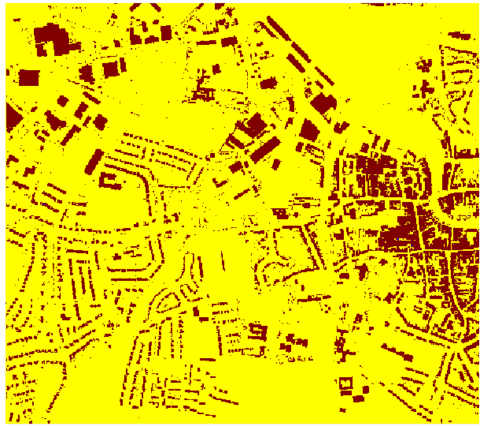
Raw Buildings (Brown)

VSNs		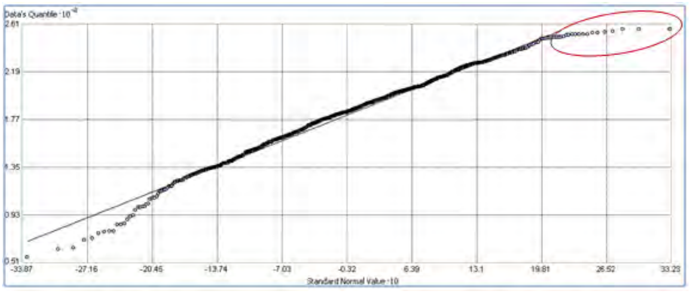
LRV		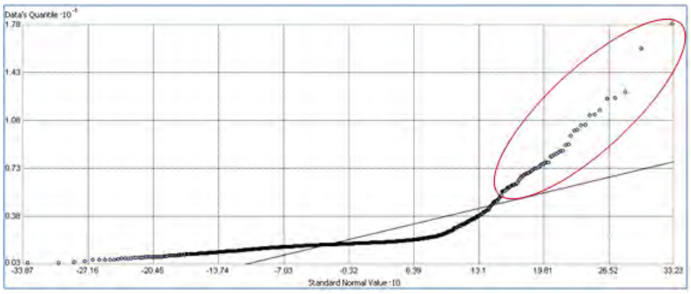
AD	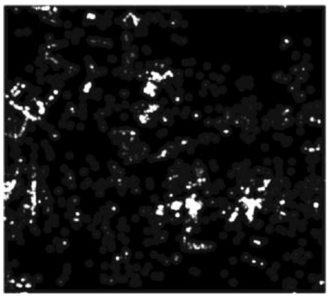	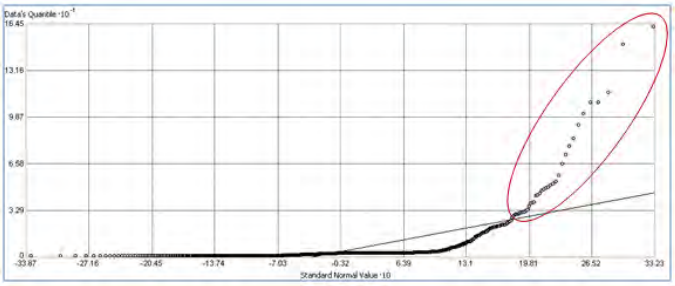
SR		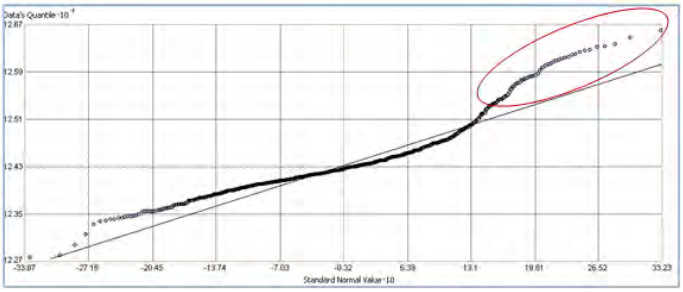

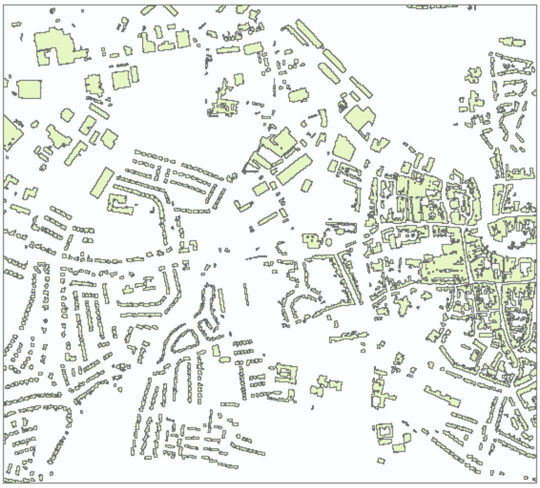

Extracted Buildings

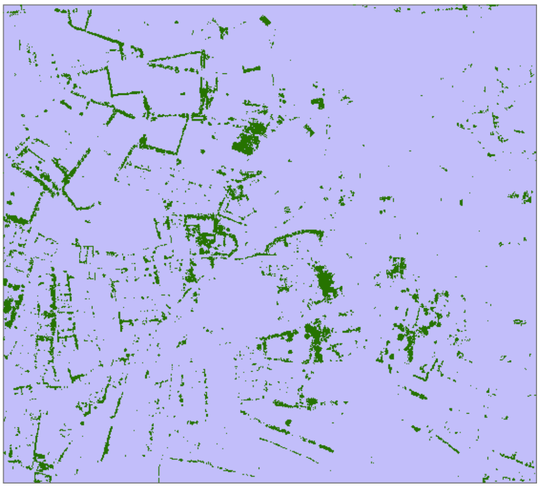

Vegetation (Green)

Trees Overlaying Orthophoto

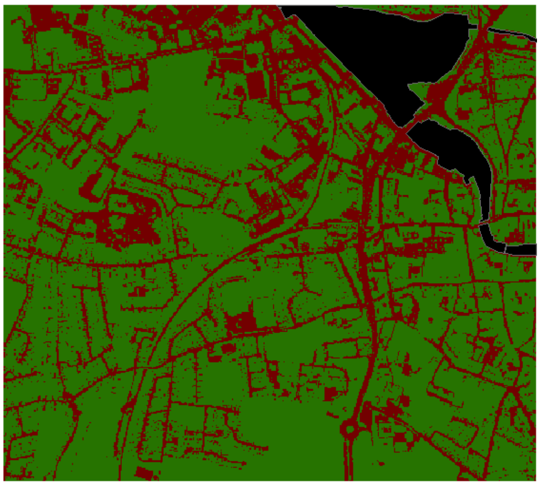

Classified Road (Red) and Ground (Green)

Roads (Red) Overlying Orthophoto

Appendix-III

RGB (Test-Area 2)

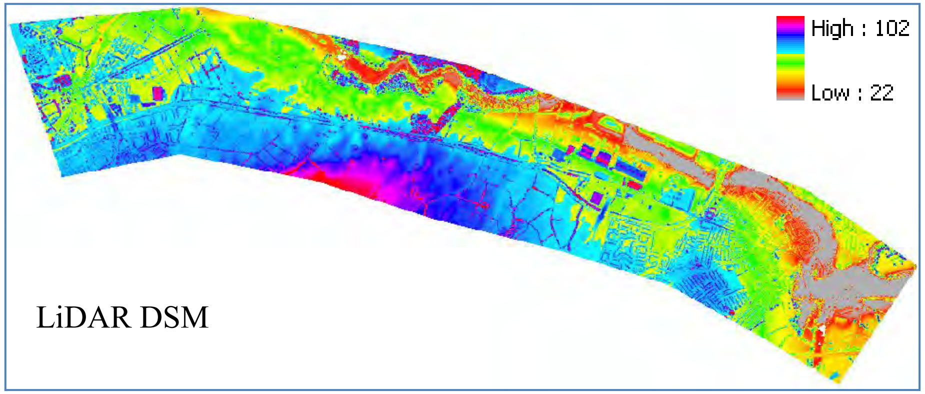

LiDAR DSM

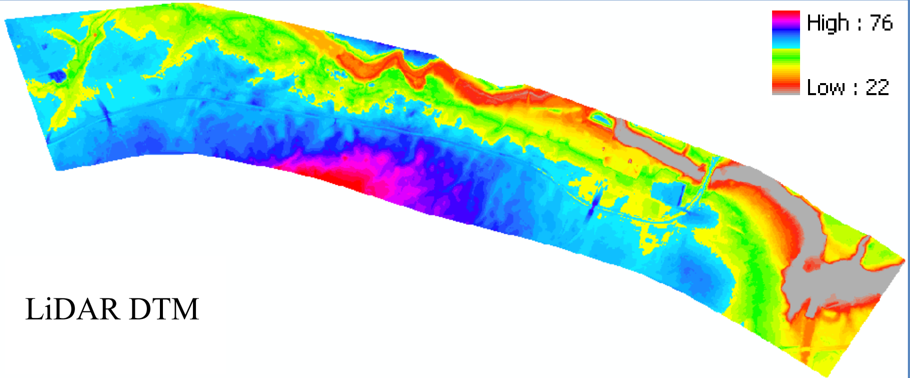

LiDAR DTM

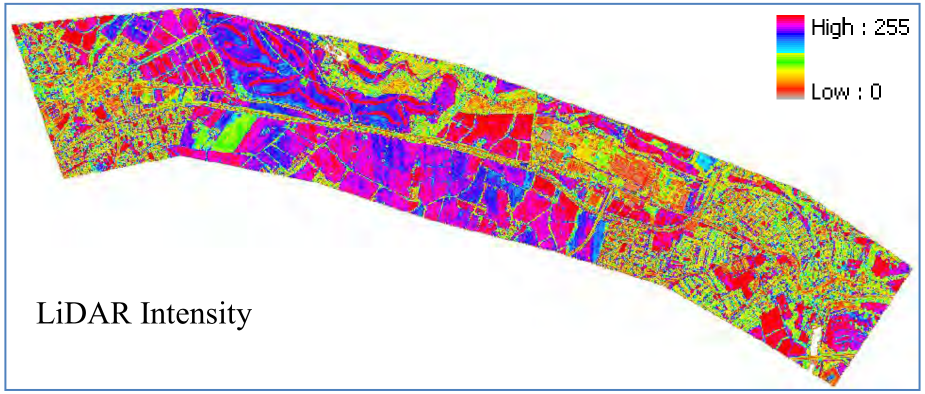

LiDAR Intensity

Appendix-III: Intermediate Results in the object extraction process for Test Area-2

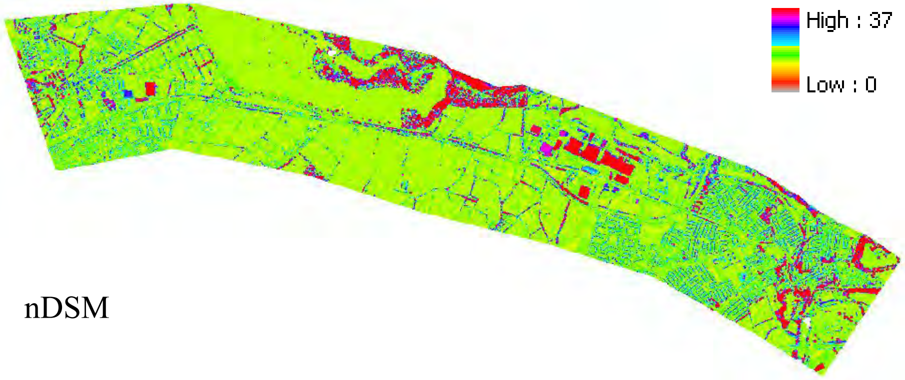

nDSM

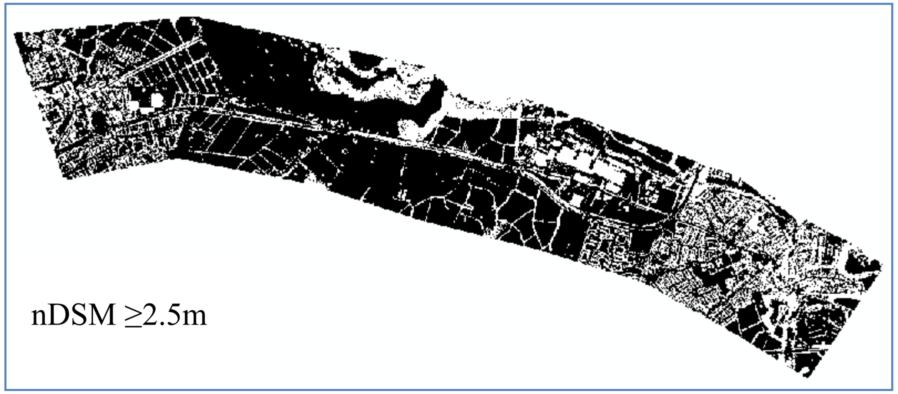

nDSM ≥2.5m

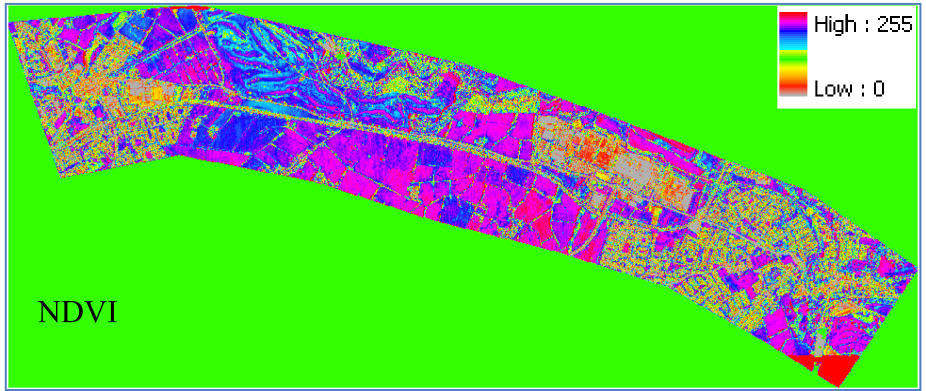

NDVI

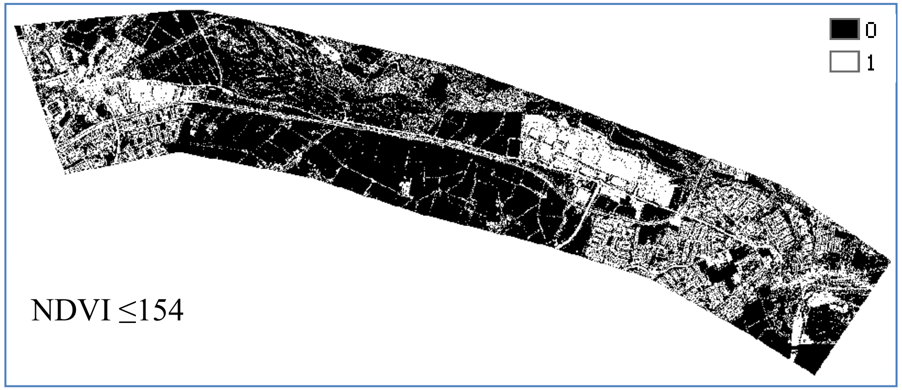

NDVI ≤154

Appendix-III: Intermediate Results in the object extraction process for Test Area-2

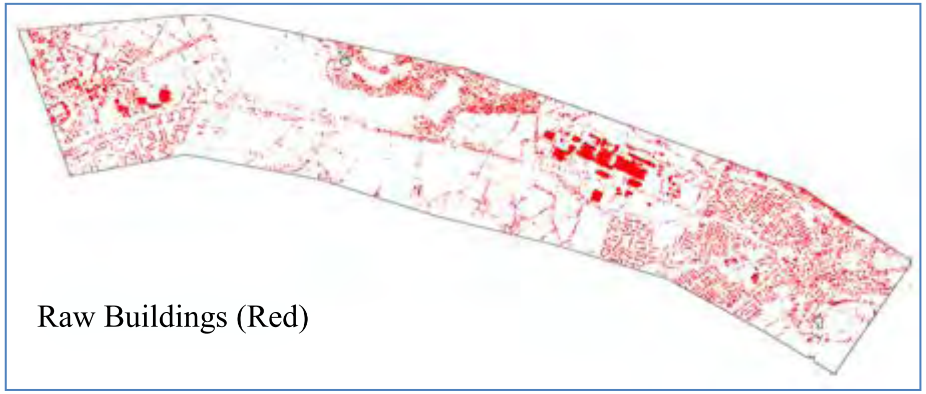

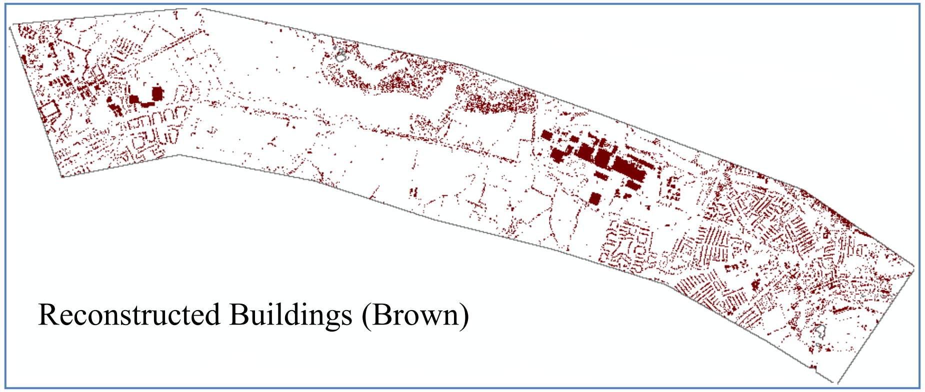

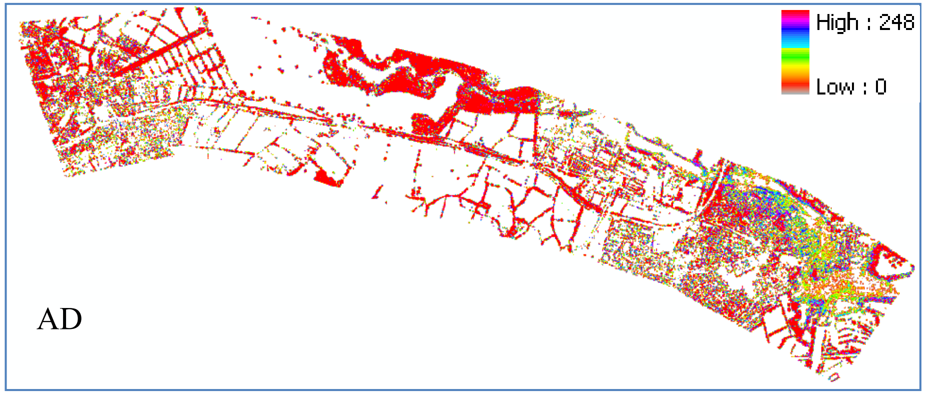

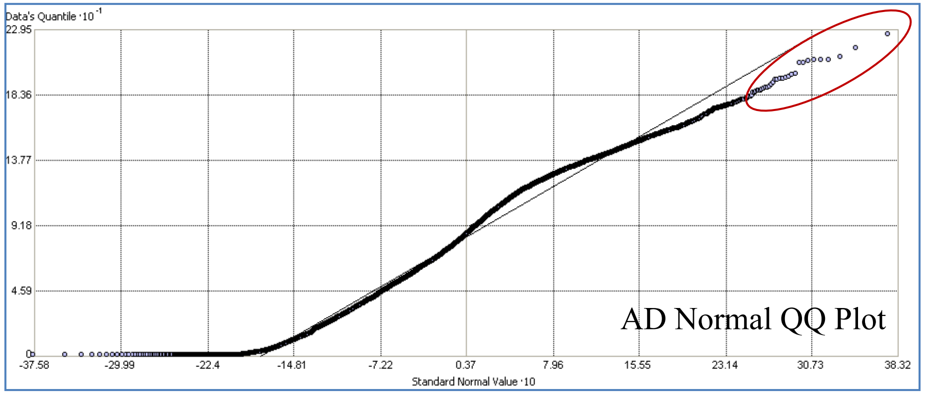

Appendix-III: Intermediate Results in the object extraction process for Test Area-2

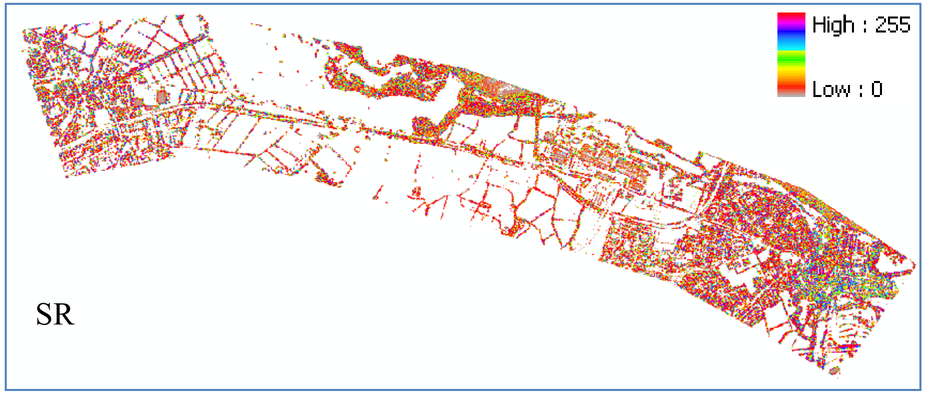

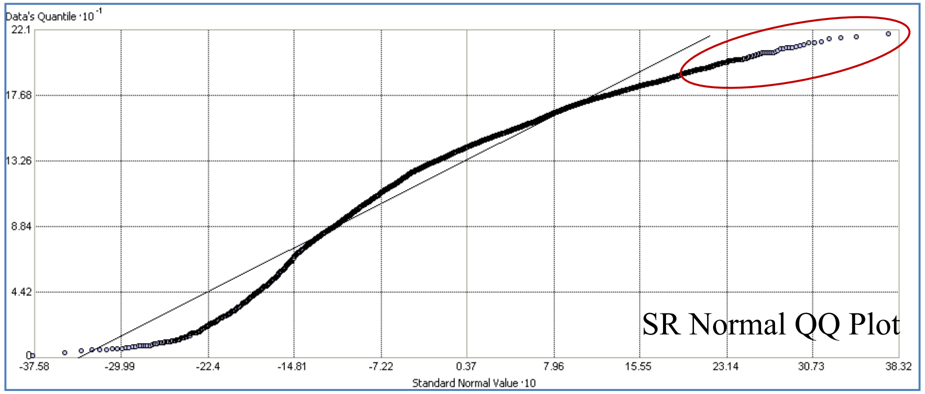

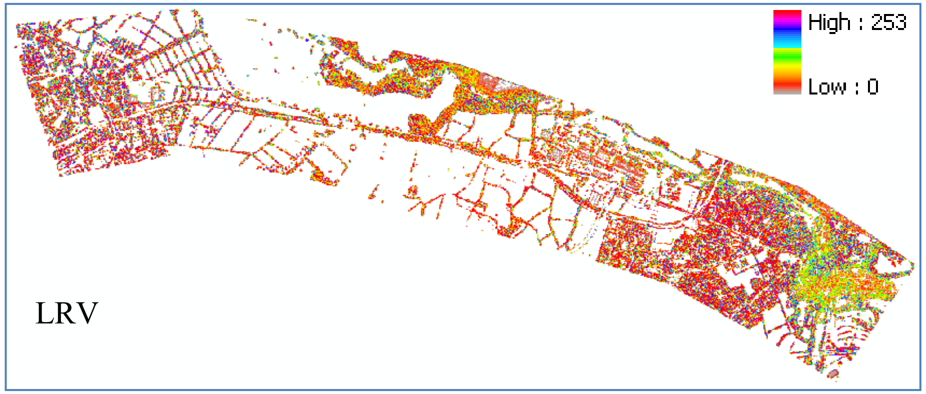

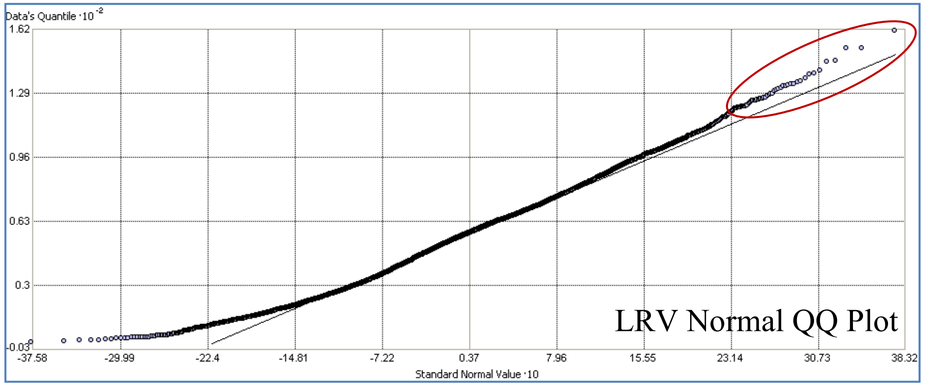

Appendix-III: Intermediate Results in the object extraction process for Test Area-2

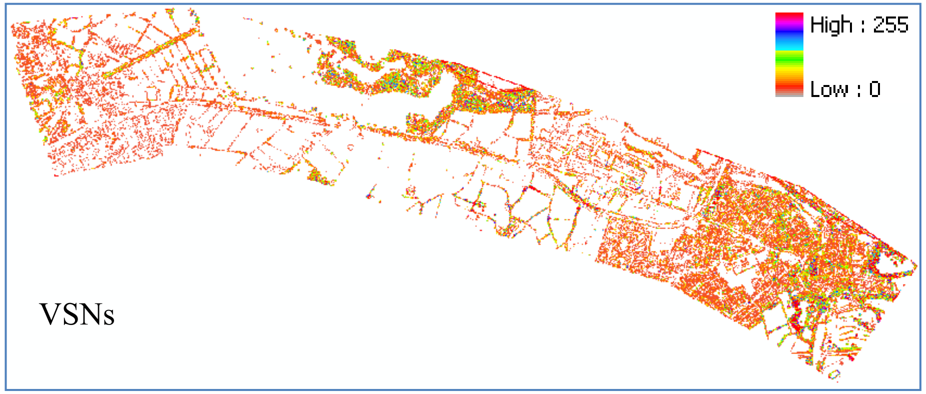

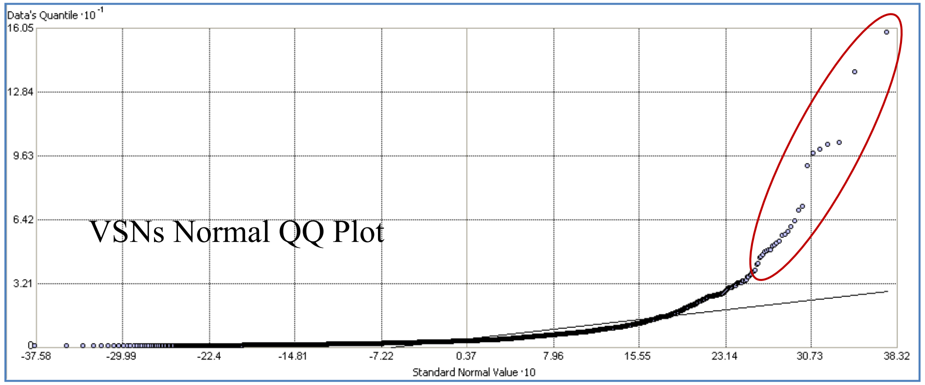

Extracted Vegetation (Green)

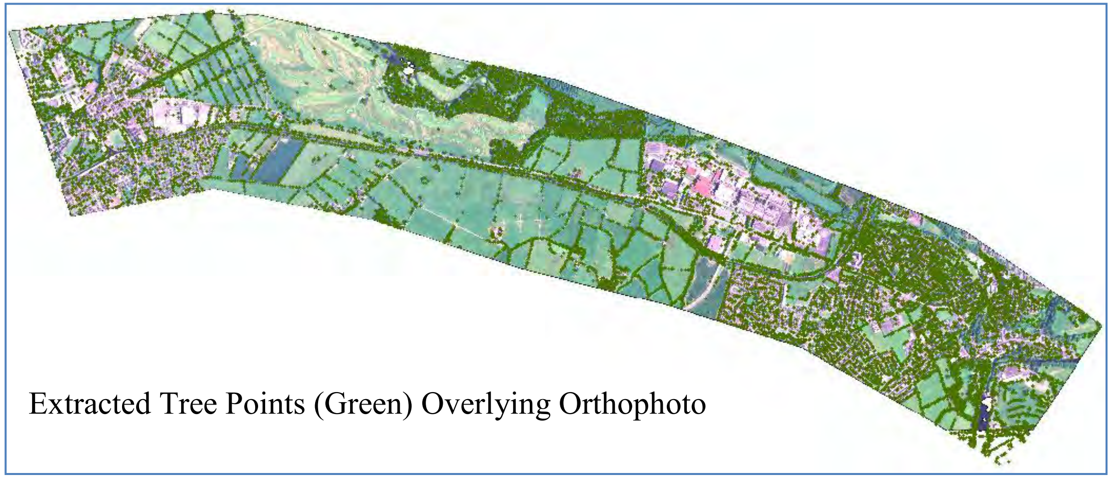

Extracted Tree Points (Green) Overlying Orthophoto

Appendix-III: Intermediate Results in the object extraction process for Test Area-2

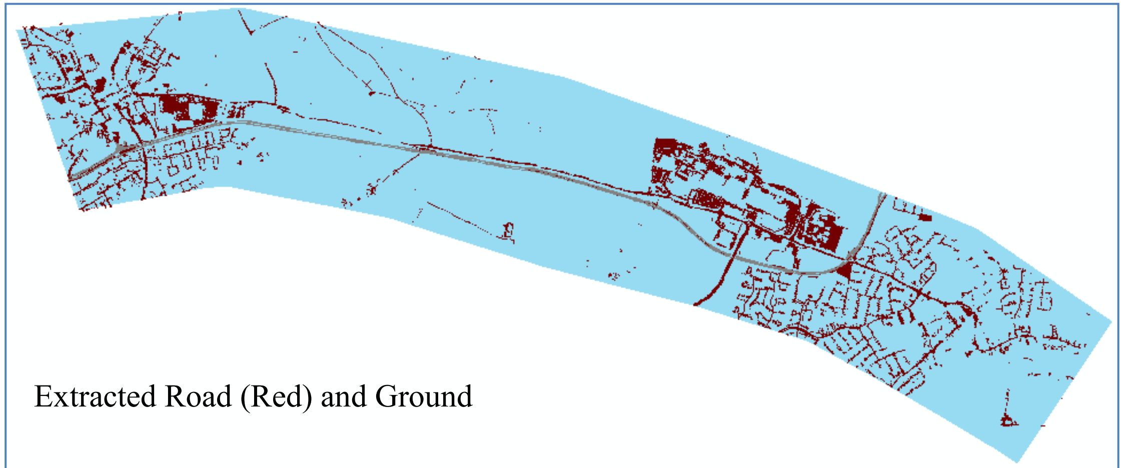

Extracted Road (Red) and Ground

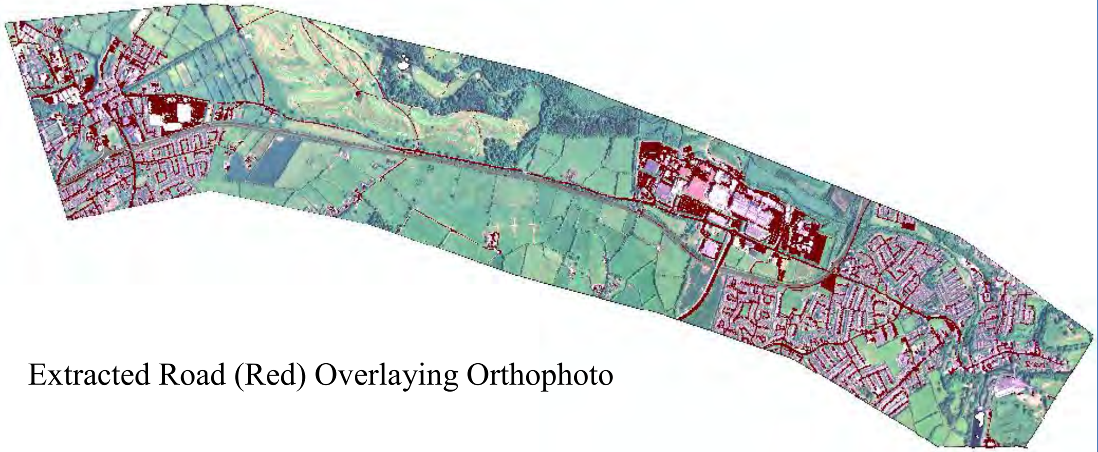

Extracted Road (Red) Overlaying Orthophoto

Appendix-IV

LiDAR Data Processing	
DSM	Point cloud exported from TerraScan and height image was created in Erdas Imagine after the adjustment of LiDAR strips.
DTM	Point cloud filtering in TerraScan to extract ground and raster image was created in Erdas Imagine. Operator knowledge of the area required for setting ground extraction parameters.
LiDAR Intensity Image	TerraScan
nDSM and thresholding (≥ 2.5 m)	Erdas Imagine
Local Range Variation	Erdas Imagine
Anisotropic Diffusion	Terrasolid and MATLAB
Variance of Surface Normals	MATLAB and Erdas Imagine
Surface Roughness	Erdas Imagine
Aerial Image Processing	
ADS40 Data Processing and Orthophotos	Leica Photogrammetric Suite (GPro and Orima)
Building Extraction	

NDVI image and its thresholding	Erdas Imagine and MATLAB
Raw Building Regions	Erdas Imagine
Building Reconstruction and mean value calculation of LiDAR classification cues in the building segments greater than 30 m^2 and exported as shape files	Definiens Ecognition
Thresholding of LiDAR classification cues for removing vegetation in the building segments	Normal QQ Plot in ArcGIS for selecting the appropriate thresholds and extracting final building objects
Vegetation Extraction	
Raw vegetation from thresholded NDVI and nDSM images	Erdas Imagine
Final Extracted Vegetation • Multi-resolution Segmentation • Gap filling • Size ≥ 5 m^2 • Shape for separating buildings and hedges • Vegetation relative border to buildings and not fully enclosed by buildings	Definiens Ecognition

Tree Extraction	
Inverted vegetation segments by reversing the height values	Erdas Imagine
Hydrological analysis for flow direction and accumulation Identifies of tree peaks Polygons to points Single tree and tree clusters	ArcGIS
Road Extraction	
Multi-resolution segmentation of nDSM, LiDAR intensity and thresholded NDVI image for extracting road surfaces	Definiens Ecognition
Gap filling	Erdas Imagine
Road Gradient	ArcGIS
Noise Barrier Extraction	
Candidate points using ground extracted from airborne LiDAR	TerraScan
Principal component analysis Robust Least Square fitting	MATLAB
Accuracy Assessment	

Building intersection	ArcGIS
Pixel-based Comparison	Erdas Imagine
Area Overlap	ArcGIS

Appendix-V

Area-1 (39 Points)		
Easting (m)	Northing (m)	Ortho. Height (m)
569525.964	837455.573	13.386
569395.23	837512.074	9.583
569372.012	837468.82	9.595
569369.838	837457.082	9.535
569368.145	837461.093	9.506
569366.297	837466.634	9.345
569371.631	837467.118	9.495
569372.809	837461.959	9.619
569373.907	837456.824	9.644
569373.873	837456.811	9.644
569382.154	837457.422	9.748
569382.257	837462.589	9.738
569389.58	837463.496	9.873
569390.444	837458.491	9.9
569396.933	837459.107	10
569397.199	837464.364	9.97
569403.694	837464.844	10.141
569404.692	837459.933	10.149
569411.952	837460.939	10.218
569411.644	837468.835	10.225
569406.415	837468.971	10.2
569406.1	837476.484	10.086
569410.663	837477.151	10.065
569410.168	837484.052	9.98
569405.205	837484.017	9.994
569404.537	837493.048	9.87
569409.167	837495.938	9.805
569408.684	837502.776	9.722
569403.552	837502.78	9.728
569402.637	837509.935	9.569
569407.833	837510.893	9.595
569406.736	837518.979	9.494
569402.164	837518.765	9.422
569395.654	837518.266	9.314
569396.163	837513.054	9.44
569402.071	837512.697	9.534
569525.932	837455.6	13.345

Area-2 (17 Points)		
Easting (m)	Northing (m)	Ortho. Height (m)
570474.605	837218.641	30.063
570475.388	837224.569	29.993
570509.094	837216.6	30.097
570488.453	837191.687	30.373
570489.444	837202.172	30.417
570488.802	837203.213	30.411
570484.798	837205.325	30.397
570482.431	837209.086	30.33
570482.343	837213.417	30.184
570484.801	837217.29	30.076
570488.596	837219.063	30.017
570493.006	837218.672	30.043
570496.596	837215.987	30.091
570498.105	837211.757	30.22
570497.07	837207.423	30.336
570493.881	837204.376	30.455
570490.047	837203.366	30.43

Area-3 (37 Points)		
Easting (m)	Northing (m)	Ortho. Height (m)
570610.019	836711.486	10.496
570673.945	836692.54	10.877
570729.28	836686.344	11.322
570729.801	836690.509	11.369
570720.551	836691.933	11.344
570720.003	836687.513	11.181
570727.624	836684.095	11.123
570721.833	836683.976	11.15
570715.194	836684.988	11.025
570709.873	836688.709	11.158
570710.132	836693.163	11.216
570700.499	836694.284	11.105
570699.829	836689.842	11.034
570690.255	836691.109	10.883
570690.535	836695.389	11.018
570681.303	836696.619	10.981
570680.038	836692.052	10.799
570671.748	836694.089	10.808
570672.037	836698.619	10.836
570663.133	836700.502	10.822
570661.601	836696.151	10.668
570652.435	836697.87	10.626
570653.063	836702.408	10.733
570644.115	836704.836	10.649
570642.621	836700.482	10.543
570634.004	836703.095	10.551
570634.975	836707.421	10.59
570626.676	836710.282	10.531
570624.553	836706.163	10.448
570617.219	836709.227	10.441
570618.638	836713.443	10.487
570612.732	836715.411	10.424
570611.535	836711.658	10.393
570609.691	836706.246	10.28
570615.682	836703.756	10.299
570621.457	836701.82	10.371
570628.132	836699.266	10.418

Area-4 (30 Points)		
Easting (m)	Northing (m)	Ortho. Height (m)
569896.165	836682.742	3.783
569908.773	836673.817	3.478
569919.444	836666.118	3.389
569902.848	836680.628	3.717
569938.161	836651.95	3.333
569947.839	836664.032	3.333
569934.769	836674.128	3.517
569922.889	836682.871	3.51
569904.869	836695.639	3.693
569913.442	836706.55	3.694
569931.867	836695.547	3.542
569944.228	836686.505	3.606
569956.52	836677.604	3.442
569965.633	836689.514	3.412
569952.883	836699.533	3.469
569940.905	836708.148	3.458
569952.029	836725.001	3.328
569973.373	836703.434	3.43
569962.945	836714.698	3.391
569976.27	836705.835	3.433
569986.104	836683.973	3.607
569976.637	836671.971	3.713
569967.725	836659.732	3.66
569958.383	836647.1	3.603
569947.879	836632.67	3.649
569938.16	836652.251	3.318
569925.411	836661.554	3.471
569913.714	836670.196	3.449
569900.995	836682.803	3.707
569943.608	836644.75	3.408

Area-5 (44 Points)		
Easting (m)	**Northing (m)**	**Ortho. Height (m)**
569889.161	837216.911	8.956
569889.096	837214.444	8.904
569889.037	837211.961	8.873
569889.004	837209.45	8.863
569888.946	837207.005	8.906
569888.935	837206.052	8.913
569888.893	837203.544	8.948
569888.837	837201.042	8.985
569888.777	837198.526	9.028
569888.73	837196.045	8.987
569888.695	837193.534	9.035
569888.654	837191.067	9.01
569888.603	837188.631	9.041
569888.583	837187.675	9.043
569888.565	837185.177	9.08
569888.488	837182.672	9.184
569888.455	837180.17	9.239
569888.412	837177.706	9.282
569888.363	837175.218	9.349
569881.881	837175.371	9.333
569881.907	837177.866	9.243
569881.967	837180.363	9.206
569882.013	837182.851	9.111
569882.079	837185.347	9.035
569882.077	837187.69	9.015
569882.098	837188.681	8.974
569882.155	837191.219	8.979
569882.212	837193.722	8.971
569882.254	837196.217	9.013
569882.27	837198.697	9.007
569882.317	837201.205	8.972
569882.347	837203.707	8.906
569882.353	837206.11	8.879
569882.403	837207.05	8.846
569882.417	837209.466	8.855
569882.483	837212.073	8.898

Area-5		
Easting (m)	**Northing (m)**	**Ortho. Height (m)**
569882.497	837214.536	8.913
569882.576	837217.032	8.97
569885.926	837219.491	9.058
569885.748	837210.597	8.955
569885.577	837201.839	9.06
569885.402	837191.993	9.062
569885.262	837181.735	9.198
569885.124	837172.997	9.414

Appendix-VI

Area-1 (44 Points)		
Easting (m)	Northing (m)	Ortho. Height (m)
694285.252	737716.458	57.27
694288.524	737713.473	57.35
694291.845	737713.673	57.337
694297.066	737713.884	57.385
694295.729	737707.414	57.452
694274.772	737706.35	57.442
694267.425	737705.853	57.421
694261.597	737705.49	57.432
694252.89	737705.004	57.432
694245.949	737704.627	57.424
694241.054	737704.391	57.434
694230.273	737703.621	57.456
694220.874	737703.289	57.449
694223.215	737693.833	57.43
694228.938	737694.167	57.418
694235.733	737694.49	57.42
694242.343	737694.89	57.438
694249.99	737695.344	57.413
694259.355	737695.757	57.446
694266.188	737696.076	57.441
694275.311	737696.514	57.474
694283.722	737696.923	57.489
694295.004	737697.643	57.522
694293.003	737672.994	57.429
694284.752	737672.475	57.251
694275.27	737672.047	57.185
694267.962	737671.557	57.142
694252.213	737670.817	57.196
694242.407	737670.32	57.204
694242.08	737673.581	57.174
694239.652	737673.296	57.157
694239.775	737670.313	57.226
694237.935	737655.395	57.2
694238.253	737647.443	57.209
694236.92	737639.729	57.204
694242.622	737638.275	57.209
694248.266	737631.995	57.221
694252.072	737623.378	57.209

Area-2 (35 Points)		
Easting (m)	Northing (m)	Ortho. Height (m)
699782.824	736799.088	40.045
699783.141	736799	40.043
699793.482	736796.452	39.835
699786.994	736795.344	39.979
699786.982	736795.368	39.965
699784.019	736793.965	40.055
699770.85	736786.893	40.399
699770.855	736786.898	40.407
699763.767	736784.465	40.565
699757.426	736782.007	40.731
699752.37	736772.898	40.927
699747.722	736774.478	40.937
699742.31	736775.239	40.739
699732.576	736776.268	40.358
699733.842	736784.12	40.157
699728.443	736790.991	39.915
699722.73	736798.387	39.603
699712.243	736802.06	39.352
699713.418	736810.097	39.263
699705.352	736809.125	39.179
699710.738	736824.388	39.598
699714.96	736826.352	39.683
699721.374	736827.538	40.039
699726.28	736824.559	40.417
699731.741	736824.539	40.699
699740.353	736821.888	41.273
699745.193	736823.174	41.306
699751.866	736818.643	41.751
699758.198	736816.884	41.849
699760.97	736814.018	41.945
699761.316	736808.311	41.948
699765.264	736805.86	41.934
699770.368	736806.239	41.76
699774.819	736807.459	41.512
699777.914	736803.867	41.051

Area-1		
694267.001	737623.33	57.223
694283.409	737624.083	57.27
694284.301	737633.982	57.248
694283.021	737649.794	57.305
694283.754	737666.019	57.277
694291.794	737675.492	57.391

Area-3 (52 Points)		
Easting (m)	Northing (m)	Ortho. Height (m)
698773.037	736716.169	56.004
698770.019	736717.508	56.057
698771.011	736719.79	56.019
698771.854	736722.146	56.031
698772.795	736724.477	56.051
698773.702	736726.773	56.076
698774.689	736729.04	56.106
698777.297	736735.273	56.082
698785.804	736732.212	56.12
698788.067	736731.254	56.106
698790.376	736730.306	56.095
698792.619	736729.362	56.103
698795.038	736728.36	56.092
698797.235	736727.467	56.052
698799.552	736726.465	56.046
698801.923	736725.493	56.055
698804.216	736724.563	56.051
698806.548	736723.567	56.07
698808.748	736722.695	56.142
698811.185	736721.67	56.127
698813.498	736720.71	56.081
698815.683	736719.8	56.1
698818.083	736718.731	56.017
698820.368	736717.795	56.029
698822.715	736716.88	56.1
698815.021	736712.322	56.113
698814.045	736710.356	56.273
698814.054	736710.118	56.212

Area-3		
Easting (m)	Northing (m)	Ortho. Height (m)
698777.3	736715.3	56.002
698777.2	736715.2	56.032
698779.1	736713.9	56.055
698780.8	736715.8	56.054
698784.8	736717.9	56.067
698789.1	736720.4	56.109
698795	736722.1	56.135
698802.2	736721.2	56.089
698805.5	736712.6	56.083
698801.5	736705.3	56.019
698799.8	736701.7	56.079
698798.2	736693.8	56.084
698793.6	736695.3	56.082
698788.3	736696.8	56.064
698781.3	736698.4	56.072
698774.7	736701.4	56.097
698766	736704.2	56.09
698761.6	736707.2	56.078
698754.2	736709.8	56.043
698747.9	736712.1	56.036
698744.6	736718	56.031
698745	736724.9	56.05
698746.8	736729.9	56.109
698751.8	736742.8	56.035